Development and Applications of Ionic Liquids and Near-Infrared Multispectral Imaging Techniques

Irena Mejac
Marquette University

Recommended Citation
Mejac, Irena, "Development and Applications of Ionic Liquids and Near-Infrared Multispectral Imaging Techniques" (2011). *Dissertations (2009 -)*. Paper 137.
http://epublications.marquette.edu/dissertations_mu/137

DEVELOPMENT AND APPLICATIONS OF IONIC LIQUIDS AND NEAR-INFRARED MULTISPECTRAL IMAGING TECHNIQUES

by

Irena Mejač, B.S.

A Dissertation submitted to the Faculty of the Graduate School,
Marquette University,
in Partial Fulfillment of the Requirements for
the Degree of Doctor of Philosophy

Milwaukee, Wisconsin
August 2011

ABSTRACT
DEVELOPMENT AND APPLICATIONS OF IONIC LIQUIDS AND NEAR-INFRARED MULTISPECTRAL IMAGING TECHNIQUES

Irena Mejač, B.S.

Marquette University, 2011

In this work, we explore novel analytical applications of Ionic Liquids and Near-infrared multispectral imaging microscopy.

Ionic liquids (ILs) belong to a group of organic salts that are liquid at room temperature and can be, due to their unique chemical and physical properties, successfully used for a variety of applications. The main goal of this study was to explore the synergistic use of ILs in chemical separations. Specifically, chiral ILs were used as novel chiral selectors for Capillary Electrophoresis and as solvents for stationary phase in Gas Chromatography. As chiral selectors IL provides baseline-separation as well as enantiomeric separation of pharmaceutical compounds, including (R)- and (S)-ibuprofen and flurbiprofen. ILs facilitated preparation of novel cavitand-impregnated ionic liquid stationary phase that can effectively separate different types of analytes, including a mixture of xylene isomers and isotopic isomers of methanol, chlorobenzene, dichlorobenzene, pyridine and 1,4-dioxane.

Near-infrared multispectral imaging (NIR-MSI) microscope was used to visualize and characterize individual gold nanoshells and nanocages as well as individual poly(N-isopropylacrylamide-co-acrylic acid) (NIPAM-co-AAc) hydrogel particles (with and without gold nanocages). Localized Surface Plasmon Resonance (LSPR), and its dependence on the dielectric constant of the medium, of individual gold nanoshells were successfully determined for the first time using the NIR-MSI microscope. The NIR-MSI microscope was also successfully used to determine Lower Critical Solution Temperature (LCST) phase transition of individual poly(NIPAM-co-AAc) hydrogels.

In addition to the applications of the NIR-MSI instrument described in the preceding paragraph, the NIR-MSI microscope was also used for classification of non-melanoma skin cancers. Specifically, both NIR and visible images as well as absorption spectra of Basal Cell Carcinoma, Squamous Cell Carcinoma and Seborrheic Keratosis (benign tumor) can be obtained by use of the microscope. Subsequent treatment of multispectral images obtained with statistical processing tools such as Linear Discriminant Analysis (LDA) made it possible to accurately diagnose different types of skin cancers.

ACKNOWLEDGMENTS

Irena Mejač, B.S.

I have learned and received help from many people. I am especially grateful to my advisor Dr. Chieu D. Tran and to members of my dissertation committee Drs. Jeanne M. Hossenlopp and Rathore Rajendra. My gratitude is extended to our collaborators, my research group members, and to Mr. Mark Bartelt and Mr. Joseph Holbus for their help with the instrument set-up. Finally, I am sincerely thankful to have such a great family and friends beside me.

TABLE OF CONTENTS

CHAPTER 6: EFFECT OF GOLD NANOCAGES ON ABSORPTION, IMAGING, AND LOWER CRITICAL SOLUTION TEMPERATURE PHASE TRANSITION OF INDIVIDUAL HYDROGEL PARTICLES

CHAPTER 7: EXPLORING THE APPLICATION OF NEAR-INFRARED MULTISPECTRAL IMAGING TECHNIQUE FOR DETERMINATION OF BASAL CELL CARCINOMA, SQUAMOUS CELL CARCINOMA AND SEBORRHEIC KERATOSIS

LIST OF TABLES

LIST OF FIGURES

CHAPTER 1

INTRODUCTION

Ionic liquids (ILs) belong to a group of organic salts that are liquid at room temperature and can be, due to their unique chemical and physical properties,[21-25] successfully used for a variety of applications. Because of their good conductivity ILs can be employed as a separation medium for capillary electrophoresis (CE). Recently developed chiral IL (S)-[3-(chloro-2-hydroxypropyl)trimethylammonium] [bis((trifluoromethyl)sulfonyl)amide] ((S)-$[CHTA]^+[Tf_2N]^-$) was found to exhibit relatively stronger enantiomeric recognition in solution.[21,22, 27] Its use as a chiral selector for CE was investigated in Chapter 2. CE was the preferred method of measurement over alternative enantioselective techniques (i.e., HPLC and GC) due to its fast analysis time, higher separation efficiency, method simplicity and small sample size requirement.[7,10-20] The purpose of the study was to develop and optimize the use of this chiral IL for chiral separation by CE. Specifically, the chiral ILs were synergistically used as a chiral selector for CE separation of a variety of pharmaceutical racemates, including atenolol, propranolol, warfarin, indoprofen, ketoprofen and flurbiprofen.

Ionic liquids are also known to be thermally stable and have high solubility power.[21-25] It is, therefore, expected that they would dissolve compounds with low solubility, such as cavitands. They (i.e., cavitands) are compounds with deep, one open-ended cavities that exhibit remarkable molecular recognition thorough host-guest interactions,[33-35] and are expected to be effective as stationary phase in separation science.

Subsequently, novel cavitand-impregnated ionic liquid stationary phase for GC was developed and its effectiveness was investigated in Chapter 3. Three ILs (i.e., octyl methylimidazolium bis((trifluoromethyl)sulfonyl)amide ($[OMIm]^+[Tf_2N]^-$), 1-butyl-3-methylimidazolium tetrafluoroborate ($[BMIm]^+[BF_4]^-$) and N-ethyl pyridinium trifluoroacetate ($[N\text{-}EtPy]^+[CF_3CO_2]^-$)) with different polarity (i.e., polarity increases from $[OMIm]^+[Tf_2N]^-$ to $[N\text{-}EtPy]^+[CF_3CO_2]^-$, respectively) were used in the study. Various types of analytes, including a mixture of xylene isomers and isotopic isomers of methanol, acetonitrile, chlorobenzene, dichlorobenzene, pyridine, and 1,4-dioxane, were tested in order to evaluate the performance of new SPs.

NIR spectroscopy has become extensively used in recent years as it provides rich information of samples throughout the whole NIR region (i.e., 800 to 2500 nm); that is C=O, O−H, N−H overtones and combination bands of the IR fundamental vibrations are observed.[65] Furthermore, due to shorter wavelengths and more energy-rich protons, NIR light penetrates sample more in depth, and as such is more applicable to in-vivo studies.[65] Different from NIR spectrometry, recently developed near-infrared multispectral imaging (NIR-MSI) microscope records NIR images for each scanned wavelength, thus providing spatial and spectral information of the measured sample.[74-78] Additionally, short analysis time (i.e., it takes 560 ms to record an NIR image for a specific wavelength) and high spatial resolution of the instrument (i.e., 0.93±0.3 µm/pixel) make it attainable to utilize an NIR-MSI microscope for a variety of applications that are not otherwise possible. In Chapter 4 individual gold nanoshells with dimensions of about 1 micron were measured, and the localized surface plasmon resonance(s) - LSPRs (i.e., strong absorption band due to the resonance between incident photon frequency and oscillation of the collective electrons)[33-35,37] of individual nanoshells were determined for the first time. Furthermore, the effect of solvents having different dielectric constants (i.e., deuterium oxide, acetonitrile-d_3, pyridine-d_5, acetone-d_6, ethyl acetate and formamide) on LSPRs was also investigated.

NIR-MSI microscope technology was further explored for characterization of hydrogel particles of dimensions ≥ 1 micron. As will be described in Chapter 5, poly(N-isopropylacrylamide-co-Acrylic acid) hydrogel particles are soluble in water below the lower critical solution temperature (LCST) whereas they shrink and become hydrophobic above the LCST.[60,93] Due to the inhomogeneity of the particle size in solution, it is important to study the LCST properties of the individual particles. Consequently, the goal of this experiment was to monitor and characterize volume transition properties of the individual PNIPAM hydrogel particles and to evaluate the relationship between the dimensions of the particles and their respective LCST transitions. Because PNIPAM hydrogels undergo volume transitions they can be potentially used in in-vivo studies as drug delivery vehicles. Effective photothermal activation of the hydrogel particles would thus greatly depend on their absorption intensity. Gold nanocages (GNs) exhibit LSPR and, due to their large LSPR absorption cross-sections,[56,130] can facilitate absorption of the sample. Such considerations prompted us to investigate the effect of GNs on the absorption and imaging of individual PNIPAM hydrogel particles as well as on their LCST transitions (Chapter 6).

Finally, the NIR-MSI microscope was investigated as means to classify non-melanoma skin cancers (i.e., basal cell carcinoma (BCC) and squamous cell carcinoma (SCC)) and benign tumor seborrheic keratosis (SK). Presently used classification methods are invasive, expensive as well as time consuming. More importantly, 50% of early malignant lesions may not be detected during routine clinical examination[147] and only 80 to 90% classification accuracy is reported for fully developed malignant tumors.[147] Consequently, NIR-MSI microscope technique was investigated as an accurate method for classification of skin cancers. Statistical technique such as linear discriminant analysis (LDA) was then employed to analyze minute differences among NIR spectra obtained in order to accurately classify different types of cancers.

CHAPTER 2

CHIRAL IONIC LIQUIDS INDUCED ENANTIOSEPARATION OF PHARMACEUTICAL PRODUCTS VIA CAPILLARY ELECTROPHORESIS

2.1 INTRODUCTION

Enantiomers are two chemically identical species that differ from each other by being non superimposable when comparing their mirror images. Such compounds are also known as chiral compounds. Due to the fact that very often only one form of enantiomers is chemically and/or biologically active, and the other(s) can reverse or limit the effect of the desired enantiomer, the enantiomeric separation is an important part of separation science and technology.[1-5] However, enantiomeric separation is not easily achieved because both enantiomers of the chiral compound behave identically in a symmetrical environment, i.e. they display identical physical and chemical properties. It is therefore not surprising that most of the synthetic chiral drugs on the market are sold as racemic mixtures. As a consequence, development of effective chiral separation methods is essential for the pharmaceutical industry. Two enantiomers can be differentiated by coupling with an auxiliary chiral reagent, thus forming diastereomers, which can then be separated using non-symmetrical separation techniques.[6] This method of separation is known as indirect enantiomeric resolution. Another approach, direct enantiomeric separation, is now commonly used. Specifically, the enantiomers are placed in a chiral environment and differentiated by the use of chiral selectors or chiral irradiation.[6] By principle, only chiral selectors (or chiral irradiation) can distinguish between two enantiomers. Enantioselectivity is achieved by transformation of the molecule into new chemical species that have different rates (kinetic enantioselectivity), or by forming adducts with different stabilities, also known as thermodynamic enantioselectivity.[6] In chromatographic systems, chiral selector(s) can be incorporated into the stationary phase as well as coated/bonded onto its surface. Such columns are therefore referred to as chiral or enantioselective columns. In cases where chiral selector(s) are in the mobile phase, the term chiral mobile phase is usually used. With chiral selectors in the stationary phase, the selectivity is based on more stable association of one enantiomer, compared to the other, therefore resulting in longer retention of that compound. Conversely, when a chiral mobile phase is used, an enantiomer that forms a stronger association with the chiral selector(s) will exhibit shorter retention times in the column.[6]

A wide variety of enantioselective columns for high performance liquid chromatography (HPLC) and gas chromatography (GC) are nowadays commercially available. As a result HPLC and GC are two of the most widely used methods for chiral separation.[1-5] Gas chromatographic chiral stationary phases are mostly based on various cyclodextrin derivatives;[7] however, novel methods also investigate the use of modified linear dextrins, dubbed acyclodextrins,[8] and chiral ionic liquids[9] as chiral stationary phases. Cyclodextrin based chiral stationary phases have a substantial use also in liquid chromatographic techniques; however, polysaccharide chiral columns are the most widely used.[6] In addition to these, chiral columns based on macrocyclic antibiotic and protein stationary phases are employed.[6]

In recent years, advances in capillary electrophoresis (CE) have provided an alternative means for chiral separation. Cyclodextrins have the ability to form inclusion complexes with various guest molecules, and have good stability in aqueous solution as well as high selectivity. Thus, it is not surprising that they are the most widely used chiral selectors in CE.[6] CE has several advantages over other enantioselective techniques (i.e. HPLC and GC) including fast analysis time, higher separation efficiency, method simplicity and small sample size requirement.[7,10-20] In contrast to chiral separation phases that are used in HPLC, there are not many known chiral selectors available for CE.[1-5,7,10-20] It is, therefore, of high importance to find/develop novel chiral selectors that can offer high selectivity and resolution for enantioseparation by CE. Chiral ionic liquids represent a good solution to this problem, because in addition to being chiral, they are also ionic liquids at room temperature and can thus serve as an electrolyte for CE.

Ionic liquids (ILs) are a group of organic salts that are liquid at room temperature.[21-25] They have unique chemical and physical properties, namely, they are air and moisture stable, have a high solubility power, good electrical conductivity and virtually no vapor pressure. Due to their non-toxicity or relatively lower toxicity they can also serve as a “green” alternative to traditionally used volatile organic solvents.[21-25] Thus far, ILs have successfully replaced traditional organic solvents in (1) organic and inorganic synthesis, (2) solvent extractions, (3) liquid-liquid extractions, (4) electrochemical reactions and (5) as a medium to enhance the sensitivity of thermal lens measurements.[21-29] In addition, chiral ILs can be used as chiral solvents for optical resolutions, for asymmetric induction in synthesis and as a chiral stationary phase in chromatography.[21,22] Thus, it may be possible to use chiral ionic liquids as a chiral selector for CE.

A disadvantage of using chiral ionic liquids as chiral selectors is associated with their commercial unavailability as well as in requirement of expensive reagents and elaborate synthetic schemes used to prepare a small number of reported chiral ionic liquids.[21,22] Due to these limitations the study and application of the chiral ILs as an electrolyte or/and chiral selector in CE have been severely hindered. The novel chiral IL that was used in our study, (S)-[3-(chloro-2-hydroxypropyl)trimethylammonium] [bis((trifluoromethyl)sulfonyl)amide] ((S)-$[CHTA]^+[Tf_2N]^-$), can be readily synthesized in an enantiomerically pure form by a simple ion exchange reaction from its corresponding chloride salt,[27,28] and therefore represents a good solution to the problem identified above. In addition, the characteristic properties of the IL are favorable for enantioselective separation. Specifically, (S)-$[CHTA]^+[Tf_2N]^-$ is liquid at room temperature and thermally stable up to a temperature of at least 300 ˚C; it does not undergo racemization at elevated temperature, i.e., besides being chemically stable it is also optically stable; exhibits strong solubility power; is soluble in aqueous solutions; and NIR and ^{19}F NMR studies with Mosher's salt show that optically active (R)- and (S)-$[CHTA]^+[Tf_2N]^-$ ionic liquids manifest relatively stronger enantiomeric recognition than other reported chiral ILs.[21,22, 27]

In this study we investigated the use of (S)-$[CHTA]^+[Tf_2N]^-$ IL as an electrolyte and/or chiral selector in capillary electrophoresis for separation of the following pharmaceutical recemates: atenolol, propranolol, warfarin, indoprofen, ketoprofen and flurbiprofen.

2.2 EXPERIMENTAL

2.2.1 Chemicals

Cholic acid, sodium salt hydrate (98%), tris(hydroxymethyl)aminomethane (99+%), (S)-(–)-3-(chloro-2-hydroxypropyl)trimethylammonium chloride ($CHTA^+Cl^-$) (99%), *N*-lithiotrifluoromethane ($Li^+Tf_2N^-$) (99.5%), atenolol, (S)-naproxen, warfarin, (R)-, (S)- and (RS)-flurbiprofen, (RS)-ibuprofen, indoprofen, (S)- and (RS)-ketoprofen were obtained from Sigma-Aldrich (Milwaukee, WI, USA). (R)-naproxen was purchased from Fluka (Buchs, Switzerland), 1-(S)-octyl-β-thioglucopyranoside (OTG) was from Pierce (Rockford, IL, USA), propranolol and (R)- and (S)-ibuprofen were from ICN Biomedicals (Aurora, OH, USA) and Biomol Research Labs (Plymouth Meeting, PA, USA), respectively. Chemical structures of chemicals used in the study are shown in **Scheme 2.1**.

(S)-[3-(chloro-2-hydroxypropyl)trimethylammonium][bis((trifluoromethyl) sulfonyl)amide] ((S)-$[CHTA]^+[Tf_2N]^-$) was prepared as follows: 1.88 g (10 mmol) of (S)-(–)-3-(chloro-2-hydroxypropyl) trimethylammonium chloride and 2.87 g (10 mmol) of *N*-lithiotrifluoromethane sulfonimide were each dissolved in 10 mL of distilled water. Two solutions were then mixed together and stirred for 2.5 h at room temperature. The mixture formed two layers. The top layer was removed and the remaining layer was washed with distilled water several times. After drying under vacuum at 60 ˚C for 10-12 h, the product was characterized by ^1H and ^{13}C NMR, IR, thermo-gravimetric analysis (TGA) and differential scanning calorimetry (DSC).[27,28]

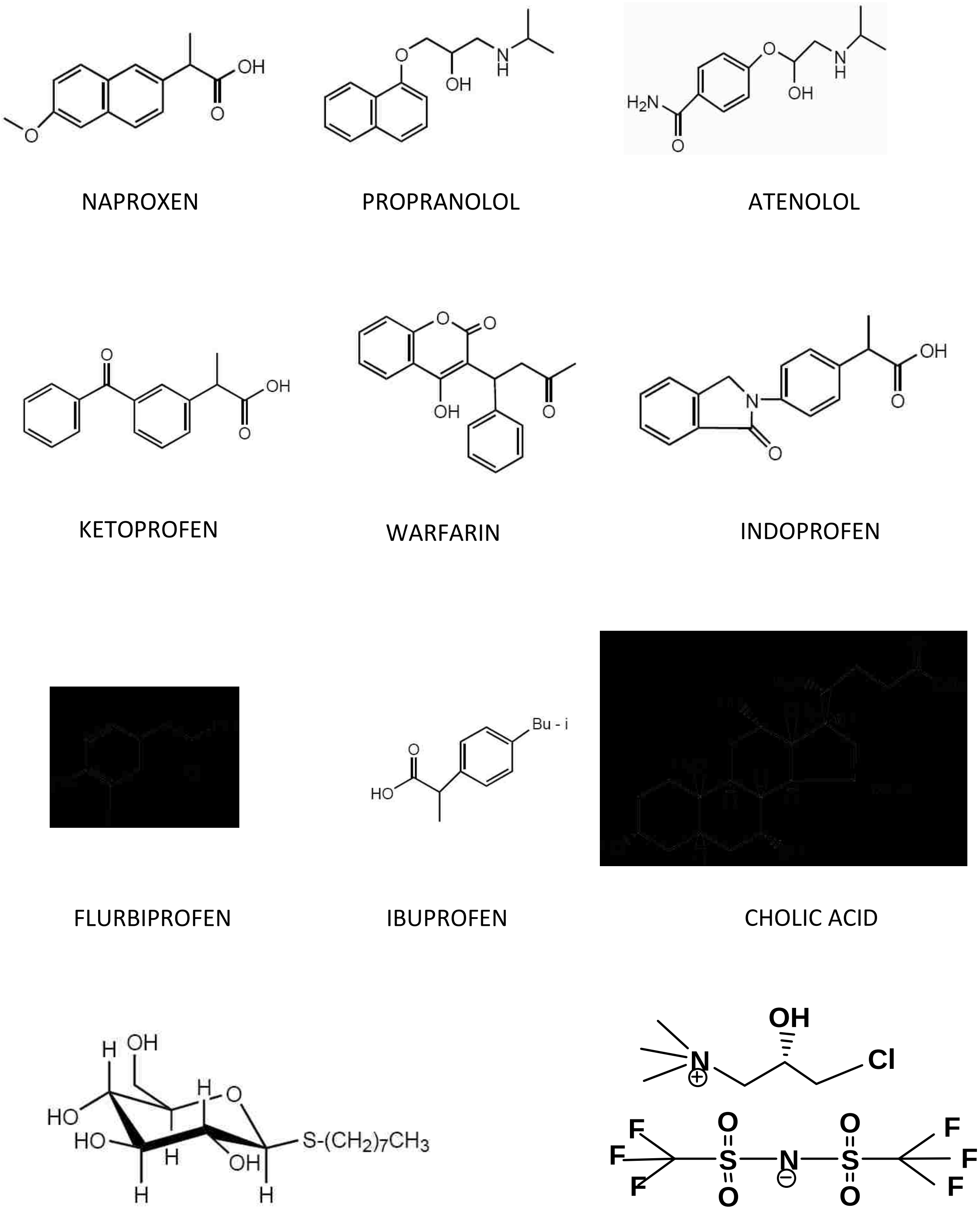

NAPROXEN

PROPRANOLOL

ATENOLOL

KETOPROFEN

WARFARIN

INDOPROFEN

FLURBIPROFEN

IBUPROFEN

CHOLIC ACID

1-S-Octyl-β-D-thioglucopyranoside

$[CHTA]^+[Tf_2N]^-$

Scheme 2.1: Structures of compounds used in this study.

2.2.2 Instrumentation and Methods

All CE measurements were performed on an ISCO Model 3850 electropherograph equipped with a UV detector (Isco, Lincoln, NE, USA) and coupled to a personal computer. Data were collected and analyzed by in-house written software. A typical CE instrument is shown in **Scheme 2.2**. Essentially it consists of a high voltage power supply, two buffer reservoirs, a capillary and detector. Migration of the species through the capillary is driven by an electric field. With the application of high voltage across the capillary, analyte ions (i.e. cations and anions) move towards the cathode and the anode, respectively. The separation mechanism of CE is based on different mobilities of species (either caused by the different electrophoretic mobilities or by different partition abilities between the buffer and the other phase); that is, zones of analytes are formed due to the different electrophoretic mobilities of ionic species. The electrophoretic mobility μ_e can be theoretically expressed as

$$\mu_e = \frac{q}{6\pi\eta r}$$

where q is the net charge of the analyte, η is the solution viscosity and r is the Stokes radius. The migration velocity ν of an ion (in cm/s) can therefore be expressed as

$$\nu = \mu_e \cdot \frac{V}{L}$$

where V is applied voltage (in Volts) and L is the length over which the voltage is apllied.[30] The electrolyte system, also called electrophoretic medium, separation medium, background electrolytes or buffer, plays an important role in CE by providing the chemical environment that solutes can migrate in. The separation medium has a variety of important functions: specifically, due to being sufficiently buffered, it provides a constant

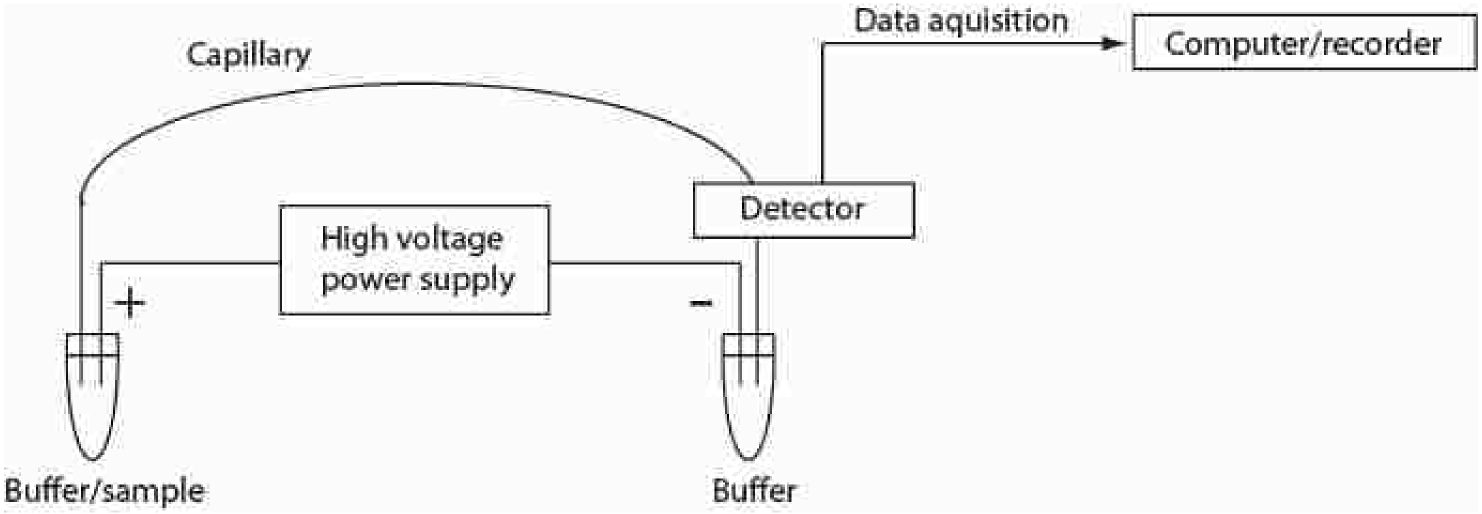

Scheme 2.2: Diagram of the essential components of a capillary electrophoresis system.

pH throughout the analysis, as well as small electric current between anode and cathode. Analytes are detected as they pass the window at the far end of the capillary. For our studies an untreated, bare fused silica capillary (MicroSolv Technology, Eatontown, NJ, USA) with dimensions of 50 cm × 50 μm I.D. (effective length to the detector: 37 cm) was used. The capillary was conditioned with 0.5 M sodium hydroxide, distilled water and running buffer (each for 10-15 min). Between analyses the capillary was rinsed with distilled water and running buffer. All samples were introduced by using vacuum injection mode (5 s injection time) and monitored at 214 nm. Migration of the sample through the capillary is driven by an electric field. In our case, voltage in the range of 10 to 30 kV with a positive potential at the injector end was applied. Sample solutions were prepared by dissolving ca. 0.5 mg of each analyte in 1 mL of the running buffer. *N*,*N*-dimethylformamide was used as a neutral marker to determine electroosmotic mobility.

Resolution values between two adjacent peaks were calculated using the following equation

$$R_S = 2\,[(t_R)_B - (t_R)_A] / (W_A + W_B)$$

where $(t_R)_A$ and $(t_R)_B$, and W_A and W_B are retention times and base widths, respectively, for two adjacent species, A and B. Selectivity factors were determined using the equation below

$$\alpha = [(t_R)_B - t_M] / [(t_R)_A - t_M]$$

where t_M is migration time for nonretained species (*N*,*N*-dimethylformamide); and $(t_R)_A$ and $(t_R)_B$ retention times for species A and B, respectively.

2.3 RESULTS AND DISCUSSION

Increasing the applied voltage resulted in a decrease of retention times. This result agrees well with the theoretical equation for migration velocity,[30] which predicts a linear increase in migration velocity, and consequently a decrease in retention times, with increased applied voltage. **Figure 2.1A** (left column) represents electropherograms of (RS)-flurbiprofen at 6 different applied voltages (i.e., 15 kV, 18 kV, 20 kV, 23 kV, 25 kV and 30 kV). It can readily be observed from the graph, that increasing the applied voltage results in shorter retention times. The linear relationship between retention times and applied voltages can be more clearly seen from **Figure 2.1A** (right column) and **Figure 2.1B**, which represent plots of retention times as a function of applied voltage (in kV) for flurbiprofen and ibuprofen, respectively. As expected, the decrease in retention times is linear (both functions fit the linear equation with $R^2 = 0.96$ and 0.98 for (RS)-flurbiprofen and (RS)-ibuprofen, respectively). Furthermore, it was found that increasing applied voltages during the measurements led to improvement in separation efficiency, i.e. (RS)-ibuprofen separated into two enantiomers only at a voltage of 25 kV or higher. In the case of (RS)-flurbiprofen, two peaks for both enantiomers were visible at the lowest voltage used in the study, that is, 10 kV. Due to the factors identified above, samples were analyzed at applied voltages ranging from 10 to 30 kV throughout the study. Optimal separation parameters were chosen based on a short retention times and separation efficiency.

Chiral ionic liquid (S)-$[CHTA]^+[Tf_2N]^-$ (molecular structure is shown in **Scheme 2.1**) has an ionic structure; therefore, it may be used as an only electrolyte for CE measurements. This possibility was tested by analyzing mixtures of eight pharmaceutical

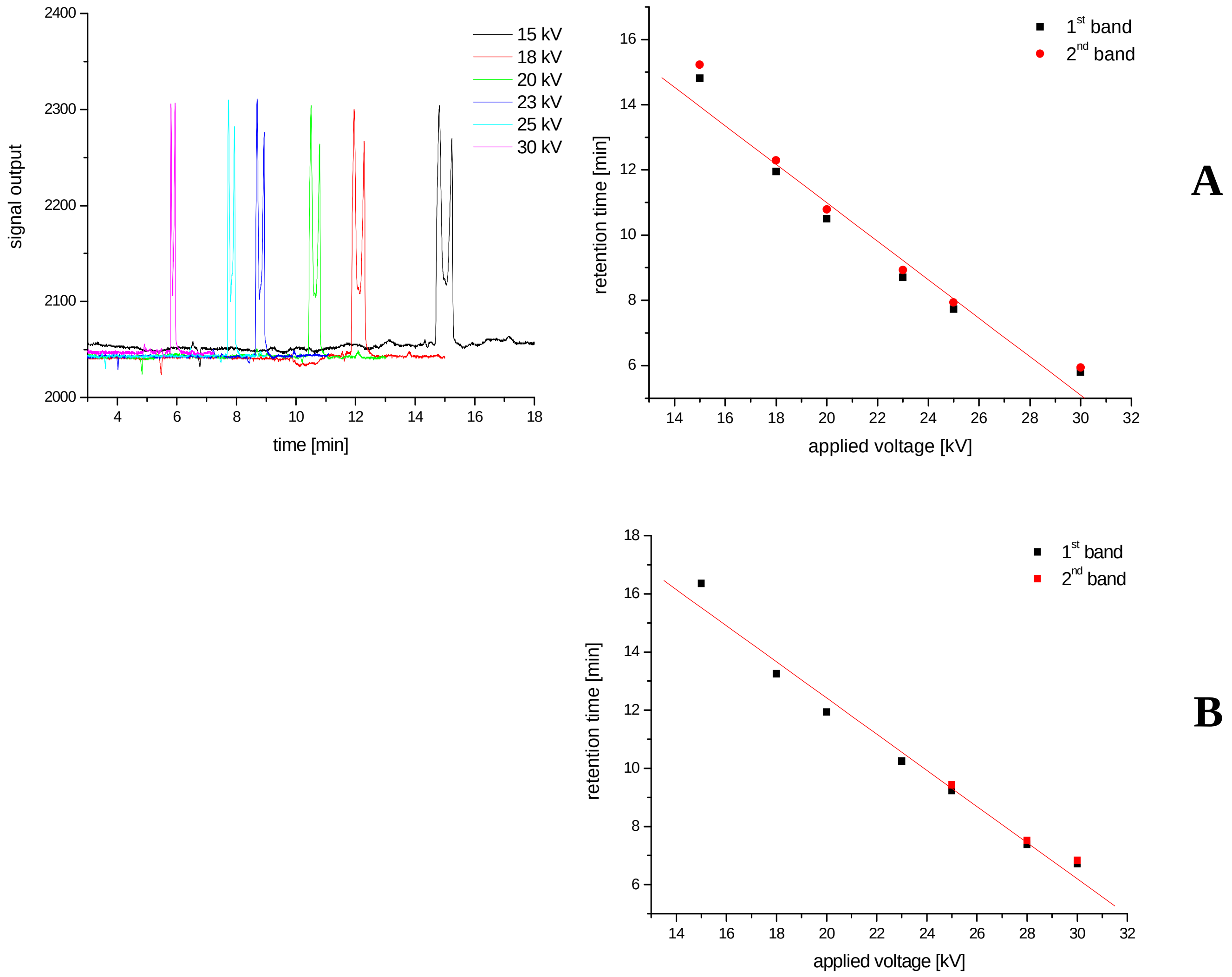

Figure 2.1: Retention times as a function of applied voltage for (RS)-flurbiprofen (A) and (RS)-ibuprofen (B).

compounds (racemic mixtures), shown in **Scheme 2.1,** using 50 mM aqueous solution of (S)-$[CHTA]^+[Tf_2N]^-$ as a separation medium. All analytes were eluted as a single broad peak (electropherogram not shown) which indicates that, even though this chiral IL can serve as an electrolyte, it does not lead to the separation of the analyzed compounds. Sodium cholate was successfully used as a background electrolyte for CE separation in a previously reported study[13] which prompted us to investigate its effect on chiral separation of pharmaceutical compounds used in our experiment. Interestingly, when 30 mM of an anionic surfactant, sodium cholate, is added to the aqueous solution of 20 mM (S)-$[CHTA]^+[Tf_2N]^-$, a baseline separation of mixture of seven pharmaceutical compounds (**Figure 2.3A**), including atenolol, propranolol, warfarin, indoprofen, ketoprofen, ibuprofen and flurbiprofen was achieved (naproxen was not included in the mixture since it was found that, with this buffer, the elution time of naproxen is almost the same as that of ibuprofen shown in **Figure 2.2**). Of most importance is band no. 6 (**Figure 2.3A**), which is divided into two equivalent peaks. Since all of the analytes were racemic mixtures it is valid to interpret these two peaks as two enantiomers of the (RS)-ibuprofen. This interpretation was tested by injecting the same mixture of seven pharmaceutical compounds, except this time the (RS) ibuprofen was replaced with (S)-ibuprofen (**Figure 2.3B**). As can be seen from **Figure 2.3B**, instead of two peaks for (RS)-ibuprofen, only one peak for (S)-ibuprofen appears. Similar results were obtained when mixtures of seven pharmaceutical products with (R)-ibuprofen were analyzed (electropherogram not shown). Data obtained indicate that separation medium consisting of 20 mM (S)-$[CHTA]^+[Tf_2N]^-$ and 30 mM sodium cholate in an aqueous solution can be used as an electrolyte with high separation efficiency as well as a chiral selector for (RS)-

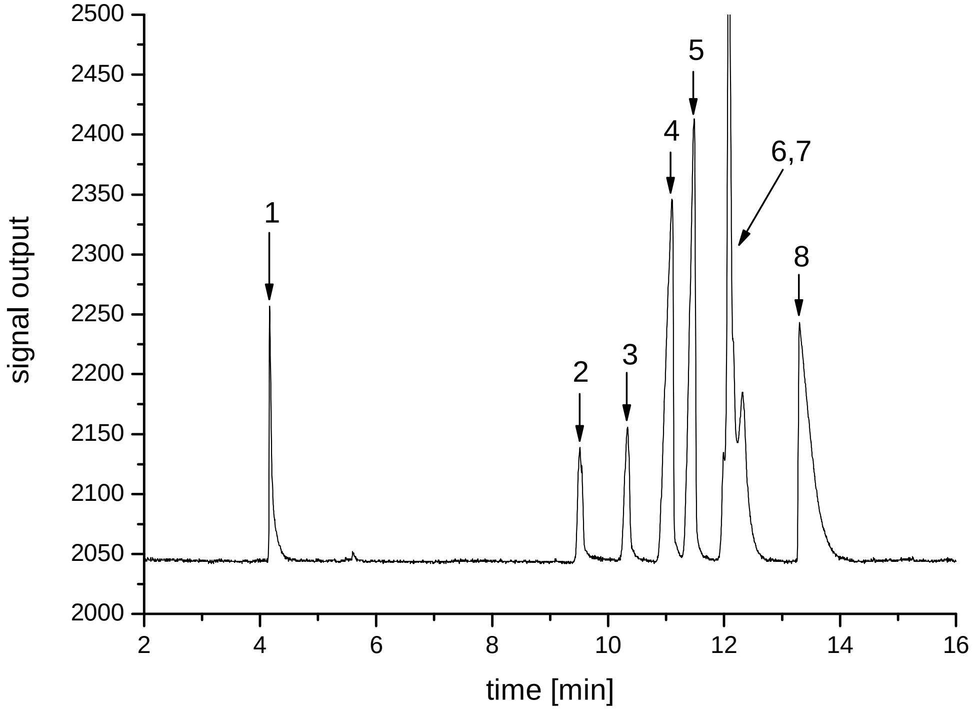

Figure 2.2: Electropherogram of a sample containing a mixture of eight compounds. Bare fused-silica capillary 50 cm (effective length: 37 cm) × 50 μm I.D; electrolyte: 20 mM (S)-$[CHTA]^+[Tf_2N]^-$, 30 mM sodium cholate; applied voltage: 20 kV; (1) atenolol, (2) propranolol, (3) warfarin, (4) indoprofen, (5) ketoprofen, (6) naproxen, (7) ibuprofen and (8) flurbiprofen.

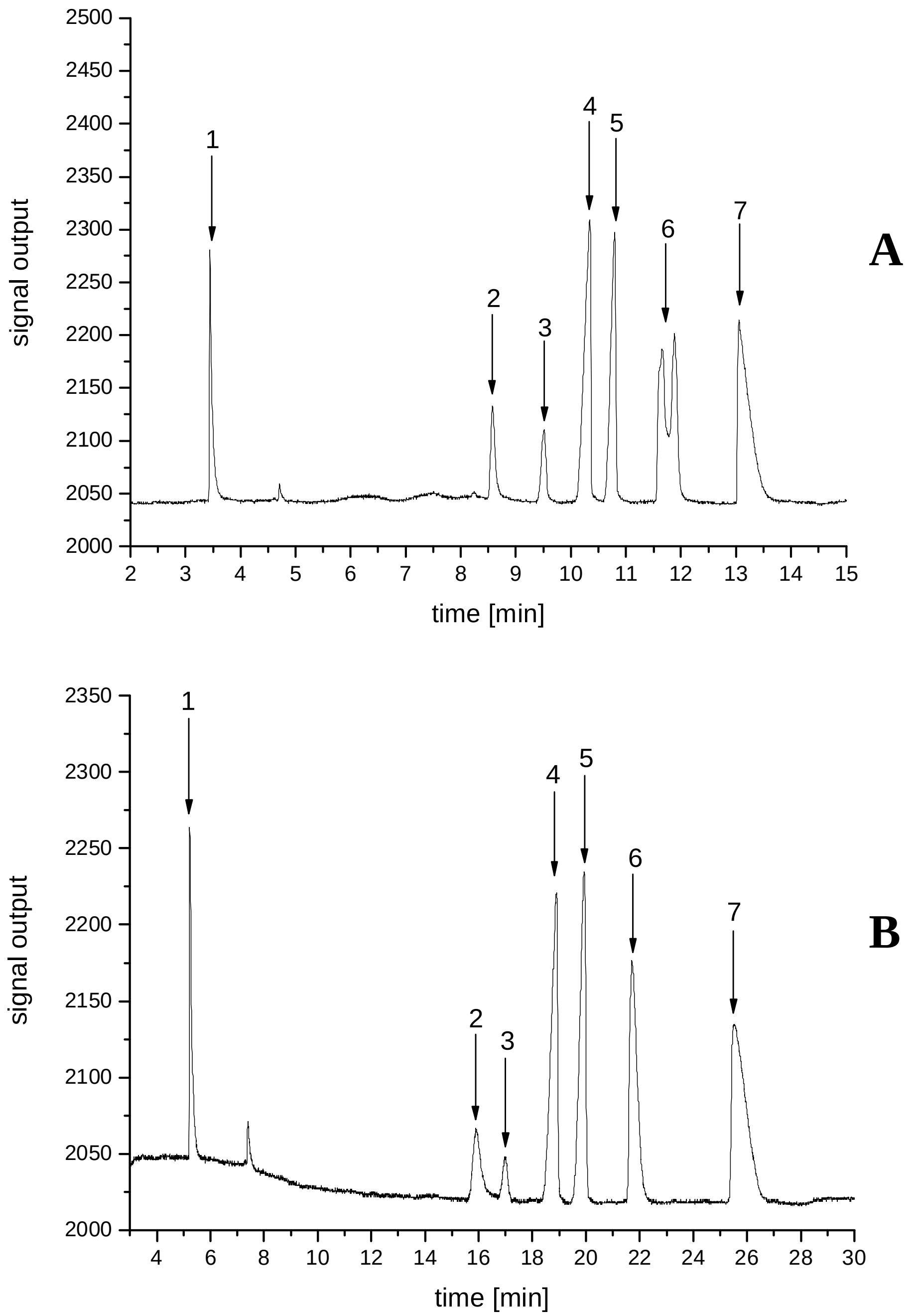

Figure 2.3: Electropherograms of a sample containing a mixture of seven compounds. Bare fused-silica capillary 50 cm (effective length: 37 cm) × 50 µm I.D; electrolyte: 20 mM (S)-[CHTA]$^+$[Tf$_2$N]$^-$, 30 mM sodium cholate; applied voltage: 25 kV (A) and 18 kV (B); (1) atenolol, (2) propranolol, (3) warfarin, (4) indoprofen, (5) ketoprofen, (6) ibuprofen and (7) flurbiprofen. (A) with (RS)-ibuprofen; (B) with (S)-ibuprofen.

ibuprofen. In order to obtain additional information about the separation mechanism, the same mixture of seven compounds (atenolol, propranolol, warfarin, indoprofen, ketoprofen,ibuprofen and flurbiprofen) was analyzed using the following buffer: 50 mM aqueous solution of sodium cholate (without the IL) (**Figure 2.4**). As illustrated, (compare electropherograms in **Figure 2.3A** and **2.4)**, separation efficiencies are relatively inferior when 50 mM sodium cholate is used as a separation medium. Specifically, it was not possible to separate (RS)-indoprofen from (RS)-ketoprofen whereas they were baseline separated with the use of a previous buffer, that is, 20 mM (S)-$[CHTA]^+[Tf_2N]^-$, 30 mM sodium cholate. Moreover, (RS)-ibuprofen was eluted as a single peak indicating no chiral recognition of sodium cholate for this specific compound whereas in the previous experiment (with addition of chiral ionic liquid to the sodium cholate) (RS)-ibuprofen was separated into two enantiomers. Data obtained therefore suggest that sodium cholate, despite being chiral and can serve as an electrolyte, when used alone, cannot induce any chiral separation. The results presented seem to suggest that interactions between chiral cholate anion and (RS)- ibuprofen only, are not sufficient to enable chiral recognition of (R)- and (S)-ibuprofen. Rather, cooperative interaction between chiral cation ((S)-$[CHTA]^+$) and chiral anion (cholate) with the analyte ((RS)-ibuprofen) are required in order for chiral recognition of the analyte to be achieved. The results are, indeed, in agreement with a three-point interaction mechanism of chiral recognition which shows, based on the stereochemistry, that two enantiomers can only be recognized by the chiral selector if at least three active positions of that selector simultaneously interact with the appropriate positions of one enantiomer whereas the corresponding positions of the other enantiomer appear in a wrong arrangement with

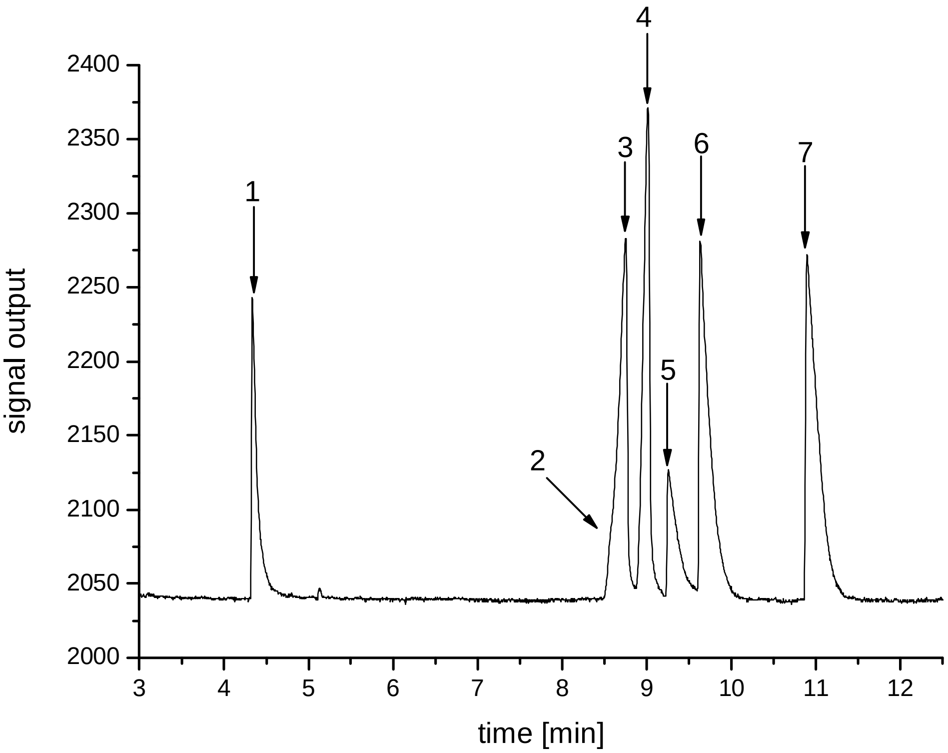

Figure 2.4: Electropherogram of a sample containing a mixture of seven compounds. Bare fused-silica capillary 50 cm (effective length: 37 cm) × 50 μm I.D; electrolyte: 50 mM sodium cholate; applied voltage: 20 kV; (1) atenolol, (2) indoprofen, (3) ketoprofen, (4) warfarin, (5) propranolol, (6) ibuprofen and (7) flurbiprofen.

respect to the same chiral selector.[2-4, 7, 31] A two-point interaction between the chiral selector and an analyte would not result in the chiral recognition due to the fact that coordinates of at least three points are required to fix the chiral species in space and subsequently, in our study, to measure the absorption of one enantiomer at a different elution time than the other enantiomer.[27]

Despite the fact that buffer containing aqueous solution of 20 mM (S)-$[CHTA]^+[Tf_2N]^-$ and 30 mM sodium cholate can successfully separate two enantiomers of (RS)-ibuprofen, it cannot serve as a chiral selector for enantioseparation of the other six compounds in the mixture, namely, atenolol, propranolol, warfarin, indoprofen, ketoprofen and flurbiprofen. The possibility that other concentrations of (S)-$[CHTA]^+[Tf_2N]^-$ and sodium cholate mixture could provide effective separation was also investigated. Separation mediums with different concentrations of IL and sodium cholate that were explored are listed in **Table 2.1**. However, no chiral separation of pharmaceutical compounds other than (RS)-ibuprofen was found. The best indication of a possible chiral recognition was found for (RS)-flurbiprofen, using the initial separation medium, that is, 20 mM (S)-$[CHTA]^+[Tf_2N]^-$ and 30 mM sodium cholate. Under such conditions, a peak with a broad shoulder was observed for (RS)-flurbiprofen. Interestingly, when only 50 mM sodium cholate is used as a separation medium, the absorption band for (RS)-flurbiprofen does not exhibit a broad shoulder (compare **Figure 2.5A** and **2.5B**). As can be observed by comparing two electropherograms, the separation efficiency is increased with the addition of the second chiral selector ((S)-$[CHTA]^+[Tf_2N]^-$) to sodium cholate solution. These results seem to suggest that the chiral separation efficiency, in the case of (RS)-flurbiporfen, can be improved by addition of

SEPARATION MEDIUM	Sodium Cholate [mM]	(S)-$[CHTA]^+[Tf_2N]^-$ [mM]
1	40	40
2	40	30
3	40	20
4	40	10
5	30	40
6	30	30
7	30	20
8	30	10
9	20	30
10	20	20

Table 2.1: Different concentrations of sodium cholate and (S)-$[CHTA]^+[Tf_2N]^-$ that were used as a separation medium.

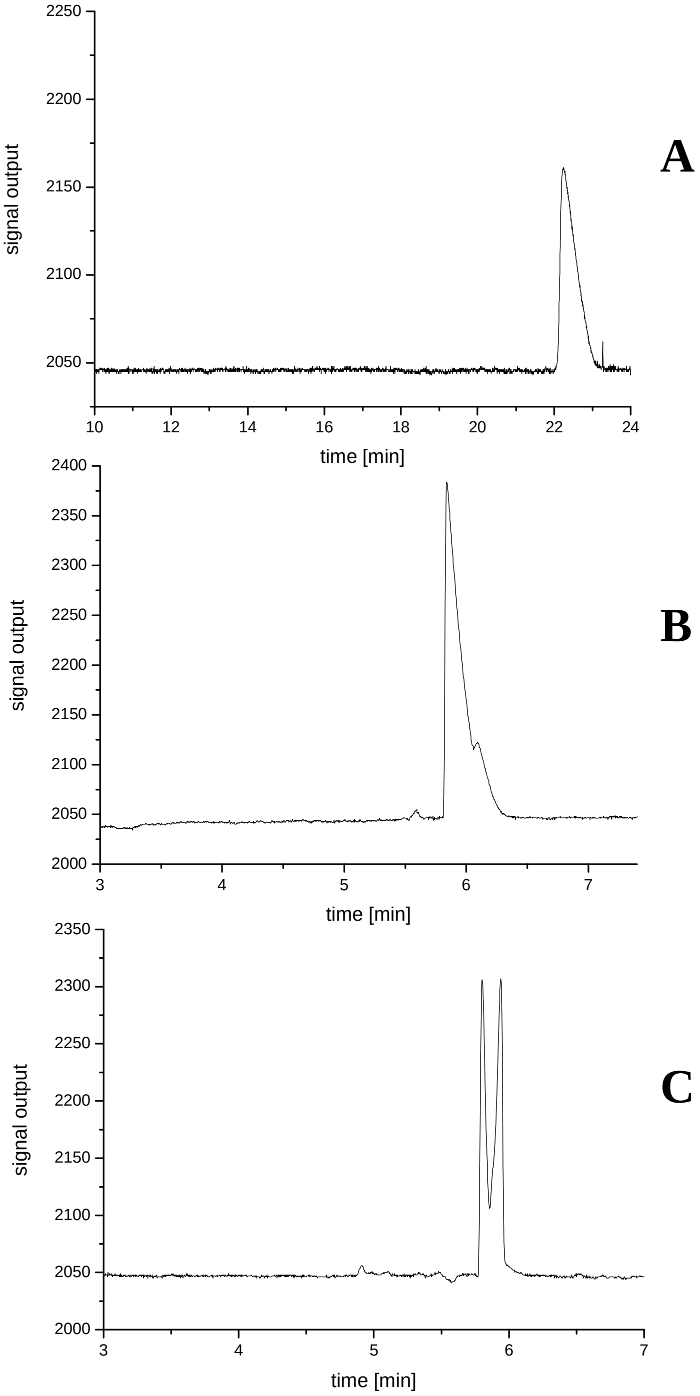

Figure 2.5: Electropherograms of a sample of (RS)-flurbiprofen. Bare fused-silica capillary 50 cm (effective length: 37 cm) × 50 µm I.D; electrolyte: 50 mM sodium cholate (A); 20 mM (S)-$[CHTA]^+[Tf_2N]^-$, 30 mM sodium cholate (B); 20 mM (S)-$[CHTA]^+[Tf_2N]^-$, 30 mM sodium cholate, 10 mM OTG (C). Applied voltage: 18 kV (A), 30 kV (B and C).

another, third, chiral selector. As expected, adding 10 mM 1-S-octyl-β-D-thioglucopyranoside (OTG), which is a neutral chiral selector, to the aqueous solution of 20 mM (S)-$[CHTA]^+[Tf_2N]^-$ and 30 mM sodium cholate leads to a substantial increase in the chiral separation efficiency (compare **Figure 2.5A-C).** The possibility that a higher concentration of OTG in the separation medium would induce chiral recognition for (RS)-flurbiprofen was further investigated. Specifically, chiral recognition for (RS)-flurbiprofen using the following buffers was studied: 10 mM OTG, 20 mM (S)-$[CHTA]^+[Tf_2N]^-$ and 30 mM sodium cholate; 20 mM OTG, 20 mM (S)-$[CHTA]^+[Tf_2N]^-$ and 30 mM sodium cholate; and 30 mM OTG, 20 mM (S)-$[CHTA]^+[Tf_2N]^-$ and 30 mM sodium cholate. **Figure 2.6** shows (RS)-flurbiprofen electropherograms and its reciprocal resolution and selectivity factor values under these conditions. As can be observed from the graphs and resolution values, increasing the concentration of OTG in the separation medium leads to reduced chiral recognition for (RS)-flurbiprofen.

Interestingly, adding third and neutral chiral selector to an aqueous solution of 20 mM (S)-$[CHTA]^+[Tf_2N]^-$ and 30 mM sodium cholate, in the case of (RS)-ibuprofen, does not improve the separation efficiency. Rather, the separation efficiency is somewhat impaired, as can be observed by comparing the electropherograms in **Figure 2.7A-B**. Most likely, the need for a third neutral chiral selector in the case of (RS)-flurbiprofen is due to the molecular structural differences between (RS)-flurbiprofen and (RS)-ibuprofen (see **Scheme 2.1**). Specifically, (RS)-flurbiprofen has an extra phenyl ring compared to the (RS)-ibuprofen. As a consequence, additional neutral chiral selector (OTG), which has a glucose ring, is needed for chiral interactions with the particular phenyl ring.

Similarly to (RS)-flurbiprofen, the possibility that a higher concentration of OTG

	Selectivity factor [α]	Resolution [R_s]
10 mM OTG	1.050	0.940
20 mM OTG	1.052	0.876
30 mM OTG	1.050	0.768

A

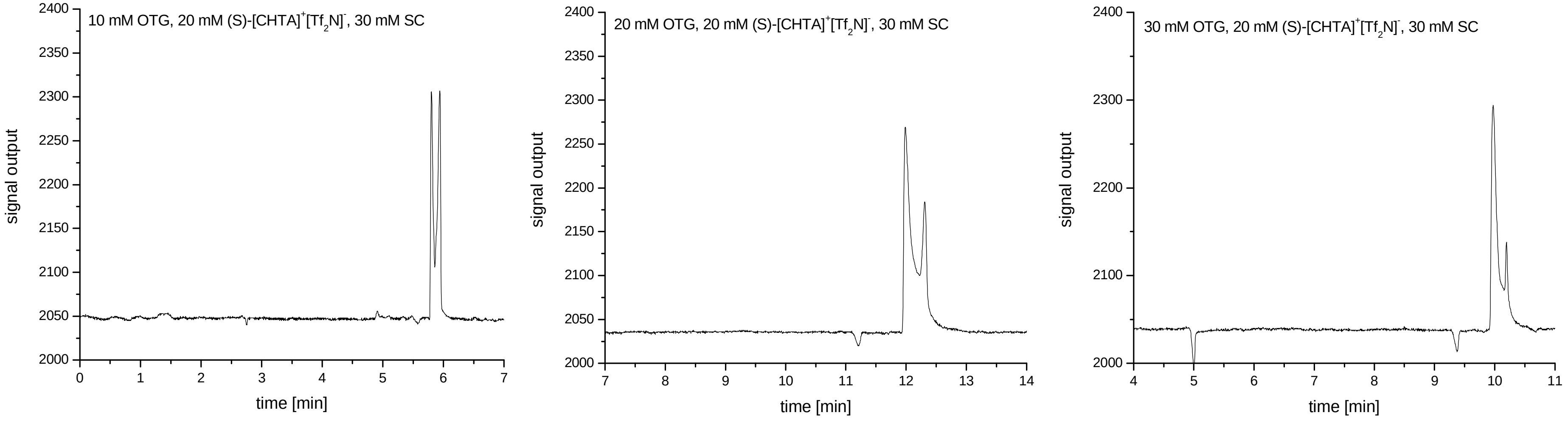

B

Figure 2.6: Selectivity factor and resolution values for (RS)-flurbiprofen (Buffer: 10/20/30 mM OTG, 20 mM (S)-$[CHTA]^+[Tf_2N]^-$, 30 mM sodium cholate) (A), and reciprocal electropherograms (from left to right: 10 mM OTG, 20 mM OTG and 30 mM OTG added to 20 mM (S)-$[CHTA]^+[Tf_2N]^-$, 30 mM sodium cholate) (B).

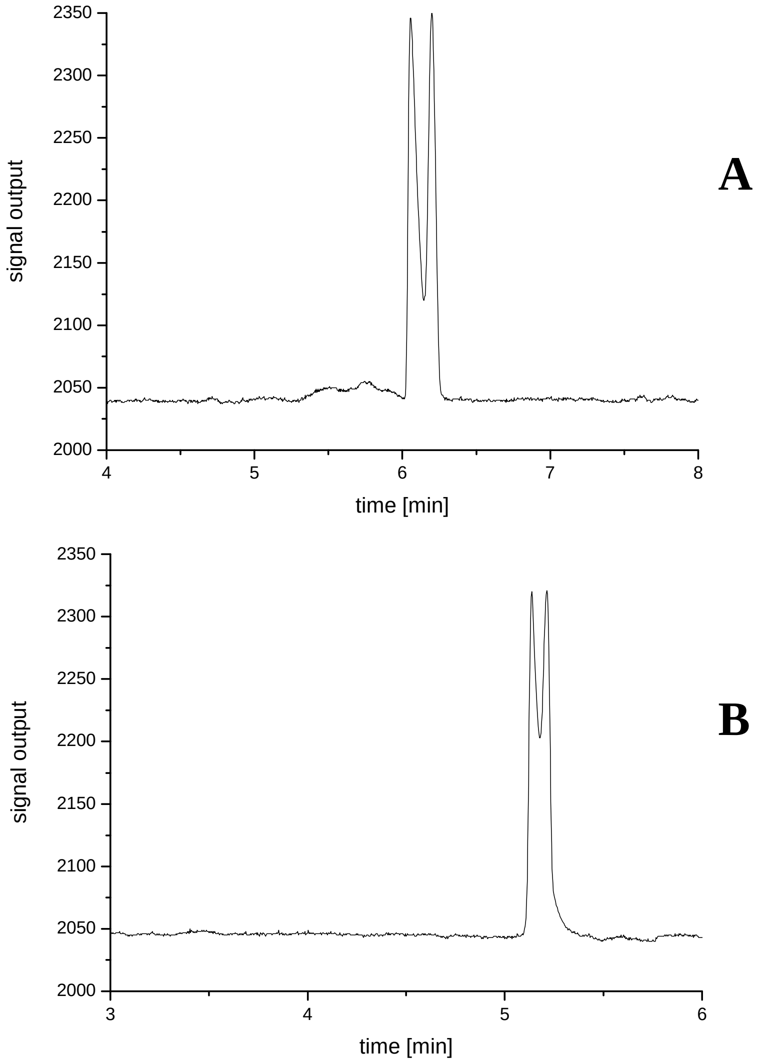

Figure 2.7: Electropherograms of a sample of (RS)-ibuprofen. Bare fused-silica capillary 50 cm (effective length: 25 cm) × 50 µm I.D; electrolyte: 20 mM (S)-$[CHTA]^+[Tf_2N]^-$, 30 mM sodium cholate; applied voltage: 25 kV. (A) Buffer contains no OTG; (B) buffer contains 10 mM OTG.

in the separation medium would induce chiral recognition for (RS)-iburprofen was also investigated. Electropherograms of (RS)-ibuprofen when 10, 20 and 30 mM of OTG are added to the previously used buffer (i.e., 20 mM (S)-$[CHTA]^+[Tf_2N]^-$ and 30 mM sodium cholate) as well as their reciprocal resolution and selectivity factor values are shown in **Figure 2.8**. As can be observed, an increasing concentration of the OTG from 10 to 20 mM results in lower resolution and selectivity factor values, as well as in broader shape of an absorption band. Furthermore, when 30 mM of OTG is added to 20 mM (S)-$[CHTA]^+[Tf_2N]^-$ and 30 mM sodium cholate, no chiral separation is achieved; only an absorption band with broad shoulder is observed. For the case of (RS)-ibuprofen (using only sodium cholate and (S)-$[CHTA]^+[Tf_2N]^-$ as a buffer), chiral separation efficiencies in terms of resolution (R_s) and selectivity (α) values, were also investigated. It was found that chiral recognition of the enantiomers is strongly dependent upon the concentration of (S)-$[CHTA]^+[Tf_2N]^-$ and sodium cholate. Shown in **Table 2.2** are resolution values and selectivity factors (triplicate measurements for each condition were made and averaged values plus standard deviations are listed). Furthermore, 3D plots of resolution values and selectivity factors as a function of concentration of sodium cholate and (S)-$[CHTA]^+[Tf_2N]^-$ (**Figure 2.9**), respectively, are presented as well. In both cases (compare **Figure 2.9A** and **2.9B**), no chiral recognition is observed with sodium cholate concentration being less than 30 mM. At 30 mM sodium cholate, the resolution and selectivity values are quite constant in the concentration range of 10 to 30 mM (S)-$[CHTA]^+[Tf_2N]^-$. At a 40 mM sodium cholate concentration, however, the range where resolution and selectivity values remain constant, shifts to higher (S)-$[CHTA]^+[Tf_2N]^-$ concentrations, that is, to the range from 20 to 40 mM. More importantly, increasing the

	Selectivity factor [α]	Resolution [R_s]
10 mM OTG	1.034	0.618
20 mM OTG	1.022	0.429
30 mM OTG	no separation	

A

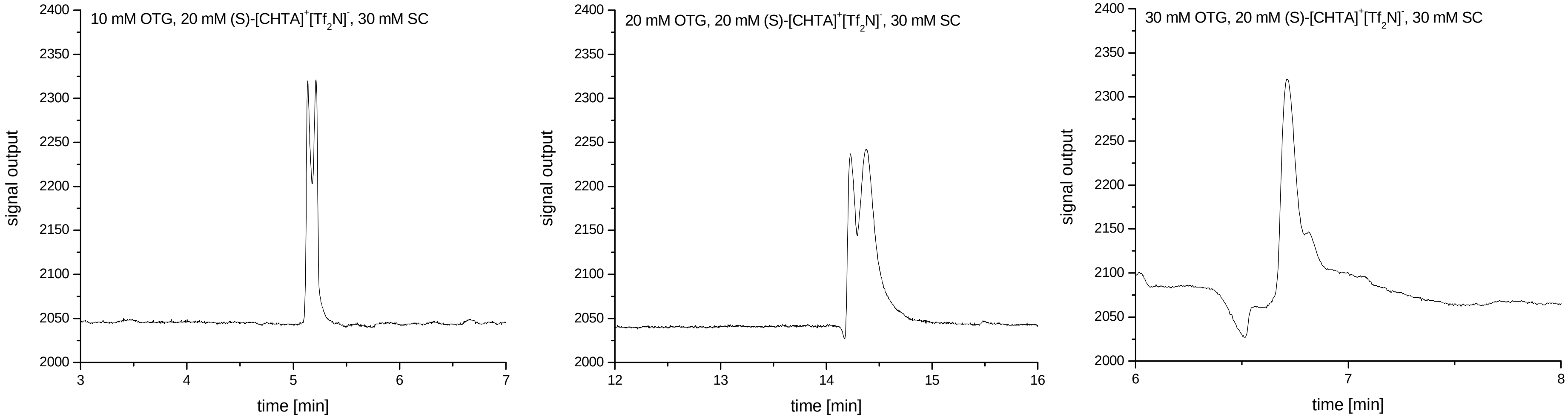

B

Figure 2.8: Selectivity factor and resolution values for (RS)-ibuprofen (Buffer: 10/20/30 mM OTG, 20 mM (S)-[CHTA]$^+$[Tf$_2$N]$^-$, 30 mM sodium cholate) (A), and reciprocal electropherograms (from left to right: 10 mM OTG, 20 mM OTG and 30 mM OTG added to 20 mM (S)-[CHTA]$^+$[Tf$_2$N]$^-$, 30 mM sodium cholate) (B).

Separation medium	**Resolution values (R_s)**	**Selectivity factor (α)**
40 mM SC/40 mM (S)-$[CHTA]^+[Tf_2N]^-$	0.66±0.04	1.050±0.004
40 mM SC/30 mM (S)-$[CHTA]^+[Tf_2N]^-$	0.61±0.08	1.048±0.001
40 mM SC/20 mM (S)-$[CHTA]^+[Tf_2N]^-$	0.61±0.04	1.034±0.005
40 mM SC/10 mM (S)-$[CHTA]^+[Tf_2N]^-$	no separation	
30 mM SC/40 mM (S)-$[CHTA]^+[Tf_2N]^-$	no separation	
30 mM SC/30 mM (S)-$[CHTA]^+[Tf_2N]^-$	0.72±0.06	1.047±0.001
30 mM SC/20 mM (S)-$[CHTA]^+[Tf_2N]^-$	0.73±0.07	1.036±0.008
30 mM SC/10 mM (S)-$[CHTA]^+[Tf_2N]^-$	0.7±0.1	1.045±0.008
20 mM SC/30 mM (S)-$[CHTA]^+[Tf_2N]^-$	no separation	
20 mM SC/20 mM (S)-$[CHTA]^+[Tf_2N]^-$	no separation	

Table 2.2: Resolution values and selectivity factors for (RS)-ibuprofen.

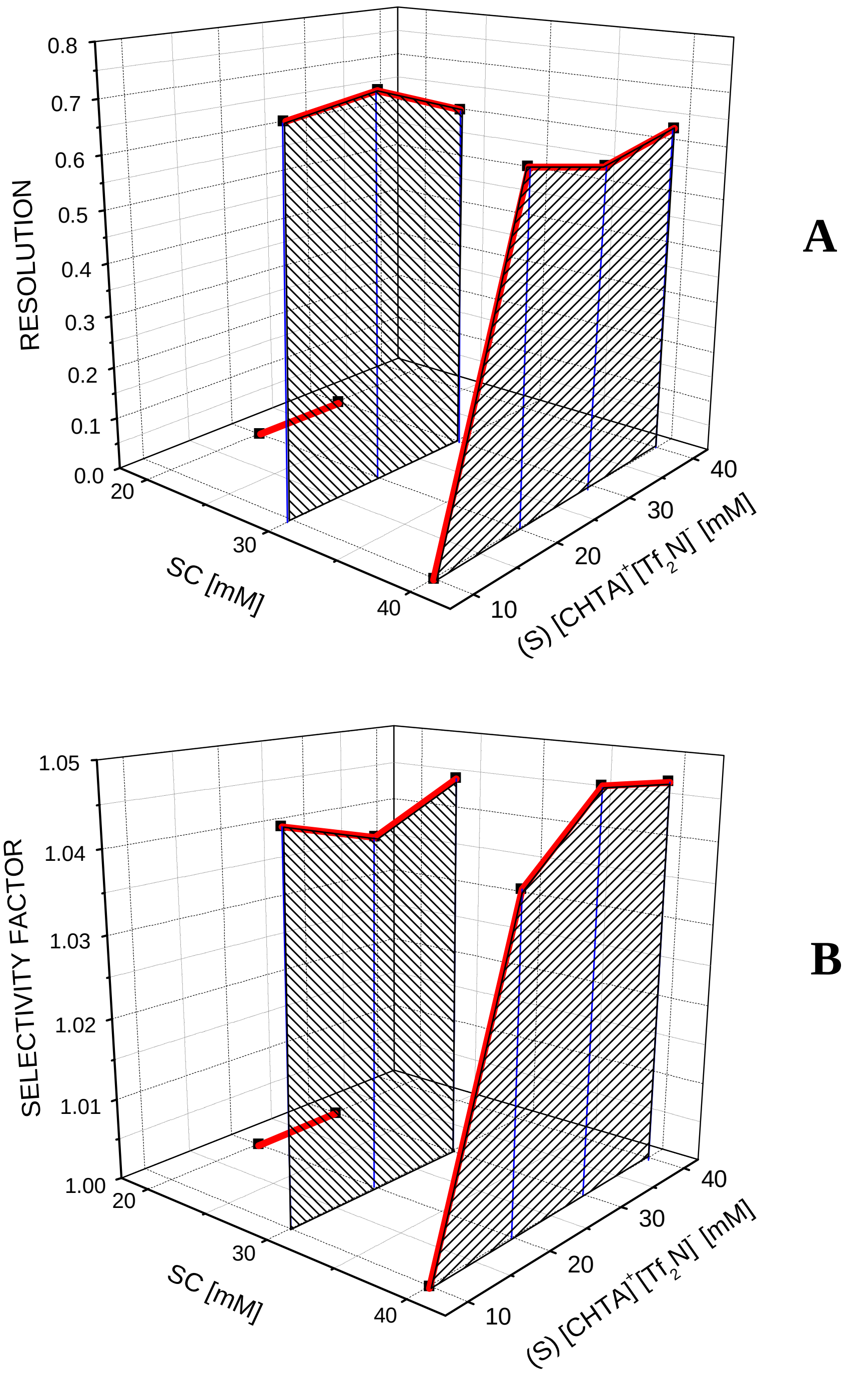

Figure 2.9: Plots of concentration of sodium cholate (SC) and (S)-$[CHTA]^+[Tf_2N]^-$ vs. resolution (A) and selectivity factor (B) for (RS)-ibuprofen.

concentration of sodium cholate to 40 mM does not result in improvement in separation efficiency in terms of resolution and selectivity values.

In addition to the previously described experiments, i.e., when (S)-$[CHTA]^+[Tf_2N]^-$ and sodium cholate are used as a separation medium, a different chiral ionic liquid was also studied as a chiral selector. Specifically, chiral IL 1-butyl-3-methylimidazolium (T-4)-bis[(2S)-2-(hydroxy-κO)-4-methyl-pentanoato-κO]borate ($[BMIm]^+[BLHcB]^-$)[32] (see **Scheme 2.3**) with sodium cholate (and without OTG) was used as a separation medium. Separation conditions as well as sodium cholate and IL concentrations were the same as in the case when (S)-$[CHTA]^+[Tf_2N]^-$ and SC were used as a separation medium. However, no chiral recognition was found for the mixture of seven pharmaceutical compounds used in the study (atenolol, propranolol, warfarin, indoprofen, ketoprofen, ibuprofen and flurbiprofen) (electropherogram not shown). The results indicate that chiral ionic liquid (S)-$[CHTA]^+[Tf_2N]^-$, indeed, plays a key role (compared to sodium cholate) in the enantioseparation of (RS)-ibuprofen; most probably due to the relatively high chiral recognition ability of this IL. In the case of (RS)-flurbiprofen, it is believed that effects of both, OTG and (S)-$[CHTA]^+[Tf_2N]^-$, are required for efficient chiral separation.

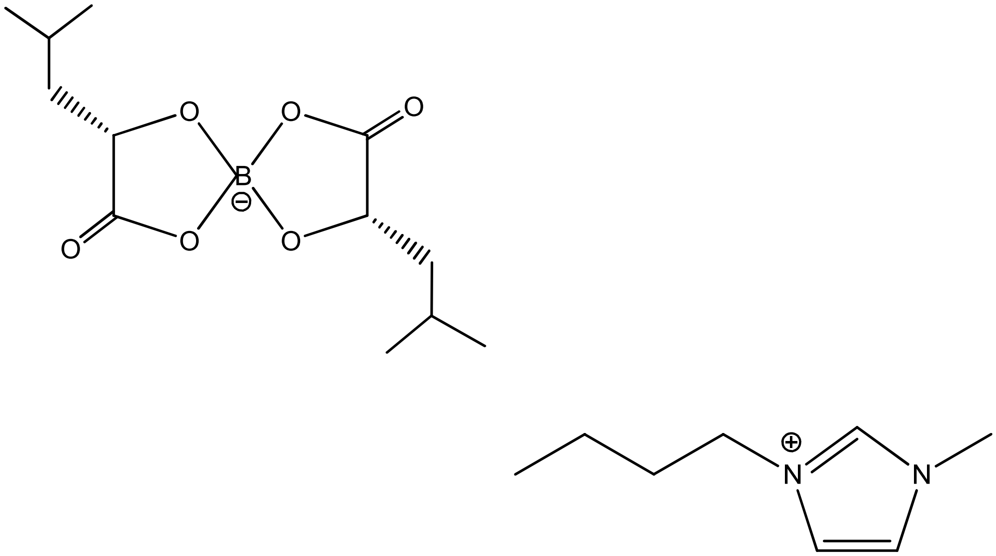

Scheme 2.3: Structure of 1-butyl-3-methylimidazolium (T-4)-bis[(2S)-2-(hydroxy-κO)-4-methyl-pentanoato-κO]borate ([BMIm]$^+$[BLHcB]$^-$).

2.4 CONCLUSION

Chiral ionic liquid (S)-[3-(chloro-2-hydroxypropyl)trimethylammonium] [bis((trifluoromethyl) sulfonyl)amide] ((S)-$[CHTA]^+[Tf_2N]^-$), which can be readily synthesized from commercially available reagents, can be used both as an electrolyte and as a chiral selector. Several pharmaceutical products, including atenolol, propranolol, warfarin, indoprofen, ketoprofen, ibuprofen and flurbiprofen, can be baseline separated using this chiral IL as an electrolyte. Moreover, with addition of sodium cholate to the solution of (S)-$[CHTA]^+[Tf_2N]^-$, chiral recognition towards (R)- and (S)-ibuprofen was achieved. In case of (RS)-flurbiprofen, addition of 1-S-octyl-β-D-thioglucopyranoside (OTG) to the sodium cholate and (S)-$[CHTA]^+[Tf_2N]^-$ buffer was needed in order to obtain chiral separation of the two enantiomers. Chirality of the IL and sodium cholate resides on a cation and anion, respectively, whereas OTG is a chiral neutral compound. Results obtained throughout the study indicate that the chiral ionic liquid (S)-$[CHTA]^+[Tf_2N]^-$ can most probably provide either one (in the case of (RS)-flurbiprofen) or two (for (RS)-ibuprofen) of the three point interaction mechanism needed for a chiral recognition of two enantiomers. Therefore, it is expected that a chiral ionic liquid with chirality on the cation as well as on the anion, would be able to serve as a sole chiral selector for the enantioseparation by capillary electrophoresis.

CHAPTER 3

SEPARATION OF ISOTOPIC MOLECULES USING A NOVEL CAVITAND-IMPREGNATED IONIC LIQUID STATIONARY PHASE IN GAS CHROMATOGRAPHY

3.1 INTRODUCTION

Cavitands are compounds with deep, one open-ended cavities (see their chemical structure in **Scheme 3.1**). Cavitands, together with cyclodextrines, calixarenes, resorcinarenes and carcerands, belong to a group of host compounds which due to their unique structures exhibit remarkable molecular recognition thorough host-guest interactions.[33-35] Cyclodextrins have larger and smaller openings on top and bottom side of the cavity, respectively, whereas calixarens and resorcinarenes exhibit a bowl-shaped structure with large, extended surfaces and functional groups for intermolecular interaction. Calixarens and resorcinarenes have, therefore, structure similar to cavitands. Adversely, carcerands are closed-surface container molecules and differ from cavitands in the terms of exchange rates; that is, due to the absence of sizeable surface opening they can bind the guest molecule indefinitely, whereas cavitands, as a result of relatively large surface opening, exhibit an easy uptake and release of the guest molecules.[35] Both cyclodextrins and calixarenes have been used effectively as stationary phases in gas and liquid chromatography for a variety of separation processes, including chiral separation.[2,3,36-40] In addition to being used as SPs in gas/liquid chromatography they can

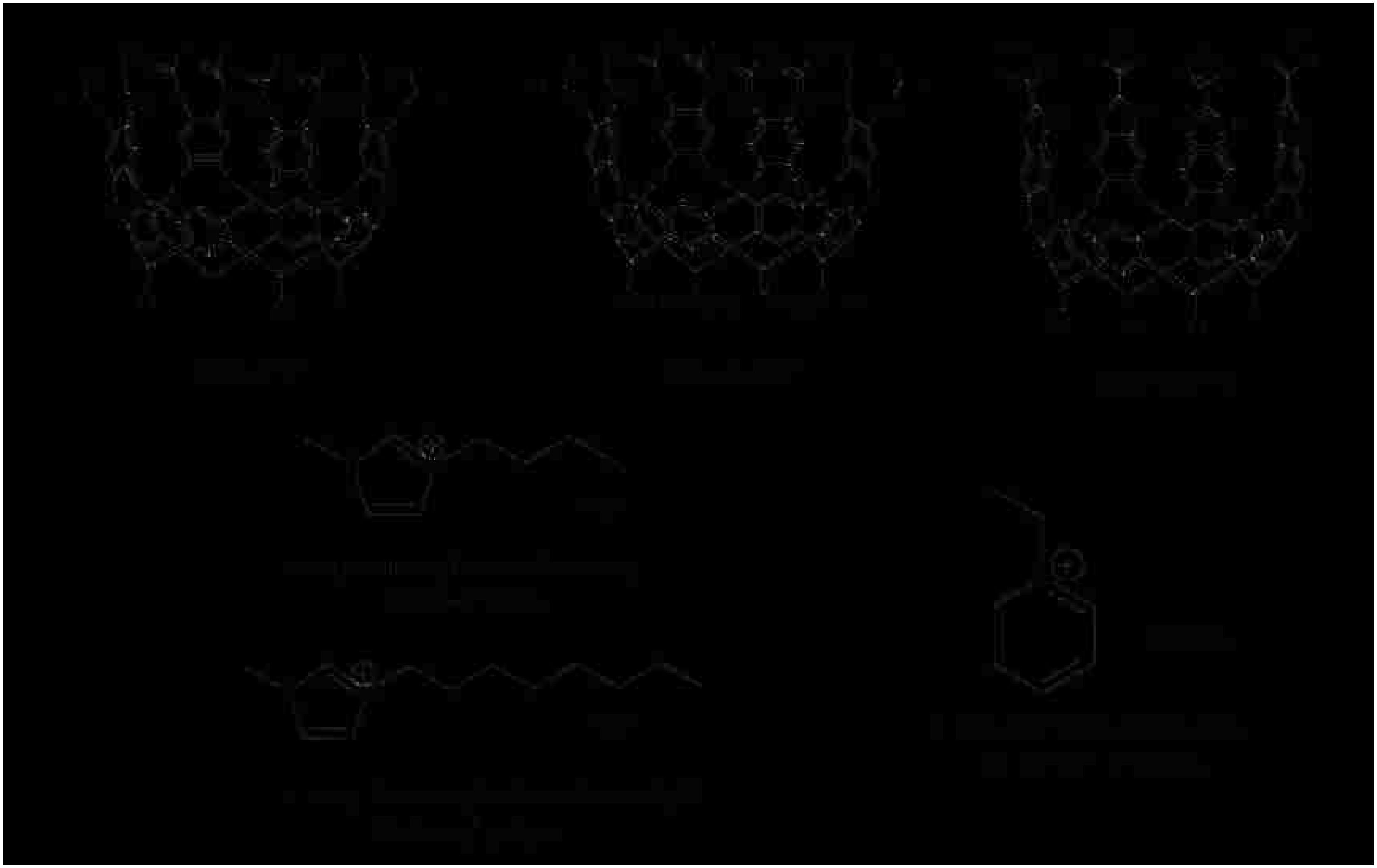

Scheme 3.1: Molecular structures of cavitands and ionic liquids used in the study.

also serve as selective modifiers in capillary electrophoresis.[41]

Isotopic isomers can be recognized and differentiated by fully enclosed capsules,[33-35] whereas such molecular discrimination has not been observed for other host compounds, including cyclodextrins and calixarens.[2,3,36-41] This observation is most probably due to the small molecular differences between two isotopomers. Molecular recognition is dependent on extent of interactions between guest and host molecule. The possibility of the molecular recognition would be realized if interactions between the two compounds are strong. Cavitands with their deep structure may provide relatively stronger host-guest interaction with isotopic molecules than cyclodextrins and calixarens. It may be possible for them to differentiate isotopic molecules when used as a stationary phase in gas/liquid chromatography. Unfortunately, use of cavitands in the separation science is limited, mostly by their low solubility which, as a consequence, makes it difficult to coat the cavitands on the columns or substrate. One way to overcome this limitation is to synthetically modify the cavitands in order to increase their solubility, or covalently bind them to a solid support. An example of the latter was a recent study where cavitands were bound to a sol-gel support and used in solid phase microextraction.[42] It was found that these cavitands substantially increased the detection of aromatic compounds, including benzene and chlorobenzene.[42] However, synthetic processes involved in modification of cavitands are quite complex, and furthermore, molecular recognition ability of cavitands may be decreased during the modification process. It is therefore highly desirable to develop a novel type of solvents which could be directly used to dissolve cavitands without any modification, as well as being part of the stationary phase (that is, as coating solvent, in gas chromatography). In our study we investigated if room temperature ionic liquids can serve as such solvents.

As described in Chapter 2, ionic liquids (ILs) are a group of organic salts that are liquid at ambient temperature. They have unique chemical and physical properties, namely, they are air and moisture stable, have a high solubility power and virtually no vapor pressure.[14,22-27,32,43-47] ILs have been used as a stationary phase in GC,[47,48] which is most probably due to their high solubility power, low vapor pressure and high boiling point. In the recent study, ILs were not used only as SP, but also as solvents to coat fullerenes (C_{60}, amino-fullerene and hydroxy-fullerene) onto GC columns.[49] It was found that ILs act synergistically with fullerenes to provide dual modal characteristics for the stationary phase. Specifically, stationary phase exhibits polar as well as nonpolar characteristics and its polarity can be adjusted by changing either the type of the ionic liquid or/and adding fullerens into the ILs.[49]

The presented information (i.e. unique properties of cavitands and ionic liquids) seems to suggest that it is possible for ILs to dissolve cavitands and moreover, to use IL-cavitand solutions as a stationary phase in GC. Therefore, in our study, we first investigated the possibility of dissolving cavitands by ILs, and afterwards the possibility of coating columns with IL-cavitand solutions for GC separation of isotopic molecules. Results obtained were compared to those of the columns coated with only ILs in order to determine the effect of cavitands on the separation efficiency.

3.2 EXPERIMENTAL

3.2.1 Chemicals

1,2-dichlorobenzene-d_4 (99 %); chlorobenzene-d_5 (99 %); ethanol-d_5 (98 %); methanol-d (99 %); methanol-d_3 (99.5 %); methanol-d_4 (99.8 %); acetonitrile-d_3 (99.8 %); pyridine-d_5 (99.5 %); p-dioxane-d_8 (99 %), p-xylene-d_{10} (98 %) were purchased from Cambridge Isotope Laboratories, Inc. (Andover, MA). P-dioxane (99 %), o-xylene (99 %), m-xylene (99 %) and pyridine (99.5+ %) were supplied by Alfa Aesar (Ward Hill, MA). All other chemicals were obtained from Sigma-Aldrich (Milwaukee, WI) and used as received.

3.2.2 Ionic liquids

Three ionic liquids were used in this study, namely octyl methylimidazolium bis((trifluoromethyl)sulfonyl)amide ($[OMIm]^+[Tf_2N]^-$), N-ethyl pyridinium trifluoroacetate ($[N\text{-}EtPy]^+[CF_3CO_2]^-$) and 1-butyl-3-methylimidazolium tetrafluoroborate ($[BMIm]^+[BF_4]^-$) (see **Scheme 3.1**). First two ILs were initially synthesized by Dr. Shaofang Yu and characterized by ^{1}H NMR and IR methods as reported previously,[27,32,49] whereas 1-butyl-3-methylimidazolium tetrafluoroborate ($[BMIm]^+[BF_4]^-$) was prepared from 1-butyl-3-methylimidazolium chloride ($BMIm^+Cl^-$) by metathesis reaction. $BMIm^+Cl^-$ was synthesized by refluxing a 1:1 molar ratio mixture of 1-methylimidazole and chlorobutane under nitrogen atmosphere at 60 ˚C for two days. The resulting viscous liquid was cooled to room temperature and washed twice with ethyl acetate. After evaporating (rotary evaporation under vacuum) ethyl acetate solution, IL was vacuum dried at 60 ˚C for 10 to 12 hours.

3.2.3 Cavitands

Cavitands (see **Scheme 3.1**) used throughout the study were synthesized in Dr. Julius Rebek's research group using procedures reported previously.[33-35] Essentially, they were built by condensation of resorcinarenes with 2,3-dichloropyrazines or 2,3-dichloroquinoxalines.

3.2.4 Dissolving cavitands in Ionic liquids

Cavitands used in the study have different polarities and consequently different solubilities. Specifically, in the scale from the lower to higher polarity is cavitand 2 ($C_{120}H_{160}N_8O_{16}$), cavitand 1 ($C_{84}H_{88}N_8O_{16}$) and cavitand 3 ($C_{72}H_{52}N_8Na_4O_{16}$). It is expected that they can be dissolved in ILs which have comparable polarity. In fact, it was found that cavitand 2 can be dissolved in relatively nonpolar $[OMIm]^+[Tf_2N]^-$; cavitand 1 is soluble in $[BMIm]^+[BF_4]^-$ which has medium polarity, and relatively polar $[N\text{-}EtPy]^+[CF_3CO_2]^-$ can dissolve cavitand 3. Namely, 1 mg of cavitand was dissolved in 0.1 mL of ionic liquid in approximately 12 hours. In order to ensure complete solubility of cavitands in ILs the sample was afterwards also vortexed for approximately 5 minutes.

3.2.5 Coating GC capillary column

A 25 mg of solution of cavitand 1 in $[BMIm]^+[BF_4]^-$ (or cavitand 2 in $[OMIm]^+[Tf_2N]^-$ or cavitand 3 in $[N\text{-}EtPy]^+[CF_3CO_2]^-$) was dissolved in 10 mL of dichloromethane and coated onto a 10 m fused silica capillary tubing (Supelco Corporation, Bellefonte, PA, USA). Specifically, a solution of cavitand 1 in $[BMIm]^+[BF_4]^-$ (or $[BMIm]^+[BF_4]^-$ only) was coated onto an untreated fused silica column (Lot no. 43248, 0.25 mm I.D.), cavitand 2 in $[OMIm]^+[Tf_2N]^-$ (as well as IL only) was coated onto an intermediate polarity fused silica column (Lot no. D6321, 0.25

mm I.D.) and solution of [N-EtPy]$^+$[CF$_3$CO$_2$]$^-$ with dissolved cavitand 3 (or [N-EtPy]$^+$[CF$_3$CO$_2$]$^-$ only) was coated onto a polar fused silica capillary column (Lot no. D6068, 0.25 mm I.D.). All columns were coated at 40 ˚C using reported procedures from the literature.[49] Essentially, the capillary column (10 m length) was immersed into the water bath (40 ˚C) (see **Scheme 3.2**) and filled with the coating solution (cavitands dissolved in ILs in dichloromethane solution or only ILs in dichloromethane solution). One end of the column was then attached to Teflon tubing and sealed with a metal clamp, whereas the other end of the column, through plastic and rubber tubing, was connected to a vacuum pump. Under these conditions, dichloromethane vapor is removed, thus leaving the cavitand in ionic liquid (or ionic liquid only) coated onto the capillary column walls. The rate of coating of the column was kept constant by appropriately adjusting the vacuum with the pressure controller (usually the pressure was -40 to -50 kPa). The same procedure was used for coating of three other 10 m capillary columns with only the ILs, that is, [BMIm]$^+$[BF$_4$]$^-$, [OMIm]$^+$[Tf$_2$N]$^-$ and [N-EtPy]$^+$[CF$_3$CO$_2$]$^-$. Coated columns were then flushed with dry nitrogen gas for 1 hour and afterwards conditioned in a GC instrument using a temperature gradient method (from 30 to 100 ˚C at 1 ˚C/min increment). They were held overnight at the upper temperature, that is, 100 ˚C.

3.2.6 Instrumentation

All separations were carried out on a Hewlett-Packard model 6890 gas chromatograph with nitrogen as a carrier gas. Split injection (split ratio of 50:1) and flame ionization detection was used for detection.

Resolution values between two adjacent peaks were calculated using the following equation:

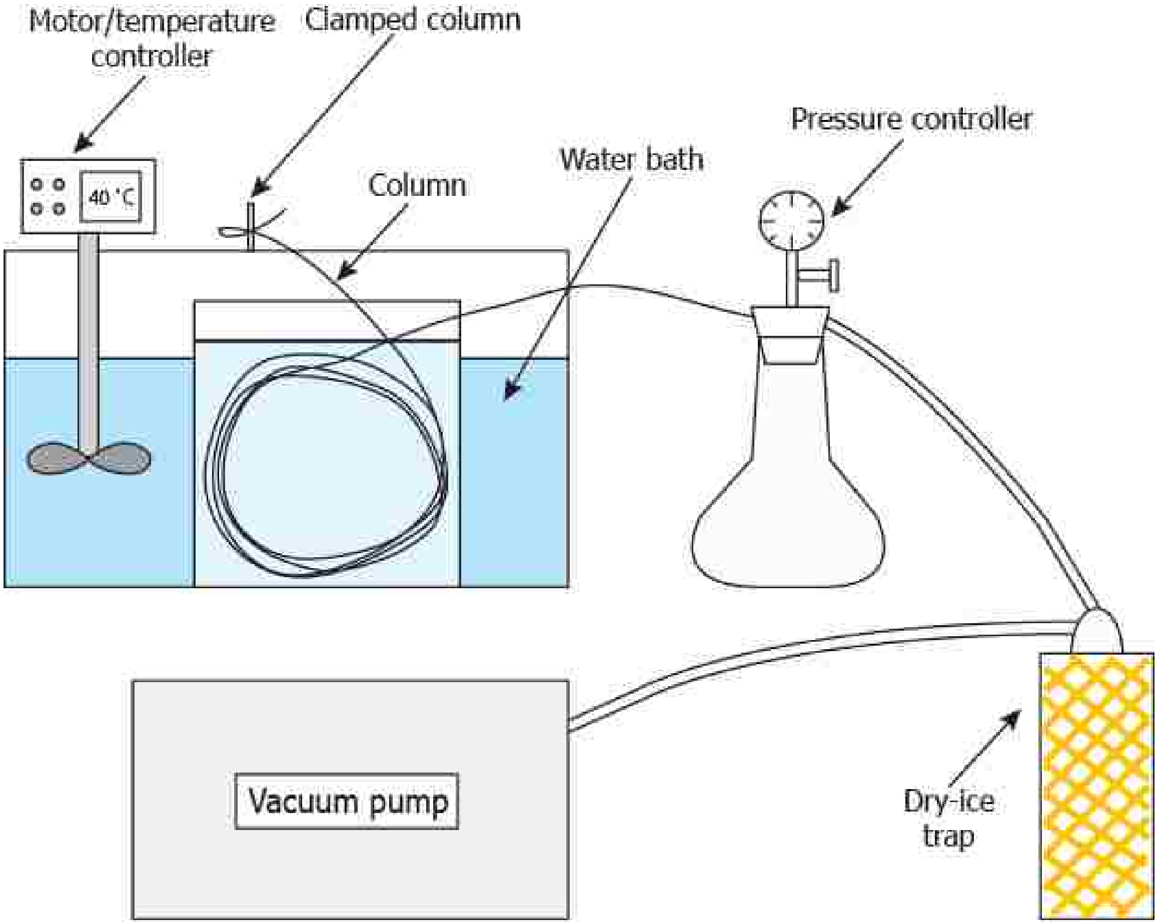

Scheme 3.2: Experimental set up for coating of the GC column.

$$R_S = 2\,[(t_R)_B - (t_R)_A] / (W_A + W_B)$$

where $(t_R)_A$ and $(t_R)_B$, and W_A and W_B are retention times and base widths, respectively, for two adjacent species, A and B. Selectivity factors were determined using the equation below:

$$\alpha = [(t_R)_B - t_M] / [(t_R)_A - t_M]$$

where t_M is migration time for unretained species; and $(t_R)_A$ and $(t_R)_B$ retention times for species A and B, respectively. In order to calculate selectivity factor we had to first determine migration time for not retained species (t_M) using the following two equations:

$$V_M = t_M \times F$$

where F is the average volumetric flow rate within the column; V_M and t_M are retention volume and time, respectively, for unretained species.

$$F = F_M \times (T_C / T) \times [(P - P_{H_2O})] / P$$

where T_C is the column temperature in degrees Kelvin, T is the temperature at the meter, F_M is the measured flow rate, P is the gas pressure at the end of the column and P_{H_2O} is vapor pressure of water. Usually P and T are taken as ambient pressure and temperature, respectively.

3.3 RESULTS AND DISCUSSION

Six columns (0.25 mm I.D. × 10 m length) were coated with either IL alone or IL plus cavitand as a stationary phase. They were: $[BMIm]^+[BF_4]^-$, $[BMIm]^+[BF_4]^-$ + cavitand 1, $[OMIm]^+[Tf_2N]^-$, $[OMIm]^+[Tf_2N]^-$ + cavitand 2, $[N\text{-}EtPy]^+[CF_3CO_2]^-$ and $[N\text{-}EtPy]^+[CF_3CO_2]^-$ + cavitand 3. The thickness of the coating film was calculated using the reported equation:[49]

$$d_f = (d \times c) / 400$$

where d_f is the film thickness in μm, d is the internal diameter of the column in μm and c is the concentration of IL solution in the coating solvent (i.e., dichloromethane) in % (v/v). In our study we dissolved 25 mg of IL solution in 10 mL of dichloromethane. It was found that all six columns have similar thicknesses, that is, from 0.116 μm to 0.129 μm for columns coated with $[OMIm]^+[Tf_2N]^-$ and $[BMIm]^+[BF_4]^-$, respectively. Complete data, together with the theoretical plate numbers, are listed in **Table 3.1**. The latter values were determined by measuring the plate number with naphthalene as solute at 100 ˚C and calculated using the following equation:

$$N = 16 \times (t_R / W)^2$$

where t_R is the retention time of naphthalene and W is the base width of naphthalene peak. As listed in **Table 3.1**, all six columns were found to have theoretical plate numbers in the range between 21,000 to 28,500 plates. Obtained data show that adding cavitands into the ILs leads to an increased efficiency of the columns. Specifically, the efficiencies of columns coated only with ILs ($[BMIm]^+[BF_4]^-$, $[OMIm]^+[Tf_2N]^-$ and $[N\text{-}EtPy]^+[CF_3COO]^-$) were increased by approximately 2,000 to 4,000 plates. These results indicate that ILs can effectively serve as stationary phase in gas chromatography, and that the addition of cavitands to the ILs further increases the efficiency of the SP.

Cavitands, used in our study, are known to exhibit remarkable molecular recognition in solution; specifically, they can differentiate molecules with very small differences in their structures, for example isotopic molecules.[34] It would therefore be interesting to determine if such discrimination is restricted to the homogenous liquid phase as observed previously or also applicable to heterogeneous conditions, that is, as a

Stationary Phase	**Column Dimensions (m x mm ID)**	**Film Thickness (µm)**	**Theoretical Plate Number**
$[BMIm]^+[BF_4]^-$	10 x 0.25	0.129	23,050
$[BMIm]^+[BF_4]^-$ + cavitand 1	10 x 0.25	0.129	25,780
$[OMIm]^+[Tf_2N]^-$	10 x 0.25	0.116	24,000
$[OMIm]^+[Tf_2N]^-$ + cavitand 2	10 x 0].25	0.116	28,460
$[N\text{-}EtPy]^+[CF_3CO_2]^-$	10 x 0.25	0.120	21,000
$[N\text{-}EtPy]^+[CF_3CO_2]^-$ + cavitand 3	10 x 0.25	0.120	23,280

Table 3.1: Parameters (dimensions, film thickness, theoretical plate number) of the novel columns.

liquid stationary phase towards gaseous solutes in GC. Separation efficiencies of columns coated with cavitands were investigated for a variety of isotopic molecules or compounds with very small differences in their structure, including a mixture of xylene isomers (o-, m- and p-xylene, as well as p-xylene-h_{10} and p-xylene-d_{10}); mixture of isotopic isomers of methanol (methanol-h_4, methanol-d_4, methanol-d_3, methanol-d); ethanol (ethanol-h_5, ethanol-d_5); acetonitrile (acetonitrile-h_3, acetonitrile-d_3); acetone (acetone-h_6, acetone-d_6); chloroform (chloroform-h_1, chloroform-d_1); tetrachloroethane (tetrachloroethane-h_2, tetrachloroethane-d_2); chlorobenzene (chlorobenzene-h_5, chlorobenzene-d_5); 1,2-dichlorobenzene (1,2-dichlorobenzene-h_4 and 1,2-dichlorobenzene-d_4); pyridine (pyridine-h_5, pyridine-d_5); 1,4-dioxane (1,4-dioxane-h_8 and 1,4-dioxane-d_8) and tetrahydrofuran (THF) (tetrahydrofuran-h_8, tetrahydrofuran-d_8). All the compounds analyzed and their respective stationary phases that were used for analysis are listed in **Tables 3.2** to **3.4**. The efficiency of the novel stationary phases was initially investigated on columns coated with ILs with cavitands. In cases when the separation between two compounds (three compounds for p-, o- and m-xylene) occured, the sample was further analyzed on GC columns coated with only ILs in order to determine the effect of cavitands on the separation efficiency. As listed in **Tables 3.2** to **3.4**, no separation was observed for the following compounds: isotopes of p-xylene, chloroform, thetrachloroethane, acetone and tetrahydrofuran. Due to the similarity of the tetrahydrofuran molecule with 1,4-dioxane, it was expected that isotopic separation would be achieved. The reasons why isotopic differentiation for this molecule is not sufficient are not clear; however, they might be due to the differences in polarity indices between these two compounds, i.e. 1,4-dioxane and tehtrahydrofurane have polarity

Column	**p -, o -, m - xylene**	**p – xylene (d_{10} & h_{10})**	**CD_3OD & CH_3OH**	**CD_3OH & CH_3OH**	**CH_3OD & CD_3OH**	**CH_3OD & CH_3OH**
$[BMIm]^+[BF_4]^-$ + cavitand 1	no separation, 2 peaks (m - , p - and o -)	no separation	separation	no separation	separation	separation
$[OMIm]^+[Tf_2N]^-$ + cavitand 2	base line separation	no separation	no separation	no separation		
$[N\text{-}EtPy]^+[CF_3CO_2]^-$ + cavitand 3	no separation, 2 peaks (m - , p - and o -)	no separation	separation	separation	no separation	
$[BMIm]^+[BF_4]^-$			separation		separation	separation
$[OMIm]^+[Tf_2N]^-$	separation					
$[N\text{-}EtPy]^+[CF_3CO_2]^-$			no separation	no separation		

Table 3.2: Combinations of compounds and stationary phases that were used in the study.

Column	**EtOH (d_5 & h_5)**	**CH_3CN & CD_3CN**	**p – dioxane (d_8 & h_8)**	**Pyridine (d_5 & h_5)**	**Chloroform (d_1 & h_1)**	**Tetrachloroethane (d_2 & h_2)**
$[BMIm]^+[BF_4]^-$ + cavitand 1	no separation	slight separation	separation	almost baseline separation	no separation	no separation
$[OMIm]^+[Tf_2N]^-$ + cavitand 2	no separation	separation	separation	separation	no separation	no separation
$[N\text{-}EtPy]^+[CF_3CO_2]^-$ + cavitand 3	no separation (disshaped peak)	no separation (disshaped peak)	separation	almost baseline separation	no separation	no separation
$[BMIm]^+[BF_4]^-$		slight separation	separation	separation		
$[OMIm]^+[Tf_2N]^-$		no separation	no separation	slight separation		
$[N\text{-}EtPy]^+[CF_3CO_2]^-$			no separation	no separation		

Table 3.3: Combinations of compounds and stationary phases used in the study.

Column	**1,2 dichlorobenzene (d_4 & h_4)**	**Chlorobenzene (d_5 & h_5)**	**Acetone (d_6 & h_6)**	**THF (d_8 & h_8)**
$[BMIm]^+[BF_4]^-$ + cavitand 1	separation	separation	no separation	no separation
$[OMIm]^+[Tf_2N]^-$ + cavitand 2	no separation	no separation	no separation	no separation
$[N\text{-}EtPy]^+[CF_3CO_2]^-$ + cavitand 3	no separation	no separation	no separation	no separation
$[BMIm]^+[BF_4]^-$	slight separation	slight separation		
$[OMIm]^+[Tf_2N]^-$				
$[N\text{-}EtPy]^+[CF_3CO_2]^-$				

Table 3.4: Combinations of compounds and stationary phases used in the study.

indices of 4.8 and 4.0, respectively.

For remaining groups of solutes (i.e., benzene derivatives, alcohols, actonitrile and heterocyclic organic compounds) the separation efficienciencies of the stationary phases varied due to the different polarities of the samples and stationary phases, as well as due to the specific molecular recognition abilities of the cavitands.

Separation of benzene derivatives

Chromatograms of the mixture of p-, m- and o- xylene are shown in **Figure 3.1**. As can be observed from **Figure 3.1A**, columns coated with $[BMIm]^+[BF_4]^-$ and cavitand is analyzed using $[N\text{-}EtPy]^+[CF_3CO_2]^-$ with cavitand 3 stationary phase (chromatogram not shown). These results can be explained by comparing the polarity of the sample and columns used. Specifically, xylenes mixture is non-polar whereas both $[BMIm]^+[BF_4]^-$ with cavitand 1 and $[N\text{-}EtPy]^+[CF_3CO_2]^-$ with cavitand 3 represent relatively more polar stationary phase, and are therefore less efficient for separation of non-polar compounds. As expected, relatively non-polar column (i.e., column coated with $[OMIm]^+[Tf_2N]^-$) did, in fact, provide separation of this non-polar mixture of xylenes (**Figure 3.1B**). However, column coated with IL ($[OMIm]^+[Tf_2N]^-$) alone does not provide baseline separation of all three isomers, i.e., p- and m-xylene are partially separated. Adding cavitand 2 to $[OMIm]^+[Tf_2N]^-$ led to a substantial improvement in the separation efficiency, providing almost baseline separation for all three isomers (see **Figure 3.1C**). Furthermore, addition of cavitand 2 into $[OMIm]^+[Tf_2N]^-$ enables the column increase of retention time for these compounds, resulting in higher separation efficiency. While the improved efficiency can be visibly observed in the chromatograms, it is more pronounced when compared in terms of R_s values listed in **Table 3.5**. As listed in the table, the increase

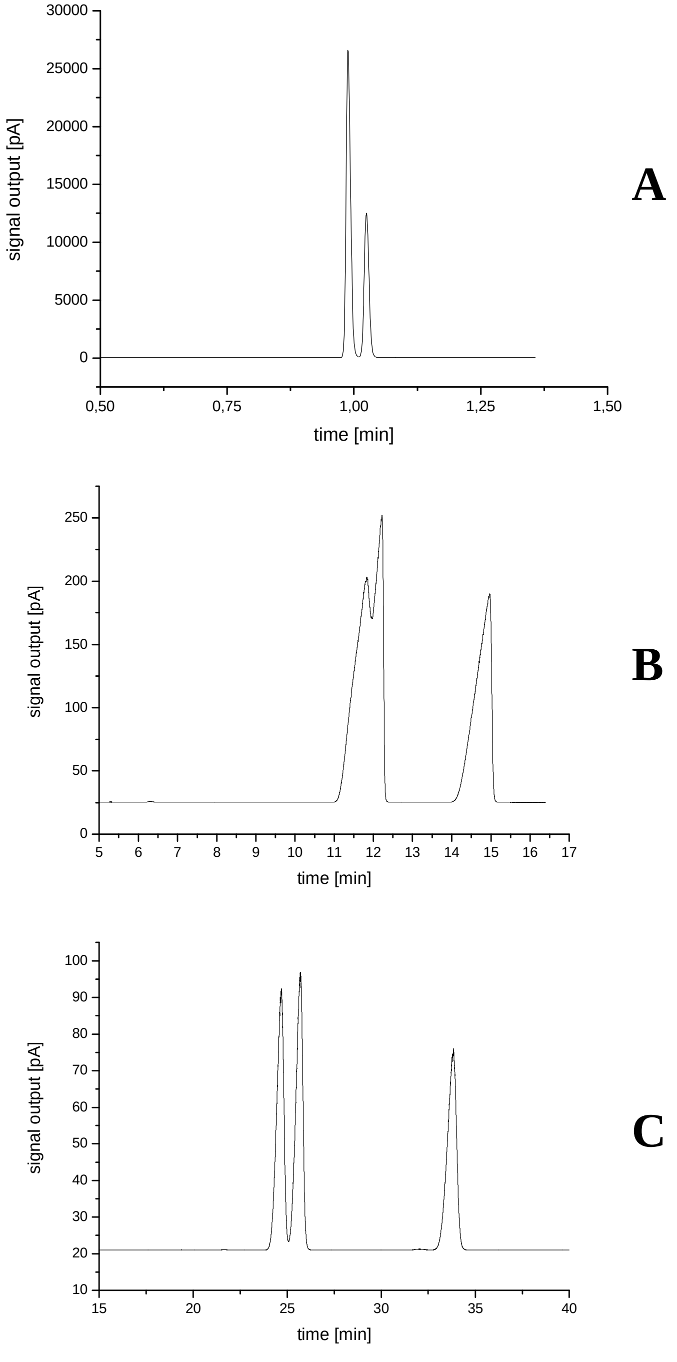

Figure 3.1: Mixture of p-, m- and o-xylene; stationary phase: $[BMIm]^+[BF_4]^-$ with cavitand 1 (A), $[OMIm]^+[Tf_2N]^-$ (B) and $[OMIm]^+[Tf_2N]^-$ with cavitand 2 (C).

in the resolution is higher in the case of $[OMIm]^+[Tf_2N]^-$ column with added cavitand 2 compared to the column coated only with IL. Specifically, R_s values of 0.378 and 2.699 for mixture of p-, m-xylene and m-, o-xylene increased by 110% and 138%, respectively, when IL with cavitand 2 was employed. Similarly, enhancement in selectivity factors (α) (see **Table 3.6**) can also be observed. That is, α values increased from 1.038 to 1.045 for p- and m-xylene, and from 1.26 to 1.34 for m-and o-xylene.

Chromatograms of mixtures of chlorobenzene-h_5 and chlorobenzene-d_5, and 1,2-dichlorobenzene-h_4 and 1,2-dichlorobenzene-d_4 separated on the columns coated with $[BMIm]^+[BF_4]^-$ (with and without cavitand 1) are shown in **Figure 3.2** and **3.3**, respectively. Other columns used in the study cannot separate these mixtures and are thus not presented in this work. A column coated with the IL ($[BMIm]^+[BF_4]^-$) alone provides low separation of chlorobenzene and 1,2-dichlorobenzene isotopes (R_s values are 0.19 and 0.214, respectively). As evident from the chromatograms (**Figure 3.2B** and **3.3B**) and **Table 3.5**, adding cavitand 1 into the IL improved separation efficiency and led to a substantial improvement in the resolution values. Specifically, R_s values increased by 163% and 96% for isotopes of chlorobenzene and 1,2-dichlorobenzene, respectively.

Separation of alcohols

Figure 3.4 shows chromatograms of C_2H_5OH and C_2D_5OH. Columns coated with IL alone ($[BMIm]^+[BF_4]^-$, $[OMIm]^+[Tf_2N]^-$ and $[N\text{-}EtPy]^+[CF_3CO_2]^-$) cannot separate the isotopic mixture of ethanol. Even though addition of cavitand 3 into the $[N\text{-}EtPy]^+[CF_3CO_2]^-$ IL does not provide separation a peak with a broad shoulder can be observed (**Figure 3.4A**) indicating the presence of two compounds. Therefore, the novel stationary phase consisting of $[N\text{-}EtPy]^+[CF_3CO_2]^-$ with cavitand 3 can differentiate

Mixture	**$[BMIm]+[BF_4]^-$**	**$[BMIm]+[BF_4]^-$ + cavitand 1**	**$[OMIm]^+[Tf_2N^-]$**	**$[OMIm]^+[Tf_2N^-]$ + cavitand 2**	**$[N\text{-}EtPy]^+[CF_3CO_2^-]$**	**$[N\text{-}EtPy]^+[CF_3CO_2^-]$ + cavitand 3**
methanol (d_4 - h_4)	0.41+0.04	0.45±0.05	-	-	-	0.34±0.01
methanol (d_3 - h_4)	-	-	-	-	-	0.34±0.02
methanol (d - h_4)	0.43±0.01	0.41±0.01	-	-	-	-
methanol (d - d_3)	0.42±0.01	0.45±0.02	-	-	-	-
p-xylene, m-xylene	-	-	0.38±0.01	0.80±0.02	-	-
m-xylene, o-xylene	-	-	2.71±0.01	6.45±0.02	-	-
chlorobenzene (d_5 - h_5)	0.19	0.50±0.01	-	-	-	-
1,2-dichlorobenzene (d_4 - h_4)	0.214	0.42±0.03	-	-	-	-
pyridine (d_5 - h_5)	0.61	0.76±0.01	0.17	0.43±0.01	-	0.69±0.03
1,4-dioxane (d_8 - h_8)	0.510	0.59±0.01	-	0.47±0.01	-	0.43±0.02
acetonitrile (d_3 - h_3)	0.23±0.02	0.24±0.01	-	0.34±0.01	-	-

Table 3.5: Resolution values (R_s).

Mixture	**[BMIm]+[BF$_4$]$^-$**	**[BMIm]+[BF$_4$]$^-$ + cavitand 1**	**[OMIm]$^+$[Tf$_2$N$^-$]**	**[OMIm]$^+$[Tf$_2$N$^-$] + cavitand 2**	**[N-EtPy]$^+$[CF$_3$CO$_2$$^-$]**	**[N-EtPy]$^+$[CF$_3$CO$_2$$^-$] + cavitand 3**
methanol (d_4 - h_4)	1.04+0.01	1.04±0.01	-	-	-	1.04±0.04
methanol (d_3 - h_4)	-	-	-	-	-	1.03±0.01
methanol (d - h_4)	1.038±0.002	1.036±0.001	-	-	-	-
methanol (d - d_3)	1.04±0.01	1.04±0.01	-	-	-	-
p-xylene, m-xylene	-	-	1.038±0.003	1.045±0.001	-	-
m-xylene, o-xylene	-	-	1.26±0.01	1.34±0.01	-	-
chlorobenzene	1.015	1.006±0.001	-	-	-	-
1,2-dichlorobenzene	1.006	1.004±0.003	-	-	-	-
pyridine (d_5 - h_5)	1.010	1.005±0.005	1.02	1.006±0.001	-	1.014±0.006
1,4-dioxane (d_8 - h_8)	1.006	1.007±0.002	-	1.006±0.002	-	1.04±0.02
acetonitrile (d_3 - h_3)	1.022±0.007	1.019±0.003	-	1.024±0.004	-	-

Table 3.6: Selectivity factors (α).

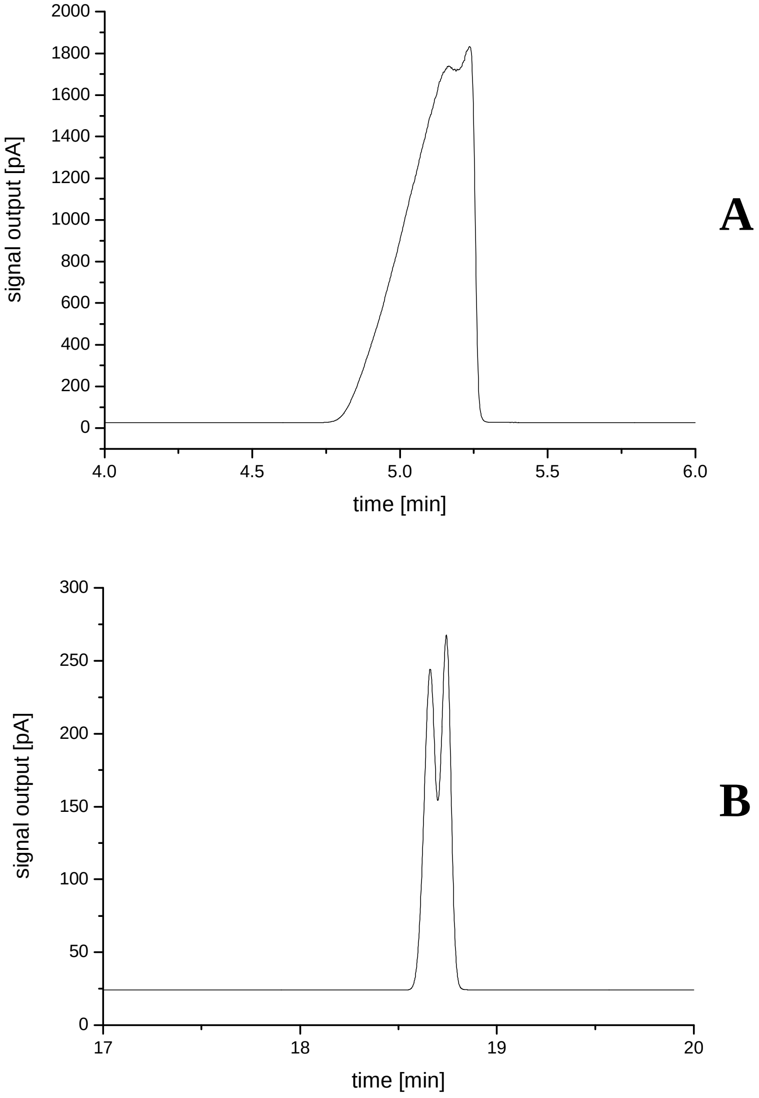

Figure 3.2: Mixture of chlorobenzene-*h*$_5$ and chlorobenzene-*d*$_5$; stationary phase: $[\mathrm{BMIm}]^+[\mathrm{BF}_4]^-$ (A), $[\mathrm{BMIm}]^+[\mathrm{BF}_4]^-$ with cavitand 1 (B).

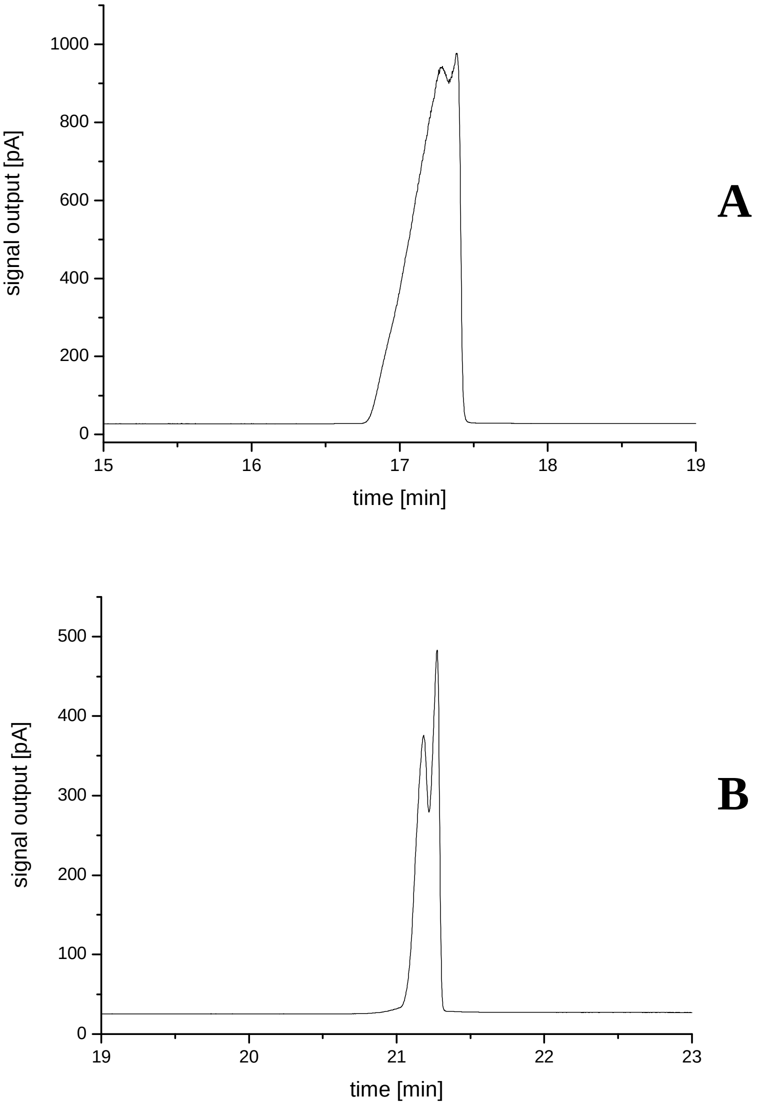

Figure 3.3: Mixture of 1,2-dichlorobenzene-h_4 and 1,2-dichlorobenzene-d_4; stationary phase: $[BMIm]^+[BF_4]^-$ (A), $[BMIm]^+[BF_4]^-$ with cavitand 1 (B).

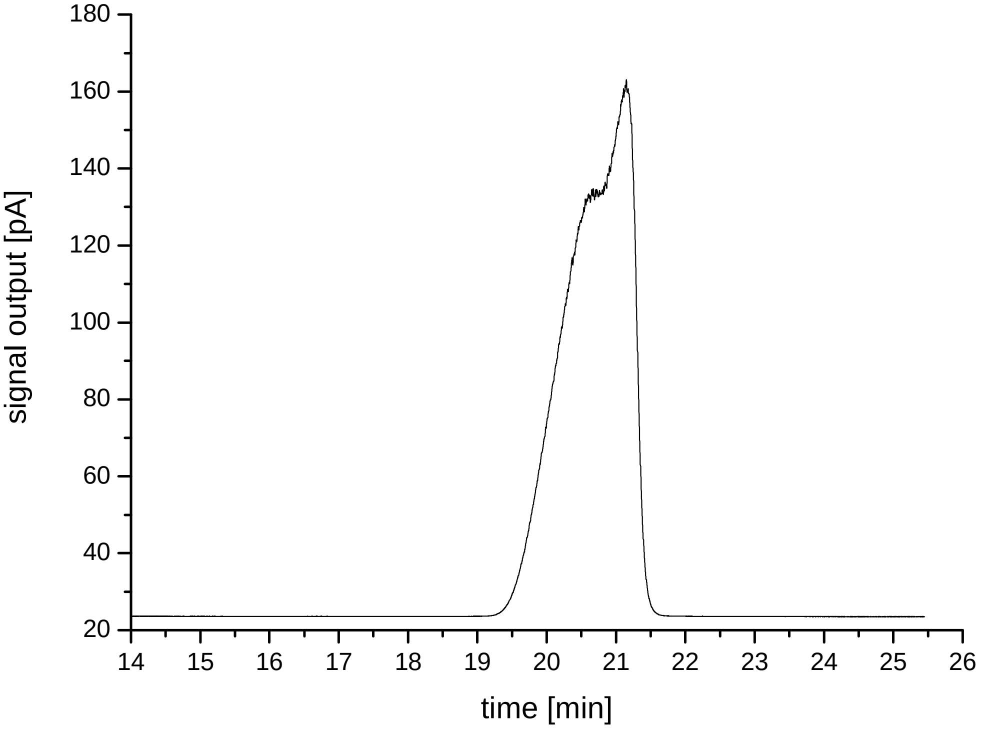

Figure 3.4: Mixture of C_2H_5OH and C_2D_5OH; stationary phase: $[NEtPy]^+[CF_3CO_2]^-$ with cavitand 3.

between C_2H_5OH and C_2D_5OH; however, the guest-host interaction of cavitand and isotopic molecules is not sufficient for discernible separation of the two isotopomers. No separation is obtained by adding cavitands 1 and 2 into the $[BMIm]^+[BF_4]^-$ and $[OMIm]^+[Tf_2N]^-$ ILs, respectively.

Four mixtures of methanol (CH_3OH and CD_3OH, CH_3OH and CD_3OD, CH_3OD and CD_3OH, CH_3OH and CH_3OD) were analyzed in the experiment. Columns coated with $[OMIm]^+[Tf_2N]^-$ and $[N\text{-}EtPy]^+[CF_3CO_2]^-$ ILs alone do not provide sufficient conditions for separation to occur. Addition of cavitands 2 and 3, respectively, results in separation of mixtures of CH_3OH and CD_3OH, and CH_3OH and CD_3OD on the latter column (i.e., $[N\text{-}EtPy]^+[CF_3CO_2]^-$ with cavitand 3) (**Figure 3.5A-B**) whereas no separation is observed on the column coated with $[OMIm]^+[Tf_2N]^-$ with added cavitand 2. Chromatograms obtained with $[BMIm]^+[BF_4]^-$ and $[BMIm]^+[BF_4]^-$ with cavitand 1 columns are shown in **Figure 3.5C-H**. Both columns were able to separate three mixtures of methanol, i.e., CH_3OH and CD_3OD, CH_3OD and CD_3OH, CH_3OH and CH_3OD. Comparison of the figures and resolution parameters (R_s values) as well as selectivity factors (α) (**Table 3.5** and **3.6**) indicates that addition of the cavitand 1 to IL $[BMIm]^+[BF_4]^-$ does not induce any improvement in the separation efficiency. It is interesting to observe that SPs, which exhibit sufficient molecular recognition to induce separation of isotopic methanol mixtures (i.e., $[BMIm]^+[BF_4]^-$ with or without cavitand 1 and $[N\text{-}EtPy]^+[CF_3CO_2]^-$ with cavitand 3), have different chromatographic properties; that is, the former ($[BMIm]^+[BF_4]^-$ with or without cavitand 1) can separate only mixtures where the hydroxide part of the molecule differs (**Figure 3.5C-H**), whereas the latter ($[N\text{-}EtPy]^+[CF_3CO_2]^-$ with cavitand 3) only separates mixtures which have different

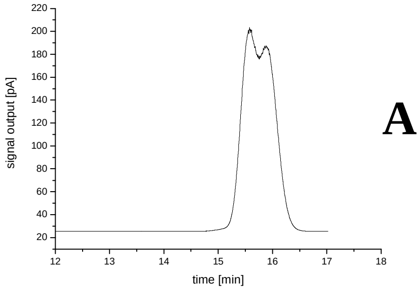

CH$_3$OH and CD$_3$OH mixture

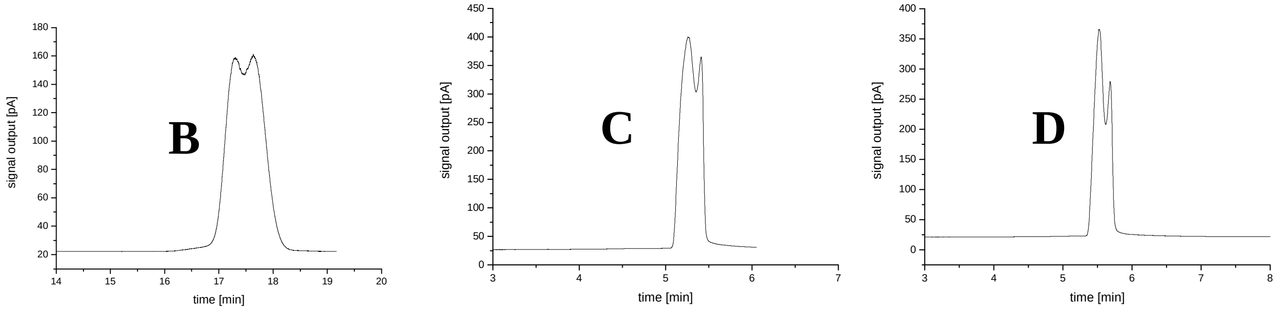

CD$_3$OD and CH$_3$OH mixture

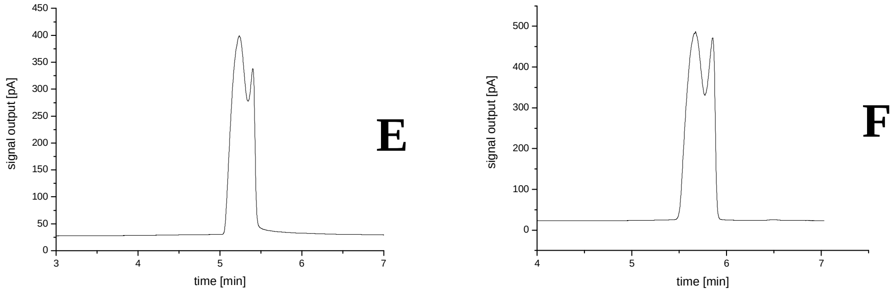

CH$_3$OD and CD$_3$OH mixture

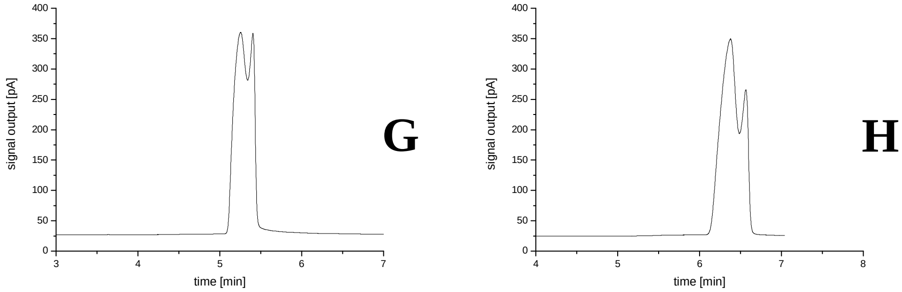

CH$_3$OD and CH$_3$OH mixture

Figure 3.5: Mixture of alcohols; stationary phase: $[NEtPy]^+[CF_3CO_2]^-$ with cavitand 3 (A, B), $[BMIm]^+[BF_4]^-$ (C, E and G), $[BMIm]^+[BF_4]^-$ with cavitand 1 (D, F and H).

methyl groups (**Figure 3.5A-B**). Furthermore, areas of two peaks separated with $[BMIm]^+[BF_4]^-$ column (with or without cavitand 1) are in ratio 2:1, whereas $[N\text{-}EtPy]^+[CF_3CO_2]^-$ with cavitand 3 column provides ca. 1:1 area ratio separation (all mixtures were made in 1:1 v/v ratio).

Additional studies were performed in order to gain a better understanding of the chemistry behind the elution of two unequal bands in ratio 2:1 when $[BMIm]^+[BF_4]^-$ and $[BMIm]^+[BF_4]^-$ with cavitand 1 were used as a SP. When CD_3OH is injected into the $[BMIm]^+[BF_4]^-$ with cavitand 1 column only one peak with retention time of 5.7 min is eluted (**Figure 3.6B**). Subsequent injection of CD_3OD into the same column results in elution of two overlapping peaks with retention times 5.7 and 5.9 min and area ratio of approximately 2:1 (**Figure 3.6C**). Further injections of CD_3OD emanate in decrease of the first band (i.e., with retention time at 5.7 min) and subsequent increase in intensity of the second band at approximately 5.9 min. This phenomenon can be cleraly observed from **Figure 3.6C-F**, which represent chromatograms after 1st (**Figure 3.6C**), 2nd (**Figure 3.6D**), 3rd (**Figure 3.6E**) and 11th injection (**Figure 3.6F**) of CD_3OD. The remaining band (at 5.9 min) exhibits a broad shoulder which coincides with retention time for the receding band at 5.7 min. Moreover, the broad shoulder abates with a growing number of injections. Conversely, injection of CD_3OH into the $[BMIm]^+[BF_4]^-$ with cavitand 1 column results in elution of a single broad band at 5.9 min (see **Figure 3.6G**). Interestingly, additional injections of CD_3OH yield an increasingly narrower band with shorter retention time at 5.7 min (compare **Figure 3.6G-J** for 1st, 2nd, 3rd and 6th injection, respectively). Adversely, injection of CD_3OH or CD_3OD into the $[N\text{-}EtPy]^+[CF_3CO_2]^-$ with cavitand 3 column results in elution of a single narrow band as

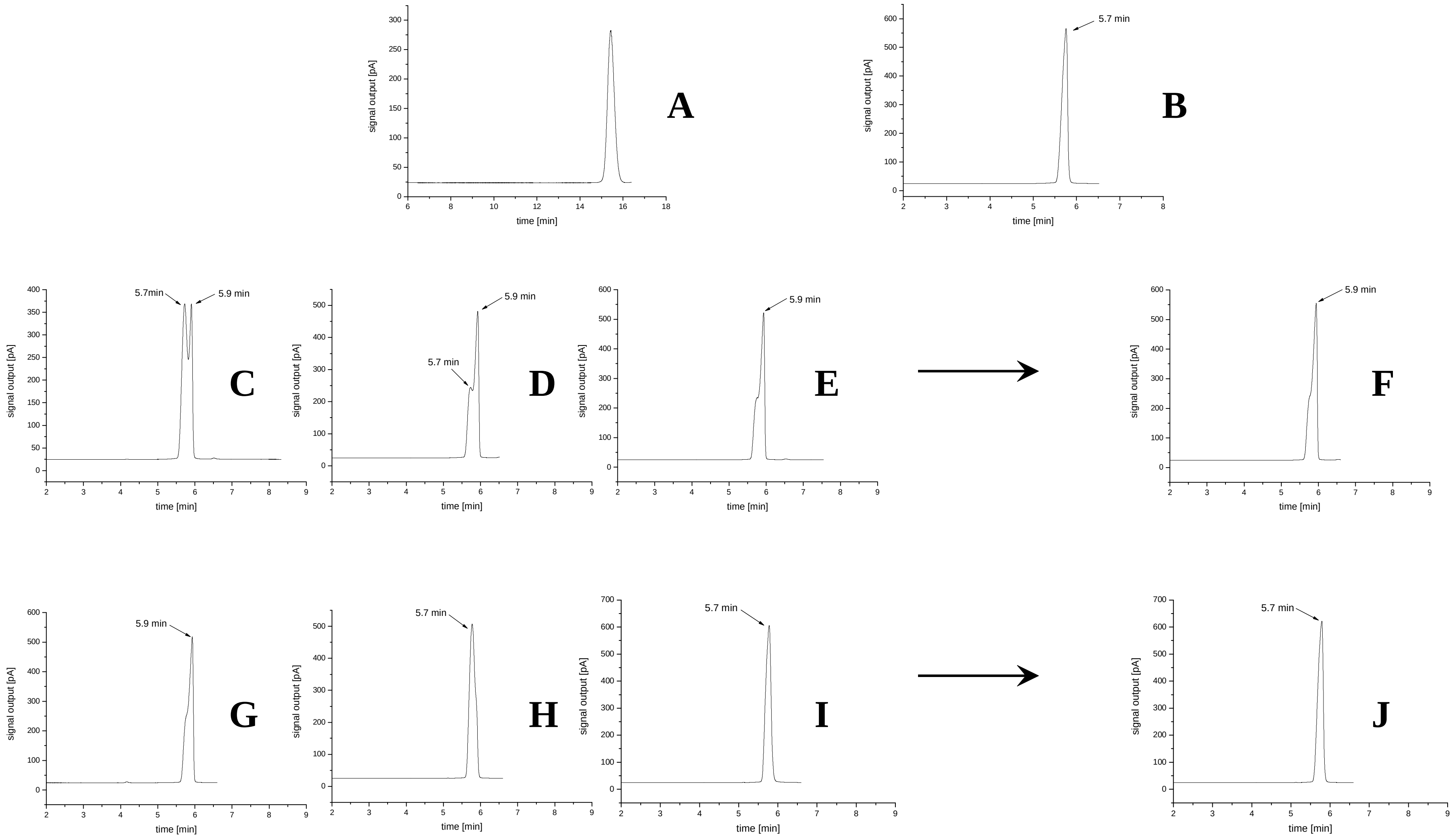

Figure 3.6: Deuterium-hydrogen exchange reactions in column; stationary phase: $[NEtPy]^+[CF_3CO_2]^-$ with cavitand 3 (A), $[BMIm]^+[BF_4]^-$ with cavitand 1 (B-J); injected sample: CD_3OH (B, G-J), CD_3OD (A, C-F).

can be seen from chromatogram in **Figure 3.6A**, representing elution of CD_3OD.

Essentially, the results obtained seem to suggest that methanol with -OD groups, when injected into the $[BMIm]^+[BF_4]^-$ column (with or without cavitand 1), undergo deuterium-hydrogen exchange with the stationary phase; i.e., -OD groups are converted into -OH groups, and therefore elution of two overlapping bands is observed. The band with retention time of 5.7 min corresponds to -OH groups whereas the second band (i.e., at 5.9 min) represents -OD groups. Reciprocated injections of CD_3OD (-OD groups) emanate in increased concentration of deuterium in the stationary phase and also increased intensity of the band at 5.9 min, which corresponds to -OD groups. Since the same phenomenon is observed also with $[BMIm]^+[BF_4]^-$ only stationary phase, the deuterium-hydrogen exchange most probably occurs between -OD groups in the alcohol and the IL; specifically, between -OD groups in the alcohol and acidic proton of the -CH group between two nitrogens of the imidazolium ring of the $[BMIm]^+[BF_4]^-$ ionic liquid (see **Scheme 3.1**). Due to the comparable structure this effect could be anticipated also for $[OMIm]^+[Tf_2N]^-$ with cavitand 2 stationary phase. Adversely, $[N\text{-}EtPy]^+[CF_3CO_2]^-$ with cavitand 3 do not have any group available for deuterium-hydrogen exchange and therefore does not exhibit such properties.

Separation of acetonitrile-h_3 and acetonitrile-d_3

Chromatograms of CH_3CN and CD_3CN are shown in **Figure 3.7**. Columns coated with only $[OMIm]^+[Tf_2N]^-$ and $[N\text{-}EtPy]^+[CF_3CO_2]^-$ cannot separate the isotopic mixture of CH_3CN and CD_3CN whereas column coated with only $[BMIm]^+[BF_4]^-$ provides slight separation with R_s value of 0.241 (**Table 3.5**, **Figure 3.7A**). Addition of cavitand 2 and cavitand 3 into $[OMIm]^+[Tf_2N]^-$ and $[N\text{-}EtPy]^+[CF_3CO_2]^-$, respectively, results in

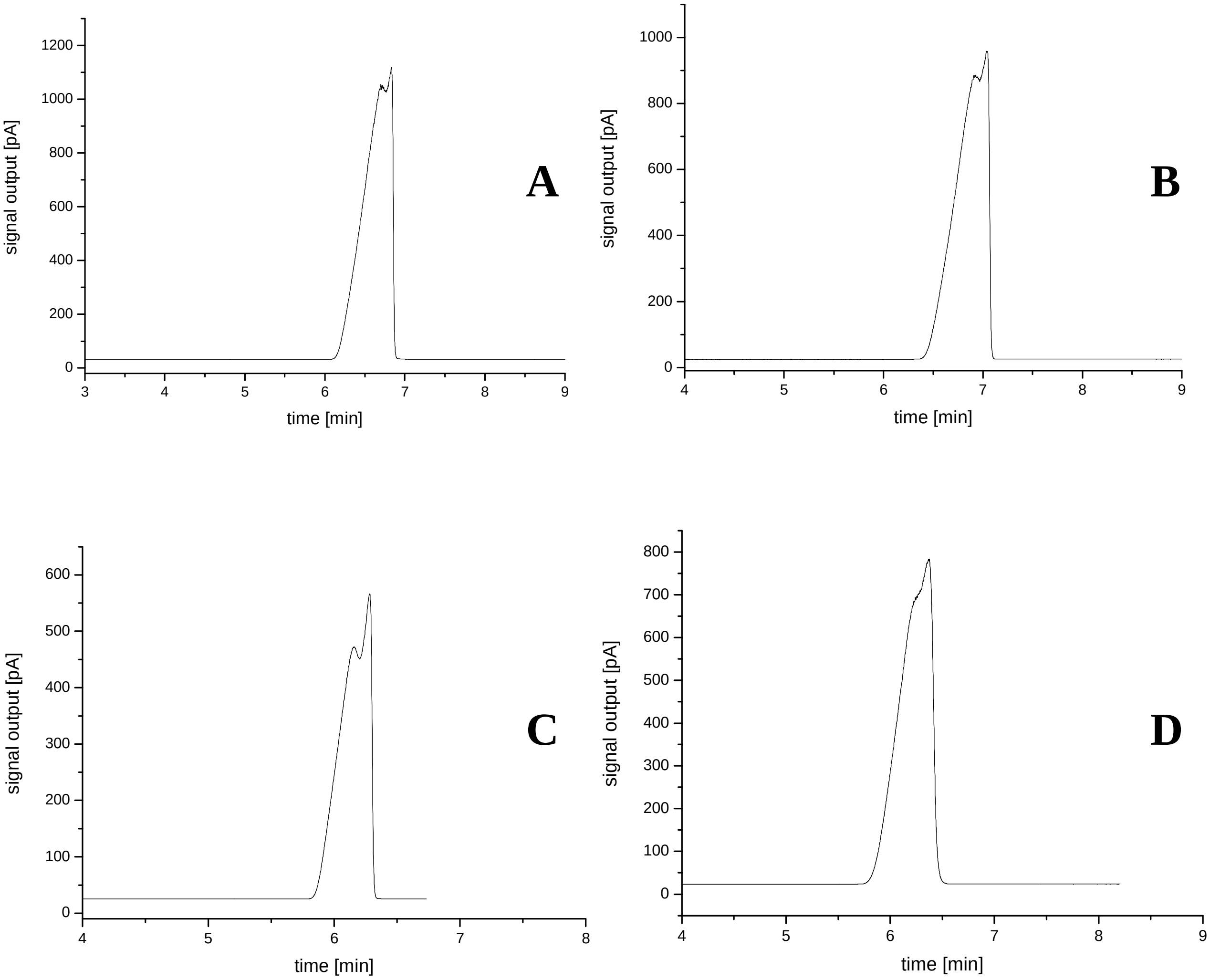

Figure 3.7: Mixture of CH_3CN and CD_3CN; stationary phase: $[BMIm]^+[BF_4]^-$ (A), $[BMIm]^+[BF_4]^-$ with cavitand 1 (B), $[OMIm]^+[Tf_2N]^-$ with cavitand 2 (C) and $[NEtPy]^+[CF_3CO_2]^-$ with cavitand 3 (D).

improved separation efficiency. Specifically, molecular recognition with limited separation is observed for the $[OMIm]^+[Tf_2N]^-$ with cavitand 2 column (**Figure 3.7C**) and broad shouldered band, which indicates the presence of two compounds in the acetonitrile mixture, is detected for $[N\text{-}EtPy]^+[CF_3CO_2]^-$ with cavitand 3 column (**Figure 3.7D**). On the contrary, adding cavitand 1 into $[BMIm]^+[BF_4]^-$ IL does not result in enhanced separation, i.e., comparison of the data (**Table 3.5** and **3.6** as well as **Figure 3.7A** and **3.7B**) suggests no significant difference between the $[BMIm]^+[BF_4]^-$ with and without cavitand 1 stationary phases.

Separation of heterocyclic compounds

Figure 3.8A and **3.8B** are chromatograms of 1,4-dioxane-h_8 and 1,4-dioxane-d_8 mixture, separated on $[BMIm]^+[BF_4]^-$ and $[BMIm]^+[BF_4]^-$ with cavitand 1 column, respectively. Inspecting R_s values listed in **Table 3.5** reveals that adding cavitand 1 into $[BMIm]^+[BF_4]^-$ column increased the resolution value from 0.51 to 0.59, however, significant improvement of separation efficiency was not obtained. Conversely, addition of cavitand 2 and cavitand 3 into $[OMIm]^+[Tf_2N]^-$ and $[N\text{-}EtPy]^+[CF_3CO_2]^-$, respectively, resulted in strong and positive effect on the separation efficiency, i.e., whereas columns coated with only IL ($[OMIm]^+[Tf_2N]^-$ and $[N\text{-}EtPy]^+[CF_3CO_2]^-$) could not separate the isotopic mixture of 1,4-dioxane latter SPs (i.e., with addition of cavitand 2 and 3, respectively) provided sufficient chromatographic conditions for separation to occur (see **Figure 3.8C-D**).

Good separation, with R_s value of 0.61, for pyridine-h_5 and pyridine-d_5 mixture was obtained using column coated with only $[BMIm]^+[BF_4]^-$ IL (**Figure 3.9A**) whereas column coated with only $[OMIm]^+[Tf_2N]^-$ provided very slight separation with Rs value

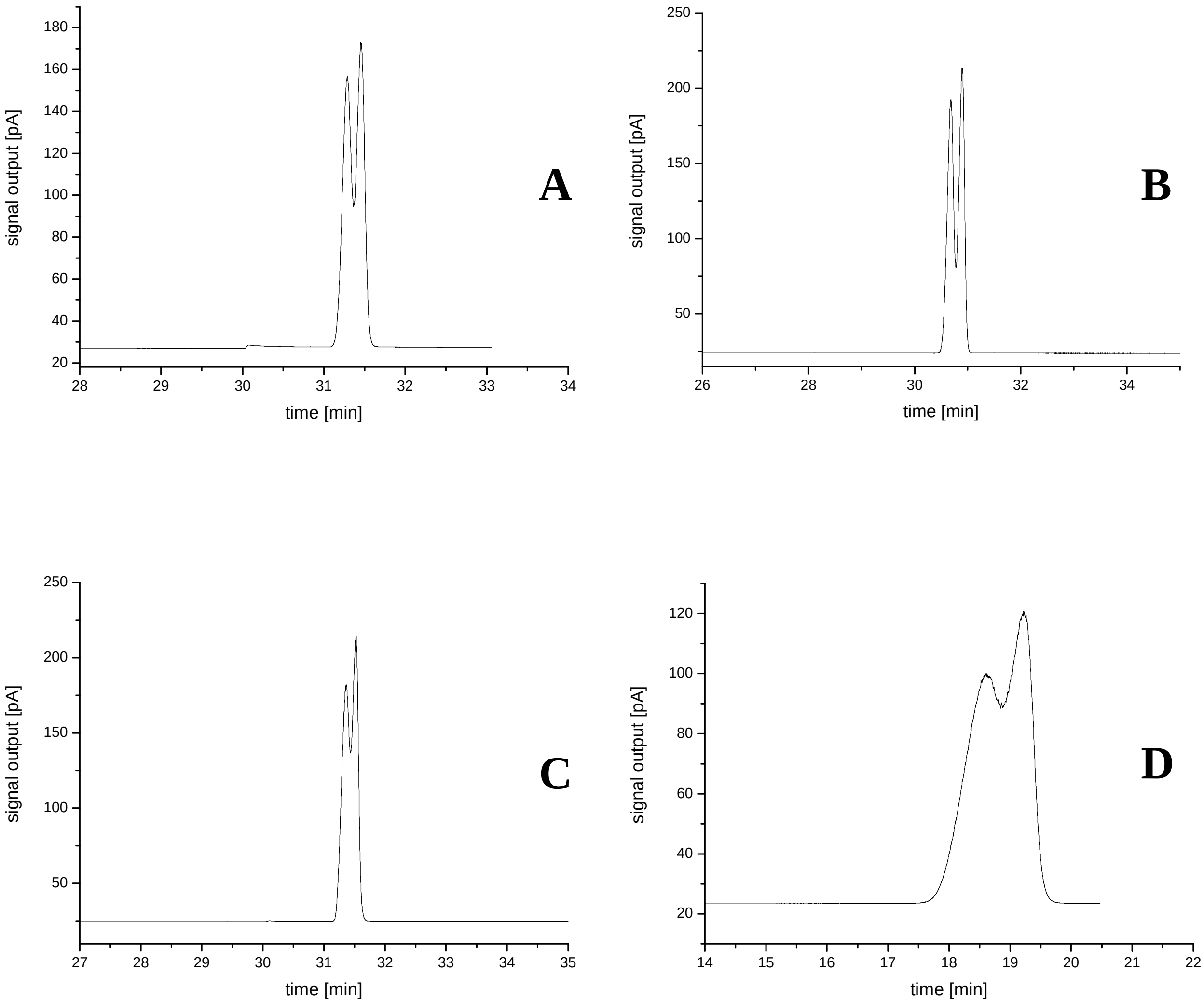

Figure 3.8: Mixture of 1,4-dioxane-h_8 and 1,4-dioxane-d_8; stationary phase: $[BMIm]^+[BF_4]^-$ (A), $[BMIm]^+[BF_4]^-$ with cavitand 1 (B), $[OMIm]^+[Tf_2N]^-$ with cavitand 2 (C) and $[NEtPy]^+[CF_3CO_2]^-$ with cavitand 3 (D).

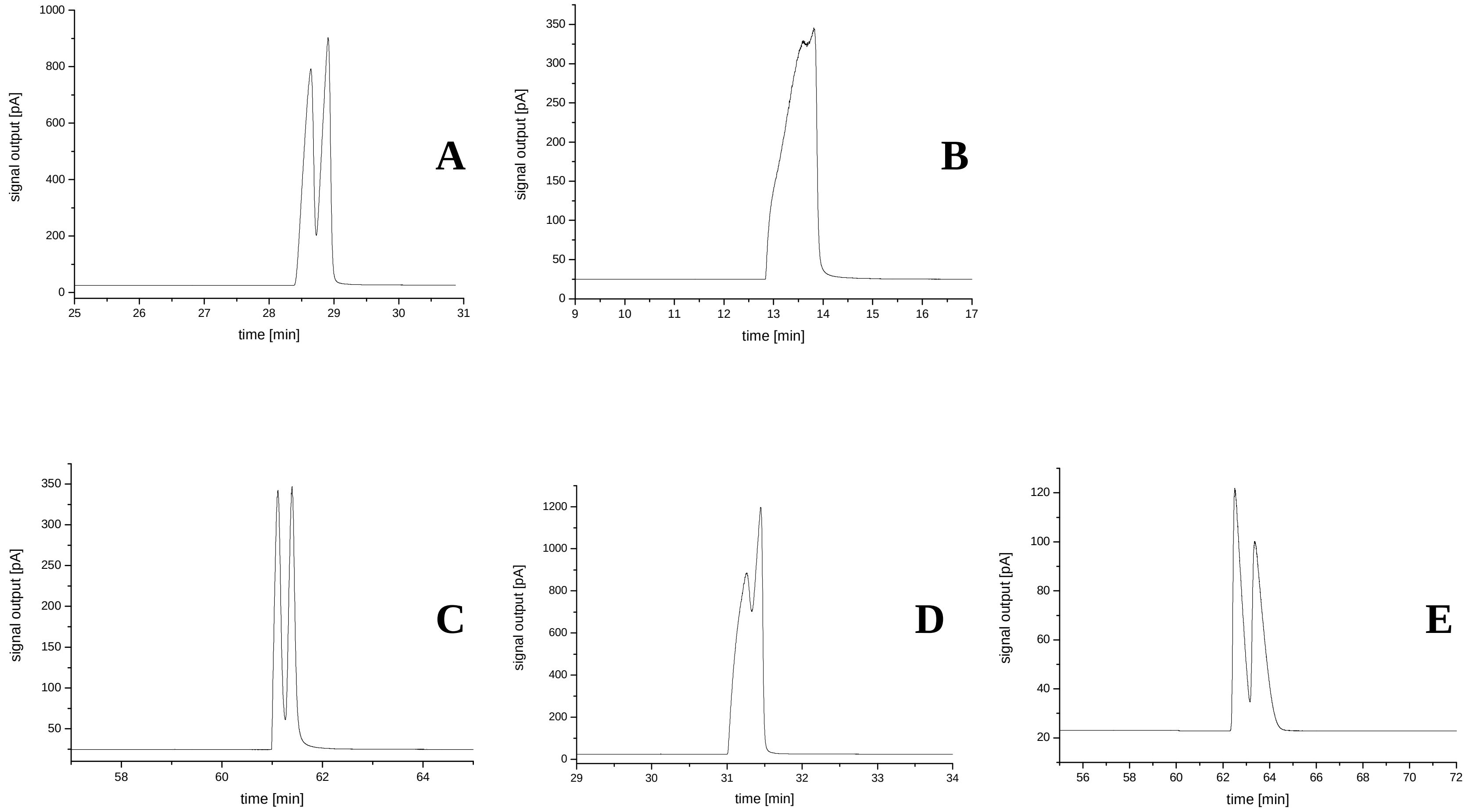

Figure 3.9: Mixture of pyridine-h_5 and pyridine-d_5; stationary phase: $[BMIm]^+[BF_4]^-$ (A), $[OMIm]^+[Tf_2N]^-$ (B), $[BMIm]^+[BF_4]^-$ with cavitand 1 (C), $[OMIm]^+[Tf_2N]^-$ with cavitand 2 (D) and $[NEtPy]^+[CF_3CO_2]^-$ with cavitand 3 (E).

of 0.17 (**Figure 3.9B**) and stationary phase which consisted of only $[N\text{-}EtPy]^+$ $[CF_3CO_2]^-$ did not induce any isotopic separation. As evident from chromatograms in **Figure 3.9C-E**, adding the cavitands into the ILs not only resulted in almost baseline separation on columns coated with $[BMIm]^+[BF_4]^-$ with cavitand 1 and $[N\text{-}EtPy]^+[CF_3CO_2]^-$ with cavitand 3 but also led to substantial improvement of the resolution values for $[OMIm]^+[Tf_2N]^-$ with cavitand 2 and $[N\text{-}EtPy]^+[CF_3CO_2]^-$ with cavitand 3 columns. Specifically, R_s values of 0.165 and 0 were increased to 0.439 and 0.612, respectively.

Interstingly, tetrahydrofuran could not be separated, even though it has a similar chemical structure as1,4-dioxane and same amount of deuterated hydrogens in the mixture (tetrahydrofuran-h_8 and tetrahydrofuran-d_8), with the six columns used in the study. The reason for that observation is not clear at this point but it might be due to the difference in polarities, i.e., tetrahydrofuran being less polar than 1,4-dioxane.

In addition to previously described studies, novel stationary phases (i.e., ILs with cavitands) were used to analyze mixtures of the following compounds: CH_3OH and CD_3OH, C_2H_5OH and C_2D_5OH, CH_3CN and CD_3CN, p-dioxane-h_8 and p-dioxane-d_8, and pyridine-h_5 and pyridine-d_5. In all cases, the baseline separation between different isotopic pairs is obtained. However, $[BMIm]^+[BF_4]^-$ with cavitand 1 stationary phase cannot separate isotopic molecules of methanol and ethanol, which elute earlier, and only a broad peak with a shoulder is observed for acetonitrile isotopic pair (see **Figure 3.10**). Conversely, good molecular recognition and separation is achieved for p-dioxane and pyridine isotopic molecules (**Figure 3.10**). Similar results are obtained when $[OMIm]^+[Tf_2N]^-$ with cavitand 2 column is employed for separation of the same mixture of compounds (**Figure 3.11**). The order of migration of the compounds is the same, with

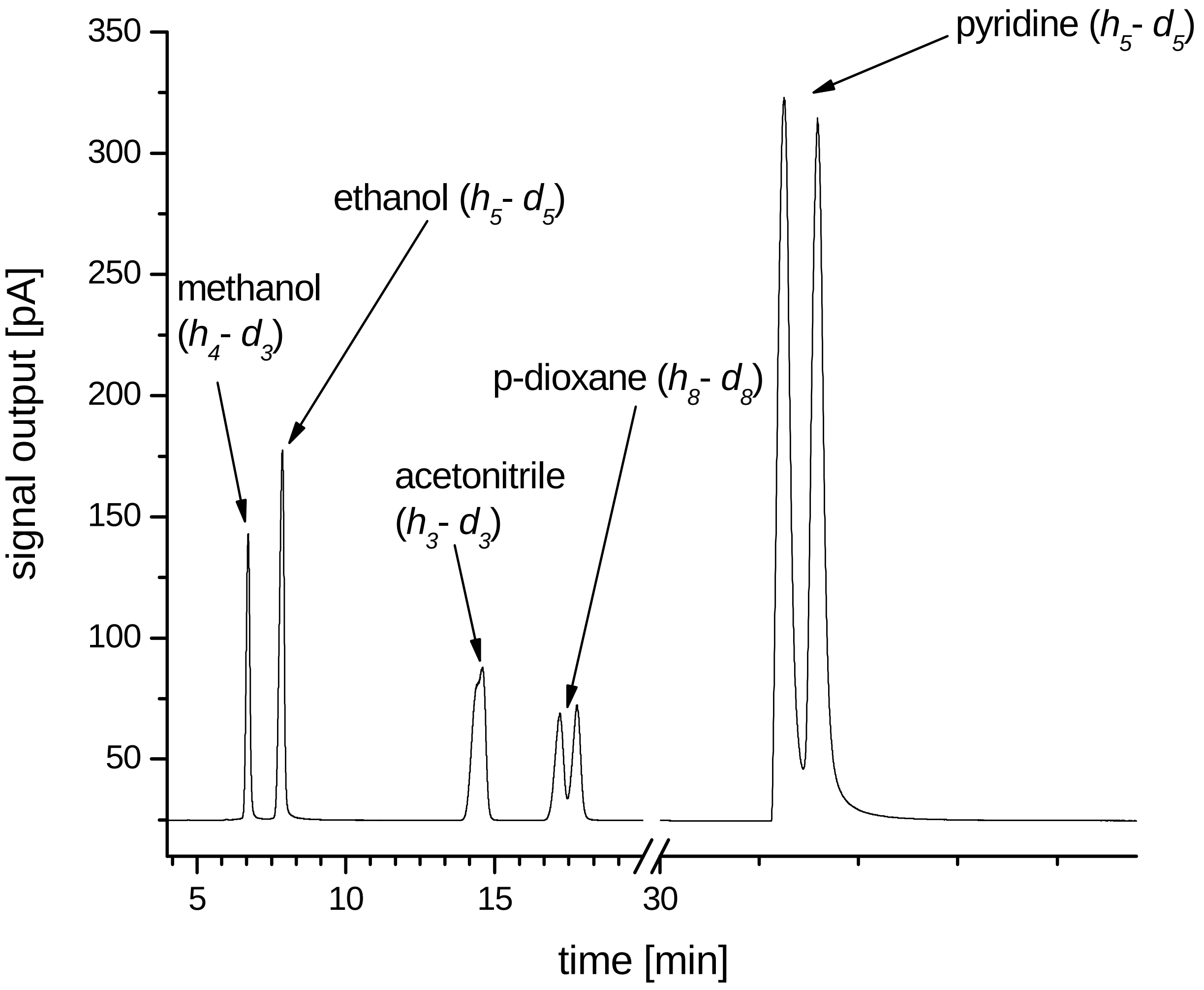

Figure 3.10: Mixture of isotopic molecules of methanol, ethanol, acetonitrile, p-dioxane and pyridine; stationary phase: $[BMIm]^+[BF_4]^-$ with cavitand 1.

methanol and ethanol isotopic compounds eluting first. Interestingly, an isotopic mixture of acetonitrile seems to interact relatively strongly with the cavitand because limited separation between two isotopomers can be observed. Contrarily, stationary phase consisting of $[NEtPy]^+[CF_3CO_2]^-$ with cavitand 3 exhibit a relatively different pattern. Specifically, broad band for isotopic mixture of acetonitrile is eluted first, followed by isotopic mixture of p-dioxane (see **Figure 3.12**). Methanol and ethanol isotopomers are retained on the stationary phase longer, and consequently exhibit separation between specific isomers. Furthermore, the separation efficiency for separation of p-dioxane-h_8 and p-dioxane-d_8 is decreased, which can be easily observed by comparing **Figures 3.10 - 3.12**.

3.4 CONCLUSION

We have demonstrated that remarkable molecular recognition ability of deep cavitands is not limited only to homogenous solutions but can be extended to a “heterogeneous two-phase system”. Migrating analytes stay in the cavitand solution for only a very short time, as they repeatedly diffuse in and out of the solution, which indicates that molecular recognition ability of the cavitands toward analytes are relatively strong. Strong molecular recognition ability of the cavitands resulted in different retention times of the analytes with very minor differences in their structures (i.e., hydrogen(s) vs deuterium(s)). Cavitands which were dissolved in a thin film of ionic liquid successfully differentiated between several different types of analytes, including a mixture of xylene isomers (o-, m- and p-xylene); mixture of isotopic isomers of methanol (CH_3OH, CD_3OD, CD_3OH, CH_3OD); ethanol (C_2H_5OH, C_2D_5OH); chlorobenzene

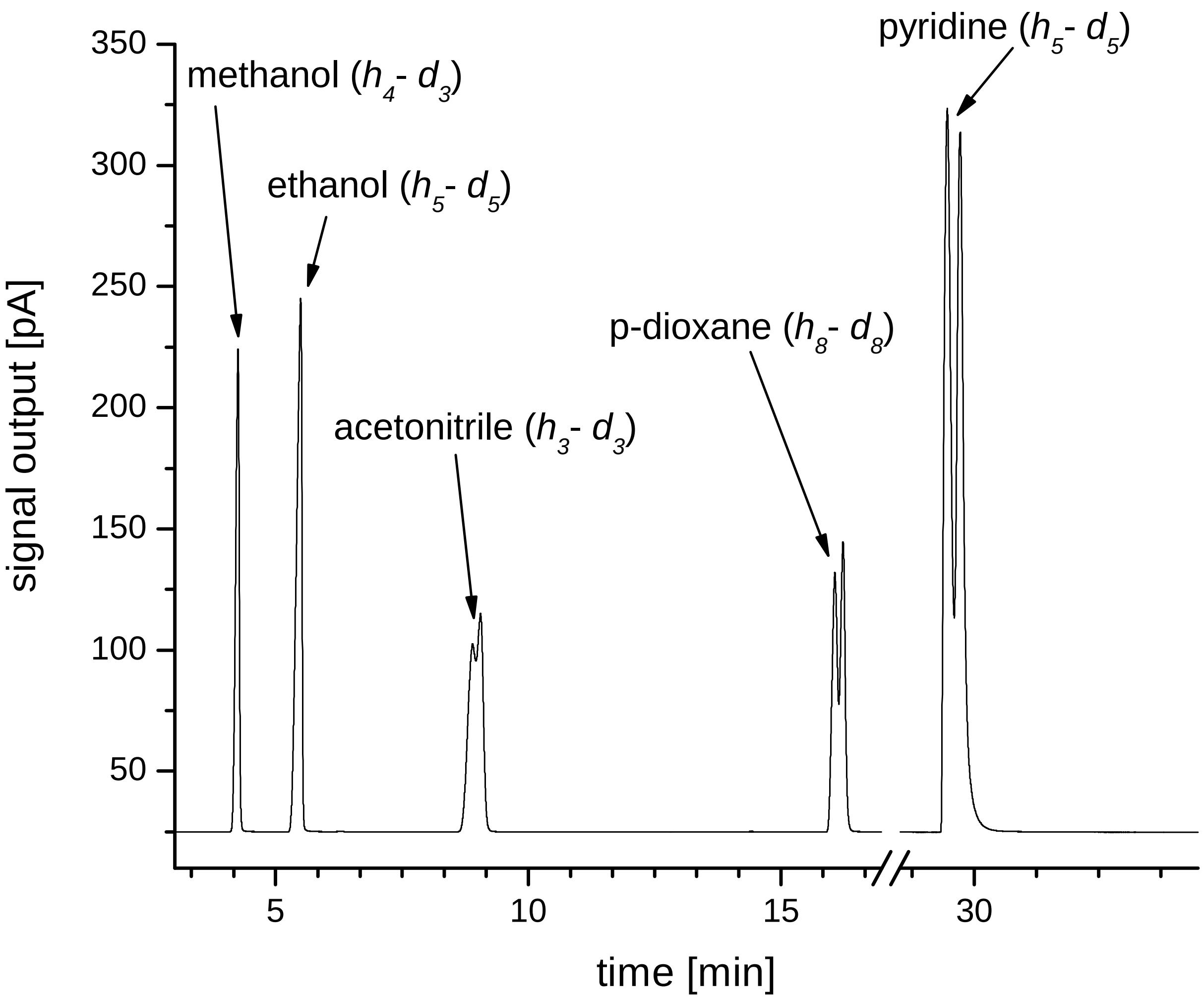

Figure 3.11: Mixture of isotopic molecules of methanol, ethanol, acetonitrile, p-dioxane and pyridine; stationary phase: $[OMIm]^+[Tf_2N]^-$ with cavitand 2.

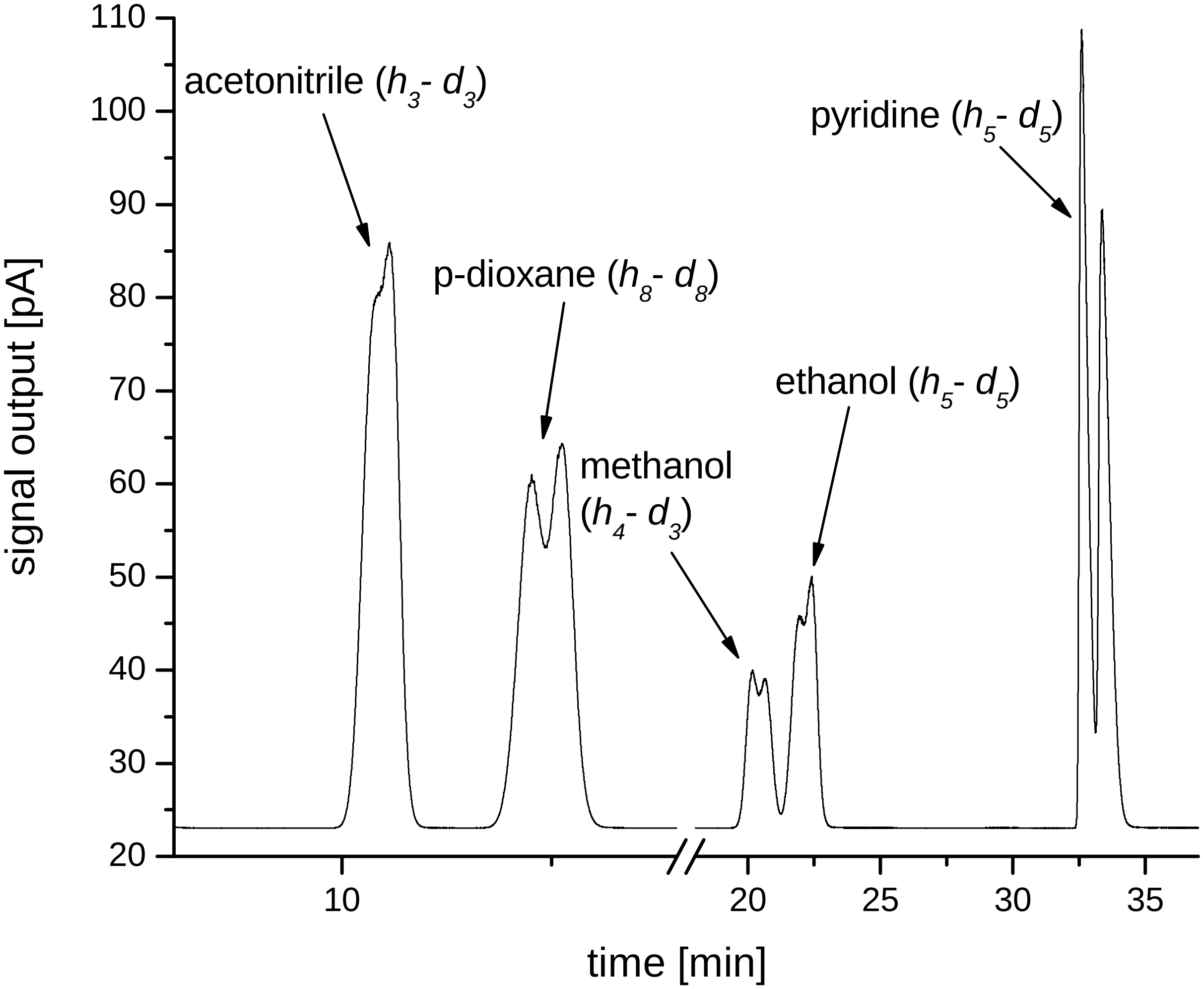

Figure 3.12: Mixture of isotopic molecules of methanol, ethanol, acetonitrile, p-dioxane and pyridine; stationary phase: $[N\text{-}EtPy]^+[CF_3CO_2]^-$ with cavitand 3.

(chlorobenzene-h_5, chlorobenzene-d_5); 1,2-dichlorobenzene (1,2-dichlorobenzene-h_4 and 1,2-dichlorobenzene-d_4); pyridine (pyridine-h_4, pyridine-d_4) and 1,4-dioxane (1,4-dioxane-h_8 and 1,4-dioxane-d_8). It is true that in some cases baseline separation could not be achieved. However, it should be recognized that all separations reported in this study were based on the use of only 10 m length. Therefore, better separation efficiencies can be expected by increasing the lengths of the columns.

Even though this is not the first observation of the separation of isotopic compounds by GC,[50-54] it is significant because with the use of cavitands dissolved in IL as a SP several different types of isotopic molecules (aromatic hydrocarbons, alcohols, etc.) can be successfully differentiated. In other reported studies,[50-54] however, only a specific class of molecules could be separated (i.e., aromatic molecules or aliphatic hydrocarbons) at higher temperatures and longer column lengths. Furthermore, by modifying functional groups of the cavitand (from Et to $C_{11}H_{23}$, or from amide to carboxylate) and thus, changing the polarity of the columns (from medium polar to nonpolar, or to polar, respectively), the application of these GC columns can be further increased.

While deuterium-hydrogen exchange behavior of columns coated with either $[BMIm]^+[BF_4]^-$ only or with $[BMIm]^+[BF_4]^-$ and cavitand 1 may complicate chromatographic separation process, it can potentially be used as a simple, inexpensive and rapid enrichment/synthesis of deuterated compounds. For example, by repeated injections of inexpensive alcohol-OD into these columns all the protons available for deuterium hydrogen exchange would be converted to deuterium (can be monitored by chromatogram when instead of two bands only one band elutes). Afterwards, the alcohol-

OH is injected into the column, and through the deuterium exchange process (reverse in this case) the -OH group of the alcohol converts into -OD group. The number of repeated injections correspond to the concentration of the -OD group in the desired alcohol.

Furthermore, the use of cavitands for GC analysis could be even further extended to the chiral separation. This could be possible by synthesis of chiral cavitands, which would exhibit different molecular recognition for two enantiomers and thus able to differentiate between them. With growing importance of chiral separation this would represent a valuable extension in application of the cavitands.

CHAPTER 4

CHARACTERIZATION OF INDIVIDUAL GOLD NANOSHELLS BY NEAR-INFRARED MULTISPECTRAL IMAGING MICROSCOPY

4.1 INTRODUCTION

Noble metal nanostructures (i.e., platinum, silver and gold) are widely used in nanoparticle-based optical and biological applications because of their unique and tunable optical, electronic and catalytic properties.[55-57] Due to their biocompatible material which enables their use in vivo studies as nanoscale biomaterials,[58,59] gold nanostructures are of particular interest. They are often synthesized or applied with organic molecules, inorganic materials, polymers (for example N-isopropylacrylamide (NIPAM) hydrogels) in order to facilitate their use.[60] Noble metal nanoparticles demonstrate localized surface plasmon resonance (LSPR), i.e. they exhibit a strong absorption band as a result of resonance between incident photon frequency and oscillation of the collective electrons.[55-57,61] In case of localized SPR, light interacts with metal particles that have dimensions significantly smaller than the incident light.[55] The properties of nanostructures can be adjusted by differences in dielectric constant of the metal and embedded medium (solvent) as well as by controlling their composition, size shape and structure (i.e., hollow vs. solid).[55,62-65] Gold shells that were used in the study consist of monodispersed silica nanoparticle (i.e., core) on which layers of gold nanoparticles are coated (i.e., shell) (see **Figure 4.1**).[61] The Localized Surface Plasmon Resonance

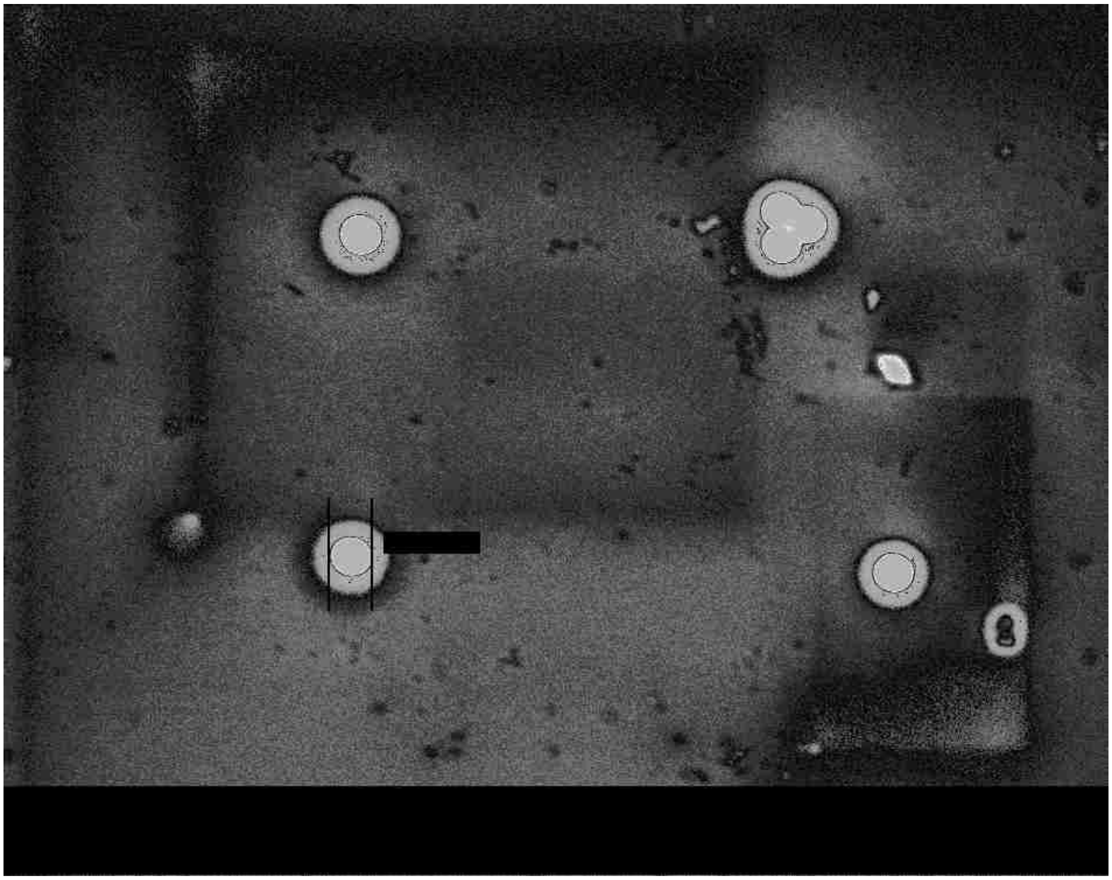

Figure 4.1: Scanning Electronic Microscope (SEM) image of gold shells with silica cores (image received from Dr. Lee’s research group, University of Houston).

absorption band of these gold shells can be tuned from the ultraviolet to the near-infrared region by varying the embedded medium, and their core size and shell thickness.[66,67] Due to these properties gold shells can be used for optical heating,[59] and since they are tunable into the near-infrared region of the spectrum they can be successfully applied to the in-vivo applications.[68]

As stated in the previous paragraph, the size and the shape of metal particles determine their spectral characteristics (i.e. position, shape and band width of plasmon resonance); therefore, important information about the properties of metal particles can be obtained by investigating the spectral data. Furthermore, the effect of structural changes of noble particles on the LSPR spectra can be studied using this method. A number of groups have reported LSPR studies of the solution of metal nanoparticles. However, these studies were performed on the whole solution of nanoparticles, and represent, therefore, variations in particle size and morphology, which result in inhomogeneities of spectroscopic data. Consequently, it is difficult to compare results and obtain a detailed knowledge of the properties of the LSPR of noble metal nanoparticles. For that reason, developments of the methods that enable studies of individual metal nanoparticles are needed. Scanning Near-field Optical Microscopy (SNOM), dark field illumination, high resolution electron energy loss spectroscopy and spatial modulation spectroscopy are techniques currently used in order to measure the LSPR of individual metal nanoparticles.[69-72] However, these techniques are complex and technically challenging; therefore, a simpler method of analysis, such as near-infrared multispectral imaging microscope, can contribute greatly to obtain in-depth knowledge about properties of noble metal nanoparticles.

A near-infrared multispectral imaging microscope instrument which can provide spatial and spectral information has been developed in our laboratory.[73-77] A multispectral imaging instrument can simultaneously gather spectral information at different positions within the sample by using focal array detector.[78] It records NIR images for each scanned wavelength, and consequently, the chemical composition and structure of the sample at different positions can be obtained from recorded images. Especially when measuring dynamic samples (for example particles in solution), it is desirable to increase the speed of the measurements. An acousto-optic tunable filter (AOTF) that is incorporated in the NIR multispectral imaging microscope, which was used for this study, represent one of the fastest electronic tunable filters available[79,80] and therefore considerably decreases the measurement time. Specifically, it takes 560 ms to record an NIR image for a specific wavelength. Furthermore, the instrument exhibits microscope for higher spatial resolution resulting in high sensitivity (i.e., single pixel resolution) and approximately 1μm spatial resolution.

Gold shells that were used in the study have dimensions around 1μm; therefore it is expected that the individual gold shells can be observed and their localized surface plasmon resonance measured using the NIR multispectral imaging (MSI) microscope instrument. Specifically, in the study presented we investigated if the NIR-MSI microscope instrument can be successfully used for characterization of LSPR of individual metal particles, and furthermore, to investigate the effect of a different embedding medium (with different dielectric constants) on the LSPR spectra of individual particles. The following solvents were used for the latter part of the study: deuterium oxide, acetonitrile-d_3, pyridine-d_5, acetone-d_6, ethyl acetate and formamide.

4.2 EXPERIMENTAL

4.2.1 Chemicals

Deuterium oxide (99.9 %); acetonitrile-*d*$_3$ (99.0 %); acetone-*d*$_6$ (99.9 %) and pyridine-*d*$_5$ (99.5 %) were obtained from Cambridge Isotope Laboratories, Inc. (Andover, MA, USA). Ethyl acetate (99.8 %) and formamide (99.5+ %) were purchased from Sigma-Aldrich (Saint Louis, MO, USA).

4.2.2 Gold shells with silica cores

Gold shells with silica cores were prepared in Dr. Lee's group as reported previously.[61] Gold shells consisted of silica cores with diameters of approximately 0.8 µm surrounded by layers of gold nanoparticles forming gold nanoshells with dimensions of approximately 35 nm (as determined by scanning electron microscope (SEM)).

4.2.3 Instrumentation

All measurements were performed on an in-house built microscopic multispectral imaging instrument (see **Scheme 4.1**) with 150 W halogen lamp serving as a light source, acousto-optic tunable filter (AOTF) as monochromator and liquid N_2 cooled, 320 × 256 pixel indium antimonide (InSb) focal plane array camera (Santa Barbara Focal Plane, Goleta, CA) as a detector. A long focal length and a high degree of magnification was further improved by employing the cassegrains into the system set-up. Monochromatic light from the AOTF is collected by cassegrain, which serves as a condenser, and focused onto the sample. Transmitted light is then collected by another cassegrain, which serves as a reflective objective, and focused onto the NIR camera. Spatial resolution of the instrument was determined to be 0.93 ± 0.03 µm/pixel. Spectra were taken in the NIR region between 1400 and 2200 nm with 2 nm interval, using 1 mm spectrophotometric

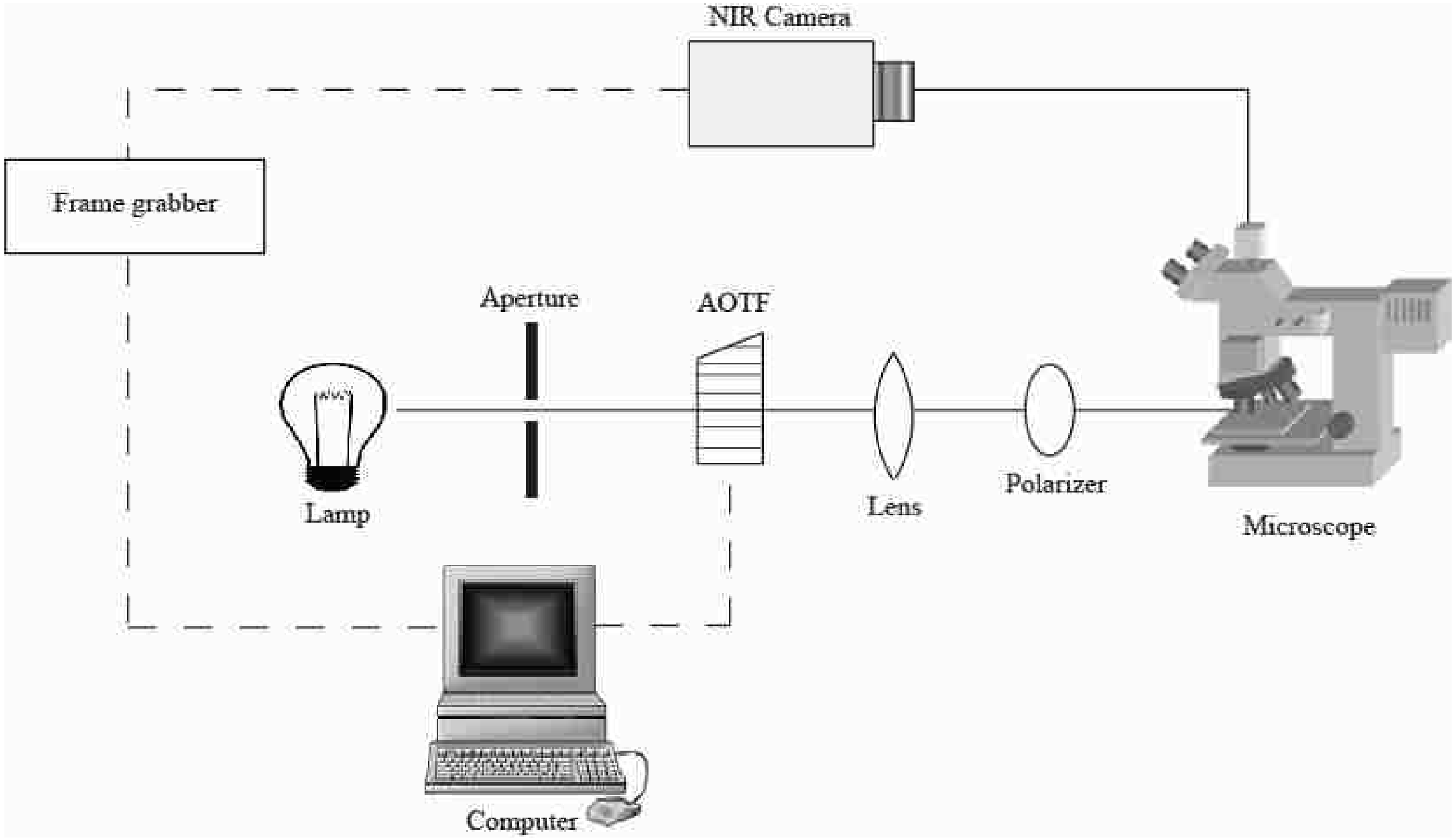

Scheme 4.1: Microscopic multispectral imaging instrument.

cells.

As described in the introduction, using an NIR multispectral imaging microscope, 2D NIR images for each wavelength of interest are captured. In order to obtain the absorption spectra of the gold shells, sample (i.e., gold shells in a specific solvent) as well as background (i.e., only solvent) needed to be measured. Thus, from NIR images of the sample and background absorption spectra of gold shells can be calculated for a specific pixel position.

3D images of absorption of gold shells were calculated from 2D NIR images (for sample and background) using publicly available image processing program ImageJ (National Institutes of Health).

4.2.4 Sample preparation

Gold shells were initially dispersed in water. However, due to the large absorption of water in the NIR region of interest (1400 - 2200 nm), water was exchanged into deuterium oxide. Specifically, a solution of gold shells was first sonicated for several minutes to obtain a homogeneous dispersion in water and afterwards centrifuged (two times for 5 min (RT, 2000 rpm)) in order to exchange solvent from water to deuterium oxide, respectively. Prior to NIR measurements the sample was sonicated for approximately 1 minute. The same procedure was used for exchanging water to other solvents, namely, deuterium oxide, acetonitrile-d_3, pyridine-d_5, acetone-d_6, ethyl acetate and formamide.

4.3 RESULTS AND DISSCUSION

The spatial resolution of the instrument is 0.93 ± 0.3 μm/pixel. In order to determine the dimensions of the pixels on the NIR image, six reference polymer particles (Duke Scientific Corporation, Palo Alto, California, USA) with diameters of 20.9 ± 0.6 μm (see **Figure 4.2**) were measured in D_2O, and pixel dimensions in μm were obtained from the known dimensions of the reference particles. Additionally, the spatial resolution of the instrument was determined using a US Air Force gold standard plate (shown in **Figure 4.3**) with known dimensions of micro structures that were made by precision electroforming. Specifically, NIR images of the enlarged segments of gold plate microstructures were measured and the number of pixels corresponding to a specific known dimension was determined. As can be seen from **Figure 4.3**, five different segments were analyzed and the average value was used as a final spatial resolution of the system. The spatial resolution of the instrument limits the size of the particles that can be measured with the instrumental set-up used in the study. However, since gold shells with silica cores measured approximately 1 μm in diameter (determined by SEM and field emission-SEM),[61] it is expected that gold shells will be visible through the microscope. Indeed, individual metal particles can clearly be observed from the NIR images measured at 1680 nm of gold shells in D_2O solution and in ethyl acetate solution shown in **Figure 4.4A** and **B**, respectively (similar images were obtained for other solvents used in the study, and are therefore not presented). As can be observed from both of the images, but is more pronounced in **Figure 4.4B**, discrete metal particles as well as their aggregates are formed in the solution. However, since the instrument set-up enables visual differentiation between individual particles and aggregates, we were able

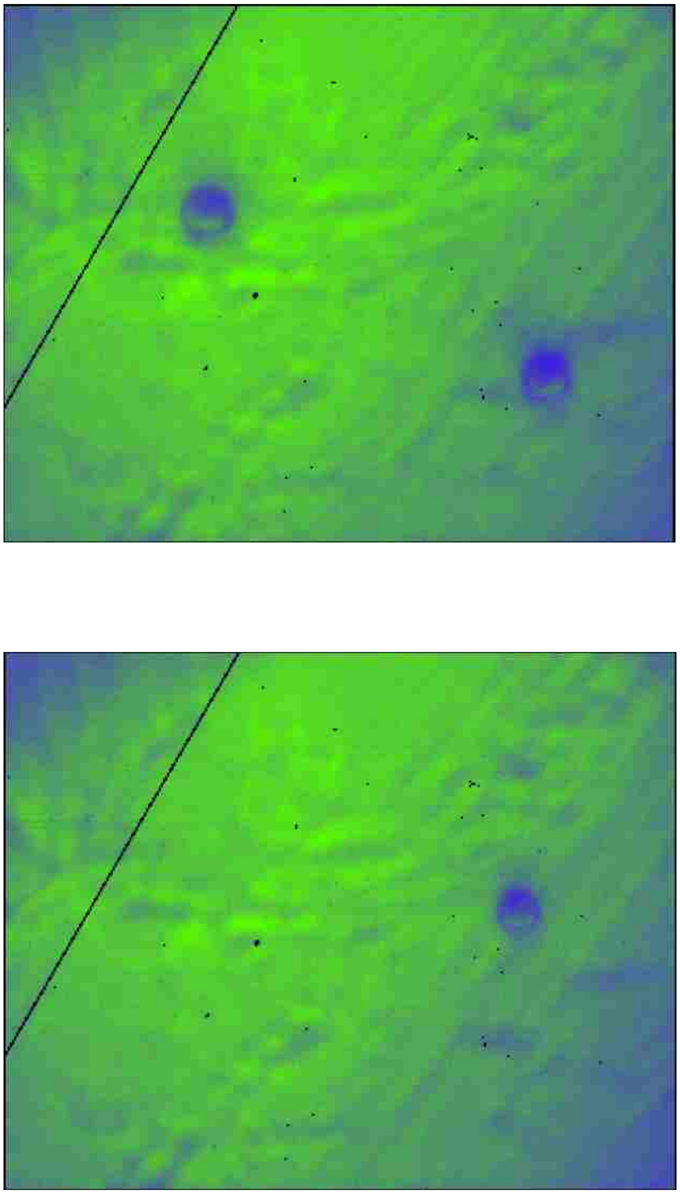

Figure 4.2: Reference polymer particles (diameter: 20.9 ±0.6 μm) in D_2O.

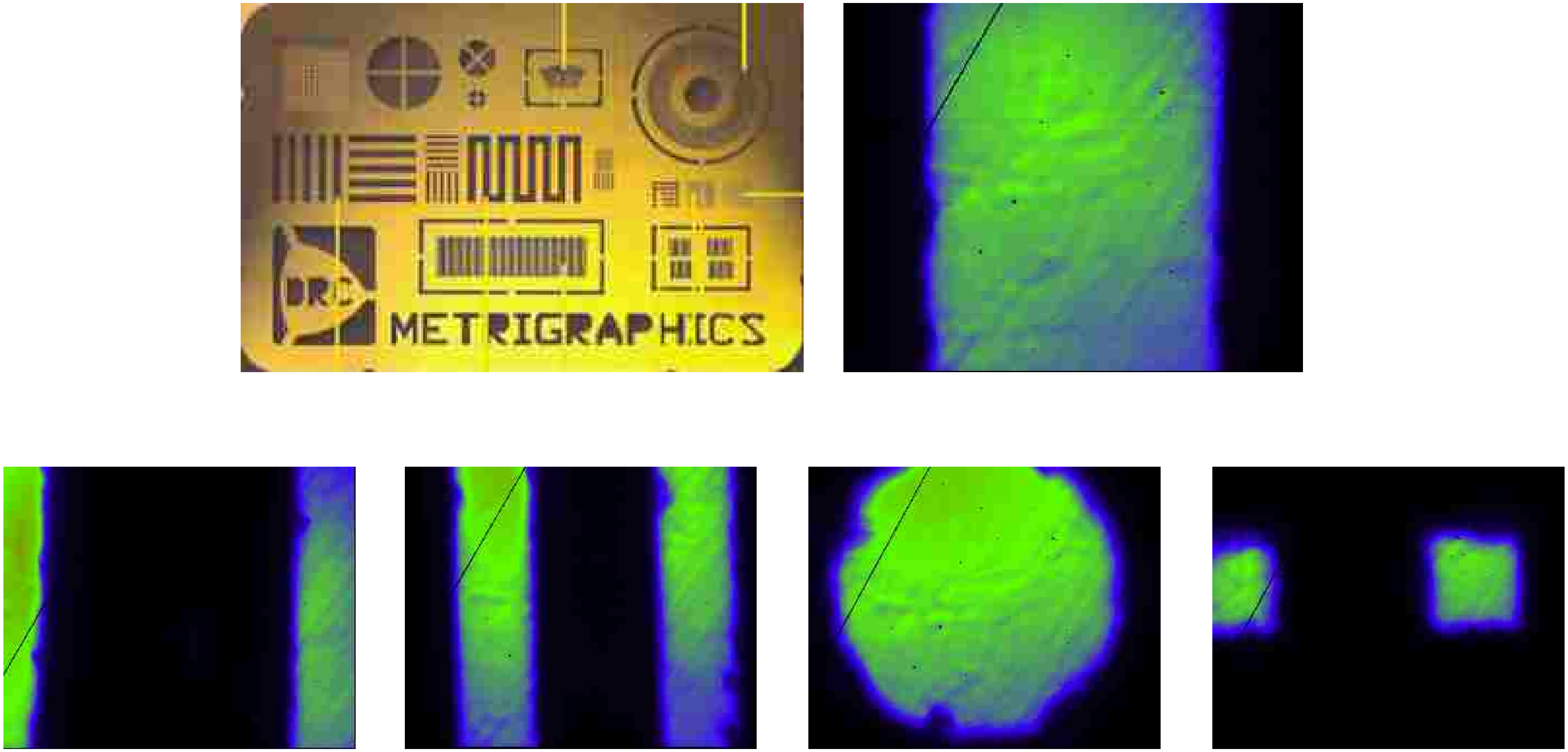

Figure 4.3: Gold plate (http://www.drc.com/metrigraphics/pdfs/precisionelectroforming.pdf) and NIR images of selected segments of micro structures.

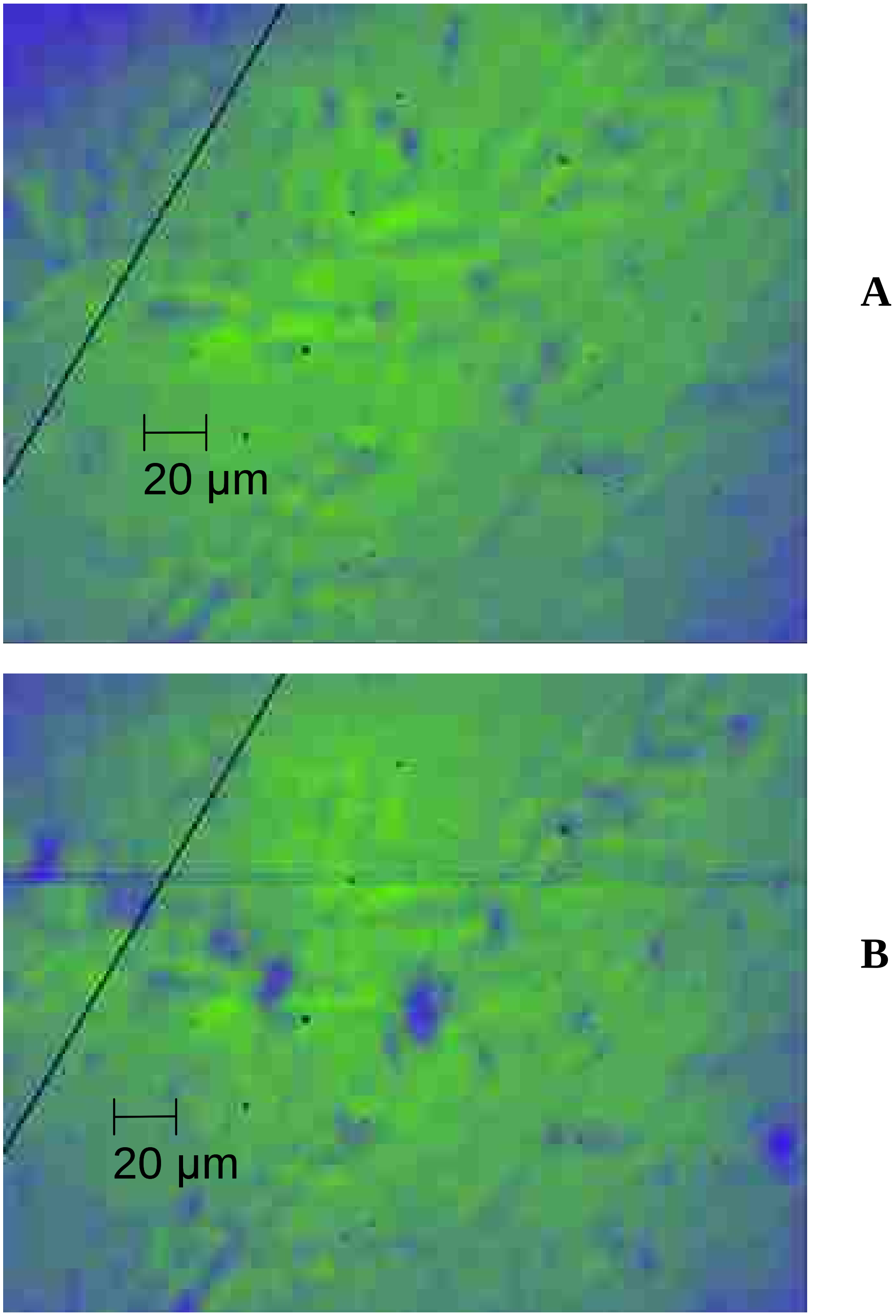

Figure 4.4: NIR images of gold shells at 1680 nm in D_2O (A) and ethyl acetate (B).

to obtain LSPR information of only discrete metal particles. Thus, on the basis of spatial resolution of the instrument, the average diameter of the gold shells was calculated to be 1.1 ± 0.2 µm. It is pleasing to observe that the identified dimensions correspond well with the gold shell dimensions obtained by SEM (i.e., approx. 0.9 µm), which provides additional conformation as to the reliability of the NIR multispectral imaging microscope.

The instrument used in the study enables observation of the gold shells through 2D NIR images, which provide information about the spatial and spectral properties of the measured metal particles. However, absorption intensities of discrete gold shells can additionally be presented in 3D space using the image processing program ImageJ. Specifically, logarithmic functions of 2D NIR images for background (i.e., solvent) and sample (i.e., gold shells in solvent) were calculated and afterwards the log function of the NIR image for sample was subtracted from the log function of NIR image for background in order to obtain a 3D absorption intensity plot. 3D absorption intensities images for gold shells in ethyl acetate and acetone-d_6 are presented in **Figure 4.5A** and **B**, respectively. 3D absorption intensities images (**Figure 4.5A** and **4.5B**, right column) were calculated for the drawn rectangles shown in 2D NIR images (see **Figure 4.5A** and **B**, left column). Absorption bands for individual gold shells as well as clusters can be clearly observed from the 3D absorption plots. Consequently, 3D images together with 2D NIR images can effectively be used in order to accurately define the measured gold shells as a discrete particle or cluster.

In our study we measured single metal particles in solution (i.e., dynamic system); therefore it is important to take into consideration the motion of the particles in the solution. Nanoparticles in solution are known to undergo Brownian motion.[81,82] However,

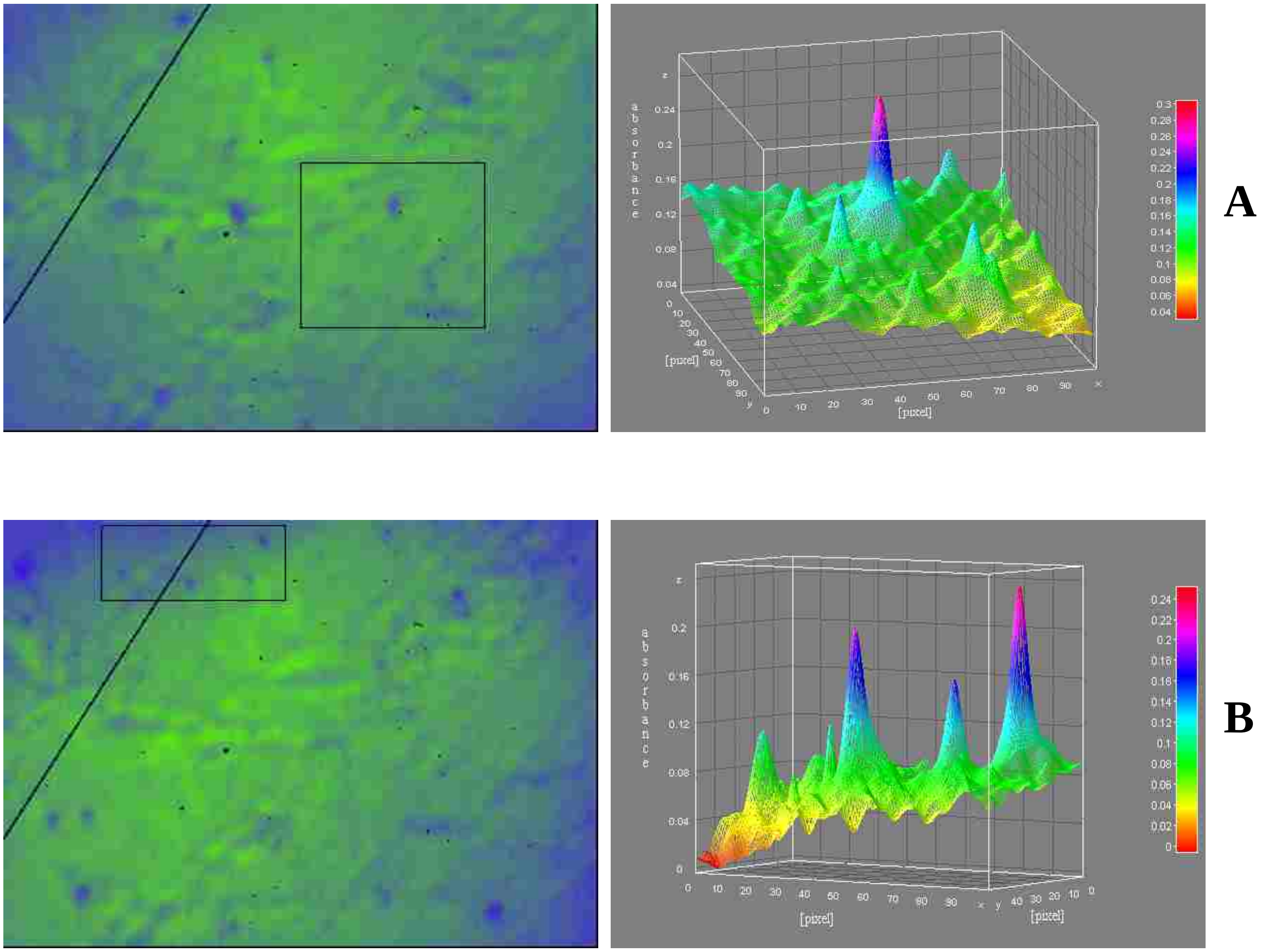

Figure 4.5: 2D NIR images of gold shells at 1680 nm in ethyl acetate (A, left) and corresponding 3D absorption spectra calculated for the drawn rectangle (A, right); 2D NIR images of gold shells at 1680 nm in acetone-d_6 (B, left) and corresponding 3D absorption spectra calculated for the drawn rectangle (B, right).

when monitoring the discrete gold shells (through 2D NIR images) during the measurement, no movement of the particles was detected for data presented in this study. The absence of observable Brownian motion of the gold shells is most probably due to the rapid time of recording (i.e., 560 ms to record NIR image at specific wavelength) as well as due to the size of the particles measured; specifically, the gold shells that were used in the study are relatively large (1.1±0.2 µm).

Due to the fact that LSPR spectra of metal particles depend on the shape and morphology of the surface,[55-57] it is possible to study the properties of the surface of gold shells by investigating their plasmon resonance spectra. **Figure 4.6A** and **B** (left column) represents LSPR spectra of a single pixel recorded at three different positions within the same gold shell in D_2O (**A**) and acetonitrile-*d*$_3$ (**B**). As can be observed from the plots, the plasmon bands at three different positions are noticeably different, that is, they exhibit different shapes as well as differences in λ_{max}. The results obtained therefore indicate that the morphology of the gold shells surface is rough and inhomogeneous. Since the spatial resolution of the system (i.e., 0.93±0.3 µm/pixel) is similar to the dimensions of the measured particle, it is expected that the plasmon resonance spectra recorded at the edges of the gold shells will constitute both absorption of gold shells and absorption of the solvent. In that case, absorbance of the solvent will be zero due to the background subtraction, and therefore plasmon resonance spectra recorded at the edges of gold shells would have lower absorption intensities. However, no differences in shape or absorption maxima should be expected. Indeed, it is observed (see **Figure 4.6**, right column) that plasmon resonance spectra of discrete gold shells in D_2O (**A**) and acetonitrile-*d*$_3$ (**B**), recorded at a single position for 1×1 pixel (black), 3×3 pixels (green) and 5×5 pixels

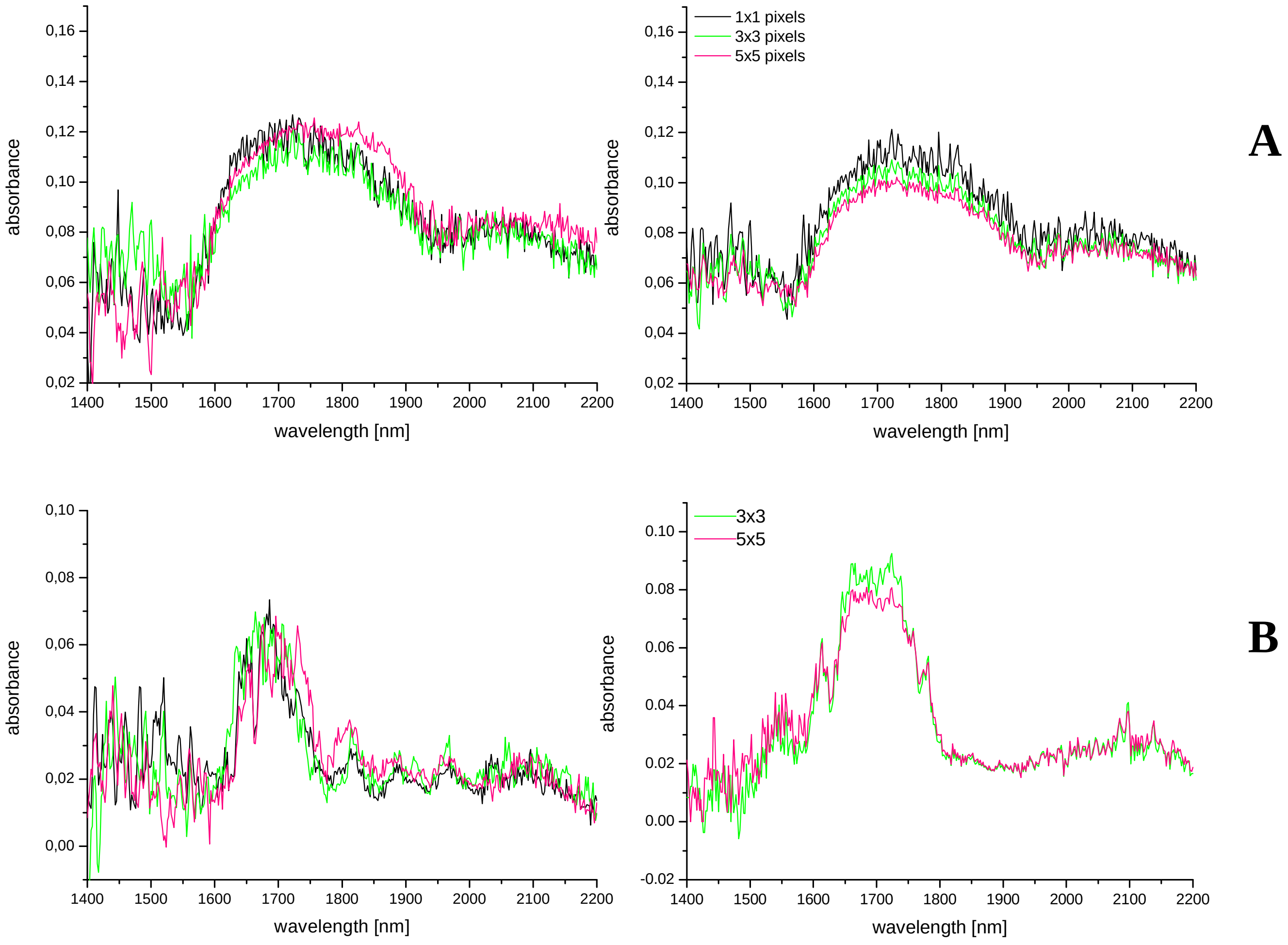

Figure 4.6: Absorption spectra of a single gold shell in D_2O calculated for 1×1 pixel at three different positions within the shell (A, left), and absorption spectra of the same gold shell calculated at one position for 1×1 pixel (black), 3×3 pixels (green), 5×5 pixels (pink) (A, right). Absorption spectra of a single gold shell in acetonitrile-d_3 calculated for 1×1 pixel at three different positions within the shell (B, left), and absorption spectra of the different single gold shell calculated at one position for 3×3 pixels (green), 5×5 pixels (pink) (B, right).

(pink) exhibit lower absorption intensities with increasing pixel range, whereas shape and the band maxima remain constant.

As described in the introduction, the localized surface plasmon absorption of metal shells can be tuned over a wide range of frequencies by changing the core size and/or shell thickness.[67] It has also been known that optical properties of the surface plasmon resonance nanoparticles can be tuned by exchanging the surrounding medium (i.e., solvents).[83-85] Therefore, we investigated the solvent effect on the optical properties of the gold shells with silica cores. As reported in previous studies,[83-85] the dielectric constants and refractive indices, as well as the capability of solvent molecules to form complexes with gold nanoparticle surfaces, play a key role in the shift of the plasmon peak position. Consequently, solvents used in the study were chosen according to the differences in dielectric constants and refractive indices. They were: deuterium oxide, acetonitrile-*d₃*, pyridine-*d₅*, acetone-*d₆*, ethyl acetate and formamide; and their dielectric constants as well refractive indices are presented in **Table 4.1**. For each individual particle in a specific solvent, plasmon resonance spectra at different positions, but within the same particle, were obtained, and the results are presented in **Figure 4.7**. As stated, gold shells were measured in D_2O (**Figure 4.7A**), acetonitrile-d_3 (**B**), ethyl acetate (**C**), pyridine-d_5 (**D**), acetone-d_6 (**E**) and formamide (**F**). All spectra were calculated for 1×1 pixel region. It can be clearly observed from the **Figure 4.7**, and is even more pronounced in **Figure 4.8**, which represents LSPR spectra of gold shells in six different solvents plotted together, that plasmon band maxima, as well as the shape of the absorption bands, differ distinctively with different solvents used. Specifically, LSPR absorption bands of gold shells in D_2O and formamide are considerably wider compared

Solvent	**dielectric constant; ε (at 20 ˚C)**	**refractive index; n (at 20 ˚C)**
D_2O	78.5	1.33
acetonitrile-d_3	35.1	1.34
ethyl acetate	6.0	1.37
pyridine-d_5	12.4	1.51
acetone-d_6	20.7	1.36
formamide	109.	1.45

Table 4.1: Dielectric constants and refractive indices of the solvents used in the study.

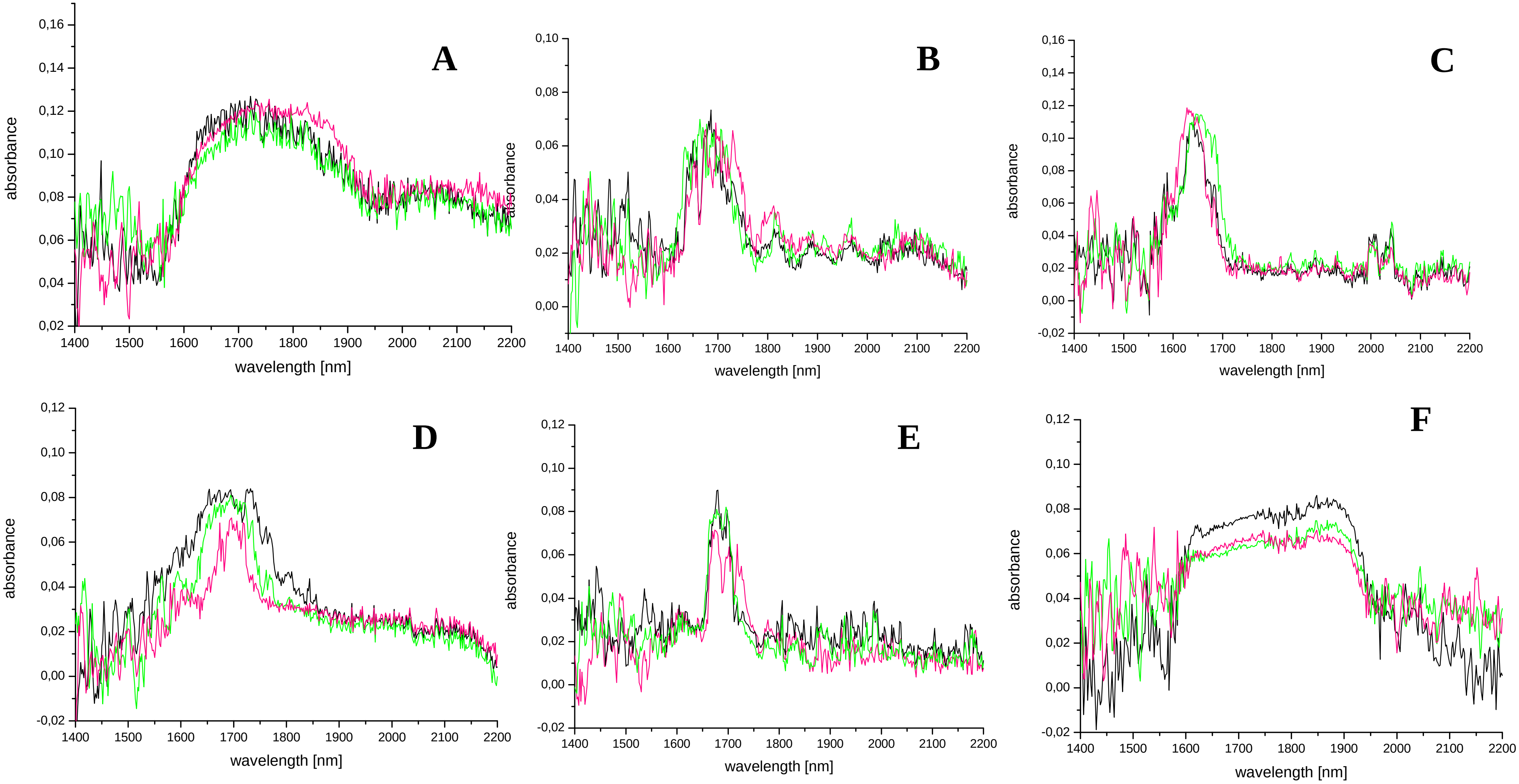

Figure 4.7: Absorption spectra of a single gold shell, calculated for 1×1 pixel at three different positions within the shell, in D_2O (A), acetonitrile-d_3 (B), ethyl acetate (C), pyridine-d_5 (D), acetone-d_6 (E) and formamide (F).

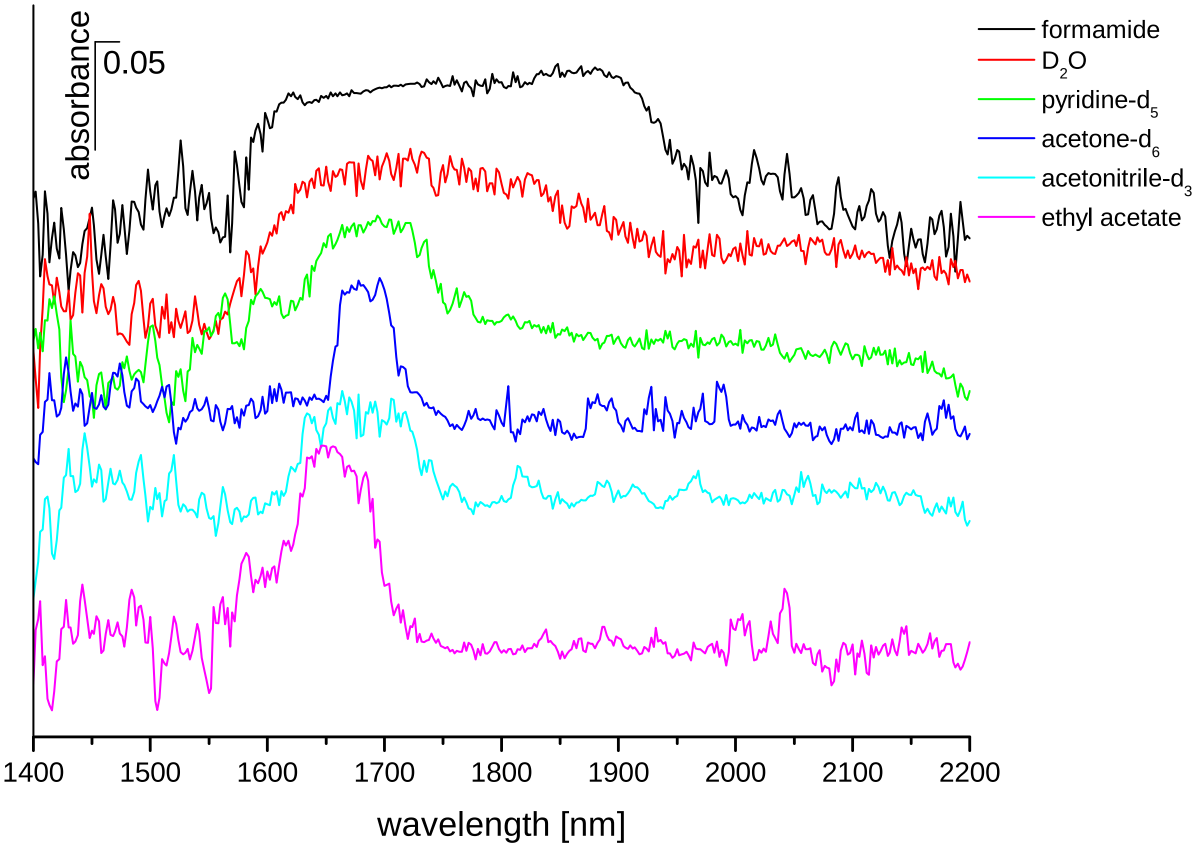

Figure 4.8: Absorption spectra (shifted vertically for easier comparison), calculated for 1×1 pixel, of a single gold shell in D_2O (red), acetonitrile-d_3 (cyano), ethyl acetate (pink), pyridine-d_5 (green), acetone-d_6 (blue) and formamide (black).

to the absorption bands that are exhibited when gold shells in other solvents (i.e., acetonitrile-d_3, pyridine-d_5, acetone-d_6, and ethyl acetate) are measured. As illustrated in **Figures 4.7** and **4.8**, the absorbance maximum for the gold nanoshells appears roughly at 1700 nm. This value is consistent with that calculated theoretically using Mie scattering for nanoshells having silica cores ~800 nm in diameter and gold shell thicknesses of ~35 nm.[86,87]

The variation of maxima of LSPR absorption bands as a function of dielectric constant of an embedded medium, for small gold nanoparticles, can be theoretically expressed through the Drude model[55,85,88] with the following equation:

$$\lambda^2 = \lambda_p^2 \left(\in^{\infty} + 2 \in_m\right)$$

where λ is a surface plasmon peak position, λ_p is the plasmon wavelength of the bulk metal,

$\in^{\infty}$ is the high frequency dielectric constant, and $\in_m$ is the optical dielectric function of the medium. $\in_m$ equals to n^2 (where n is refractive index of the medium), therefore plasmon peak position should increase linearly with larger refractive indices. However, LSPR bands of gold shells that were measured in this study exhibit relatively broad spectral bandwidths (see **Figure 4.7** and **4.8**) (for example values of the full width at half maximum (FWHM) of the LSPR bands of the gold shells in formamide are as large as 300 nm), and therefore it is difficult to determine their plasmon peak positions accurately. Consequently, for broad LSPR, it is more applicable to consider the ratio of λ and FWHM (i.e., λ/FWHM) rather than λ alone.[89,90] **Figure 4.9** shows plot of the square of the ratio between absorption maximum and full-width at half-maximum, i.e., $(\lambda/\text{FWHM})^2$, as a function of $2n^2$ for six different solvents used in the study. As can be

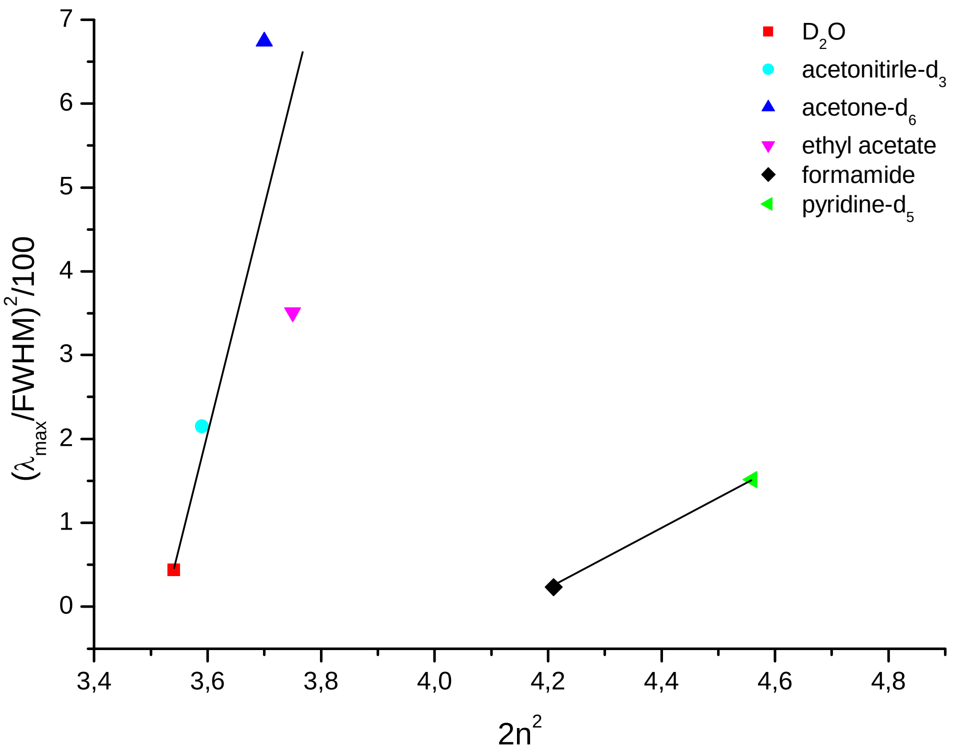

Figure 4.9: Plot of the square of the ratio between absorption maximum and full-width at half-maximum (FWHM) as a function of $2n^2$ in D_2O (red), acetonitrile-*d*$_3$ (cyano), ethyl acetate (pink), pyridine-*d*$_5$ (green), acetone-*d*$_6$ (blue) and formamide (black).

observed, the linear relationship is observed for D_2O, acetonitrile-d_3, ethyl acetate (with slight deviation) and acetone-d_6 solutions, whereas formamide and pyridine-d_5 exhibit distinctly different correlations. Specifically, formamide and pyridine-d_5 have relatively larger values of $2n^2$ compared to the other solvents used (i.e., 4.21 and 4.56, respectively); however, their respective $(\lambda/\mathrm{FWHM})^2$ values are relatively smaller than $(\lambda/\mathrm{FWHM})^2$ values for the other four solvents. The different behavior of gold shells in formamide and pyridine-d_5 might be due to the interaction between the solvent and gold shells; namely the solvent might chemically interact/bind to the surface of gold shells. Consequently, this chemical interaction has an effect on the linearity of the $(\lambda/\mathrm{FWHM})^2$ as a function of $2n^2$, i.e., it annuls the expected increase in $(\lambda/\mathrm{FWHM})^2$ with increasing $2n^2$ values. Similar deviation of the linear relationship has previously been observed for LSPR characterization of metal particles in solvents and adsorbates.[84,85,91,92]

4.4 CONCLUSION

Gold shells exhibit localized surface plasmon resonance[55-57,61] and their LSPR band can be tuned in the near-infrared region. Specifically, the absorption properties of plasmon resonance can be adjusted by differences in dielectric constant of the embedded medium[55] as well as by varying core size and shell thickness.[66,67] NIR multispectral imaging microscope technology can be successfully used to measure discrete gold shells in solution, and therefore obtain detailed information about LSPR properties of individual gold shells. Thus, the results provided are not hindered by the inhomogeneity of the metal particles in solution. It was found that plasmon resonance spectra are noticeably different (i.e., they exhibit different shapes and λ_{max}) when recorded at different positions within the same gold shell; therefore, it can be deduced that the surface of gold shells used in the study is rough and inhomogeneous. Furthermore, it was found that plasmon resonance positions depend greatly on the dielectric constant of the embedded medium, with absorbance maximum for the gold nanoshells appearing roughly at 1700 nm. It is pleasing to observe, and thus giving further admission to the NIR-MSI microscope, that this value is consistent with that calculated theoretically using Mie scattering for nanoshells having silica cores ~800 nm in diameter and gold shell thicknesses of ~35 nm.[86,87] However, due to the very broad absorption bandwidths in some solvents (for example values of the full width at half maximum of the LSPR bands of the gold shells in formamide are as large as 300 nm) the relationship cannot be simply explained with the Drude model. In such cases it is more appropriate to plot $(\lambda/\mathrm{FWHM})^2$ as a function of $2n^2$ which results in linear relationship for D_2O, acetonitrile-d_3, ethyl acetate (with slight deviation) and acetone-d_6 solutions, whereas formamide and pyridine-d_5 solutions exhibit distinctly different correlations. Different behaviors exhibited by gold shells in formamide and pyridine-d_5 might be due to the chemical interaction/binding between the solvent and surface of gold shells, which annuls the expected increase in $(\lambda/\mathrm{FWHM})^2$ with increasing $2n^2$ values.

CHAPTER 5

APPLICATION OF NEAR-INFRARED MULTISPECTRAL IMAGING MICROSCOPE FOR CHARACTERIZATION OF THERMO RESPONSIVE INDIVIDUAL HYDROGEL PARTICLES

5.1 INTRODUCTION

In general, hydrogels are divided into two categories: conventional and intelligent hydrogels. Of particular interest are the latter because they respond (i.e., change their volume, size and shape) upon external stimuli such as pH,[93,94] temperature[93-96] and light.[97] Water soluble and thermally sensitive polymeric hydrogels composed of (N-isopropylacrylamide) (NIPAM) play an important role in a variety of technological applications, including chemical separations, catalysis and drug delivery.[98-101] PNIPAM hydrogels are hydrophilic and highly soluble in water, which allows for large volumes of water to be contained within their three-dimensional structures (see **Figure 5.1**).[102] Specifically, they are soluble in water at temperatures below the lower critical solution temperature (LCST), whereas above the LCST they become hydrophobic and partially desolvated[60,93] as a consequence of fluctuation of hydrophobic interactions and hydrogen bonding.[103] Moreover, PNIPAM hydrogels undergo reversible swelling-deswelling volume transition that is strongly dependent on the LCST.[60,93-96] Pure PNIPAM hydrogels (i.e., without addition of other copolymers) undergo volume transitions at fixed temperature with the LCST of the solution being about 32 ˚C.[60,93-96,104] This volume

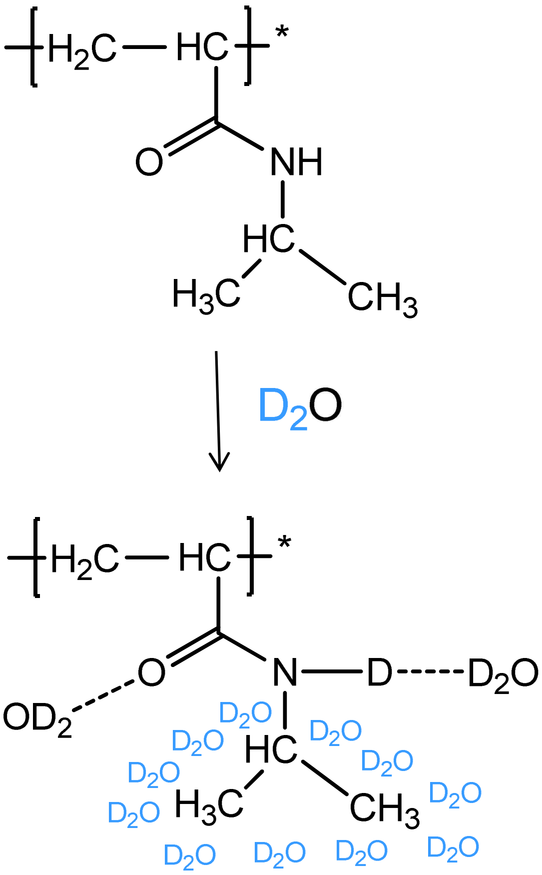

Figure 5.1: Poly(N-isorpropylacrylamide) in D_2O.

transition temperature, however, can be adjusted by introducing acrylic acid (AAc) or acrylamide (AAm) into the PNIPAM backbone which, as a consequence, can shift the LCST of the copolymer anywhere from 30 to 60 °C[103] and, therefore, increased applicability of the poly(NIPAM-co-AAc) or poly(NIPAM-co-AAm) is achieved. Due to the volume transition properties (i.e. swelling-deswelling of the hydrogel particles), high biocompatibility of hydrated PNIPAM hydrogels, as well as similarity between hydrated networks and hydrated body tissues; PNIPAM hydrogels have been widely used in biomedical and pharmaceutical applications.[105] Furthermore, by incorporating different concentrations of AAc or AAm into the PNIPAM hydrogels, volume transition temperature can be adjusted close to the physiological temperature, thereby increasing the applications for such hydrogels.

Various experimental techniques (i.e., calorimetry, NMR, fluorescence, dynamic light scattering (DLS)) have been used for characterization of the miscibility behavior of PNIPAM in water,[96,106-112] and a number of groups have reported volume transition temperature studies of the PNIPAM hydrogel particles in solutions. However, these studies were based on measuring the absorption of an entire sample of all hydrogels,[60,93,94] and represent, therefore, variations in particle size and stability, resulting in inhomogeneous spectroscopic information. Consequently, it is difficult to compare results obtained from different experiment and gain a detailed knowledge of the LCST liquid-liquid miscibility behavior of PNIPAM hydrogels. For that reason, instrumental methods that enable studies of individual metal nanoparticles, such as near-infrared multispectral imaging (NIR-MSI) microscope, are needed. The NIR-MSI microscope instrument, based on an acousto-optical tunable filter (AOTF) and with spatial resolution of 0.93±0.3 μm/pixel, was developed in our research group.[73,75,113-116] As described in detail in Chapter 4, the instrument provides spatial as well as spectral information of the measured sample. Moreover, this technique can provide insight into behavior of hydrogel nanoparticles because spectroscopic images of individual hydrogel particles can be taken during the measurements (i.e., at different temperatures) and directly in the solution thus mimicking the in-vivo conditions. Conversely, previously used methods for characterization of individual hydrogel particles,[60,93] that is, field emission scanning electron microscopy (FE-SEM) and transmission electron microscopy (TEM), employed the use of dried hydrogel sample.

Poly(N-isopropylacrylamide-co-acrylic acid) hydrogel particles that were used in the study had dimensions larger than 1 μm. Since the spatial resolution of the instrument was determined to be 0.93±0.3 μm/pixel, the individual hydrogel particles were expected to be visible through the microscope. Consequently the goal of the study was to investigate the use of NIR-MSI microscope for characterization of LCST behavior of discrete hydrogel particles by obtaining spectral information of the sample at various different temperatures. Additionally, relationship between the size of the individual hydrogel particles and corresponding volume transition temperature was explored. Thereupon, the obtained results would enable the comparison of independent studies, performed on hydrogel particles with different sizes.

5.2 EXPERIMENTAL

5.2.1 Chemicals

Deuterium oxide (99.9 %) was obtained from Cambridge Isotope Laboratories (Andover, MA); acetamide (99 %) and glacial acetic acid (99.7+ %) were purchased from Sigma-Aldrich (Milwaukee, WI).

5.2.2 Poly(NIPAM-co-AAc) Hydrogel Particles

Poly(NIPAM-co-AAc) hydrogel particles were synthesized in Dr. Lee's group (University of Houston, Texas) using procedures adopted from the literature.[60,93] The sample was prepared in water.

5.2.3 Sample Preparation

Due to the strong absorption of water in the NIR region of interest (1400-2200 nm), aqueous hydrogel solutions were redispersed in deuterium oxide prior to analysis. This isotopic solvent exchange was accomplished by centrifuging an aliquot of hydrogel solution in water in a 1.5 mL centrifuge tube at 22 ˚C for 3 h at 5000 rpm. The aqueous supernatant was discarded, and the hydrogel particles were redispersed in D_2O. The solvent exchange procedure was repeated once more in order to completely exchange water to D_2O. 1 mm spectrophotometric cells were used for the measurements.

5.2.4 Instrumentation

All hydrogel measurements were performed on an in-house build microscopic multispectral imaging instrument which is described in detail in Chapter 4. However, modifications to the instrument were made in order to obtain spatial and spectral information of the LCST behavior of hydrogel particles as a function of increased temperature. Essentially, a home built temperature controlled cell holder, equipped with

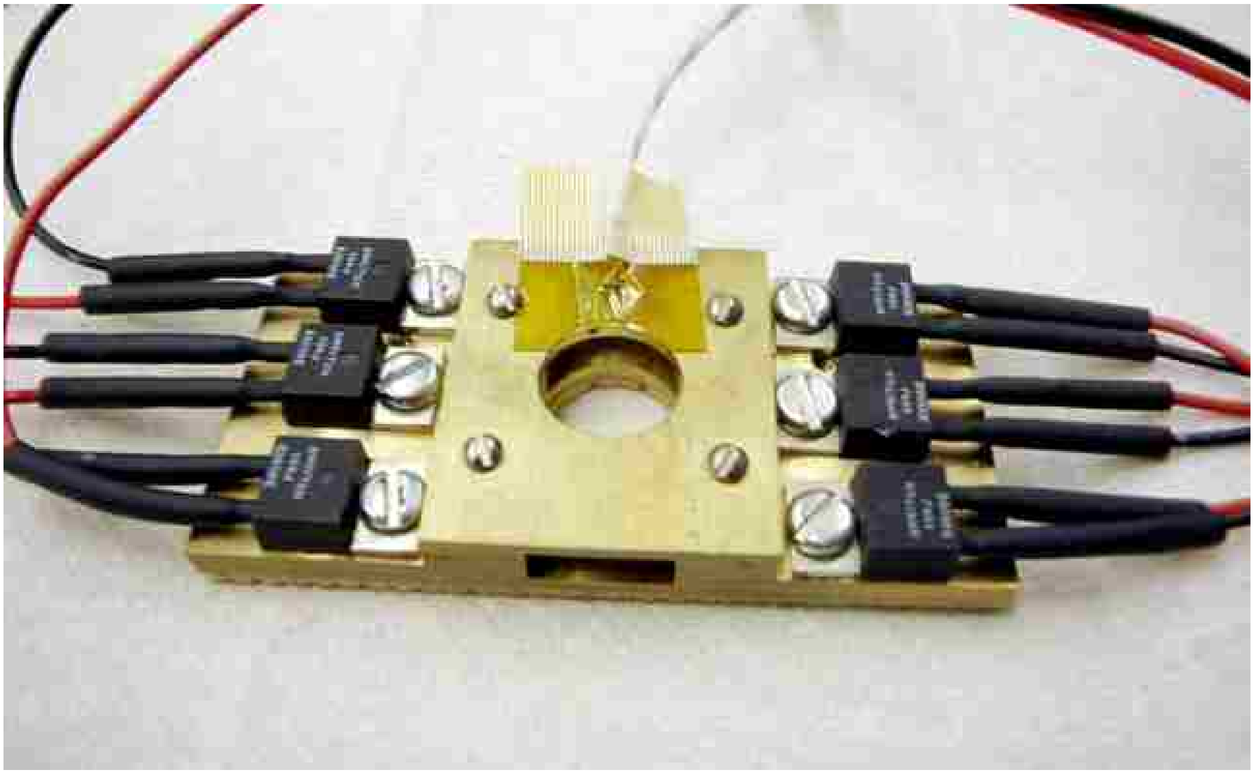

Figure 5.2: A home built temperature controlled cell holder, equipped with six resistors.

six resistors powered by the Tenna model PS-12 power supply (see **Figure 5.2**), was used. The temperature was controlled by an RTD temperature controller (Athena Controls, Inc.; Model no. 4200-B-185). The spectrophotometric cell was placed onto the plate and the temperature was set via temperature controller. First two measurements were taken at the room temperature and 25 ˚C, respectively; afterwards four degrees increments were used. The difference between the temperature on the brass metal plate and in the spectrophotometric cell was determined and obtained results adjusted accordingly to reflect actual temperature inside the sample.

Spectra were taken in the NIR region between 1400 and 2200 nm with 2 nm increments, using 1 mm spectrophotometric cells. 3D images of absorption intensity of poly(NIPAM-co-AAc) hydrogel particles were calculated from 2D NIR images (for sample and background) using publicly available image processing program ImageJ (National Institutes of Health).

5.3 RESULTS AND DISCUSSION

The size of the poly(NIPAM-co-AAc) hydrogel particles used in the study was determined by dynamic light scattering (DLS) technique, and found to be larger than one micron. Considering the spatial resolution of the NIR-MSI microscope, which was determined by US Air Force standard gold plate (see Chapter 4 for details) and ascertained to be 0.93±0.3 µm/pixel, it is expected that hydrogel particles will be visible through the microscope. Indeed, individual hydrogel particle can clearly be observed in **Figure 5.3** which represents recorded 2D NIR image at 1764 nm (**A**) and corresponding 3D absorption image calculated for a drawn rectangle in the 2D NIR image (**B**). As stated

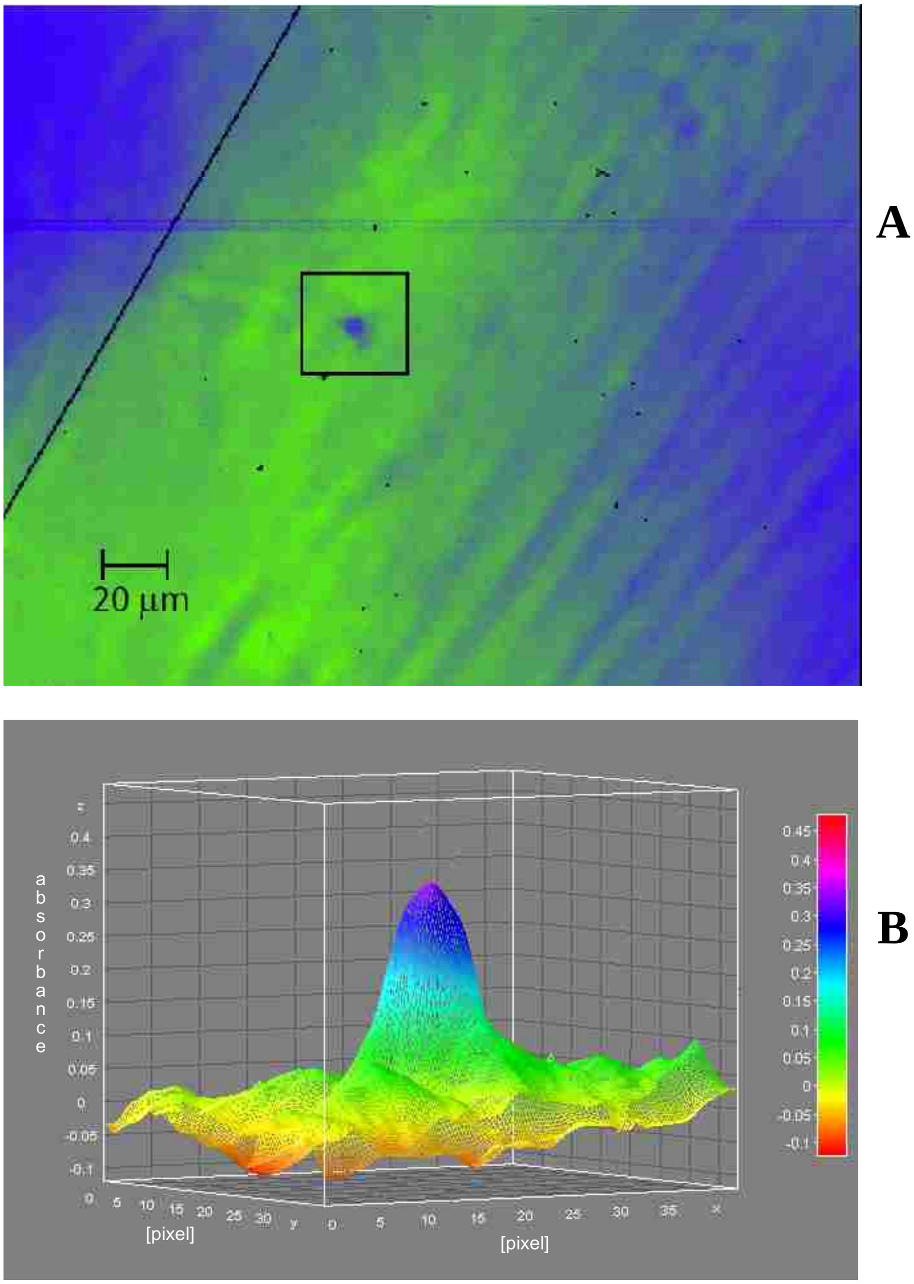

Figure 5.3: 2D image at 1764 nm of poly(NIPAM-co-AAc) hydrogel particle in D_2O (A) and (B) corresponding 3D absorption image of the drawn square section in (A). In the 2D image, the hydrogel particle is blue, the background is green, and the black line is the marking of the NIR camera. Units for x, y, and z axes are pixel, pixel, and absorbance at 1764 nm, respectively.

previously in Chapter 4, 2D NIR images provide information about spatial and spectral properties of the measured hydrogel particles. However, since hydrogel particles are prone to aggregation, before obtaining the absorption spectra, particle dimensions were estimated from the 2D NIR, as well as 3D absorption images. Consequently, 3D images together with 2D NIR images can be sufficiently used in order to accurately define the state of measured hydrogels, i.e.,discrete particle or aggregate. Thus, on the basis of spatial resolution of the instrument, the average diameter of the measured hydrogel particle was calculated to be 4.2 ± 0.5 µm.

The properties of poly(NIPAM-co-AAc) hydrogels were further investigated by collecting NIR 2D images of additional individual particles in D_2O and room temperature conditions. Thus, eight different particles were analyzed in order to investigate the reproducibility of the method. Their absorption spectra, as well as an averaged absorption spectrum with corresponding variances between different particles are plotted in **Figure 5.4A** and **5.4B,** respectively. Spectral information was collected in the range from 1400 to 2200 nm at 1×1 pixel resolution. As can be observed from **Figure 5.4A** absorption spectra of different measured particles closely resemble each other, which indicates that the poly(NIPAM-co-AAc) hydrogel particles used in our study are chemically homogeneous. The homogeneity of the sample is further confirmed by investigating the variance between NIR spectra of the measured particles. As illustrated, the discrepancy between absorption spectra is relatively low, that is, less than 5% for all measured samples. Additionally, two distinct absorption bands at approx. 1714 and 2016 nm can be observed in **Figure 5.4**. The former band can be attributed to C-H overtones and combination transitions,[95, 117-122] whereas the latter is due to the overtones of O-D

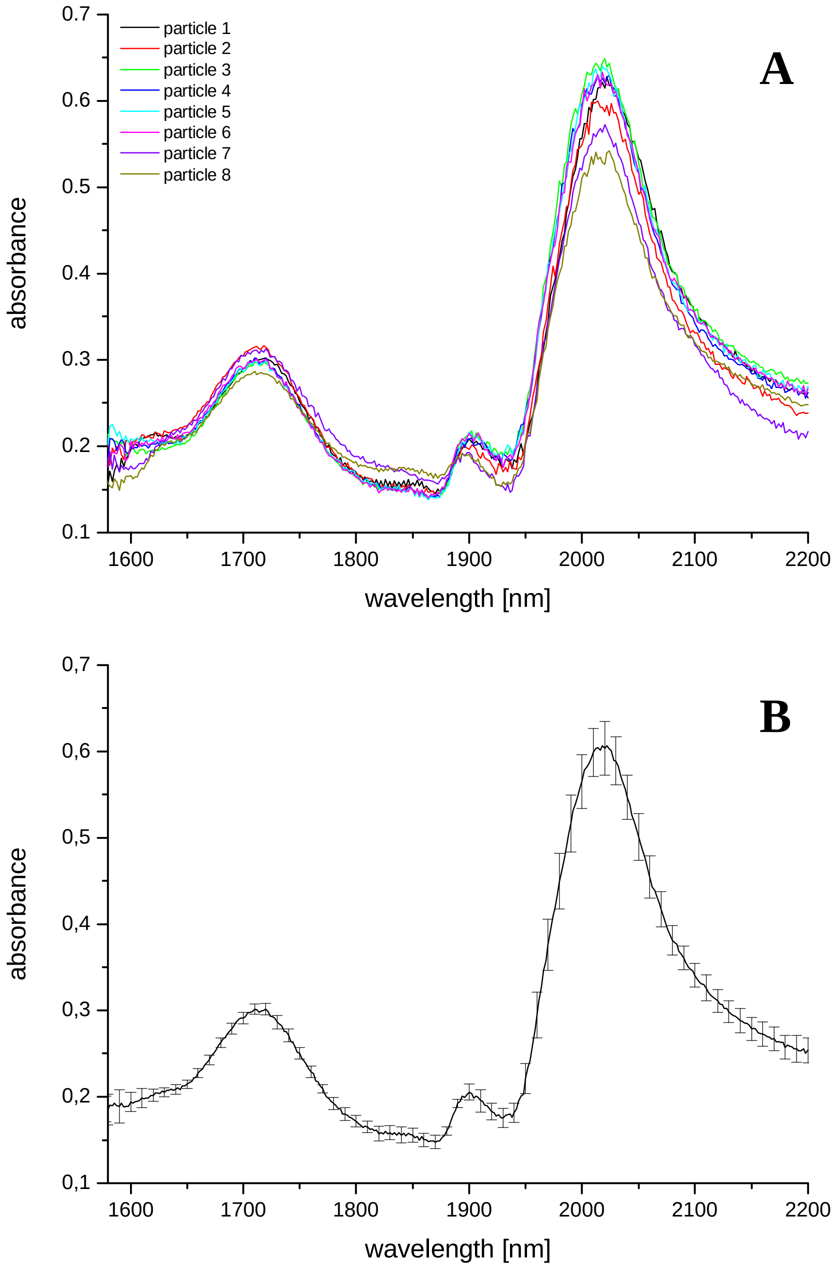

Figure 5.4: (A) Absorption spectra of eight different hydrogel particles in D_2O. (B) Average absorption spectrum of the hydrogel particles.

transitions in D_2O and the carboxylic acid group of the hydrogels (through isotopic exchange with D_2O).[95,117-122]

As described in the introduction, PNIPAM hydrogels are soluble in water at temperatures below the LCST, whereas above the LCST they become hydrophobic and partially desolvated[93, 97] as a consequence of fluctuation of hydrophobic interactions and hydrogen bonding.[98] That is, they undergo reversible volume transition (i.e., they are swollen at temperatures below the LCST, and decreased in size at temperatures above the LCST). This feature is of particular importance for drug delivery applications and was explored in detail in the following experiment. Instrument set-up with temperature controlled cell holder (see **Figure 5.2**) makes it possible to record images of the same individual hydrogel particle at different temperature. Prior to the measurement, performance of the temperature controlled cell holder in terms of the temperature stability was investigated. **Figure 5.5** shows plots of different set temperatures as a function of time. It was necessary to obtain information about the temperature properties on the metal brass surface (red) and in the sample solution (black) due to the fact that only temperature on the metal surface could be controlled and adjusted during the measurements, and that the temperature on the metal surface is not the same (i.e., somewhat higher) than that in the sample solution. Actual sample solution temperature can therefore be determined using the correction factor for specific set temperature on the metal surface. Additionally, from the plots we were able to determine the necessary time (i.e., time needed prior to the analysis, after setting the temperature) required for temperature to reach equilibrium, after being set. Thus, 15 min time period for each increasing temperature and 30 min time period for each decreasing temperature were found to provide reliable results and were

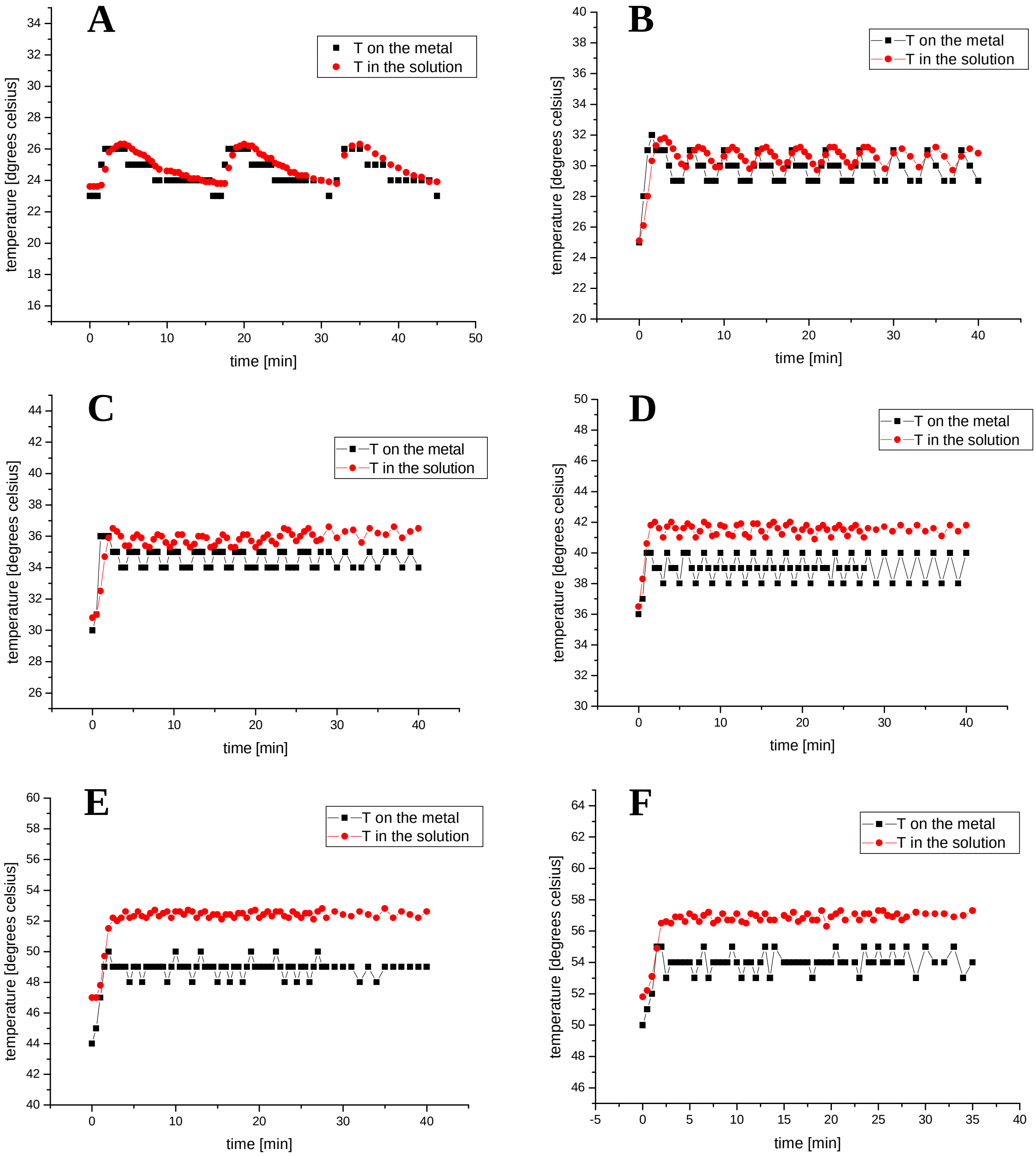

Figure 5.5: Measured temperature on metal brass surface (red) and in the sample solution (black) as a function of different set temperatures: 25 °C (A), 30 °C (B), 35 °C (C), 40 °C (D), 50 °C (E) and 55 °C (F). Six resistors were used in the set-up.

used in the proceeding experiments. It should be noted that, in order to obtain the most stable temperature values (as a function of specific temperature) other configurations, regarding the number of resistors used, were also investigated. Namely, metal cell holders with two and four resistors were made and tested for temperature stability. **Figure 5.6A-C** show plots of temperature stability as a function of time at 25 °C, 30 °C and 35 °C with only two resistors used. As can be observed the temperature stability is significantly lower than in previous set-up (i.e., when six resistors were used) and therefore it was not necessary to carry anymore experiments with this configuration at higher temperatures (i.e., 40 °C, 50 °C and 55 °C). Temperature stability increases when four resistors are used in the application (data not shown), however, the results are still relatively inferior compared to the metal cell holder designed with six resistors.

Relative to the hydrogel particles at room temperature, it was found that particles move relatively faster when the solution is heated. The NIR-MSI instrument makes it possible to follow a single particle in its dynamic pathway. In order to investigate the dynamic motion of hydrogel particles, an experiment was designed, under equivalent conditions for each measurement, that is, after setting the temperature, we waited 15 min prior to the measurement, in order for the temperature to stabilize. In **Figure 5.7**, single hydrogel particle’s dynamic motion was monitored at increasing temperature from 23.0 °C to 29.6 °C, 31.3 °C, 34.5 °C, 39.7 °C, 43.7 °C, 46.8 °C, 50.5 °C, 53.6 °C and 57.5 °C by labeling positions of the particle at each temperature. Specifically at room temperature x and y positions of the hydrogel particle were 131 and 120 pixels, respectively (dimensions of the whole image are 316×256 pixels) whereas at final measured temperature, the position of the particle changed to 167 and 113 pixels for x and y,

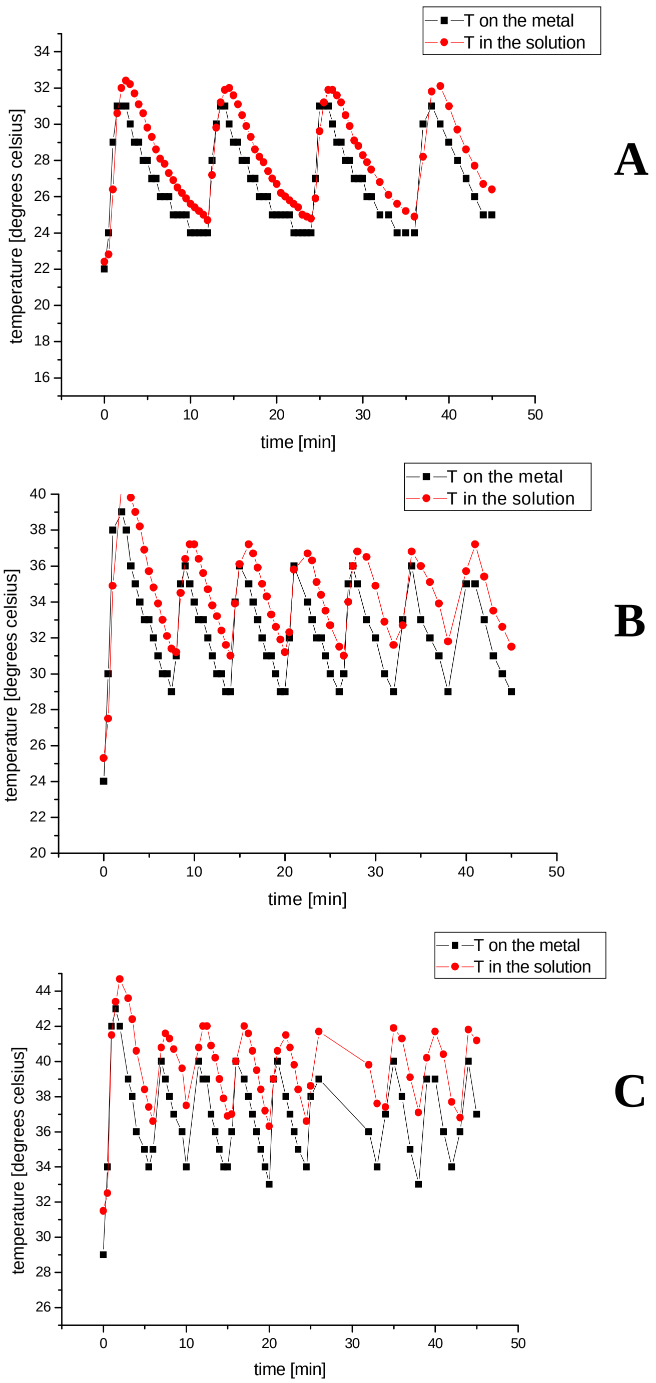

Figure 5.6: Measured temperature on metal brass surface (red) and in the sample solution (black) as a function of different set temperatures: 25 °C (A), 30 °C (B), 35 °C (C). Two resistors were used in the set-up.

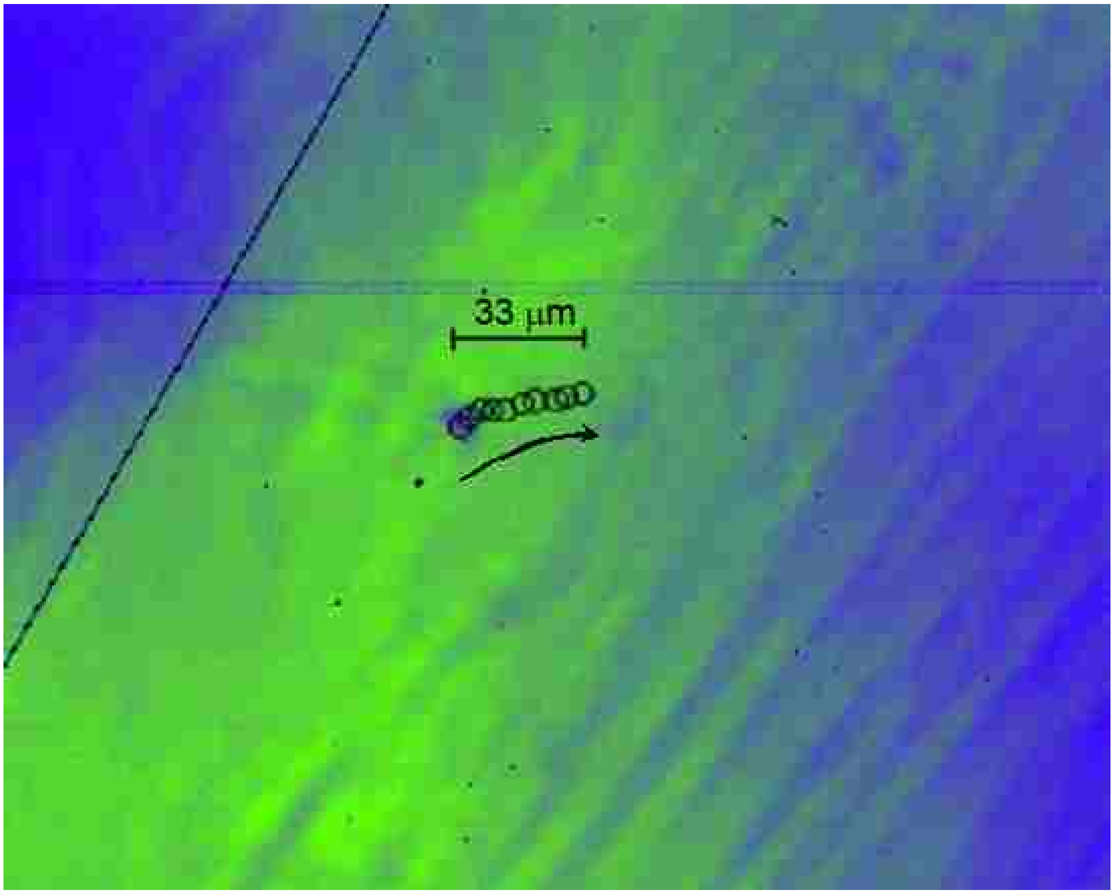

Figure 5.7: Movement of the hydrogel particle in solution at increasing temperatures.

respectively. Therefore, based on the spatial resolution of the system (i.e., 0.93±0.3 µm/pixel), the particle moved for approximately 34 microns. Additionally, it was found that the distances which the hydrogel particle travels between the temperature measurements exhibit similar patterns with possibly faster movements (longer distance) of the particle between the measurements occurring at higher temperatures. Dynamic motion of the hydrogel particles during the measurements (i.e., scanning of the wavelengths) can affect the absorption spectral properties. Therefore it is very important to understand the dynamics of the particles in solution. However, when monitoring the hydrogel particles (through 2D NIR images) during the measurement, no movement of the particle was found for data presented in this study; that is, hydrogel particles exhibit observable mobility only over longer periods of time. The lack of observable migration of the hydrogel particles is most probably due to the rapid time of recording (i.e., 560 ms to record NIR image at specific wavelength) as well as due to the size of the particles measured; specifically hydrogel particles that were used in the study are relatively large (for example 4.2±0.5 µm). Furthermore, hydrogel particles become reduced in size at temperature above LCST which might explain why their mobility is more pronounced at higher temperatures and not very observable at room temperature.

After the measurement conditions were optimized and dynamic motion of the hydrogel particles in solution understood, we monitored and recorded NIR multispectral images of the same individual hydrogel particle as a function of temperature, by heating the particle from room temperature to 67.9 °C and then cooling to 31.0 °C. 2D NIR images and corresponding 3D absorption images of a drawn rectangle in 2D NIR images (recorded at 1764 nm) at room temperature (23.0 °C) to increasing temperatures (i.e.,

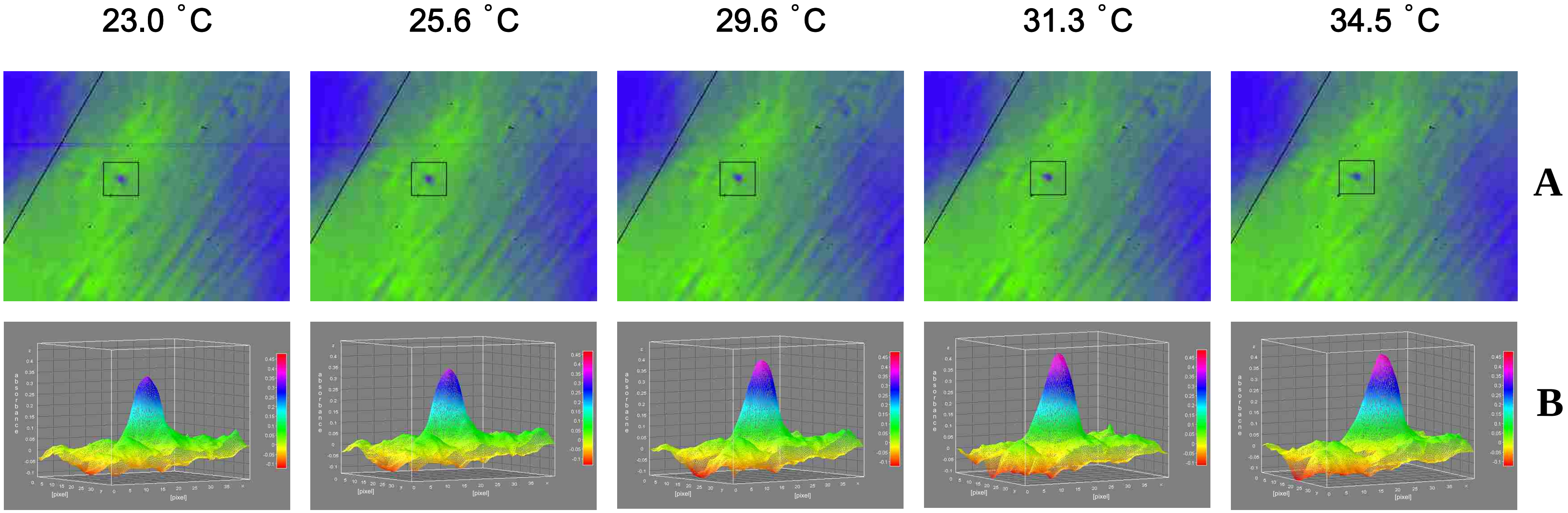

Figure 5.8: 2D images and corresponding 3D images of absorption at 1764 nm of the same single hydrogel particle at different temperatures. (See detailed description in the text).

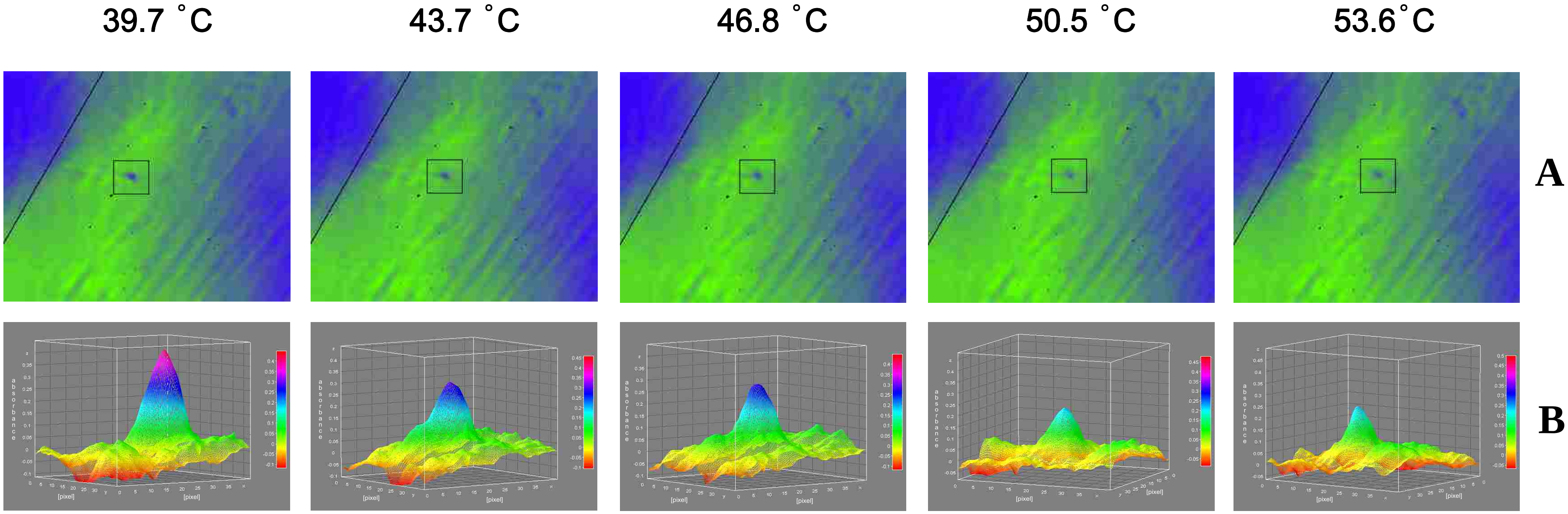

Figure 5.9: 2D images and corresponding 3D images of absorption at 1764 nm of the same single hydrogel particle at different temperatures. (See detailed description in the text).

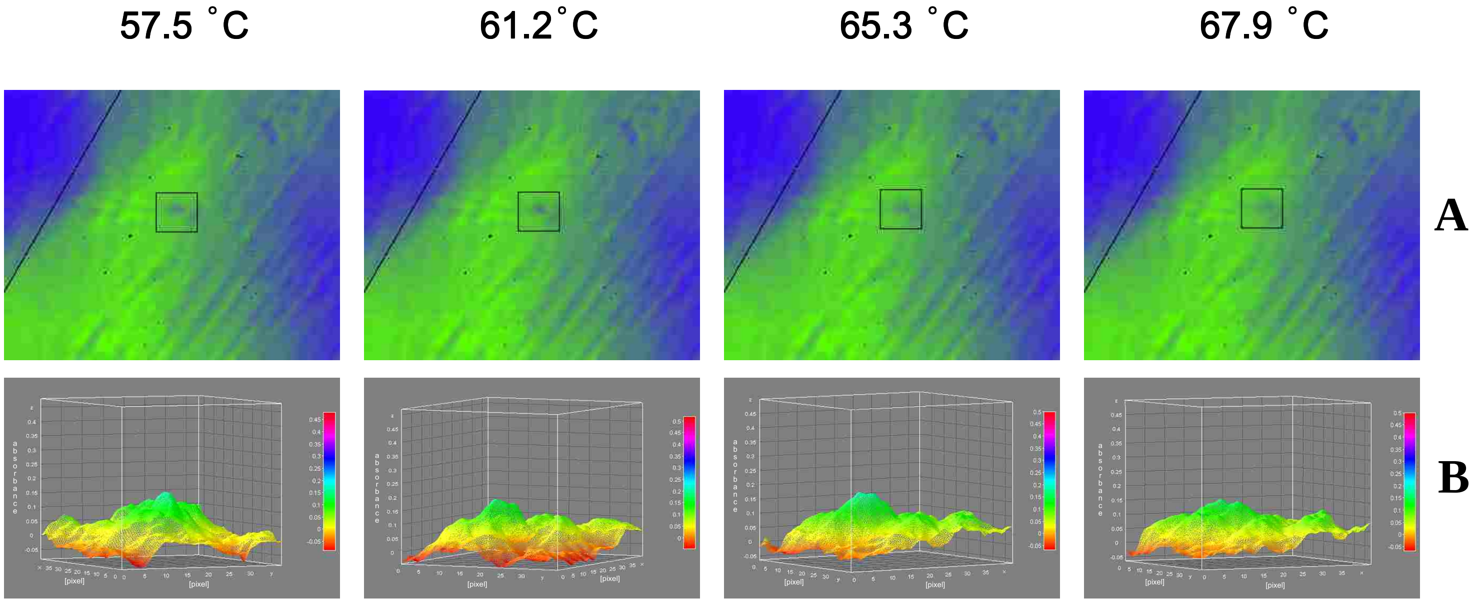

Figure 5.10: 2D images and corresponding 3D images of absorption at 1764 nm of the same single hydrogel particle at different temperatures. (See detailed description in the text).

25.6 °C, 29.6 °C, 31.3 °C, 34.5 °C, 39.7 °C, 43.7 °C, 46.8 °C, 50.5 °C, 53.6 °C, 57.5 °C, 61.2 °C, 65.3 °C, and 67.9 °C) are presented in **Figure 5.8-10A** and **B**, respectively. As illustrated from the 2D NIR images (**A**), the hydrogel particle is well focused and clearly visible up to 39.7 °C. Thereafter, the particle can be still clearly observed; however, it becomes gradually less focused with increasing temperature until it is difficult to discern the hydrogel particle at temperatures higher than 61.2 °C. The volume transition temperature behavior is even more pronounced when taking into the consideration 3D absorption images (**B**) that were obtained for drawn rectangles in the 2D NIR images. A similar trend as with 2D NIR images can be distinguished; namely, absorption intensity remains relatively constant throughout increasing temperature from 23.0 to 39.7 °C. Thenceforth, a sharp decrease in absorption intensity, followed by the gradual disappearing of the absorption band from 50.5 °C forward can be observed (see **Figures 5.8-10B**). Importantly, the particle becomes visible again and absorption intensity increases when cooled back to temperature below LCST (images for particle shown in Figures **5.8-10B** were not recorded, however, **Figure 5.11** represents 2D NIR and 3D absorption images for a different particle at 29.6 °C (**A**), when heated to 57.5 °C (**B**), and finally cooled to 31 °C (**C**)).

Additional information about the volume transition temperature and LCST behavior can be obtained by plotting absorption spectra of hydrogel particle as a function of increasing temperature (**Figure 5.12A**). As can be observed from the figure, absorption bands attributed to the C-H overtones and combination transitions (at approx. 1714 nm) are blue shifted towards lower wavelengths and exhibit decrease in absorption intensities when the temperature is increased. Additionally, the absorption band at

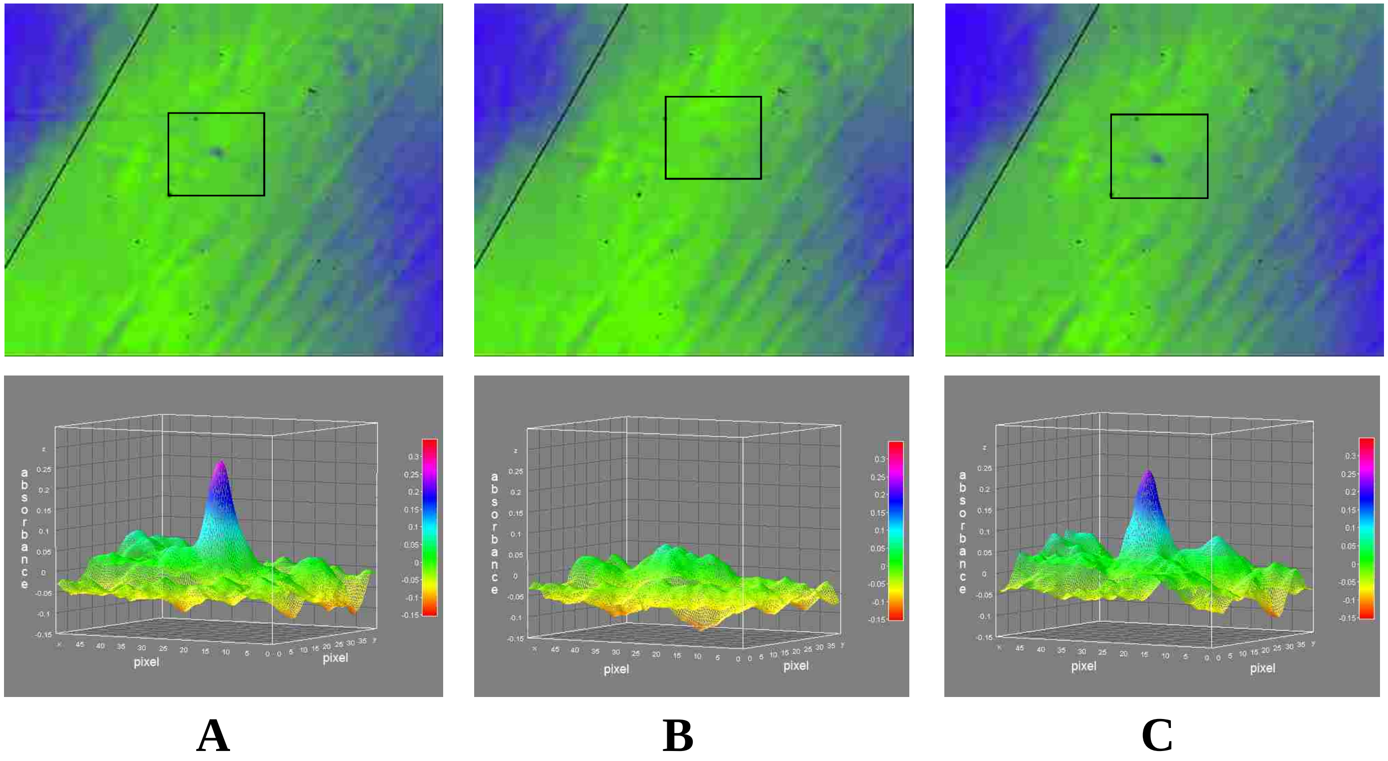

Figure 5.11: 2D images and corresponding 3D images of absorption at 1764 nm of the same single hydrogel particle at different temperatures: 29.6 °C (A), 57.5 °C (B) and cooled to 31 °C (C).

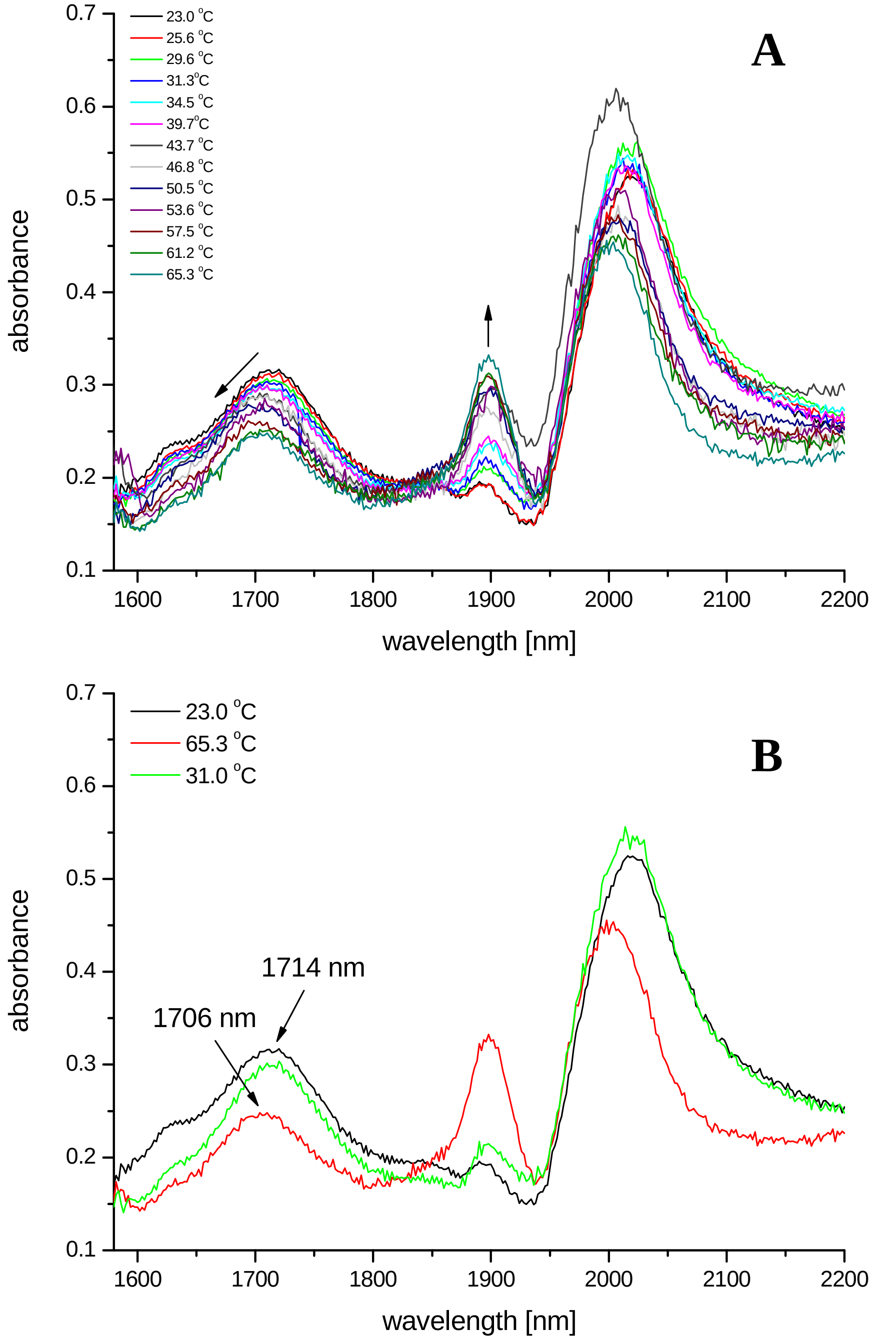

Figure 5.12: (A) Absorption spectra of single hydrogel particle in D_2O at different temperatures. (B) Comparison of the absorption spectra at final and initial temperatures.

approximately 1900 nm becomes more pronounced with higher temperatures. Differences in the absorption spectra due to the increasing temperature, however, are more apparent in **Figure 5.12B** which represents comparison of absorption spectra at initial and final temperatures; specifically, absorption maxima undergo wavelength shift from 1714 nm to 1706 nm at room temperature (black curve) and 65.3 °C (red curve), respectively. Interestingly, the absorption maximum shifts back to the initial position, that is, approx. 1714 nm, when the sample is cooled to 31.0 °C. The observed transitions of the C-H band might be due, in part, to the fact that, upon heating, the hydrogel moieties lose their sphere of hydration, which subsequently leads to an increase in the attractive interactions among the polymer chains, and is consequently reflected by a blue shift of the C-H band. This phenomenon corresponds to the known collapse of the hydrogel network, which leads to a reduction in size.[123-126] The process is reversible, i.e., upon cooling the C-H band is red shifted to the initial wavelength position.

In order to explain the increased absorbance at approximately 1900 nm, additional experiments were conducted. Hydrogel particles in D_2O that were used in the study consisted of poly(N-isopropylacrylamide-co-AAc) (95:5, w/w) and therefore chemically resemble an acetamide and acetic acid (95:5, w/w) mixture in D_2O. Accordingly, the absorption spectra of neat acetic acid, acetamide in D_2O, and neat D_2O were collected as a function of increased temperature using identical experimental conditions as for hydrogel measurements (spectra not shown). **Figure 5.13** represents difference absorption spectra obtained by subtracting the spectra at room temperature (23.0 °C) from the spectra of the same solution heated to 65.3 °C for D_2O (**A**), acetamide in D_2O (**B**), neat acetic acid (**C**), and combined subtracted spectra of a single hydrogel particle in

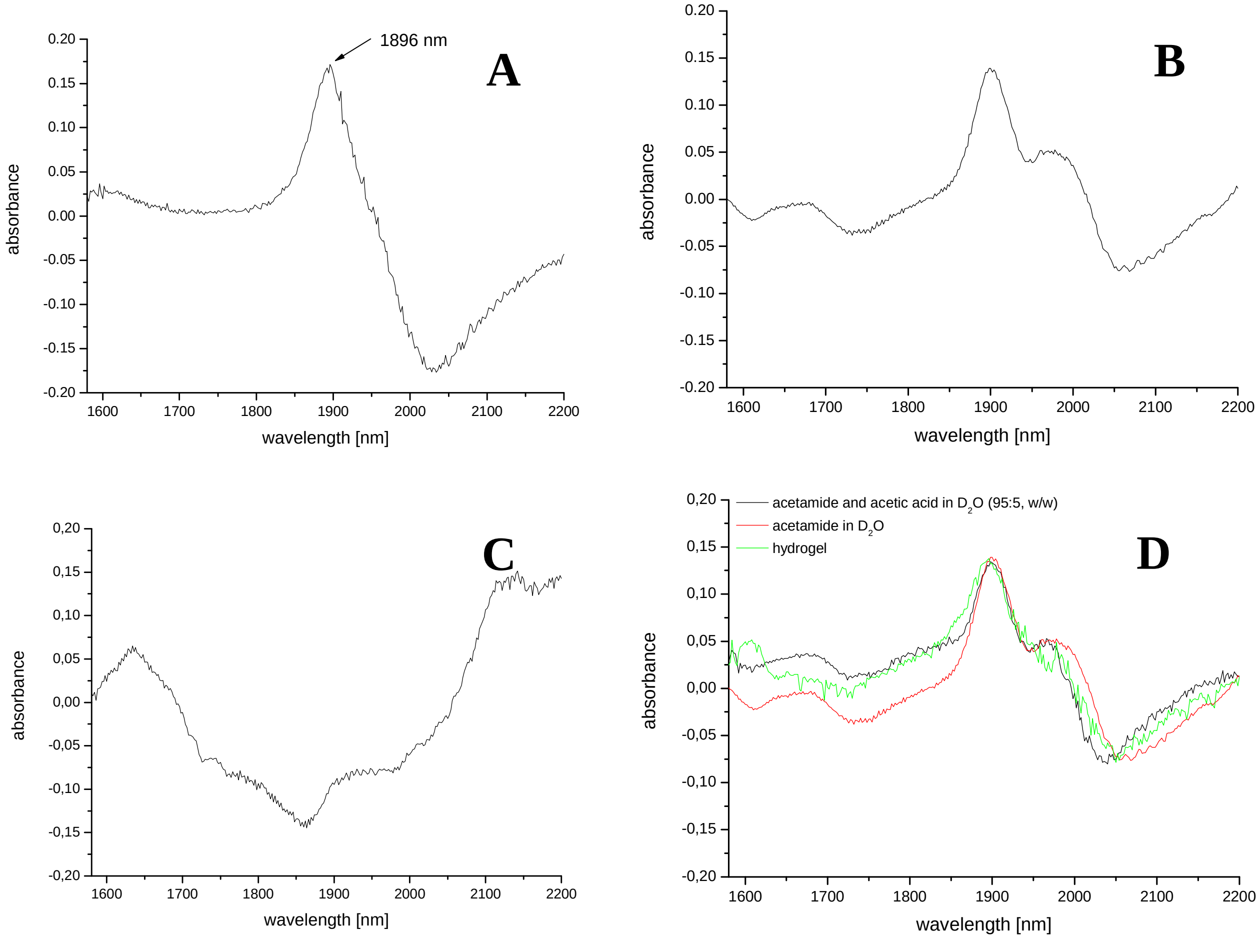

Figure 5.13: Subtracted absorption spectra (final T - initial T) for D_2O (A), acetamide in D_2O (B), and neat acetic acid (C). Comparison of subtracted absorption spectra (final T - initial T) between acetamide and acetic acid in D_2O (95:5, c/c), acetamide in D_2O and hydrogel particle in D_2O (D).

D_2O (green curve), acetamide in D_2O (red curve), and a 95:5 w/w mixture of acetamide:acetic acid in D_2O (black curve) (**D**). An absorption band at approx. 1900 nm can be observed for D_2O and acetamide in D_2O solutions. Conversely, neat acetic acid does not exhibit absorption at the same wavelength region. Subtracted absorption spectra for, acetamide in D_2O, a 95:5 w/w mixture of acetamide-acetic acid in D_2O, and a single hydrogel particle in D_2O are relatively similar; however, after closer inspection, it can be observed, that the latter two (i.e., mixture of acetamide-acetic acid in D_2O, and a single hydrogel particle in D_2O) resemble each other more closely (see **Figure 5.13D**). The obtained results attest that mixture of acetamide and acetic acid in D_2O is chemically comparable to the hydrogel particle in D_2O. Furthermore, the absorption band at around 1900 nm was observed for D_2O, acetamide in D_2O, mixture of acetamide-acetic acid in D_2O and for an individual hydrogel particle in D_2O, therefore it was assigned as a hot band of the O-D groups.

As described, the LCST behavior of single hydrogel particle can be characterized from the spectral data at different temperature represented in **Figure 5.12**. Specifically, the plot of λ_{max} of the 1714 nm absorption band as a function of increasing temperature (see **Figure 5.14A**) demonstrates no significant change in the peak position prior to 30 °C. Afterwards, significant shift towards lower wavelengths can be observed. The peak position comes to being relatively constant again at temperature 45 °C and above. Consequently, the phase transition temperature was determined from the second derivative (see **Figure 5.15A**) of the Boltzmann curve in **Figure 5.14A** and it was found to be 41 ± 2 ˚C. Additionally, volume transition temperature can also be obtained from spectral data by plotting normalized changes in total absorption of the hydrogel particle

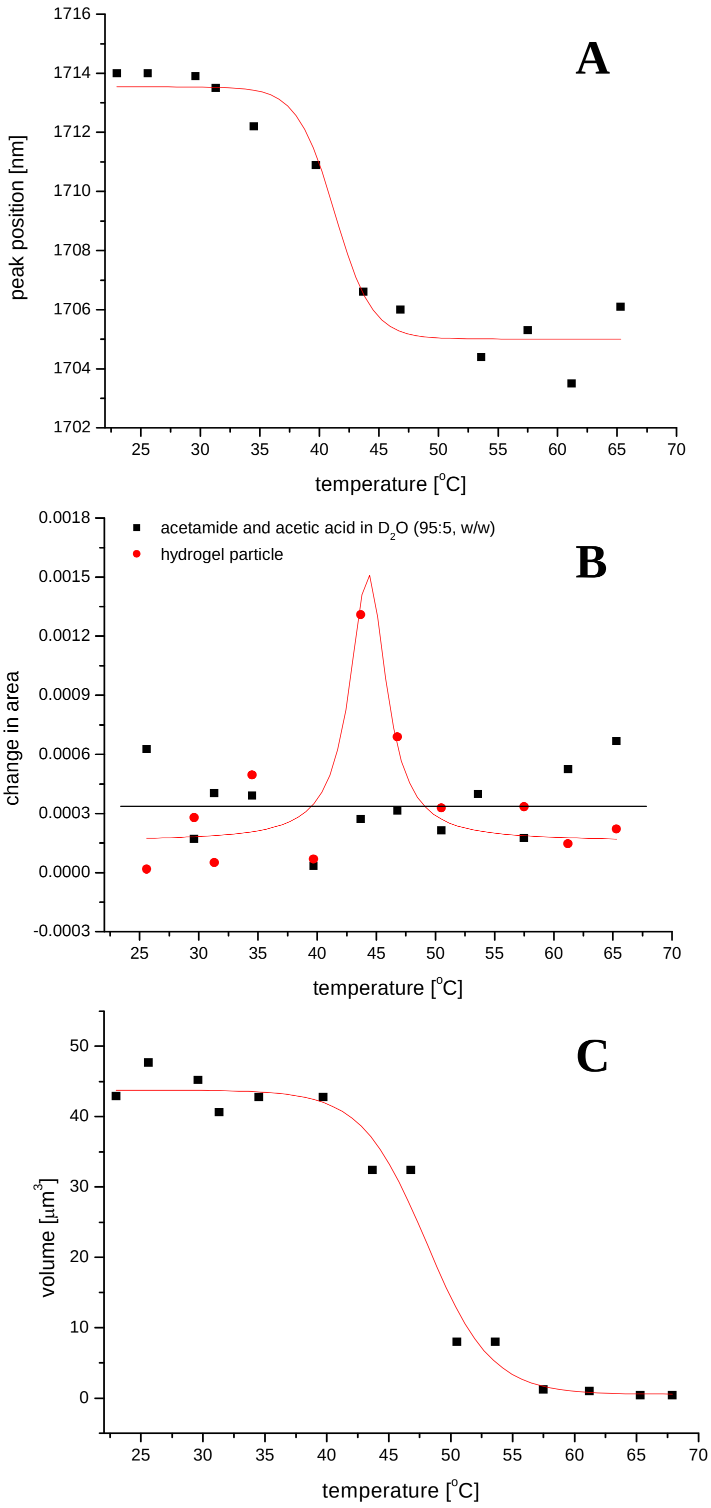

Figure 5.14: Band position (C-H absorptions) as a function of increased temperature (A), change in area (between two consecutive temperature increments) as a function of increased temperature (B), and volume of the hydrogel particle as a function of increased temperature (C).

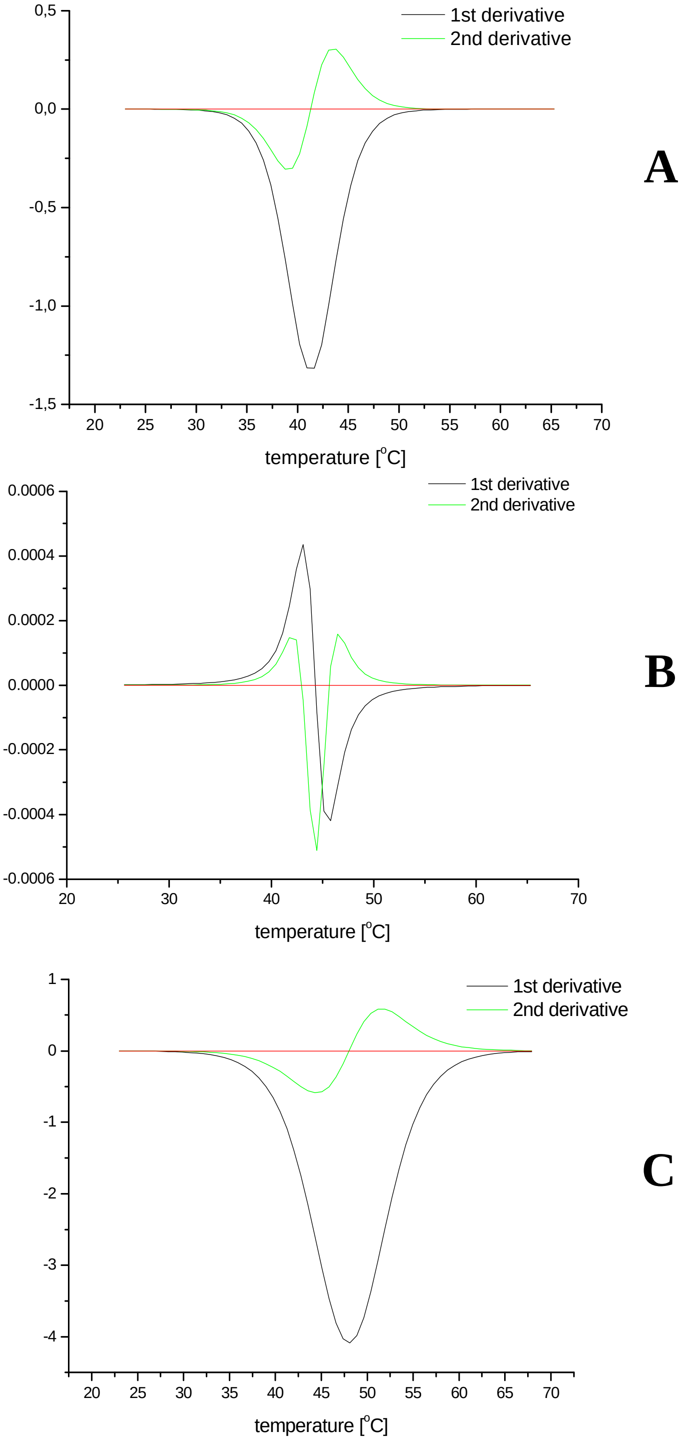

Figure 5.15: Second derivatives of the best fit curves. See text for a detailed description.

(i.e., areas under the absorption curves represented in **Figure 5.12A**) as shown in **Figure 5.14B**. It can be observed that significant changes in area occur at approx. 45 °C, indicating volume transition temperature. Indeed, a volume transition temperature of 44 ± 2 ˚C was established from the second derivative of the Lorentz curve (see **Figure 5.15B**). Interestingly, no transitions are exhibited when normalized changes in total absorption of the acetamide-acetic acid mixture (95:5, w/w) are plotted as a function of increasing temperature, which therefore indicates that volume transition is indeed characteristic to the hydrogel particles. An alternative method to obtain information about the volume transition temperature of hydrogel particle employed 2D NIR images. Specifically, the hydrogel particle was assumed to be spherical, and its diameter dimensions (in x and y direction) were estimated based on the spatial resolution of the system. Consequently, changes in the volume of the particle at different temperatures were plotted. A similar pattern as when λ_{max} was plotted against temperature was observed. Essentially, the volume of the hydrogel particle remains relatively constant up to 40 °C whereas it substantially decreases between 40 °C and 55 °C. Correspondingly, a volume transition temperature of 48 ± 3 °C was determined from the second derivative of the Boltzmann line (see **Figure 5.15C**). It is pleasing to observe that volume transition temperature values obtained from first two methods (i.e., derived from spectral data) correlate well within the experimental error. The higher transition temperature value (i.e., 48 ± 3 °C) obtained from changes in the volume of the hydrogel particle might be due to the fact that hydrogel particle does not have sharp focused edges (as can be seen from **Figures 5.8-10A**) and, therefore, the dimensions were roughly estimated. Conversely, definite peak positions could be determined from the spectral data.

Relationship between the dimensions of the hydrogel particles and their corresponding LCST transition was further investigated. Specifically, six particles with varying sizes (from 1.2 ± 0.4 μm to 5.9 ± 0.5 μm) were analyzed and their volume transition temperatures determined. Consequently, transition temperatures were plotted as a function of the volume of individual hydrogel particles (see **Figure 5.16**). It can clearly be observed, from the figure, that particle size has a direct effect on LCST; that is, volume transition temperature increases with the size of the measured particles. As stated previously, upon heating, hydrogel particles become dehydrated. Therefore it is expected that smaller particles, which have fewer hydrated sites, would undergo volume transition at relatively lower temperature compared to larger hydrogel particles with more hydrated sites.

5.4 CONCLUSION

The results presented demonstrate that near-infrared multispectral imaging microscope can be successfully used to observe and measure directly images and spectra of individual hydrogel particles. Single hydrogel particles in solution can be analyzed using this technique. Moreover, the individual hydrogel particle can be monitored directly during the measurements by means of both, spectroscopy and imaging, thus providing additional insight into the properties and dynamics of volume phase transition for hydrogel polymer. The microscope instrument used in the study makes it possible to determine volume transition temperature based on three different methods; namely from the position of the absorption band maxima, changes in areas under the absorption curves, and from volume changes as a function of increasing temperature. Furthermore,

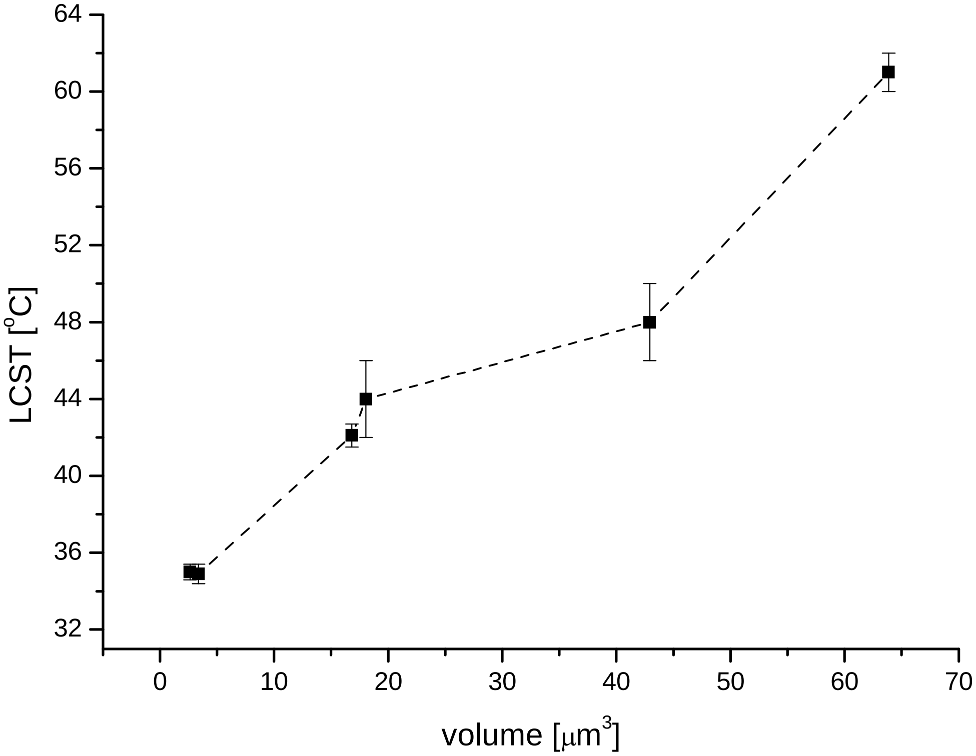

Figure 5.16: LCST as a function of the volume of single hydrogel particles.

consistency of the results further affirms the validity of the instrument and methods.

Due to the fact that individual hydrogel particles in solution can be characterized with NIR-MSI microscope, we were able to investigate the relationship between dimensions of the particles and their respective transition temperatures. It was found that LCST values are directly affected by particle size, i.e., larger hydrogel particles exhibit higher LCST values and, conversely, smaller particles undergo volume transition at relatively lower temperatures.

CHAPTER 6

EFFECT OF GOLD NANOCAGES ON ABSORPTION, IMAGING, AND LOWER CRITICAL SOLUTION TEMPERATURE PHASE TRANSITION OF INDIVIDUAL HYDROGEL PARTICLES

6.1 INTRODUCTION

N-isopropylacrylamide (NIPAM) based hydrogels are described in detail in Chapter 5. Concisely, these hydrogels are hydrophilic and highly soluble in water at temperatures below the lower critical solution temperature (LCST), whereas above the LCST they become hydrophobic and partially desolvated[60,93] as a consequence of fluctuation of hydrophobic interactions and hydrogen bonding.[103] Moreover, NIPAM hydrogels undergo a reversible swelling-deswelling volume transition that is strongly dependent on the LCST.[60,93-96]

Hydrogels are often synthesized with noble metal nanostructures (i.e. platinum, silver, and gold) in order to facilitate their use.[58,60,127,128] Due to their unique and tunable optical, electronic and catalytic properties (i.e. they exhibit localized surface plasmon resonance (LSPR)), noble metal nanostructures are widely used in nanoparticle-based optical and biological applications. As previously described in Chapter 4, the localized surface plasmon resonance (LSPR) of noble metal nanostructures is a phenomenon that occurs when the incident light is being scattered and absorbed at a resonant frequency as a consequence of collective oscillation of conductive electrons.[129] The properties of nanostructures can be adjusted by controlling their composition, size, shape and structure.[62-65] Due to their biocompatible material, which enables their use in vivo studies as nanoscale biomaterials,[58,59] gold nanostructures are of particular interest. In the research study described herein, gold-based nanocages were employed. However, the gold nanocages (GNs) were not synthesized together with the poly(NIPAM-co-AAc) hydrogels (for example, as hydrogel coated gold nanostructure),[60] but rather separately for subsequent adding to the already prepared hydrogel suspension. They are hollow, porous structures with dimensions smaller than 200 nm. They were prepared by a galvanic replacement reaction between solutions containing metal precursor salts ($HAuCl_4$) and Ag nanostructures synthesized through polyol reduction.[56] The relative intensity of the scattering and/or absorption of the incident light depends highly on the size of the nanocages and can, therefore, be tuned by varying the dimensions of the GNs.[56] It was found that light absorption is favored when nanocages are small (smaller than 45 nm) whereas light scattering predominates with larger cages.[56] Due to the fact that LSPR peak positions of gold nanocages can be tuned throughout the visible and into the near-infrared region,[56] and that gold nanocages exhibit large absorption/scattering cross-sections in the near-infrared region[56,130] they can be used for calorimetric sensing and biomedical applications, especially in cases when absorption of light in vivo is required.[130-132]

Our long term goal is to develop and characterize an effective in-vivo method for drug delivery based on photothermal activation by NIR light of poly(NIPAM-co-AAc) hydrogels. Specifically, drug-impregnated hydrogels are expected to undergo volume transition (i.e. polymer shrinks) at the temperatures above the LCST, which would lead to the release of the drug into the local environment. Therefore, it is very important for the hydrogels to have high absorption in the NIR region of interest which, as a consequence, would result in more efficient photothermal activation of the hydrogel particles. Effect of gold nanocages (GNs) upon absorption intensity of the individual hydrogel particles was investigated using near-infrared multispectral imaging microscope,[73,75,113-116] which was developed in our lab and described in detail in previous chapters of the thesis.

6.2 EXPERIMENTAL

6.2.1 Chemicals

The monomer *N*-isopropylacrylamide (NIPAM), comonomer acrylic acid (AAc), crosslinker *N*,*N*-methylenebisacrylamide (BIS) (see **Figure 6.1**) and polymerization initiator ammonium persulfate (APS) (Aldrich, 99 %) were obtained from Sigma-Aldrich. The NIPAM monomer was recrystallized from hexane and dried under vacuum prior to use. Deuterium oxide (99.9 %) was purchased from Cambridge Isotope Laboratories. Deionized water was distilled prior to use.

6.2.2 Synthesis of poly(N-isopropyl-co-Acrylic acid) hydrogel particles

Poly(NIPAM-co-AAc) hydrogel particles were synthesized via surfactant-free radical, precipitation polymerization under argon atmosphere as described elsewhere.[60,98,133] Specifically, NIPAM (0.95 g) with AAc (0.05 g) (95:5, w/w), and cross-linker *N*,*N*-methylenebisacrylamide (BIS) (0.115 g) were dissolved in 195 mL of deionized distilled water by continuous stirring under argon atmosphere in a three-necked flask equipped with condenser and placed in a heating bath. Thereafter, the solution was slowly heated to 70 ˚C while it continued to be purged with argon. Ammonium persulfate

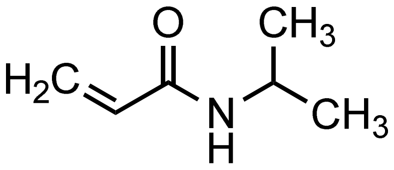

N-isopropylacryl amide (NIPAM)

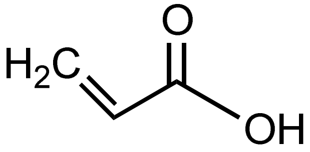

Acrylic acid (AAc)

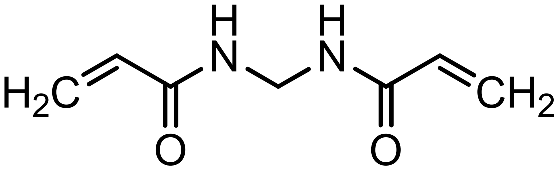

N,*N*-methylenebisacrylamide (BIS)

Figure 6.1: Chemical structures of *N*-isopropylacrylamide (NIPAM), acrylic acid (AAc), and *N*,*N*-methylenebisacrylamide (BIS).

(APS) (0.12 g) dissolved in 5 mL of deionized and distilled water was then added into the solution in order to initiate the polymerization. The solution turned turbid after about 5 minutes, and the reaction was allowed to proceed for 5 to 6 hrs. at 70°C under argon atmosphere. After the reaction was stopped, the solution was cooled to room temperature. At the end, the solution was dialyzed (4 Spectra/Por 4) for several days against deionized distilled water in order to remove any unreacted matter. Finally, the solution was filtered through a 5 µm membrane filter (Sartorius Stedim Biotech, Gottingen, Germany) to remove particulate matter.

In order to calculate the concentration of hydrogel particles, the molecular weight of hydrogel particles in D_2O was first ascertain by MALDI-TOF-MS (Matrix Assisted Laser Desorption Ionization Time-of-Flight Mass Spectrometry) measurements (Microflex LT, Bruker Daltonics, Billerica, MA). The average molecular weight of the hydrogel was determined to be approx. 40,000 (see MALDI mass spectrum in **Figure 6.2**). The hydrogel dispersion was then lyophilized to obtain dry hydrogel mass. Specifically, knowing the volume of the hydrogel dispersion that was lyophilized (50 mL) we were able to calculate hydrogel mass for the dispersion volume that was used in the sample (6 mL). Thus, the dry hydrogel mass that corresponds to the samples analyzed in the study was determined to be 19.5 mg. Using these values (i.e., M.W. = 40,000 and mass of hydrogel = 19.5 mg), the concentration of the hydrogel particles was found to be 2.4×10^{-5} M. Additionally, hydrogel mass was also estimated by weighing the hydrogel precipitant and accounting for water mass in the sample. Specifically, fully swollen PNIPAM particles contain between 90 and 99 % of water by volume,[127,136] therefore the mass of the water was subtracted. Accordingly, the hydrogel mass and hydrogel

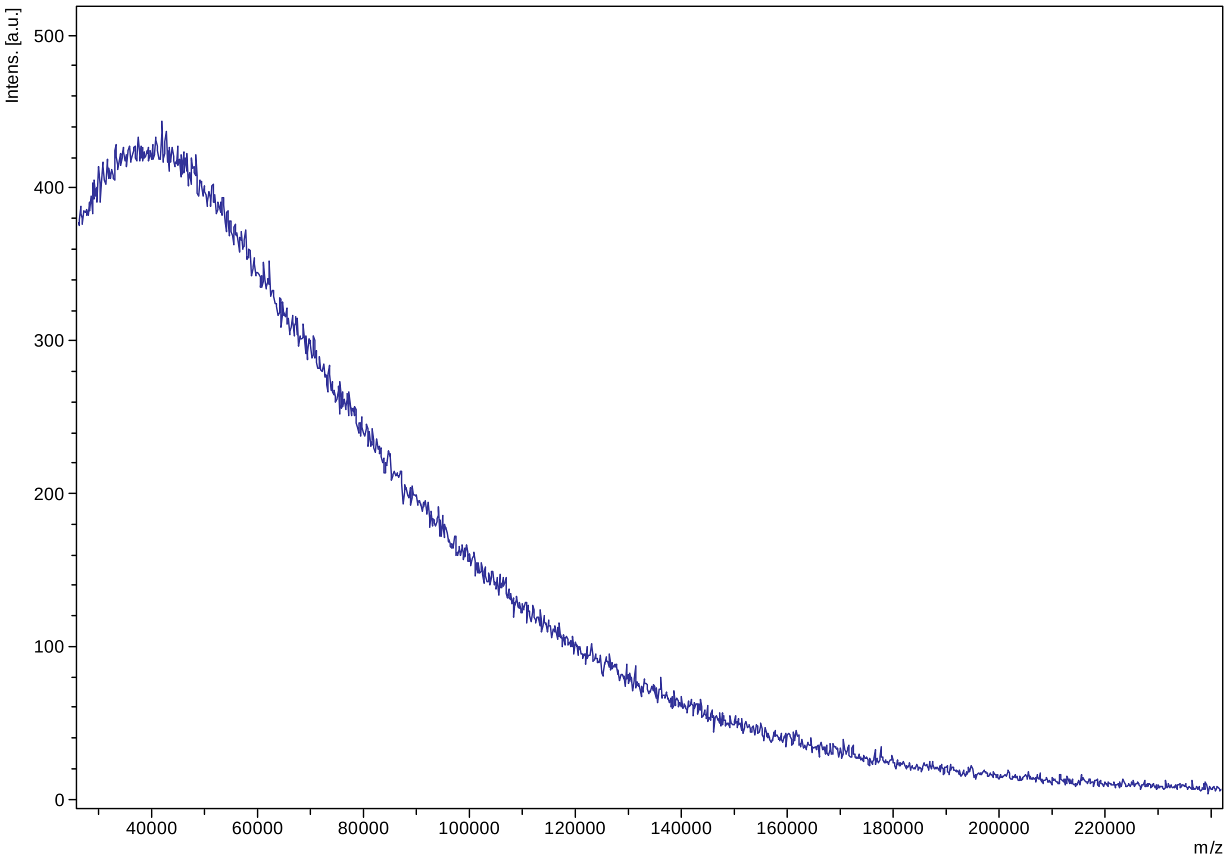

Figure 6.2: MALDI mass spectrum of hydrogel particles in D_2O.

concentration were then calculated to be 7.8 mg and 9.8×10^{-6} M, respectively. It is expected that the bulk of the polymers in the hydrogel solution are linear polymers, and hydrogel spherical particles represent only a small portion of the sample. Therefore, due to the difficulty of differentiating between linear and spherical polymers (i.e., hydrogel particles) we could only give an estimation of the final concentration of the hydrogel particles, i.e, in the range of 10^{-7} and 10^{-8} M.

6.2.3 Gold nanocages

Gold nanocages were prepared in Dr. Xia's group (Washington University, St Louis) as reported previously.[134,135] They were prepared in D_2O. The concentration of metal ions in GNs dispersion was determined by ICP-MS measurements combined with TEM analysis and calculated to be 2.8×10^{-11} M.

6.2.4 Sample preparation

As described, NIPAM-AAc hydrogels were prepared as an aqueous suspension (i.e., dispersed in H_2O). To avoid complications due to the strong OH absorbance in NIR region of interest, deuterium oxide was used instead during the study. Hydrogel nanoparticles were therefore centrifuged in 1.5 mL centrifuge tube for 3 h (RT, 5000 rpm) prior to the analysis and solvent was exchanged to deuterium oxide. The procedure was repeated one more time in order to completely exchange water to D_2O. Gold nanocages were dispersed in deuterium oxide and were used as received.

6.2.5 Instrumentation

All measurements were performed on an in-house built microscopic multispectral imaging instrument which is described in detail in Chapter 4. Temperature controlled cell holder, equipped with six resistors powered by the Tenna model PS-12 power supply was used for the temperature dependent studies (see Chapter 5 for a detailed description). Spectra were taken in NIR region between 1400 and 2200 nm with 2 nm increments, using 1 mm spectrophotometric cells. Finally, image processing program ImageJ (National Institutes of Health) was utilized to calculate 3D absorption images.

6.3 RESULTS AND DISCUSSION

As stated in the previous chapters, the spatial resolution of the NIR-MSI microscope instrument was determined to be 0.93 ± 0.03 μm/pixel. The average diameter of eight individual hydrogel particles without the gold nanocages, calculated from this relationship, was found to be 2.3 ± 0.7 μm and they were found to have spherical shape, whereas the average diameter of eight individual hydrogel particles with the gold nanocages was determined to be 2.6 ± 0.7 μm. Due to the fact that measured particles are larger in size than the spatial resolution of the system, we were consequently able to observe individual hydrogel particles. 16 hydrogel particles (eight without and eight with GNs) were measured. 2D images and corresponding 3D absorption spectra of four of these hydrogel particles without and with the gold nanocages, at wavelength 1764 nm (and calculated at one pixel resolution) are shown in **Figures 6.3A** and **6.3B-D**, respectively. Dimensions of the individual particle without GNs (**Figure 6.3A**), calculated from 2D NIR image and based on the spatial resolution of the instrument, was found to be 3.1 ± 0.4 μm. Comparable sizes were determined for other two hydrogels with GNs, i.e. 2.8 ± 0.3 μm and □ 3.5 μm shown in **Figure 6.3B** and **6.3C**, respectively (due to the high degree of the defocusing, dimensions were not calculated for hydrogel particle in **Figure 6.3D**). The average size of the gold nanocages used in our study was

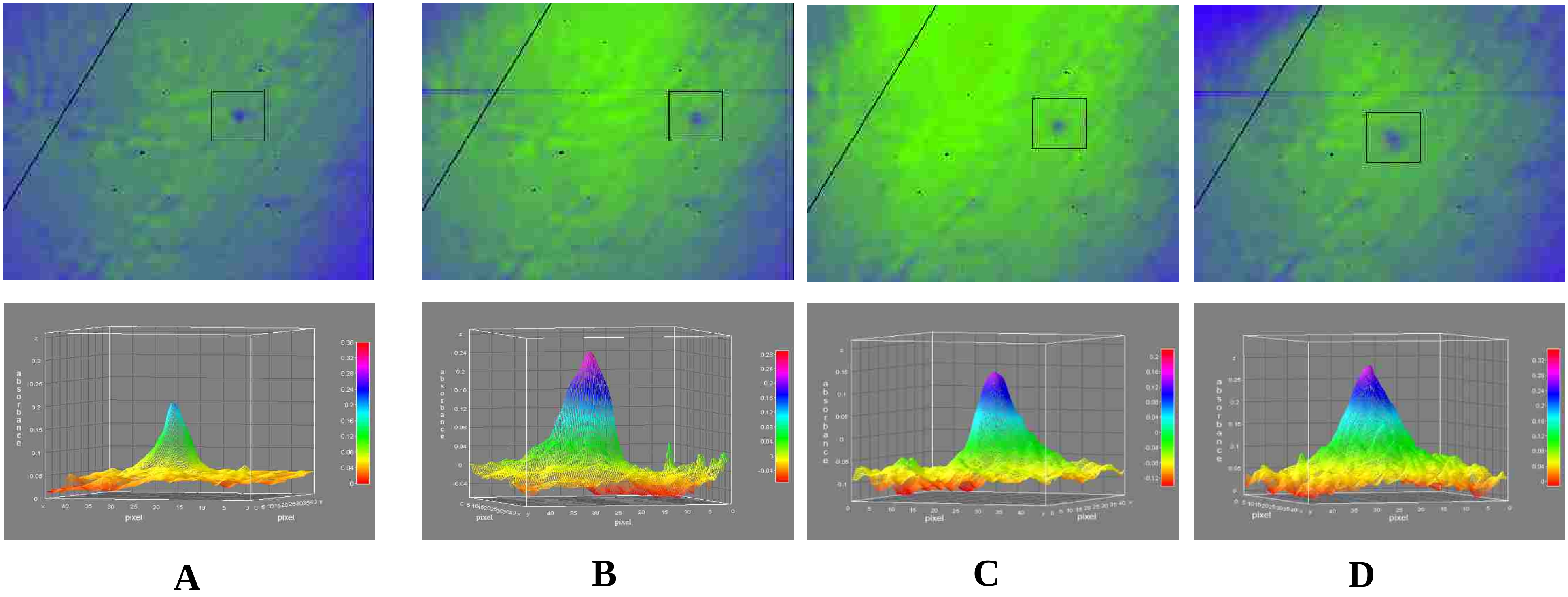

Figure 6.3: 2D images and corresponding 3D absorption images of the drawn rectangular section calculated at 1764 nm for hydrogel particle without gold nanocages in D_2O (A), and with gold nanocages (B-D). Units for x, y and z axes are pixel, pixel, and absorbance at 1764 nm, respectively (one pixel corresponds to 0.93 μm).

determined to be 183 nm, therefore, due to the limitation by the spatial resolution of the instrument (i.e., 0.93 ± 0.03 μm/pixel), the individual gold nanocages were not visible. However, it can be observed from the 2D NIR images that the hydrogel particles with GNs are less focused (or somewhat defocused) compared to the hydrogel particles without GNs (compare **Figure 6.3A** and **6.3B-D**). Moreover, it seems that the absorption band of a hydrogel particle without GNs is relatively narrower than spectral bandwidths for other three hydrogel particles (i.e., with GNs) with comparable dimensions. These observations might be due to the photothermal effect of the GNs. Specifically, irradiation of the metal nanoparticles may lead to generation of heat and vapor bubbles around the nanoparticles.[135] It is anticipated that GNs strongly interact with hydrogel particles, which would consequently generate defocusing (of an image)[135] and result in broadening of the absorption bands of hydrogel particles.

As described previously, the multispectral imaging system enables us to measure the NIR absorption of the individual hydrogel particle in the suspension. That is, the images in the region of interest are recorded, and the absorption spectra at any pixel position within the image can be determined. In order to evaluate the effect of the GNs on the absorption intensity of the poly(NIPAM-co-AAc) hydrogel particles it is necessary to first characterize spectral properties of the solution of hydrogel particles that is identical to the solution of hydrogel particles with GNs, except for the absence of GNs. **Figure 6.4A** represents absorption spectra of eight different, individual hydrogel particles (without GNs). Two distinctive absorption bands at 1716 nm (1) and 2010 nm (2) can be attributed to the C-H overtone and combination transitions, and O-D overtone transitions of D_2O and the carboxylic acid group of the hydrogels, respectively. Interestingly, even

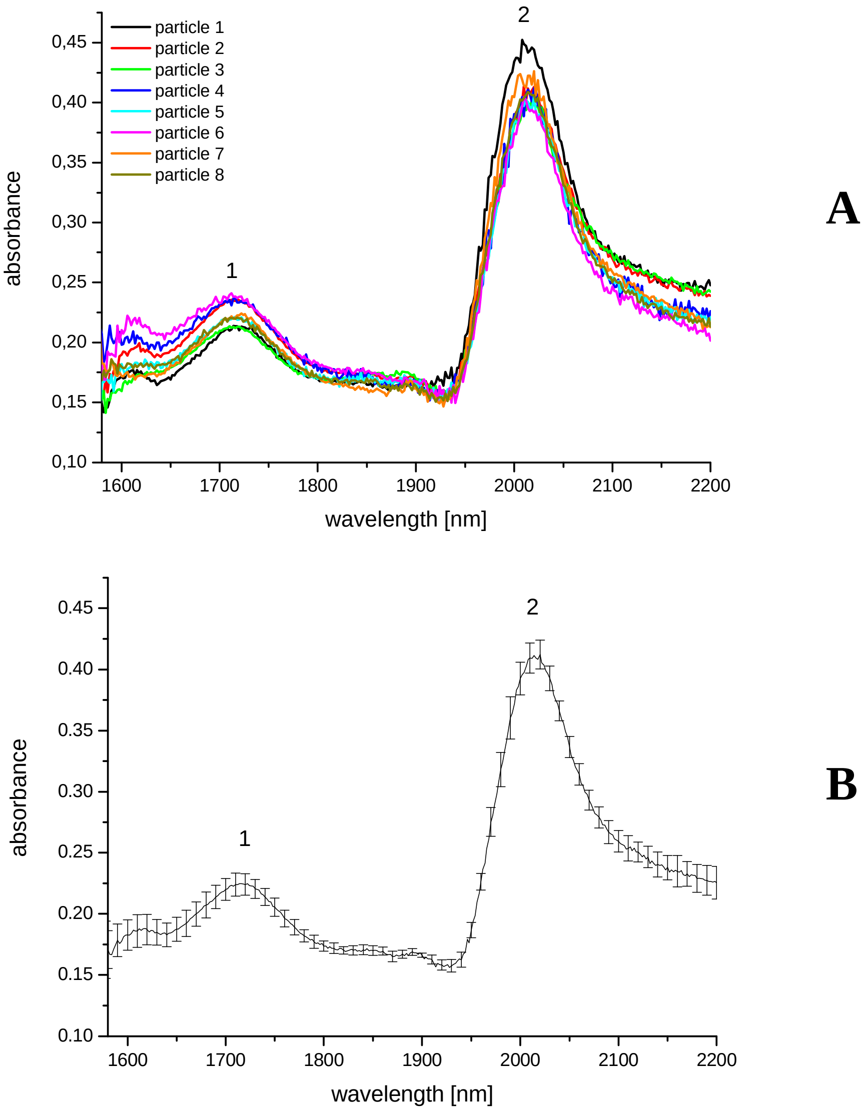

Figure 6.4: (A) Absorption spectra of eight different hydrogel particles in D_2O. (B) Averaged spectrum calculated from eight spectra shown in Fig. 6.4A.

though the dimensions of the measured hydrogel particles varied between 1.4 and 3.19 μm, the absorption spectra are very similar, indicating that the size of the hydrogel particles does not have a significant effect on the particles' absorption spectra. Moreover, it appears that different hydrogel particles within the sample solution are chemically homogeneous. The resemblance of the spectra can be further observed in **Figure 6.4B** where averaged absorption spectrum of eight particles is presented. The relative error was calculated to be 3.8 %. It is valid, therefore, to use this data as a reference absorption spectrum for hydrogel particles without the addition of gold nanocages.

Localized surface plasmon resonance (LSPR) band position can be tuned, by modifications of the galvanic replacement reaction, throughout the visible and into the near-infrared light.[56] As a result of the synthesis conditions, the gold nanocages, that were used in this study exhibit absorption maximum at 1304 nm (measured in D_2O with commercial UV-Vis-NIR spectrophotometer, Shimadzu Model 3101) as shown in **Figure 6.5**. Due to the large scattering and absorption cross-sections of gold nanocages in the near-infrared region it is, therefore, expected that addition of gold nanocages into the NIPAM-AAc hydrogel suspension (in D_2O) will increase the absorption of hydrogel polymer. The effect of GNs on the enhancement in absorption intensity was subsequently investigated. Specifically, sample solutions with same concentration of hydrogel (10^{-7} to 10^{-8} M) and different concentrations of GNs were prepared; i.e., 5.6×10^{-12} M (solution B), 1.4×10^{-11} M (solution C), 1.8×10^{-11} M (solution D). Additionally, a sample solution consisting of only hydrogel particles in D_2O (solution A) (hydrogel concentration was the same as for solutions B, C and D) was used as a reference sample. At least eight different hydrogel particles were measured from each solution and the results obtained were

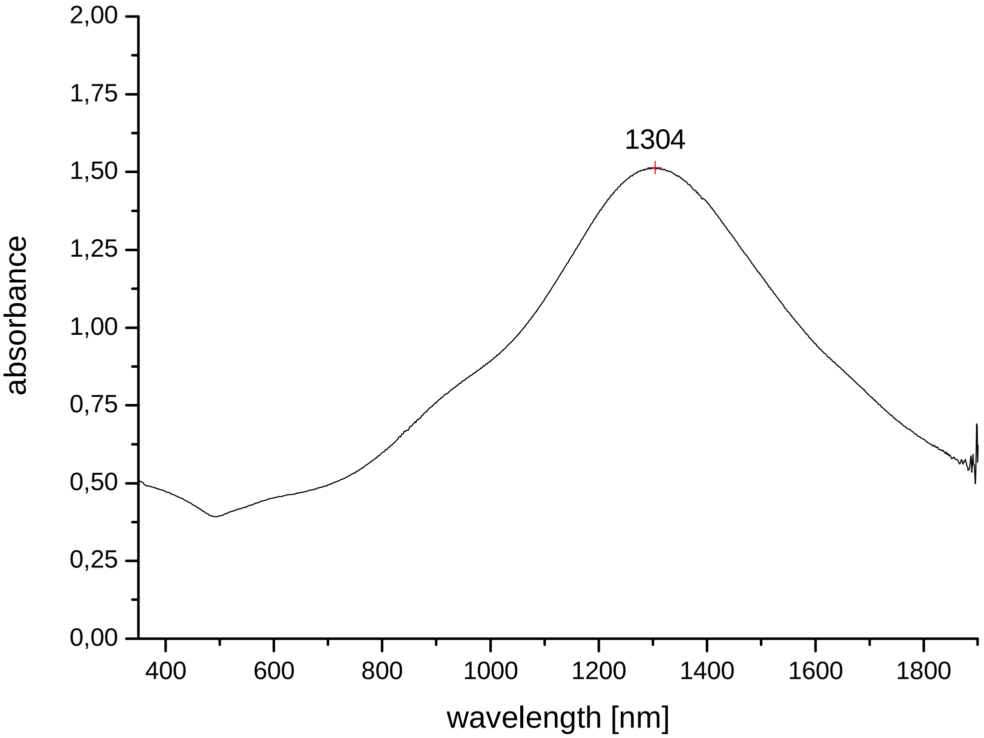

Figure 6.5: NIR absorption spectrum of gold nanocages in D_2O, measured on a UV-Vis-NIR spectrophotometer.

compared to the reference sample, i.e., hydrogel particles without GNs. No enhancement in absorption intensity was found for hydrogel particles in solution B (i.e., 5.6×10^{-12} M concentration of GNs) and obtained 3D absorption images were comparable to the 3D absorption images of the reference sample (i.e., without GNs) (see **Figure 6.6A** and **B**). Interestingly, significant enhancement in absorption intensity was observed when concentration of GNs in the sample was increased to 1.4×10^{-11} M (solution C) (see **Figure 6.6C**, second column). Similarly, consequential increase in absorption intensity can be detected when hydrogel particles with 1.8×10^{-11} M concentration of GNs (solution D) were measured (compare **Figure 6.6A** with **6.6D**, right column). Interestingly, even at higher concentrations of GNs, enhancement in absorption intensity was not observed for all hydrogel particles measured; specifically, only four and three particles (out of eight measured) were found to exhibit enhancement in absorption intensity in solution C and D, respectively. The rest of the measured particles show absorption intensity values that are comparable to hydrogel particles without the addition of gold nanocages (compare **Figure 6.6 A-D**, left column).

Similar results as presented in the preceding paragraph were found when absorption spectra, calculated from the 2D NIR images, of individual hydrogel particles from solution A (no GNs added), B (5.6×10^{-12} M), C (1.4×10^{-11} M) and D (1.8×10^{-11} M) were investigated. **Figure 6.7** shows absorption spectra of several individual hydrogels in solution with different concentrations of GNs; i.e., 5.6×10^{-12} M (**B**), 1.4×10^{-11} M (**C**) and 1.8×10^{-11} M (**D**). Spectra in red represent absorption of hydrogel particles with GNs, whereas blue spectra are for hydrogel particles without GNs. Specifically, in the first column all spectra are plotted together (eight for particles without GNs and eight for

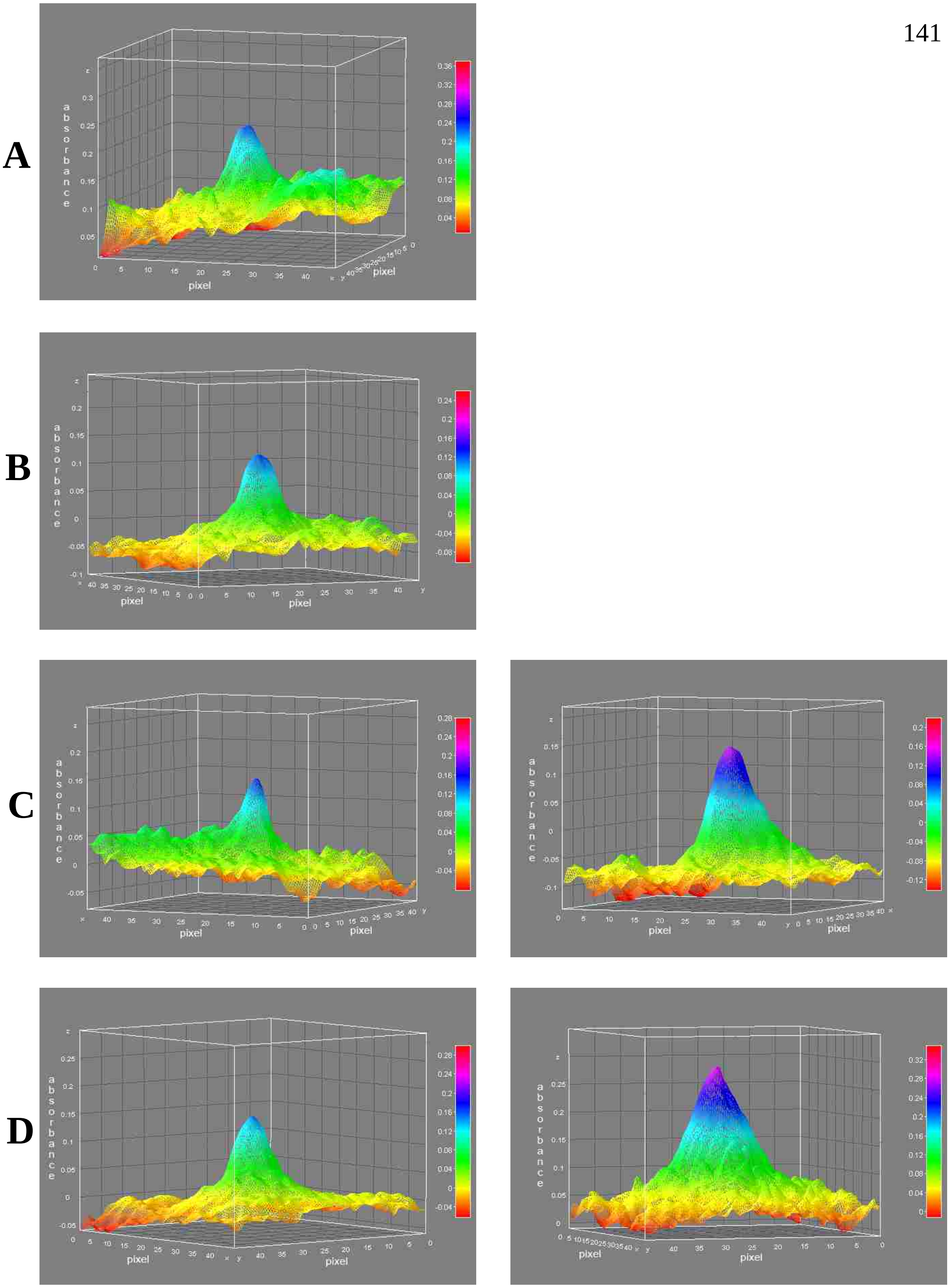

Figure 6.6: 3D absorption images of a single hydrogel particle in solutions with different concentrations of GNs: without GNs (A), with 5.6×10^{-12} M GNs (B), 1.4×10^{-11} M (C) and 1.8×10^{-11} M (D). Images on the left column are for unenhanced hydrogel and images on the right column are for enhanced hydrogel particles.

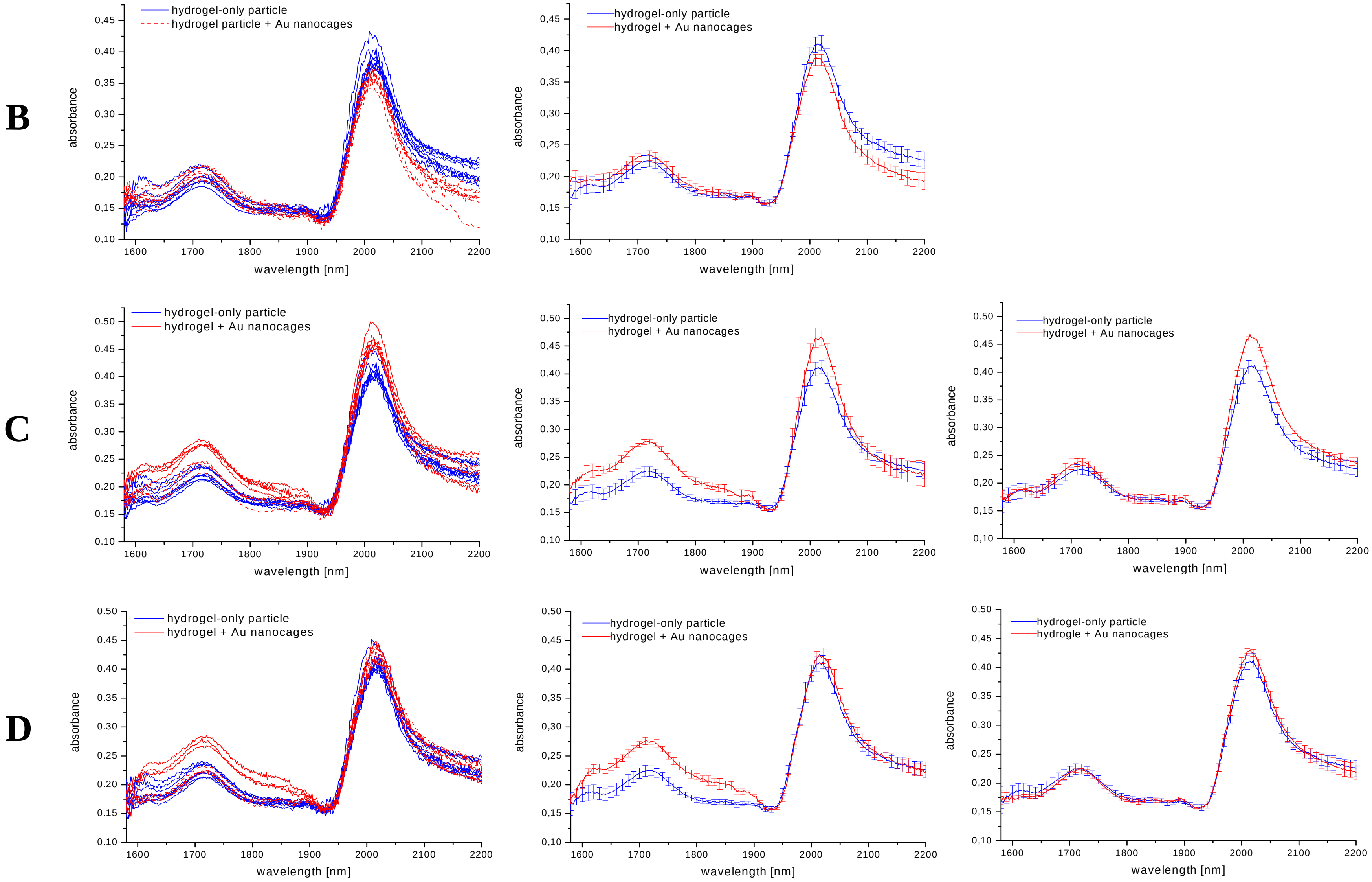

Figure 6.7: Absorption spectra, in red, of several individual hydrogel particles in solution with different concentrations of GNs: (B) with 5.6×10^{-12} M GNs, (C) 1.4×10^{-11} M and (D) 1.8×10^{-11} M. Spectra in blue are those of individual hydrogel particles without GNs.

particles with GNs). As can be observed, no significant difference in absorption intensity can be observed by comparing the absorption spectra of hydrogel particles in solution B to the absorption spectra of the reference sample (i.e., without GNs) (see **Figure 6.7B**, first column). Conversely, some of the absorption spectra of hydrogel particles from solution C and D exhibit substantial enhancement in absorption intensity compared to the reference hydrogel particles without GNs (blue) (see **Figure 6.7C-D**, first column). The absorption spectra of remaining hydrogel particles with GNs correspond well to the absorption spectra of hydrogel particles without the addition of GNs. These observations become more pronounced when averaged absorption spectra are plotted together. Subsequently, **Figure 6.7** (second and third column) show averaged absorption spectrum for enhanced particles (red) and averaged absorption spectrum for unenhanced particles (blue), respectively. That is, averaged spectra of hydrogel particles with GNs in second and third column are compared to averaged spectrum of hydrogel particles without GNs (blue).

As can be observed from both, **Figure 6.6** and **6.7**, not all of the hydrogel particles with GNs exhibit enhancement in absorption. The obtained results are most probably due to the lower concentration of the GNs in the sample solution compared to the concentration of hydrogel. Specifically, concentration of hydrogel was estimated to be in the 10^{-7} to 10^{-8} M range whereas concentrations of the GNs in the sample solutions were many magnitudes lower, i.e., less than 1.8×10^{-11} M. Therefore it is expected that only hydrogel particles which associate directly with GNs would exhibit enhancement in absorption intensity. Moreover, it seems that GNs have significantly more pronounced effect on absorption intensity of the 1716 nm band (compared to the absorption band at □

2010 nm) which is most probably due to the fact that the band at 1716 nm is attributed to C-H groups, which are specific to the hydrogel particles, whereas 2010 nm absorption band is attributed to O-D overtone transitions in D_2O.

As detailed in Chapter 5, the size and chemical structure of hydrogel particles have a significant effect on the volume transition temperature. It would, therefore, be particularly interesting to investigate LCST properties of hydrogel particles with GNs. As observed in Chapter 5 and seen from 2D NIR and 3D absorption images in **Figures 6.8-9**, hydrogel particle (without GNs) undergoes substantial decrease in dimensions as well as in absorption upon heating. Specifically, a particle is well focused and exhibits relatively constant absorption intensity until 34.5 °C after which a sharp decrease in absorption, as well as defocusing and reduction in dimensions of the particle can be observed. That is, absorbance of the hydrogel particle decreased by 69% of its initial value when it was heated to 57.5°C (i.e., from an absorbance of 0.42 to 0.13). When cooled back to the room temperature, the hydrogel recovered its absorbance (not shown).

Conversely, when an individual hydrogel particle with GNs from solution C (1.4×10^{-11} M), that exhibits enhancement in absorption, is heated from room temperature (23.0 °C) to 57.5 °C, a different response compared to the hydrogel particle without GNs can be observed (see **Figures 6.10-11**). Specifically, the hydrogel particle is clearly visible throughout the whole temperature range and the absorption intensity seems to decrease linearly and relatively slowly compared to that for the hydrogel without GNs. Indeed, when heated to 57.5 °C the absorbance was decreased only by 27% which is about 2.5 fold less compared to that in the absence of GNs. Interestingly, when cooled back to room temperature, the absorption intensity seems to be increase to its initial

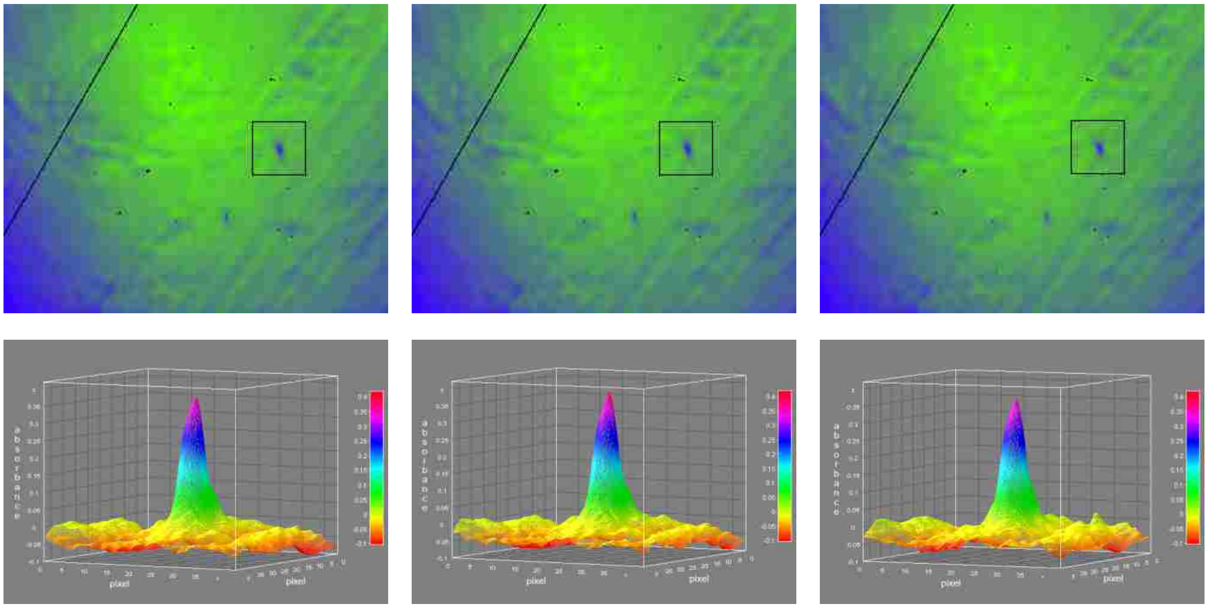

24.0 ˚C 25.6 ˚C 29.6 ˚C

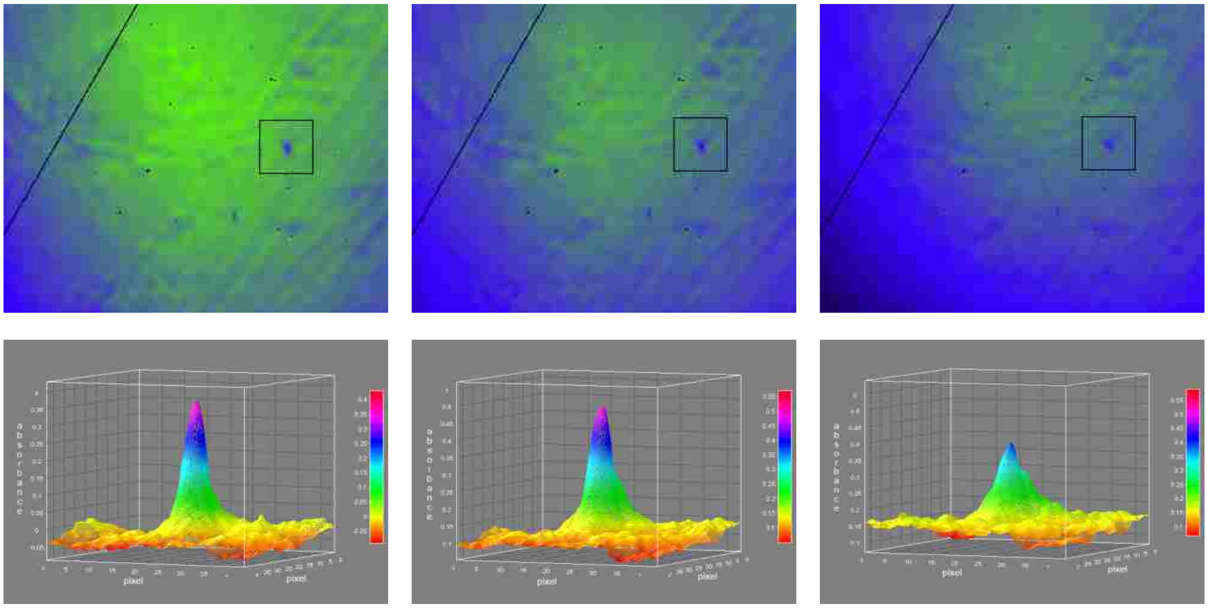

31.3 ˚C 34.5 ˚C 39.7 ˚C

Figure 6.8: 2D images and corresponding 3D images of absorption at 1764 nm of the same single hydrogel particle (without GNs) at different temperatures. (See detailed description in the text).

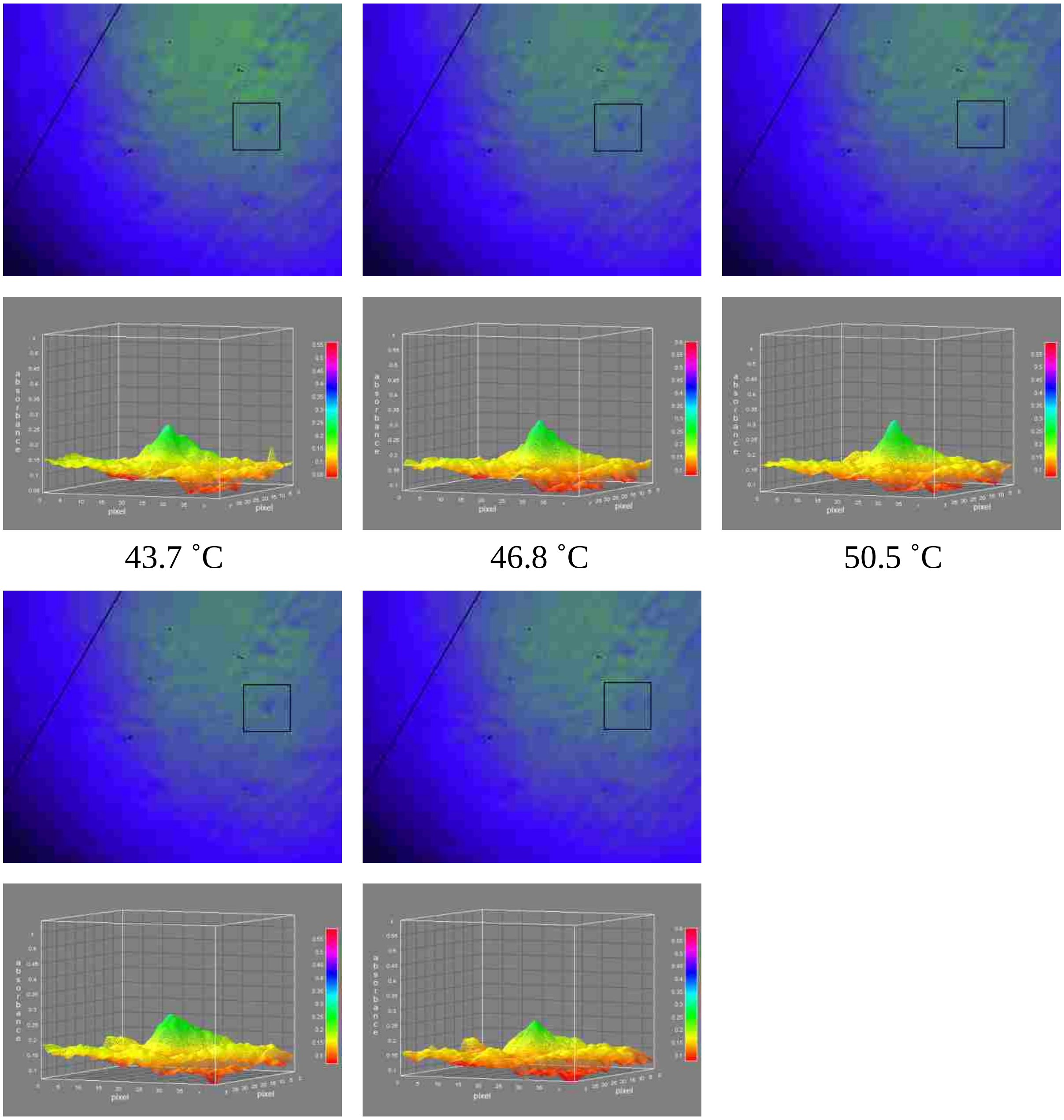

43.7 ˚C

46.8 ˚C

50.5 ˚C

53.6 ˚C

57.5 ˚C

Figure 6.9: 2D images and corresponding 3D images of absorption at 1764 nm of the same single hydrogel particle (without GNs) at different temperatures. (See detailed description in the text).

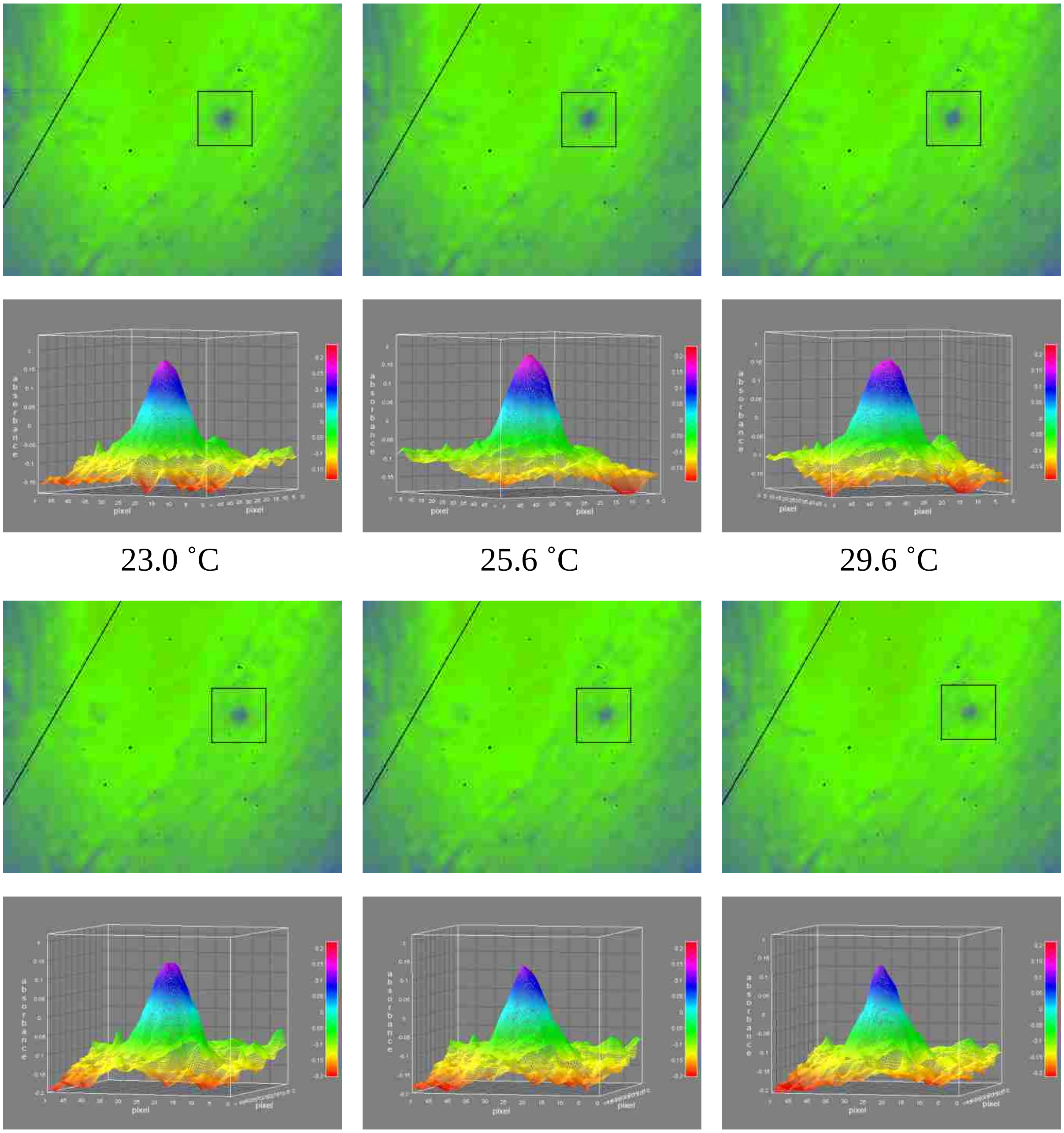

23.0 ˚C

25.6 ˚C

29.6 ˚C

31.3 ˚C

34.5 ˚C

39.7 ˚C

Figure 6.10: 2D images and corresponding 3D images of absorption at 1764 nm of the same single hydrogel particle (with GNs) at different temperatures. (See detailed description in the text).

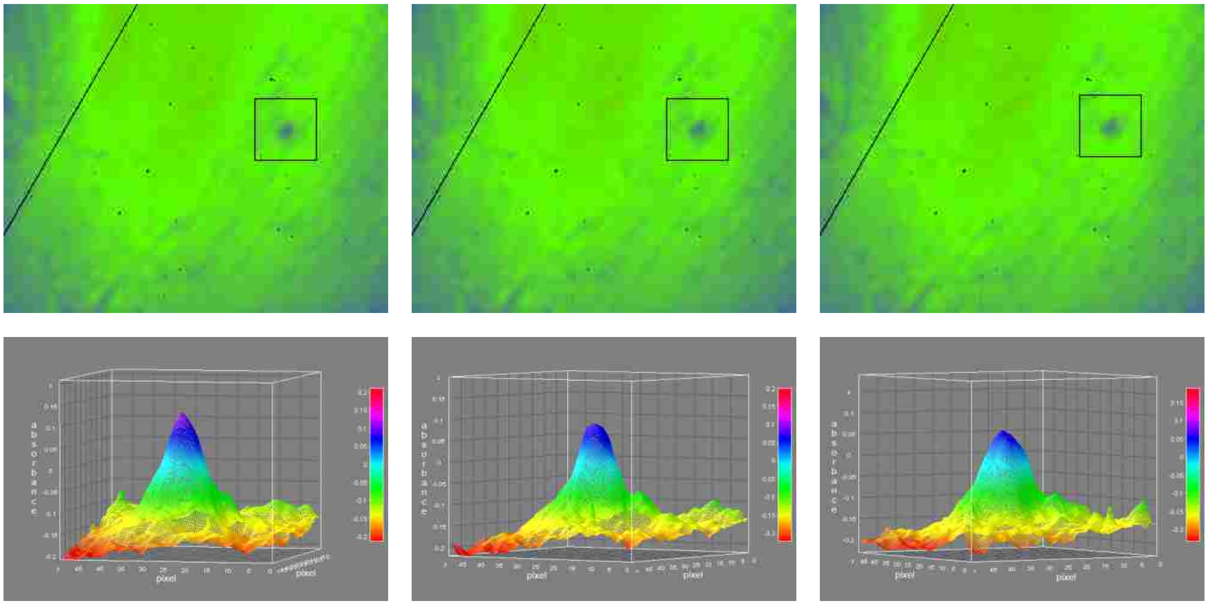

43.7 ˚C 46.8 ˚C 50.5 ˚C

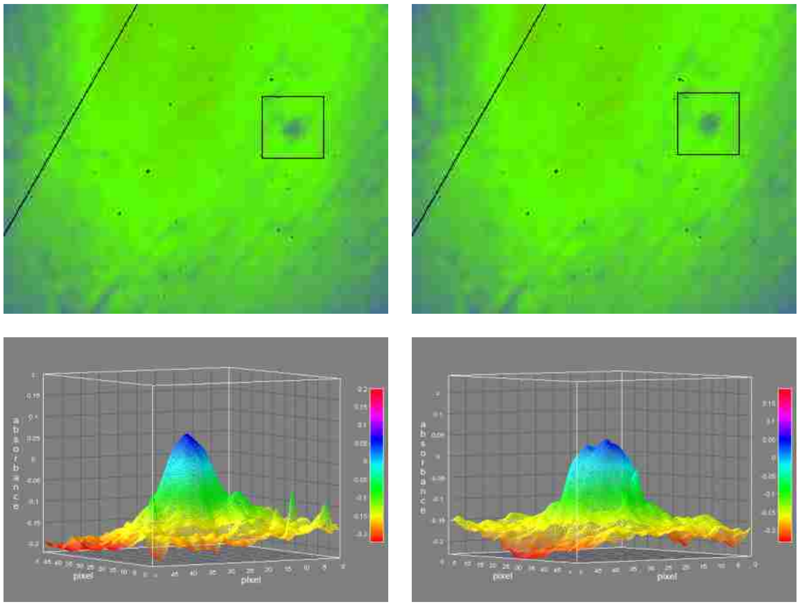

53.6 ˚C 57.5 ˚C

Figure 6.11: 2D images and corresponding 3D images of absorption at 1764 nm of the same single hydrogel particle (with GNs) at different temperatures. (See detailed description in the text).

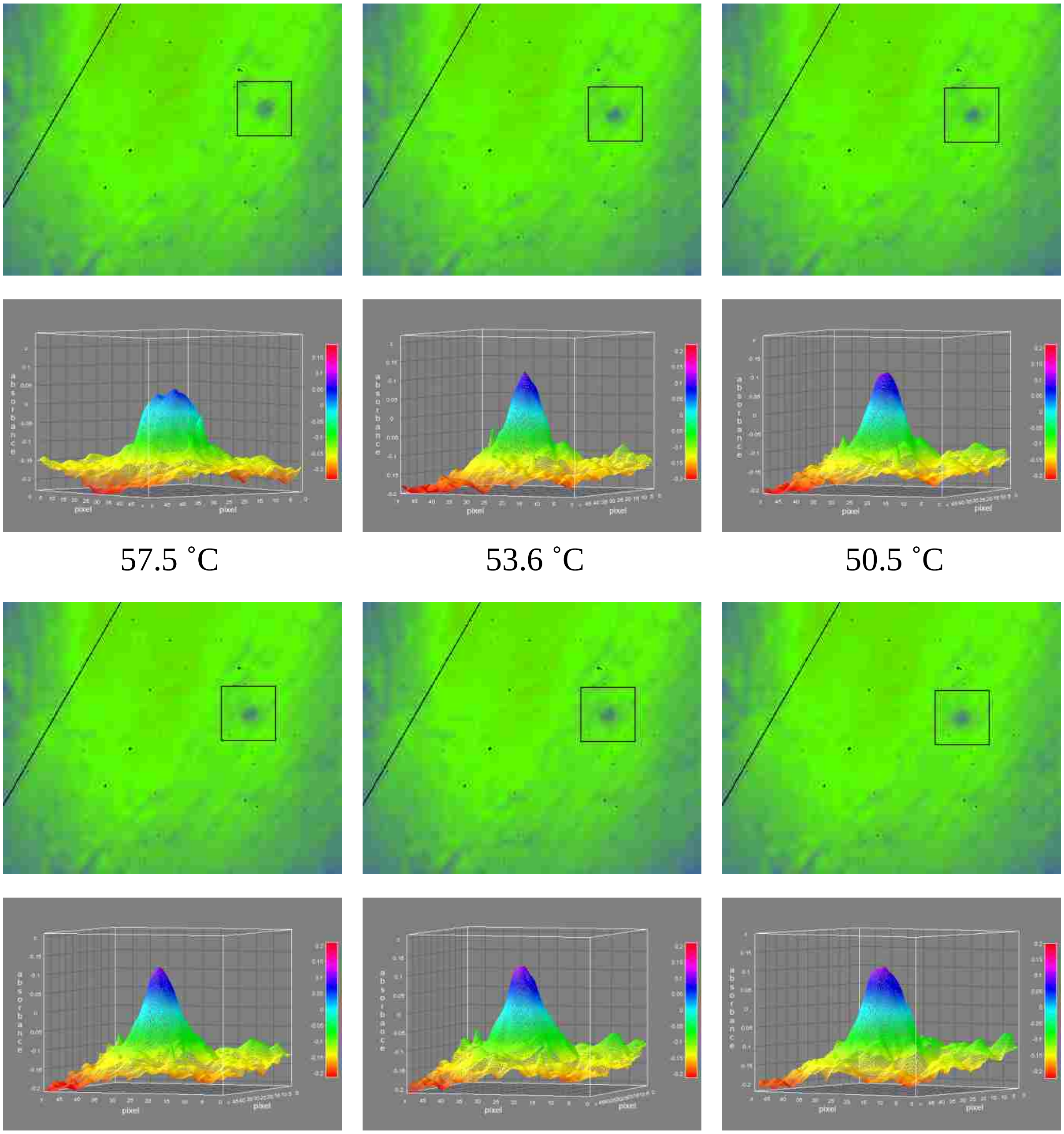

57.5 ˚C 53.6 ˚C 50.5 ˚C

46.8 ˚C 43.7 ˚C 39.7 ˚C

Figure 6.12: 2D images and corresponding 3D images of absorption at 1764 nm of the same single hydrogel particle (with GNs) at different temperatures. (See detailed description in the text).

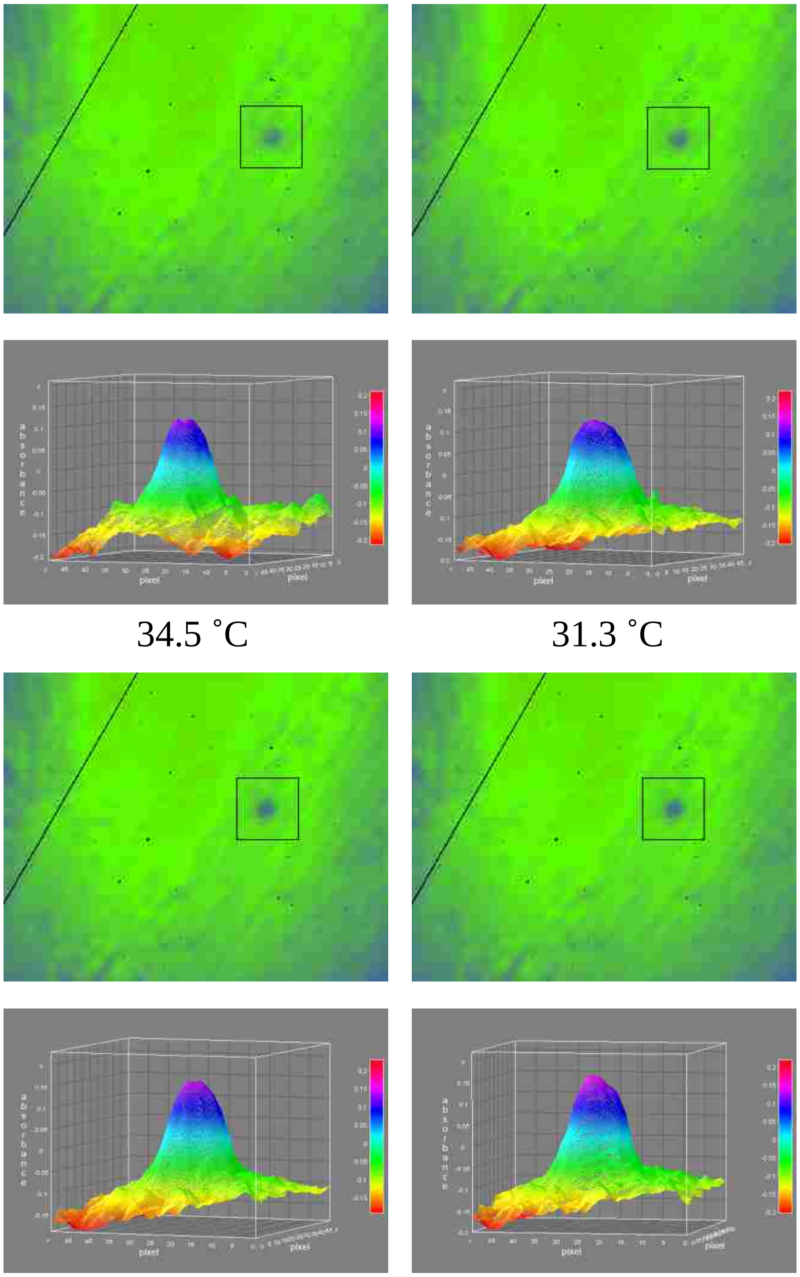

34.5 ˚C

31.3 ˚C

29.6 ˚C

25.6 ˚C

Figure 6.13: 2D images and corresponding 3D images of absorption at 1764 nm of the same single hydrogel particle (with GNs) at different temperatures. (See detailed description in the text).

value, thereby indicating that the reversibility of the swelling-deswelling behavior is preserved when GNs are added to the hydrogel sample (see Figures **6.12-13**).

Since 2D NIR and 3D absorption images provide information only at one specific wavelength (i.e, 1764 nm), it is more informative to investigate spectral data throughout the whole spectral range (1580 nm to 2200 nm) in order to obtain additional knowledge about the effect of GNs on the LCST transitions. Consequently, absorption spectra of hydrogel particle without GNs and hydrogel particle with GNs at different temperatures were plotted (see **Figure 6.14A** and **B**, respectively). As seen from the upper two graphs in **Figure 6.14**, in both cases (i.e., without and with GNs) the absorption spectra is blue shifted and a decrease in absorption intensity can be observed with increasing temperature. Additionally, the absorption band at around 1900 nm, attributed as a hot band of the O-D groups of hydrogel particle in D_2O,[137] becomes more pronounced upon heating. Interestingly however, the decrease in absorption intensity is more obvious in the former case; that is, when hydrogel particle without GNs was measured. These observations are even more noticeable when only two absorption spectra (at room temperature and 57.5 °C) are plotted together (see **Figure 6.14**, lower graphs). In order to explore the LCST transitions of hydrogel particles with GNs further, λ_{max} values as a function of temperature were plotted for hydrogel particle without and with GNs (**Figure 6.15A** and **B**, respectively). In case of hydrogel particle without GNs, a sharp blue shift can be observed when temperature is increased above 35 °C, whereas relatively constant λ_{max} values are resumed at approximately 48 °C. Therefore, the volume transition temperature (obtained from second derivative) can be determined and found to be 42±2 °C.

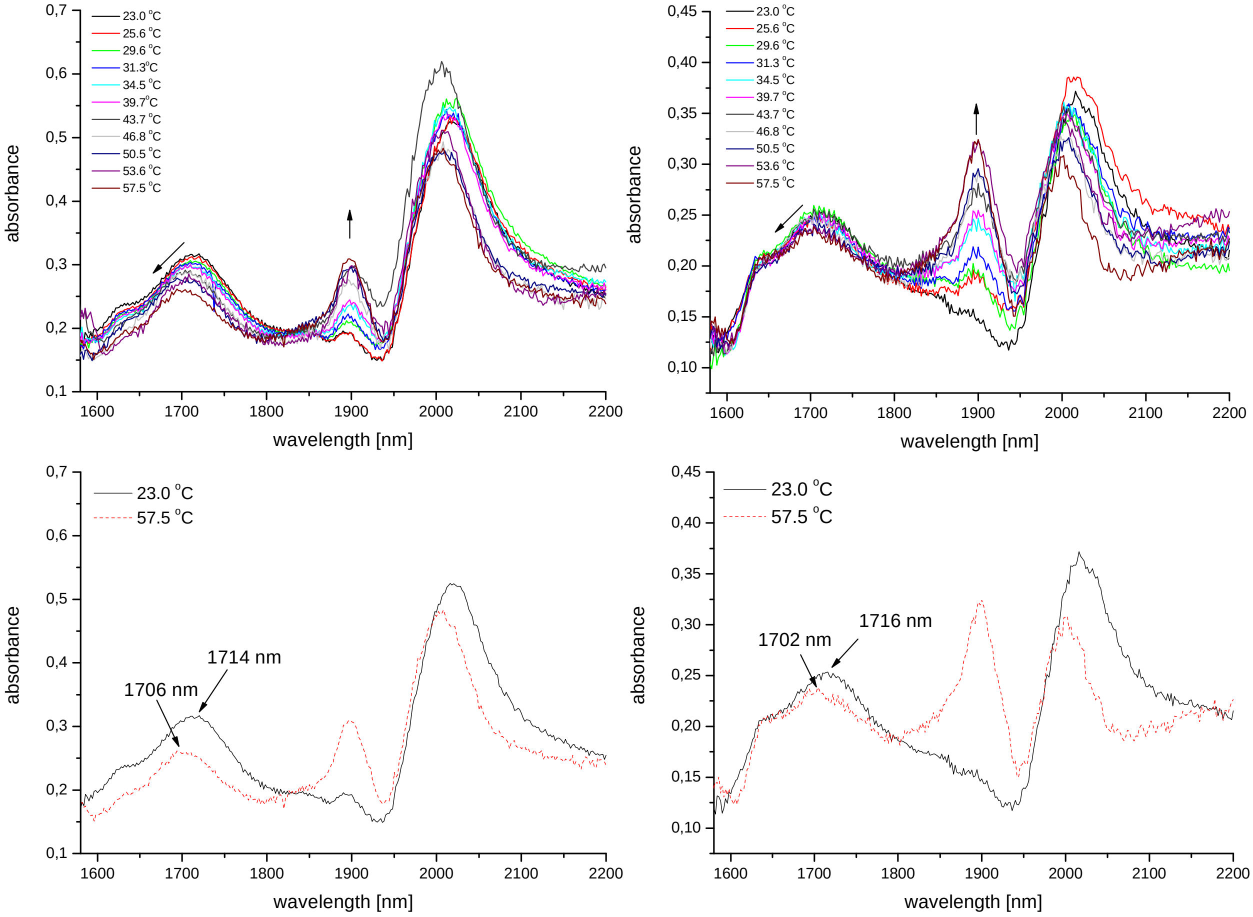

A **B**

Figure 6.14: Absorption spectra of a single hydrogel particle in D_2O without GNs (A) and with 1.8×10^{-11} M of GNs (B), at different temperatures. Lower plots (A and B) are comparison of the absorption spectra at final and initial temperatures for hydrogel particle without (A) and with GNs (B), respectively.

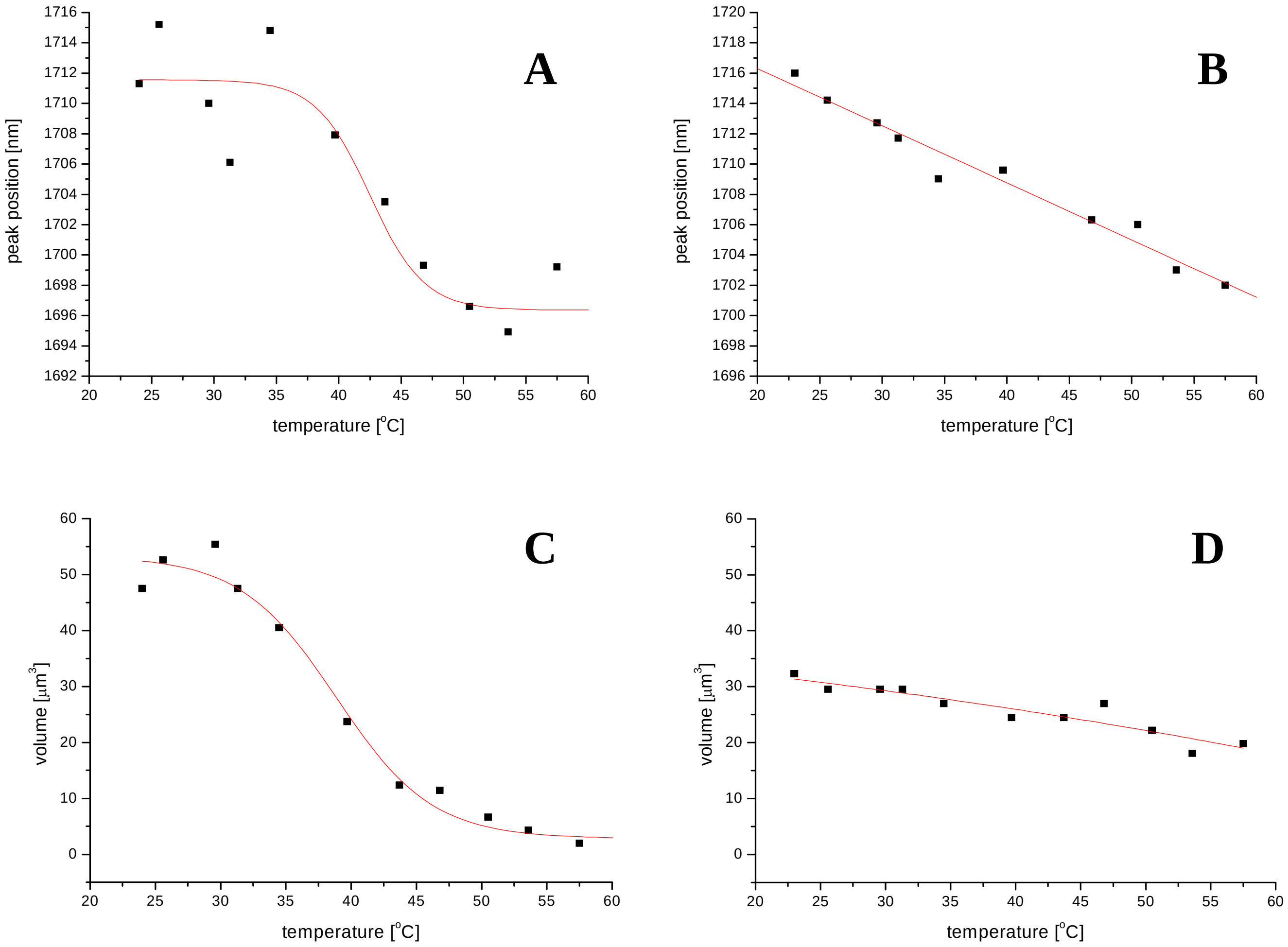

Figure 6.15: Plots of (A and B) λ_{max} of the C-H band and (C and D) change in volume of the same single hydrogel particle without (A, C) and with 1.8×10^{-11}M of GNs (B and D) as a function of temperature.

On the other hand, λ_{max} values plotted as a function of increasing temperature, for hydrogel particle with GNs, results in relatively linear shifts towards lower wavelengths (see **Figure 6.15A** and **B,** respectively). Specifically, throughout the whole heating range, no distinctive sharp decline towards lower wavelengths was observed.

Additionally, effect of GNs on the volume transition properties of hydrogel particles can be investigated when volume of the individual particles is plotted as a function of temperature. As can be elucidated from **Figure 6.15C**, a hydrogel particle (without GNs) shrinks rapidly in temperature range between 33 °C and 45 °C, and thereafter remains relatively stable in size. Equivalently to the procedure described in the preceding paragraph, the volume transition temperature was determined to be 39±4 °C. It is satisfying to observe that transition temperatures, within the experimental errors, obtained from two different methods correlate very well. Likewise, good correlation between two different methods for transition temperature determination was found when hydrogel particle with GNs was measured (see **Figure 6.15D**). Essentially, no transition temperature but rather gradual and linear decrease in volume as a function of temperature can be observed. The disappearance of the phase transition temperature for hydrogel particles with added GNs might possibly be due to the absorption of GNs which would consequently result in generation of heat and vapor bubbles around GNs. Hence, the vapor bubbles can act as a thermal insulator, and have defocusing effect on the hydrogel particles.

6.4 CONCLUSION

In summary, near-infrared multispectral imaging technique can be successfully used for characterization of poly(NIPAM-co-AAc) hydrogels with gold nanocages added to the sample. Moreover, images of individual particles can be recorded using this technique. As a consequence, significant increase (i.e., 25 %) in absorption intensity of individual hydrogel particles, when gold nanocages are added to the sample, can be observed. Due to the fact that only a portion (50 and 37.5 %) of measured hydrogel particles exhibited absorption enhancement, such improvement in absorption of hydrogel particles could not be observed with conventional single channel spectrophotometers. These results (i.e., approximately 50 % samples which exhibit enhancement) are most probably due to lower concentration of the GNs, compared to the hydrogel concentration. Thus, it is expected that only a portion of the hydrogel particles would interact with GNs. Furthermore, the results indicate different volume transition behavior between the hydrogel with and hydrogel particles without GNs. Specifically, no transitions, but rather gradual and linear response are observed in the former case (i.e., with GNs) whereas the latter (i.e., hydrogel particles without GNs) exhibit distinct volume transition as a function of temperature. The obtained results seem to indicate that hydrogel particles with GNs lose LCST when affected by GNs.

CHAPTER 7

EXPLORING THE APPLICATION OF NEAR-INFRARED MULTISPECTRAL IMAGING TECHNIQUE FOR DETERMINATION OF BASAL CELL CARCINOMA, SQUAMOUS CELL CARCINOMA AND SEBORRHEIC KERATOSIS

7.1 INTRODUCTION

Skin cancers are separated into two groups: melanoma and non-melanoma. There are several types of non-melanoma skin cancers, however, the most common representatives of this group are Basal Cell Carcinoma (BCC) and Squamous Cell Carcinoma (SCC). According to the American Cancer Society, more than two million cases of non-melanoma skin cancers are reported annually in United States.[138] For comparison, 68,130 cases of melanoma were reported in year 2010.[138] BCC, which represents 75% of total classified skin cancers,[138] is the most common type of non-melanoma skin cancers. Cumulative ultraviolet (UV) exposure (especially when exposure to the UV light results in severe sunburns), fair complexion, older age and male gender, occupational exposure to carcinogens, and genetic susceptibility, are risk factors for BCC.[139-141] Most commonly, BCC cancers occur on the neck and head region, especially nose; that is, on hair-bearing and not on mucosal surfaces.[142,143] BCCs start growing from the lowest layer of epidermis, also called basal cell layer. In the early stages, they appear as small, dome shaped bumps, which are often covered by small superficial blood vessels.[142,143] The growth of the BCC is unpredictable, i.e., it usually progresses slowly, taking months, or years, to become sizeable, however, it may also grow rapidly with consecutive outbursts of extension of the tumor.[142,143] BCCs are rarely metastatic, however, they can be locally invasive, and if left untreated, can slowly spread to surrounding tissue.[143,144] It is often difficult to recognize Basal Cell Carcinomas from benign growth (i.e., moles), therefore, partial or complete biopsy of the growth is required for correct diagnosis.[142,143]

Squamous Cell Carcinoma (SCC) is a malignant tumor that starts growing from epidermis, specifically from keratinocytes of the skin or mucosal surfaces.[142,145] Appearance of the earliest stage of Squamous Cell Carcinoma resembles rough, red bumps on the scalp, face and ears.[142,145] Numerically, SCC represents a much smaller percentage (approximately 20%) of all non-melanoma cancers,[138] however, the importance of early detection and treatment is probably greater compared to the Basal Cell Carcinomas. That is due to the fact that SCC can reoccur and **metastasize** more easily than BCC, especially in cases of deeper and larger tumors (i.e., larger than 2 cm and deeper than 6 mm), and are, therefore, responsible for the majority of deaths by non-melanoma skin cancers.[142,145] Particularly prone to the metastatic growth is the location of lower lip.[141,146] Similarly to BCC, they are most commonly found on the neck and head areas, with most important risk factor being exposure to solar radiation.[141,142,146]

Seborrheic Keratosis (SK) is a noncancerous (benign) form of a skin tumor.[143] They are of unknown origin and have no malignant potential.[143] SKs appear as smooth, round embedded beads, or rough, dry and cracked growths; and their dimensions can vary between 0.2 cm and more than 3 cm in diameter.[143] Due to the similarity with malignant tumors, it is important to differentiate between all the variations and characteristics of SKs, in order to prevent unnecessary destructive procedures. They usually do not require any treatment and can be easily and quickly removed.[143]

Presently, the classification of a skin lesion (either to a specific tumor, or just determination if the lesion is benign/malign) is performed by a pathologist/dermatologist. First, the biopsy is performed, and afterwards the pathological samples are stained in order for the tissue content to be observed through the visible microscope. Gniadecka *et al.* (1997) reported that up to 50% of early malignant lesions may not be detected during a routine clinical examination.[147] Furthermore, experts, using invasive and expensive determination techniques, achieve only 80 to 90% accuracy in classification of malignant tumors.[147] It is, therefore, highly desirable to develop non-invasive, fast, non-expensive and reliable (even at early tissue diagnostics) methods of classification of malignant skin lesions. Near-infrared (NIR) multispectral imaging microscopy, through absorption spectra, could be used for classification of tumor samples. The use of NIR spectroscopy is preferred over the use of visible and IR spectroscopy because it provides rich information of the measured samples throughout the whole NIR region (i.e., C=O, O−H, N−H overtones and combination bands of the IR fundamental vibrations are seen).[148] Furthermore, due to the shorter wavelengths and more energy-rich protons, NIR light penetrates animal and human tissue easily and more in depth, which is of high importance for biological applications.[148] Consequently spectral information about epidermal and dermal skin layers can be obtained.[149-151] This method also provides simplified sample preparation procedure of histopatological samples, i.e., no staining of the samples is required.

Due to the complexity of the NIR absorption spectra, small intensities of the absorption bands, and similarity of the absorption spectra, implementation of statistical processing tools is used in order to reduce the data complexity and illuminate the features that have a significant effect on the distinguishability of the measured samples.[152] Principal Component Analysis (PCA), Linear Discriminant Analysis (LDA) and Partial Least Square Discriminant Analysis (PLSDA) are commonly used techniques for data classification and dimensionality reduction.[152-157] PLSDA analysis is usually performed in order to increase separation between different groups, by rotating principal components (i.e., uncorrelated variables that account for most of the variance in the observed variables) in such a way that the maximum distinguishability between observed groups can be obtained. It is based on the PLS (Partial Least Square) model[158] where a dependent variable is chosen to represent the group membership. That is, known values are given to the dependent variables (in cases, when two groups are to be classified, these values are usually 1 and -1 or 0).[159] LDA method is similar to PLSDA in that it produces similar results in cases when the number of analyzed samples extents the dimensionality of the data set. LDA method determines discriminatory function that maximizes the variance in the data between different groups and minimizes the variance within the same group.[153,154,160] Specifically, LDA aims to differentiate between analyzed groups on the basis of characteristics (i.e., discriminant variables) that are specific for each group. For the purpose of classification, mathematical equations called discriminant functions are therefore derived.[153] The prime difference between LDA and PCA is that LDA performs data classification, as opposed to PCA, which operates more on the feature classification. Specifically, in PCA, shape and location of the original is adjusted when transformed to a different space whereas LDA only provides more class separabilty and determines discriminatory regions between the given groups.[153]

As described in preceding section, up to 50% of early malignant lesions may not be detected by routine clinical examination, and even with the use of invasive techniques (i.e., biopsy and optical classification) at late stages of malignant tumor development, currently used techniques of detection prove not to be completely succesful.[142] Additionally, these techniques are expensive and time consuming. Therefore, new methods of classification of non-melanoma skin cancers are highly desirable, and the use of NIR imaging microscopy for such application was investigated in this experiment.

7.2 EXPERIMENTAL

7.2.1 Skin Samples

Histopatological samples were obtained from a certified laboratory. Specifically, they were fixed in formalin and afterwards embedded in paraffin. Usually samples for microscopic examinations are cut to 4-5 µm thickness, however, in our case, in order to increase the absorption intensity; samples with ten micron thickness were used. Tissue samples were stained using a mixture of hematoxylin and eosin dyes resulting in coloring of protein-rich regions pink and nucleic acid-rich regions blue. Tissue samples that were used in the study were mounted onto the commercially available microscopic slides and protected with the cover slips. Using optical microscopy, contrasted tissue samples were then classified based on cellular morphology as Basal Cell Carcinoma, Squamous Cell Carcinoma and Seborrheic Keratosis.

7.2.2 Instrumentation and data collection

The instrument developed for NIR studies of tissue samples is similar to the one used in Chapters 4 to 6, and is described in detail in Chapter 4. However, modifications to the instrument were made in order to obtain visual and corresponding NIR images of the analyzed samples. Essentially, the in-house build instrument which is shown in **Scheme 7.1** operates as follows: the incident beam from the halogen lamp can be spectrally split by a moveable IR long pass filter, thus producing an option of selecting visible light, together with the IR light, to be focused on the sample, or, when interested only in the NIR spectral data and images, blocking the visible light completely. In the former case (i.e., when visible and IR light are passing through the sample), the transmitted light from the sample and Cassegrain (acting as a reflective objective) is further split by the ZnSe window. Thus, the visible portion of light is diffracted to the visible camera (Moticam 2300, Motic, China), whereas the IR portion of the light is collected by NIR InSb focal plane array camera. Consequently, visible and corresponding NIR images of the same region of the sample can be obtained. Since microscopic anatomy of the sample tissue cannot be observed through the NIR images, this is necessary in order to accurately obtain spectral information for the desired region of interest. Tissue samples that were initially prepared for optical microscopy, i.e., they were mounted onto the commercially available microscopic slides and protected with the cover slips, were measured in the study. Spectral data were taken in the NIR region between 1580 and 2400 nm with 2 nm increments and measured at ten or less different regions per each tissue sample. Background data were obtained from the same microscopic slide as sample, but in the region without the tissue.

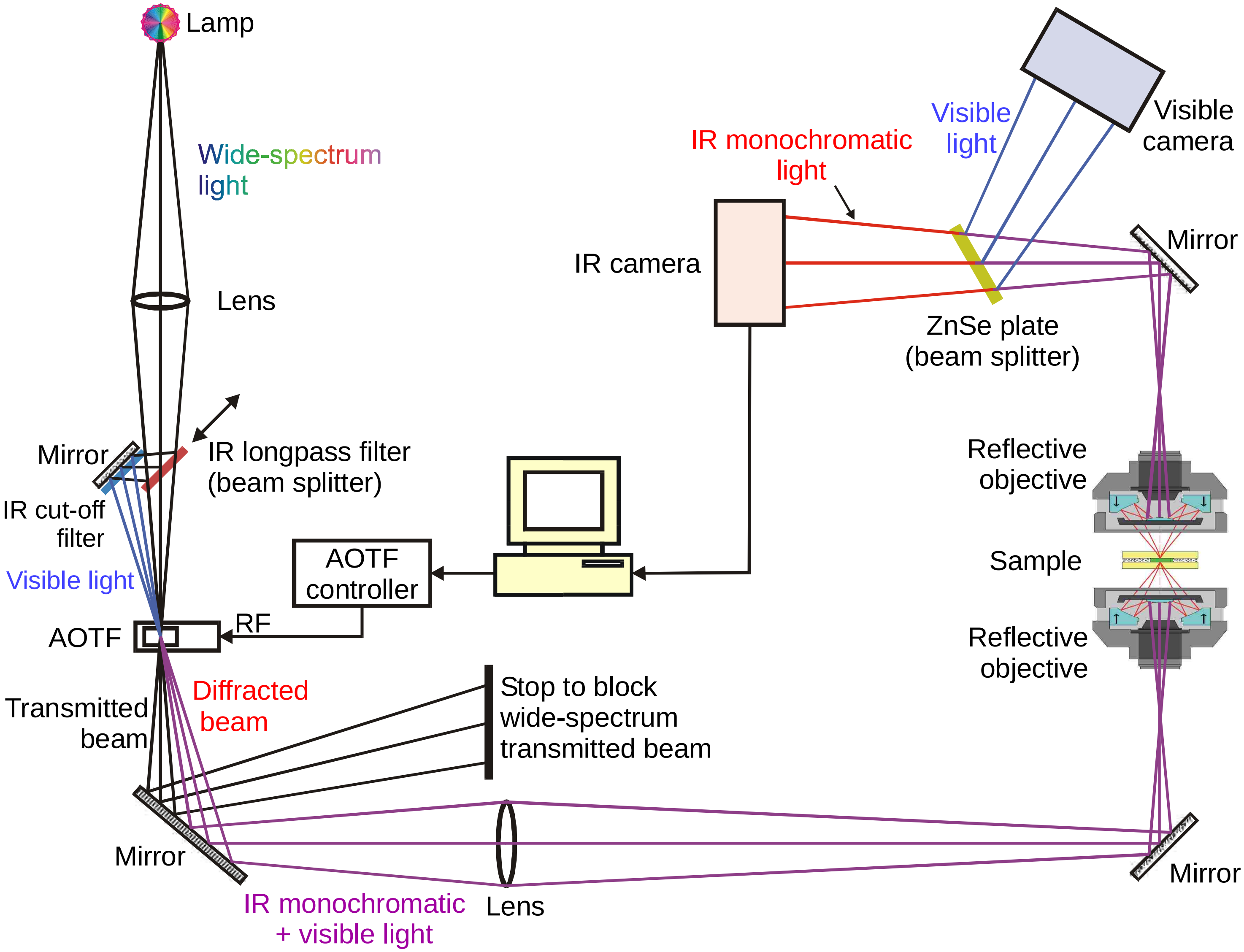

Scheme 7.1: NIR imaging microscopy instrument.

7.2.3 Statistical Analysis

Linear Discriminant Analysis (LDA) and Partial Least Square Discriminant Analysis (PLSDA) diagnostic algorithms were used to classify tissue samples into three separate groups, i.e., BCC, SCC and SK. PASW Statistics software (Version 18, IBM, Corporation, Somers, NY) was utilized for LDA model, whereas PLSDA was run using Unscrambler X (Version 10.1, CAMO Software AS, Oslo, Norway). In both cases, the entire spectral range (1580 – 2400 nm) was employed; therefore, each spectrum was represented as a set of 411 intensities (variables).

Each spectral data was normalized prior to classification with LDA, using the following equation:

$$\frac{x_i - \bar{x}}{\sqrt{\sum_{i=1}^{n}(x_i - \bar{x})^2 \big/ (n-1)}}$$

where x_i is absorption intensity at a specific wavelength for each tissue sample measured, $\bar{x}$ is averaged absorption intensity at a specific wavelength for one group (i.e., either BCC, SCC or SK) and n is number of tissue sample for each group. Stepwise discriminant analysis module with Wilks’ lambda was applied. Generalizability of the classification method was estimated using leave-one-out cross validation. Specifically, each case was extracted once and treated as test data, whereas the remaining cases were treated as a new dataset. In case of PLSDA classification, spectral data were preprocessed using algorithms available in the Unscrambler X software. Pretreatment of the data included unit vector normalization, noise reduction, and correlation optimized warping (i.e., alignment of the shifted data). Validity of the factor analysis was assessed using full cross validation, where a single case was selected as a test set (i.e., ungrouped data) and the remaining cases were selected as a training set (i.e., classified/grouped data).

7.3 RESULTS AND DISCUSSION

As described in experimental section, the instrument used in the study enables us to obtain NIR as well as visible images of the samples measured. Visible images and their corresponding NIR images (recorded at 1700 nm), with dimensions of 256×316 pixels, of tissue samples of BCC, SCC and SK are shown in **Figure 7.1A, B and C**, respectively. Visible images are presented in the first column, whereas NIR images are shown in the second column of the **Figure 7.1**. As can be observed, regions of the tissue samples that contain cells with nuclei and other elements of the skin can clearly be recognized on the visible images, whereas very little information about the microscopic anatomy of the investigated lesions can be directly observed in the NIR images. Therefore, it is necessary to refer to the corresponding visible images when obtaining the spectral information about the lesions. Specifically, regions of the lesions that had relatively uniform contents (i.e., mostly cells, as seen through the visible images) were selected for analysis and corresponding NIR images were recorded. Therefore, based on the visual images, we were able to determine, with certainty, the region of interests on the NIR images. Consequently, central areas from the NIR images, with dimensions of 101×101 pixels, were used in order to calculate the absorption intensity of the measured sample. The nature of the spectral data obtained by NIR multispectral imaging instrument is illustrated in **Figure 7.2A-B** (first column) which shows representative absorption spectra from each of the three groups, that is, BCC, SCC and SK, respectively. These three spectra

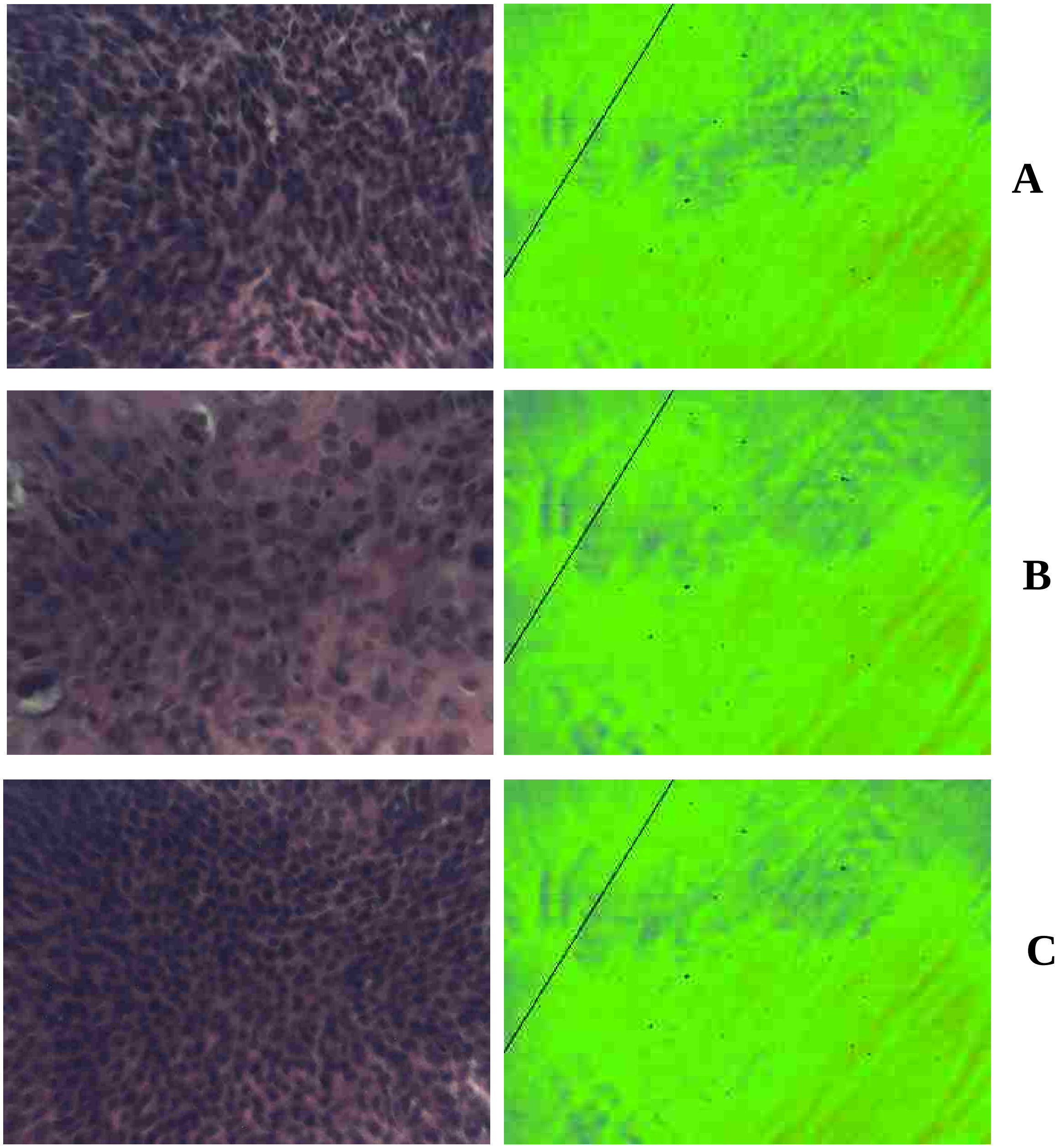

Figure 7.1: Visible and NIR images of BCC (A), SCC (B) and SK (C) tissue samples, (as seen through the microscope).

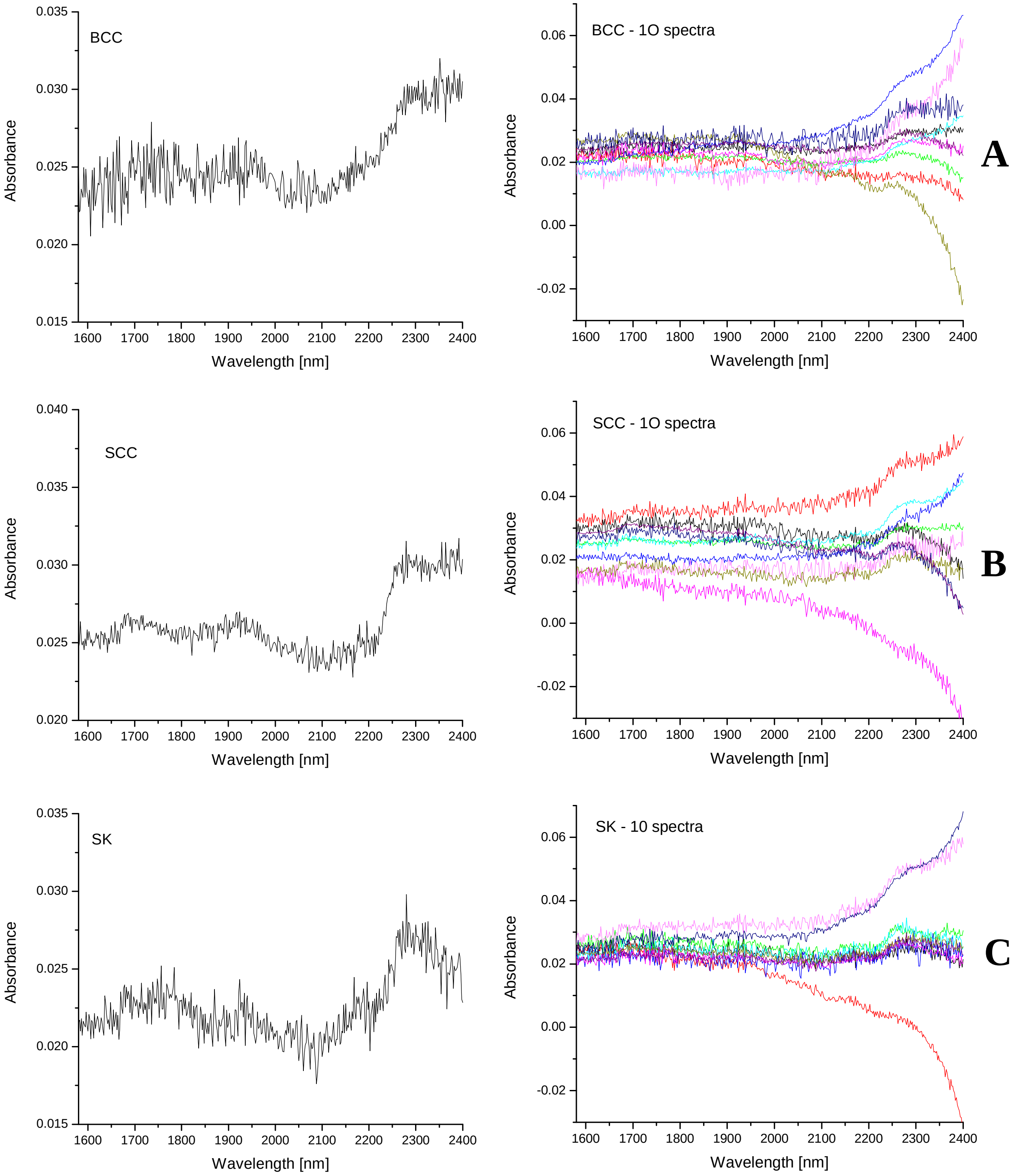

Figure 7.2: NIR absorption spectra of BCC (A), SCC (B), and SK (C).

exhibit relatively low absorption bands. Small absorption bands in region from 1700 to 1800 nm and at 2180 nm, as well as a more pronounced absorption band at around 2280 nm can be distinguished from all three graphs. In order to perform classification of the data based on the absorption spectra, a number of spectra are needed. Consequently, set of 165, 175 and 145 absorption spectra each were obtained for BCC, SCC and SK, respectively. In **Figure 7.2A-C** (right column) are plots of ten different absorption spectra (number of spectra reduced for easier observation) for BCC, SCC and SK, respectively. As can be observed, the absorption spectra differ, not only between separate groups of interest, but also within the same group (i.e., BCC, SCC or either SK). Specifically, the absorption bands are not only shifted but also vary in the intensity values. Furthermore, the general shape of the absorption spectra exhibit different patterns, especially at higher wavelengths (i.e., the general absorption intensity line either increases at higher wavelengths, remains relatively constant, or, in some cases exhibit decreasing pattern in the absorption intensity values). The reason behind the inconsistency of the spectral data at higher wavelengths might be due to low transmitted light intensity in this region (due to the high absorptivity). In order to obtain more general information about the spectral properties of the non-melanoma skin cancers (BCC and SCC) and SK, total absorption spectra for each group were normalized and averaged, and afterwards plotted in **Figure 7.3**. Interestingly, the averaged absorption spectra differ distinctively between BCC, SCC and SK with the most prominent difference occurring between the former two groups (i.e., BCC and SCC). Specifically, a small absorption band at around 1700 nm is visible for the SCC group, whereas the same band is not observed in averaged absorption spectrum of the BCC group. Similarly, an absorption

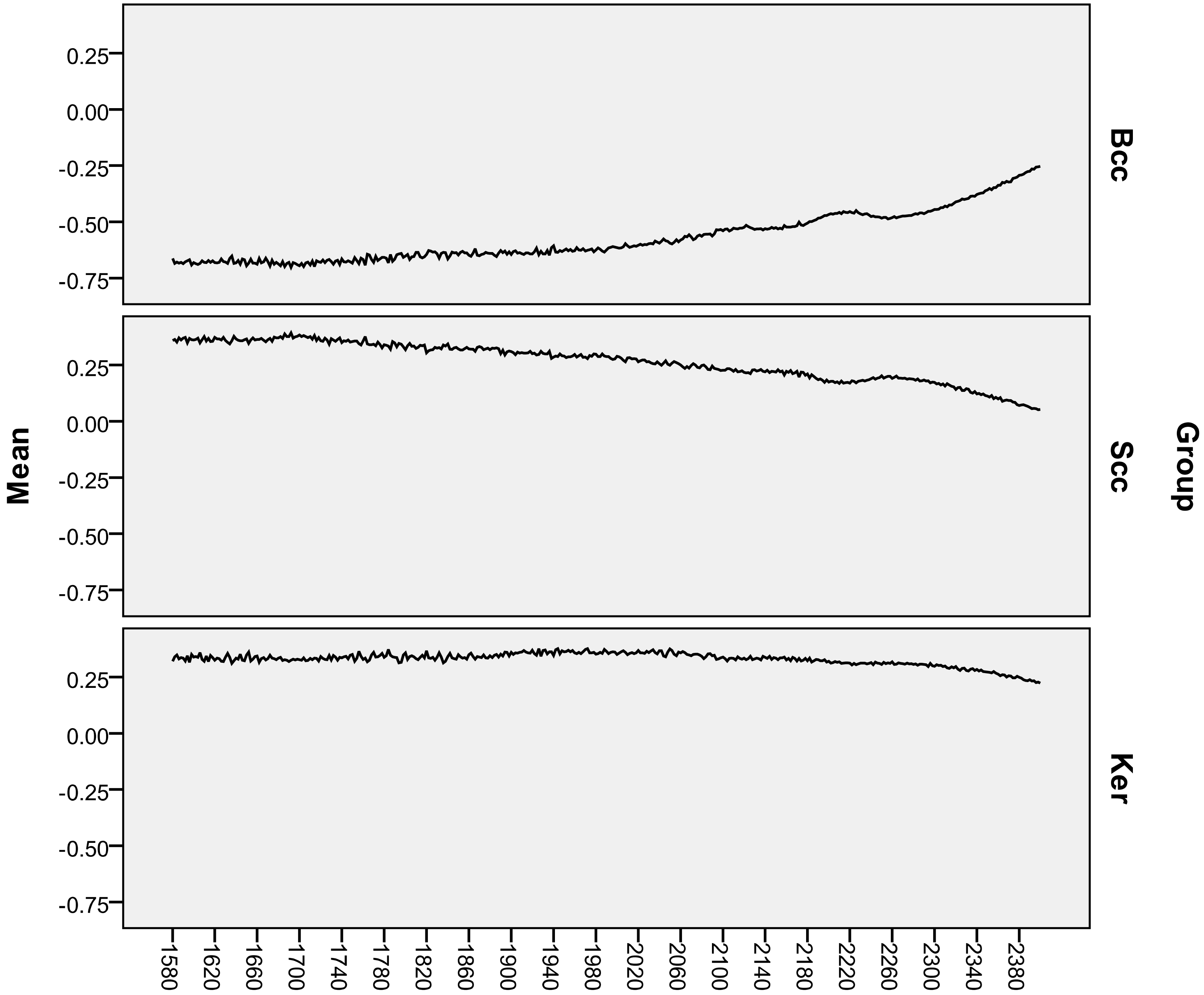

Figure 7.3: Averaged NIR absorption spectra of BCC (first row), SCC (second row), and SK (third row).

band at around 2250 nm can be seen for SCC, whereas this is not the case for BCC. On the contrary, an absorption band is visible at around 2200 nm in the averaged spectrum of BCC and not in the averaged spectrum of SCC. Compared to BCC and SCC, averaged spectrum for SK (Seborrheic Keratosis) has relatively constant absorption intensity throughout the whole wavelength region that was measured (i.e, from 1580 to 2400 nm), and provide less information about the spectral characteristics of the sample.

By carefully investigating the spectral data for all the measured lesions (individual and averaged) it seems that there are differences among three different groups: BCC, SCC and SK. However, due to the complexity of the NIR absorption spectra, small intensities of the absorption bands, and similarity of the absorption spectra, it is generally not possible to classify spectral data in separate groups or to identify fragments that vary most significantly between the samples by direct visual inspection. It is therefore necessary to utilize suitable statistical analysis techniques to reduce the data complexity and to extract features that can be used to distinguish different types of measured samples.[152]

Linear Discriminant Analysis is a commonly used technique for data classification. This method increases the ratio of between-group variance as opposed to the within-group variance, i.e. variance between different analyzed groups is maximized, resulting in maximized separation between groups. Due to the high dimensionality of spectral data, stepwise LDA was used. According to this method, at each step of the analysis, all eligible variables are considered for removal and entry, based on the respective F to enter and F to remove values. The F value for specific variable indicates its statistical significance in the discrimination between groups. Therefore, the dimensions of the data can be reduced by using only those variables that play a role in the discrimination between groups. 2D plot of spectral data classified into three groups (BCC, SCC and SK) is shown in **Figure 7.4**. Spectral data were obtained from 59 different tissue samples, and the total number of absorption spectra used in the analysis was 485; that is, 165 spectra for BCC group, 175 for SCC, and 145 absorption spectra for SK. As observed from the figure, data were successfully classified into three distinctive groups with significantly different groups' centroid positions. However, overlap of the data points between groups can be observed. Discrimination between groups is significantly increased when only two groups are compared to each other. **Table 7.1** represents classification results between BCC and SCC groups with SK. In former case, 94.5% and 91.7% of cross validated grouped data for BCC and SK, respectively, are correctly classified (**Table 7.1A**). When spectral data of SCC and SK are classified, the number of correctly classified cross-validated cases decreases to 83.4% and 81.4% for SCC and SK, respectively (**Table 7.1B**). The reason for lesser classification efficiency in the latter case is not clear at this time. It might be that some of the SCC lesions were in early stages of cancer development, and their spectral properties would, therefore, resemble benign tumor, such as Seborrheic Keratosis. Discrimination between malignant tumor groups, i.e. BCC and SCC combined as one group (i.e., cancer), was also investigated with results shown in **Table 7.2A**. The malignant tumor groups can be distinguished from benign group (SK) with 84.1% accuracy. The lower values in the classification accuracy in this case are most probably due to the variance in absorption spectra between BCC and SCC groups, which can be clearly observed when comparing averaged absorption spectra of both

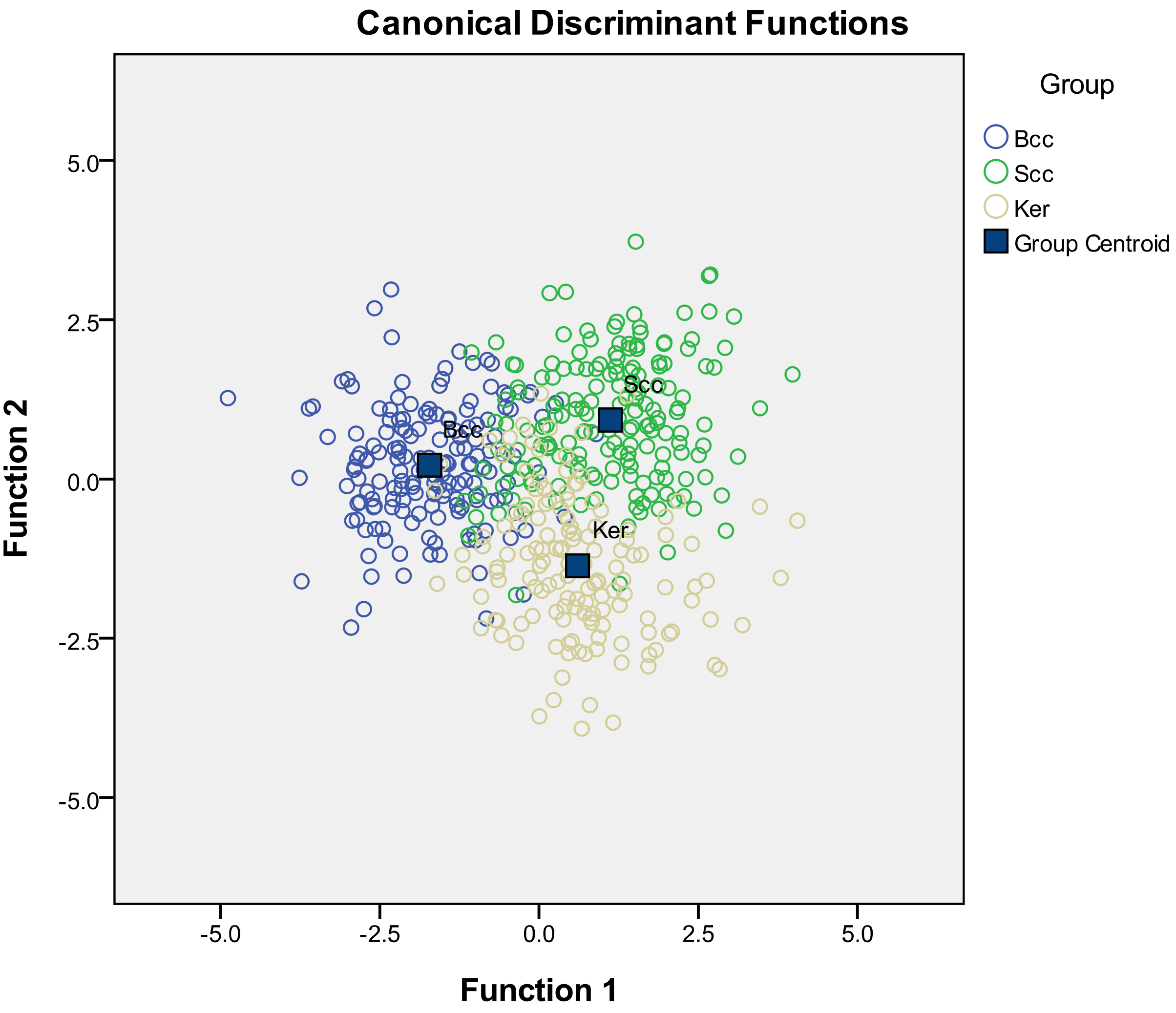

Figure 7.4: 2D plot of spectral data classified into three groups (i.e., BCC, SCC and SK).

Classification Results[b,c]

			Predicted Group Membership		
		Group	Bcc	Ker	Total
Original	Count	Bcc	162	3	165
		Ker	4	141	145
	%	Bcc	98.2	1.8	100.0
		Ker	2.8	97.2	100.0
Cross-validated[a]	Count	Bcc	156	9	165
		Ker	12	133	145
	%	Bcc	94.5	5.5	100.0
		Ker	8.3	91.7	100.0

a. Cross validation is done only for those cases in the analysis. In cross validation, each case is classified by the functions derived from all cases other than that case.

b. 97.7% of original grouped cases correctly classified.

c. 93.2% of cross-validated grouped cases correctly classified.

A

Classification Results[b,c]

			Predicted Group Membership		
		Group	Scc	Ker	Total
Original	Count	Scc	160	15	175
		Ker	9	136	145
	%	Scc	91.4	8.6	100.0
		Ker	6.2	93.8	100.0
Cross-validated[a]	Count	Scc	146	29	175
		Ker	27	118	145
	%	Scc	83.4	16.6	100.0
		Ker	18.6	81.4	100.0

a. Cross validation is done only for those cases in the analysis. In cross validation, each case is classified by the functions derived from all cases other than that case.

b. 92.5% of original grouped cases correctly classified.

c. 82.5% of cross-validated grouped cases correctly classified.

B

Table 7.1: Classification results – BCC and SK (A); SCC and SK (B).

Classification Results[b,c]

		Group	Predicted Group Membership		Total
			Cancer	Normal	
Original	Count	Cancer	303	37	340
		Normal	19	126	145
	%	Cancer	89.1	10.9	100.0
		Normal	13.1	86.9	100.0
Cross-validated[a]	Count	Cancer	286	54	340
		Normal	30	115	145
	%	Cancer	84.1	15.9	100.0
		Normal	20.7	79.3	100.0

A

a. Cross validation is done only for those cases in the analysis. In cross validation, each case is classified by the functions derived from all cases other than that case.

b. 88.5% of original grouped cases correctly classified.

c. 82.7% of cross-validated grouped cases correctly classified.

Classification Results[b,c]

		Group	Predicted Group Membership		Total
			Bcc	Scc	
Original	Count	Bcc	162	3	165
		Scc	7	168	175
	%	Bcc	98.2	1.8	100.0
		Scc	4.0	96.0	100.0
Cross-validated[a]	Count	Bcc	154	11	165
		Scc	14	161	175
	%	Bcc	93.3	6.7	100.0
		Scc	8.0	92.0	100.0

B

a. Cross validation is done only for those cases in the analysis. In cross validation, each case is classified by the functions derived from all cases other than that case.

b. 97.1% of original grouped cases correctly classified.

c. 92.6% of cross-validated grouped cases correctly classified.

Table 7.2: Classification results – malignant tumor (i.e., cancer) and SK (A); BCC and SCC (B).

groups (**Figure 7.3**). Indeed, the classification results shown in **Table 7.2B**, confirm the variation between these two groups. As observed, malignant tumor groups (BCC and SCC) can be distinguished with accuracy of 92.0% or higher.

In addition to leave-one-out validation method, the classification model was validated also with testing-training method. Specifically, 70% of the total number of absorption spectra was randomly chosen as testing set, i.e., group classification is known. Remaining 30% of the randomly selected absorption spectra were labeled as unknown, that is, without group classification. Results that were obtained are presented in **Table 7.3**. As can be seen, the classification accuracy is smaller in most investigated cases: 70% of malignant tumors were correctly classified, whereas only 63.3 and 61.5% of BCC and SCC, respectively, was correctly classified when compared to the SK. Interestingly, the greatest classification accuracy was found when discrimination between BCC and SCC was investigated. Specifically, 75.5% of BCC spectra and 84.6% of SCC spectra were correctly classified. Lower accuracy of classification, when training-testing validation method is used, is probably due to the lower number of samples used in the analysis. The strength of discrimination function for the training-testing method is therefore smaller compared to the leave-one-out validation method, where all spectra, but one, are used. Good classification results in case of BCC and SCC separation are most likely due to the higher variations in the absorption spectra between these groups, which can also be observed from their averaged spectra (see **Figure 7.3**). Classification results with different ratios of training-testing data were also explored. Namely, 80% or 90% of total spectral data were randomly chosen as a training set, and 20% or 10%, respectively, as a testing set.

CASE	**Tested groups**	**Correctly classified cases [%]**
1	BCC and SCC	**70.3**
	SK	48.8
2	BCC	**63.3**
	SK	69.8
3	SCC	**61.5**
	SK	55.8
4	BCC	**75.5**
	SK	**84.6**

Table 7.3: Classification results obtained with training (70%) - testing (30%) validation method.

The classification results when 80% and 90% of total absorption spectra were used as a training set are presented in **Table 7.4A** and **B**, respectively. As can be observed, the classification results are not improved by increasing the number of training data set, and similarly to the previously used training set (i.e., 70% of total number of data) the highest classification result is obtain when comparing BCC and SCC groups. Due to the fact that strength of the discriminant function for the training-testing method is smaller compared to the leave-one-out validation method, where all spectra, but one, are used as a training set, the lower accuracy in classification values for training-testing sets was to be expected. However, the classification values obtained were significantly lower than the ones obtained with leave-one-out analysis; namely all groups were classified with accuracy 81% or higher in the latter case (see **Tables 7.1** and **7.2**). Carefully inspecting the visible images for Seborrheic Keratosis group reveals that the images of the measured lesions differ significantly depending on the SK subgroup they belong to. Different anatomic structures can be clearly observed in **Figure 7.5A** which represents visible images of two SK subgroups that were analyzed in the study. Therefore it might be possible that NIR multispectral imaging microscope technique is sensitive enough to differentiate between subgroups of Seborrheic Keratosis. Indeed, when only one subgroup of SK is included in the data set, the classification results of training-testing validation method (i.e., 70% of total data set as training set and 30% of total data set as testing set) are significantly improved for classification of non-melanoma skin cancers (see **Figure 7.5B**). Specifically, 88% of BCC and 79% of SCC were correctly classified. Additionally, when BCC and SCC are grouped together (as cancer group) more than 80% of cases were correctly classified. Conversely, classification results are distinctively

CASE	**Tested groups**	**Correctly classified cases [%]**
1	BCC and SCC	**66.2**
	SK	51.7
2	BCC	**60.6**
	SK	51.7
3	SCC	**77.1**
	SK	44.8
4	BCC	**66.7**
	SK	**82.9**

A

CASE	**Tested groups**	**Correctly classified cases [%]**
1	BCC and SCC	**69.7**
	SK	50.0
2	BCC	**56.3**
	SK	57.1
3	SCC	**76.5**
	SK	64.3
4	BCC	**68.8**
	SK	**88.2**

B

Table 7.4: Classification results obtained with training-testing validation method; 80% training - 20% testing (A), 90% training - 10% testing (B).

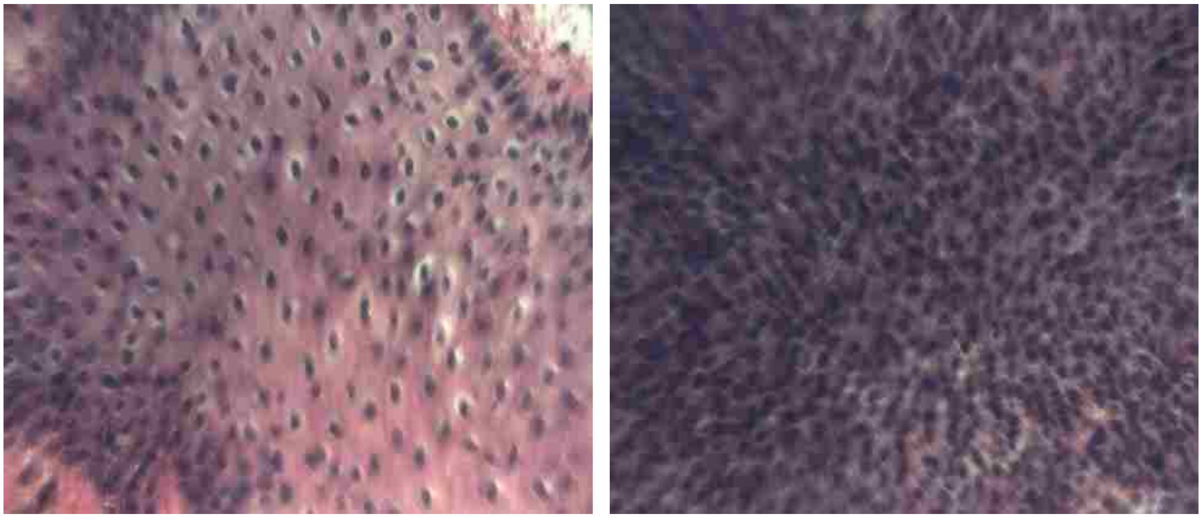

A

CASE	Tested groups	Correctly classified cases [%]
1	BCC and SCC	**80.2**
	SK	46.2
2	BCC	**87.8**
	SK	61.5
3	SCC	**78.8**
	SK	38.5

B

Figure 7.5: Visible images of Seborrheic Keratosis subgroups (A); classification results using training (70%) – testing (30%) validation method when only one SK subgroup is analyzed (B).

lower for SK, which is most probably due to the initially small number of data set for SK group (since only one subgroup has been included into the discriminant analysis).

An additional statistical method that was used for classification of three groups (BCC, SCC and SK) was PLSDA. Partial Least Square Discriminant Analysis is a statistical method very similar to LDA, however, it can perform dimensional reduction together with classification in a single calculation.[152] It is expected that LDA and PLSDA would produce similar results when the number of analyzed samples extents the dimensionality of the data set. However, when this is not the case, PLSDA statistical technique is likely to perform better.[156] That is why, in addition to LDA, the distinguishability between two different groups of samples was investigated using also PLSDA. After preprocessing the spectral data using standard functions available within Unscrambler X software package, analyzed cases were successfully classified into two completely distinguishable groups. **Figures 7.6 and 7.7** represent 2D and 3D scores plots of discrimination between BCC and SCC compared to SK, respectively. Furthermore, good discrimination was achieved also in the case when two malignant tumor groups (BCC and SCC) were compared to each other (see **Figure 7.8**). As can be observed for all three cases, the model can be successfully used for classification of malignant and benign skin tumors, that is, Basal Cell Carcinoma, Squamous Cell Carcinoma, and Seborrheic Keratosis. However, for accurate PLSDA classification of the complex spectra, the number of samples needed increases exponentially with the number of variables measured.[159] In cases when the number of the samples is less than that, PLSDA score plots tend to over fit, i.e., the model describes training data well, but the unknown samples are poorly classified.[159] The over-fitting of the PLSDA scores plot happens due

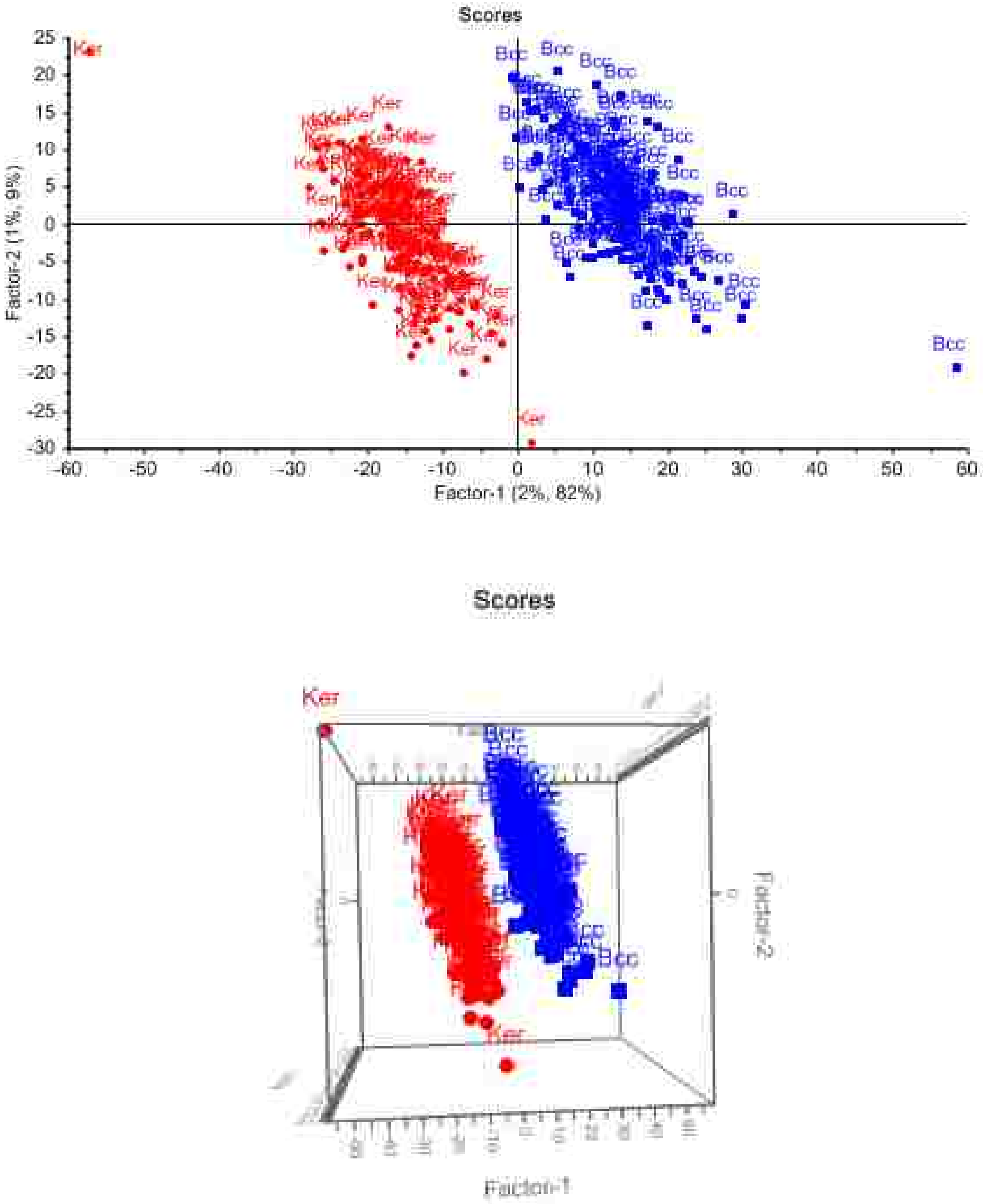

Figure 7.6: 2D and 3D scores plot of BCC and SK classification.

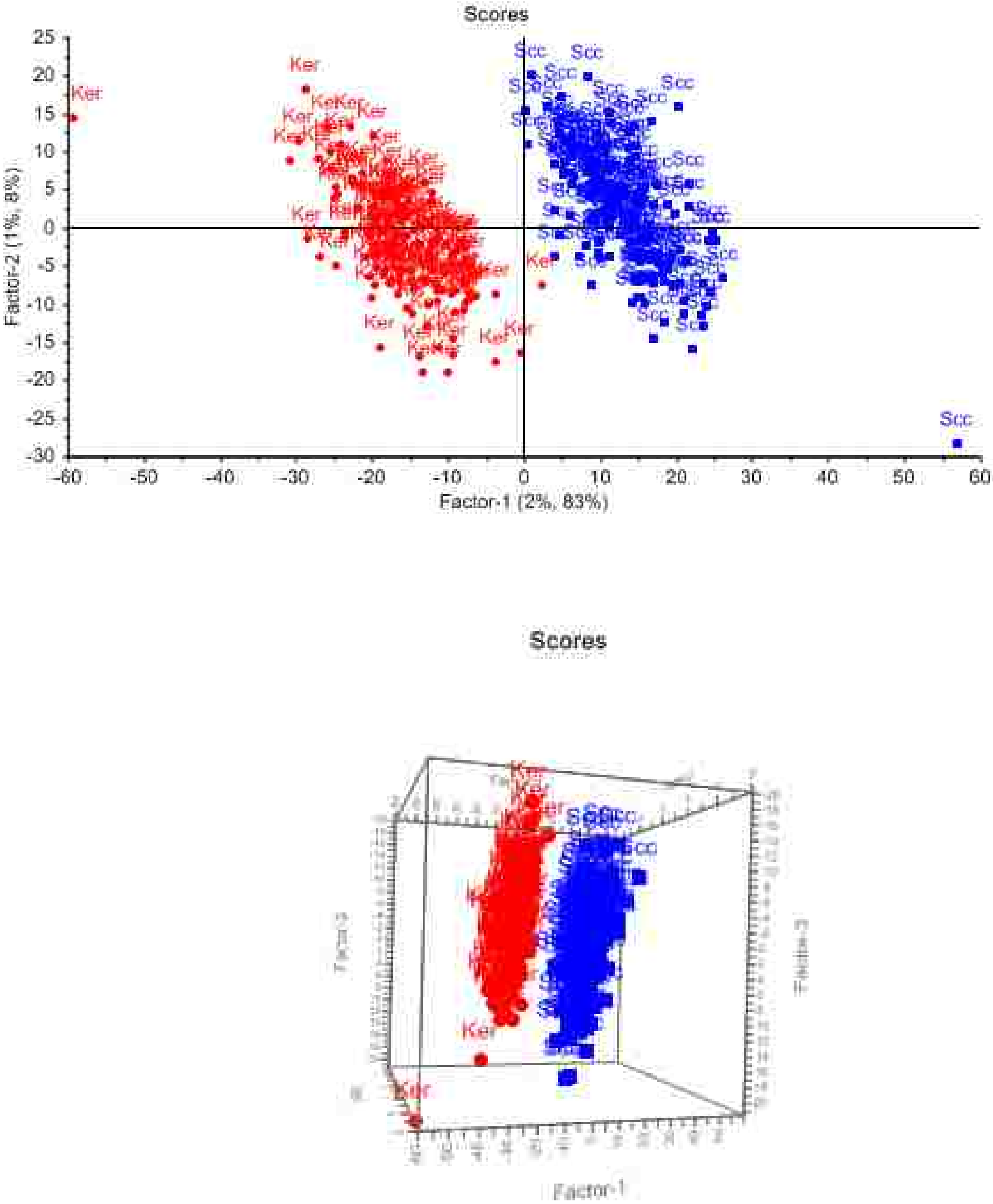

Figure 7.7: 2D and 3D scores plot of SCC and SK classification.

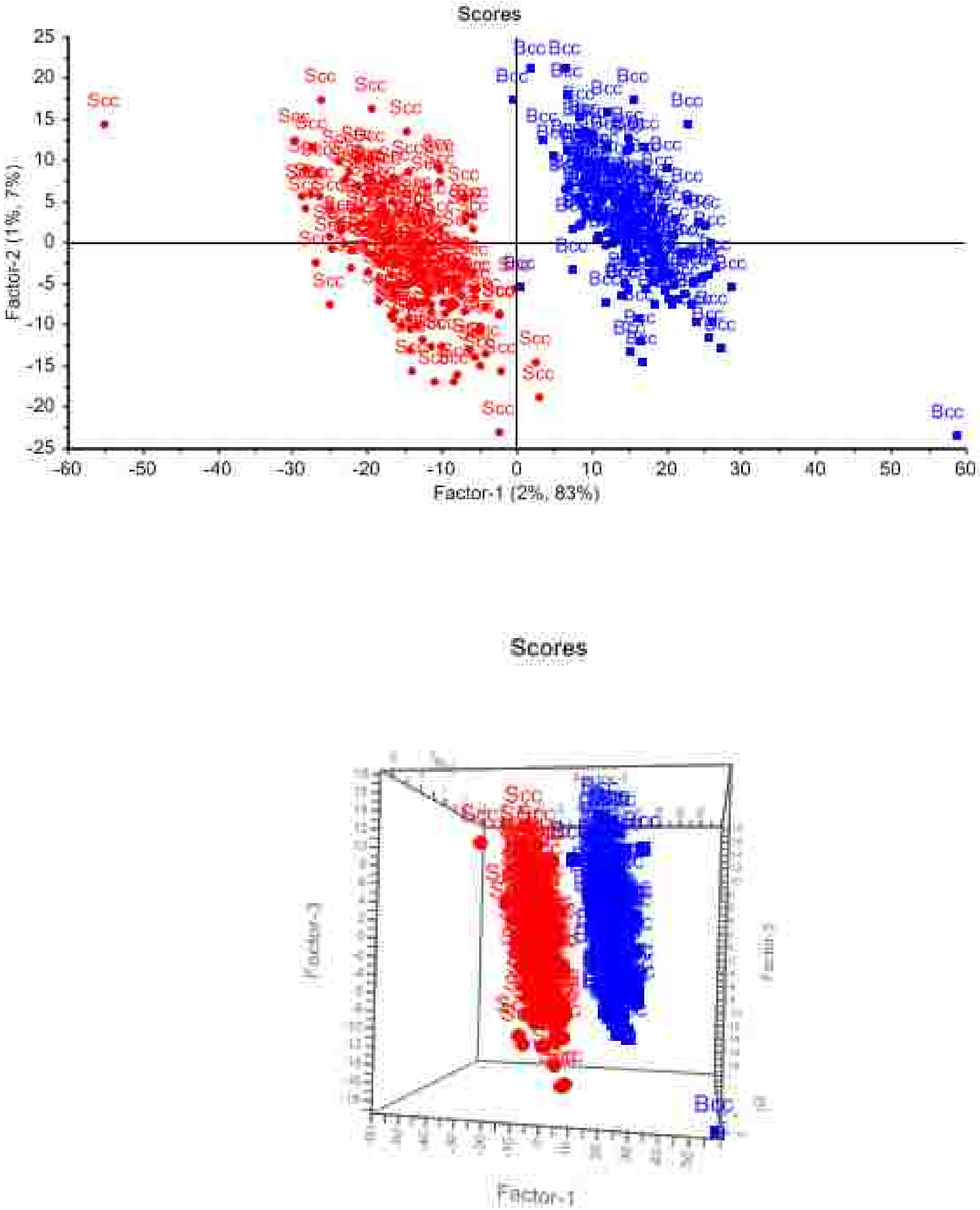

Figure 7.8: 2D and 3D scores plot of SCC and SK classification.

to the high dimensional megavariate space (depending on the number of measured variables) and, consequently, in such a high dimensional space, good separation between small number of samples can easily be obtained.[159] In our study, the number of variables and samples measured were 411 and 485, respectively. The over-fitting of the method can be investigated by comparing scores plot with predicted R-square values using full cross validation algorithm. The analyzed groups (i.e., BCC and SK, SCC and SK, BCC and SCC) show distinct separation when represented in scores plot. However, their R-square values are less than expected from scores plot; namely predicted R-square values are 0.75 for the former two cases (i.e., BCC and SK, SCC and SK) and 0.77 when BCC and SCC groups are analyzed. The results therefore indicate that PLSDA scores plots are indeed over-fitted to some degree and a larger sample set is needed in order to obtain valid PLSDA scores plots.

7.4 CONCLUSION

Near-infrared multispectral imaging microscope can be successfully used to observe and collect spectral information of Basal Cell Carcinoma, Squamous Cell Carcinoma and Seborrheic Keratosis. However, due to the complexity, low absorption intensities and signal to noise ratio, suitable statistical method, such as Linear Discriminant Analysis, is needed for classification of the spectral data into separate groups. Consequently, by employing validation method leave-one-out analysis, 83% or more non-melanoma skin cancers were correctly classified. Additionally, training-testing method of validation was investigated resulting in lower percentage of correctly classified cases. However, it was found that NIR multispectral imaging microscope technique can differentiate between subgroups of Seborrheic Keratosis, and when only one SK subgroup is used in the analyzed data set, significant improvement in prediction results can be observed. Specifically, more than 79% or non-melanoma cancers are correctly classified using training-testing validation method. The results seem to indicate that combination of NIR multispectral imaging microscope and LDA can be successfully used for classification of non-melanoma skin cancers, however SK groups have to be separated into individual subgroups and a large enough number of samples is consequently needed. In addition to LDA, Partial Least Square Discriminant Analysis was used for classification of the data. Scores plots provided distinct separation between analyzed groups; however, by investigating the R-square values, it was found that PLSDA scores plots tend to be over-fitted. Accurate PLSDA classification of the complex spectra requires number of samples to increase exponentially with the number of measured variables,[159] therefore, in order to obtain valid scores plots, a larger data set is needed.

REFERENCES

(1) *Chem. Eng. News* 1990, 68, 38-44; 1992, 70, 46-79; 2001, 79, 45-56, 79-97.

(2) Hinze, W. L. *Sep. Purif. Methods* 1981, 10, 159-237.

(3) Hinze, W. L.; Armstrong, D. W. *Ordered Media in Chemical Separation*, American Chemical Society, Washington DC, 1987.

(4) Wainer, I. W.; Ducharme, J.; Granvil, C. P.; Parenteau, H.; Abdullah, S. *J. Chromatogr. A* 1995, 694, 169-179.

(5) Tran, C. D.; Dotlich, M. J. *J. Chem. Educ.* 1995, 72, 71-73.

(6) Davankov, V. A. *Pure Appl. Chem.* 1997, 69, 1469-1474.

(7) Ward, T. J. *Anal. Chem.* 2006, 78, 3947-3956.

(8) Sicoli, G.; Jiang, Z.; Jicsinsky, L.; Schurig, V. *Angew. Chem. Int. Ed.* 2005, 44, 4092-4095.

(9) Ding, J.; Welton, T.; Armstrong, D. W. *Anal. Chem.* 2004, 76, 6819-6822.

(10) Ward, T. J.; Hamburg, D.M. *Anal. Chem.* 2004, 76, 4635-4644.

(11) Ward, T. J.; Rabai, C. M. *Methods Mol. Biol.* 2004, 243, 255-263.

(12) Yu, L.; Qin, W.; Li, S. F. Y. *Anal. Chim. Acta* 2005, 547, 165-171.

(13) Vaher, M.; Koel, M.; Kaljurand, M. *Electrophoresis* 2002, 23, 426-430.

(14) Mwongela, S. M.; Numan, A.; Gill, N. L.; Agbaria, R.A.; Warner, I. M. *Anal. Chem.* 2003, 75, 6089-6096.

(15) Mwongela, S. M.; Siminialai, N.; Fletcher, K. A.; Warner, I. M. *J. Sep. Sci.* 2007, 30, 1334-1342.

(16) Yanes, E. G.; Gratz, S. R.; Balwin, M. J.; Robinson, S. E.; Stalcup, A. M. *Anal. Chem.* 2001, 73, 3838-3844.

(17) Tran, C. D.; Kang, *J. Chromatogr. A* 2002, 978, 221-230.

(18) Tran, C. D.; Kang, J. *Chromatographia* 2003, 57, 81-86.

(19) Chankvetadze, B.; Burjanadze, N.; Crommen, J.; Blaschke, G. *Electrophoresis* 2001, 22, 3281-3285.

(20) Francois, Y.; Verenne, A.; Juillerat, E.; Villemin, D.; Gareil, P. *J. Chromatogr. A* 2007, 1155, 134-141.

(21) Tran, C. D. *Anal. Lett.* 2007, 40, 2447-2464.

(22) Wasserscheid, P.; Welton, T. (Eds.) *Ionic Liquids in Synthesis*, Wiley-VCH, Weinheim, Germany, 2003.

(23) Tran, C. D.; Lacerda, S. H. P. *Anal. Chem.* 2002, 74, 5337-5341.

(24) Tran, C. D.; Lacerda, S. H. P.; Oliveira, D. *Appl. Spectrosc.* 2003, 57, 152-157.

(25) Mele, A.; Tran, C. D.; Lacerda, S. H. P. *Angew. Chem. Int. Ed.* 2003, 42, 4364-4366.

(26) Tran, C. D.; Challa, S.; Franko, M. *Anal. Chem.* 2005, 77, 7442-7447.

(27) Tran, C. D.; Oliveira, D.; Yu, S. *Anal. Chem.* 2006, 78, 1349-1356.

(28) Tran, C. D.; Oliveira, D. *Anal. Biochem.* 2006, 356, 51-58.

(29) Frez, C.; Diebold, G. J.; Tran, C. D.; Yu, S. *J. Chem. Eng. Data* 2006, 51, 1250-1255.

(30) Skoog, D. A.; Holler, F. J.; Nieman, T. A.; *Principles of Instrumental Analysis*, Harcourt College Publishers, 1998.

(31) Davankov, V. A. *Chromatographia* 1989, 27, 475-482.

(32) Yu, S.; Lindeman, S.; Tran, C. D. *J. Org. Chem.* 2008, 73, 2576-2591.

(33) Saito, S.; Rebek, Jr. J. *Biorg. Med. Chem. Lett.* 2001, 11, 1497-1499.

(34) Rechavi, D.; Scarso, A.; Rebek, Jr. J. *J. Am. Chem. Soc.* 2004, 126, 7738-7739.

(35) Rudkevich, D. M.; Rebek, Jr. *J. Eur. J. Org. Chem.* 1999, 1991-2005.

(36) Clark, T. E.; Makha, M.; Sobolev, A. N.; Dalgarno, S. J.; Atwood, J. L.; Raston, C. L. *Crystal Growth & Design* 2007, 7, 2059-2065.

(37) Sokolieb, T.; Menyes, Y.; Roth, U.; Jira, T. *J. Chromatogr. A* 2000, 898, 35-52.

(38) Sokolieb, T.; Menyes, Y.; Roth, U.; Jira, T. *J. Chromatogr. A* 2002, 948, 309-319.

(39) Hashem, H.; Jira, T. *Combinat. Chem. High. Through. Screen.* 2007, 10, 387-396.

(40) Zhang, L. F.; Chen, L.; Lu, X. R.; Wu, C.Y.; Chen, Y. Y. *J. Chromatogr. A* 1999, 840, 225-233.

(41) Yang, W. C.; Yu, X. D.; Yu, A. M.; Chen, H. Y. *J. Chromatogr. A* 2001, 910, 311-318.

(42) Bianchi, F.; Mattarozzi, M.; Betti, P.; Bisceglie, F.; Careri, M.; Mangia, A.; Sidisky, L.; Ongarato, S.; Dalcanale, E. *Anal. Chem.* 2008, 80, 6423-6430.

(43) Compton, D. L.; Laszlo, J. A. *J. Electroanal. Chem.* 2002,520, 71-78.

(44) Quinn, B. M.; Ding, Z.; Moulton, R.; Bard, A. J. *Langmuir* 2002, 18, 1734-1742.

(45) Laszlo, J. A.; Compton, D. L. *Biotech. Bioeng.* 2001, 75, 181-186.

(46) Tran, C. D.; Mejac, I. *J. Chromatogr. A* 2008, 1204, 204-209.

(47) Armstrong, D. W.; He, L.; Liu, Y. S. *Anal. Chem.* 1999, 71, 3873-3876.

(48) Berthod, A.; He, L.; Armstrong, D. W. *Chromatographia* 2001, 53, 63-68.

(49) Tran, C. D.; Challa, S. *Analyst* 2008, 132, 455-464.

(50) Root, J. W.; Lee, E. K. C.; Rowland, F. S. *Science* 1964, 143, 676-678.

(51) Bruner, F.; Cartoni, G. P.; Liberti, A. *Anal. Chem.* 1966, 38, 298-303.

(52) Van Hook, W.; Kelly, M. E. *Anal. Chem.* 1965, 37, 508-511.

(53) Liberti, A.; Cartoni, G. P.; Bruner, F. *J. Chromatogr.* 1963, 12, 8-14.

(54) Shi, B.; Davis, B. H. *J. Chromatogr. A* 1993, 654, 319-325.

(55) Willets, K. A.; Van Duyne, R. P. *Annu. Rev. Phys. Chem.* 2007*, 58,* 267-297.

(56) Skrabalak, S. E.; Chen, J.; Sun, Y.; Lu, X.; Au, L.; Cobley, C. M.; Xia, Y. *Acc. Chem. Res.* 2008, *41*, 1587-1595.

(57) Sun, Y.; Xia, Y. *Anal. Chem.* 2002, *74*, 5297-5305.

(58) Zhu, M. Q.; Wang, L. Q.; Exarhos, G. J.; Li, A. D. Q. *J. Am. Chem. Soc.* 2004, 126, 2656-2657.

(59) O'Neal, D. P.; Hirsch, L. R.; Halas, N. J.; Payne, J. D.; West, J. L. *Cancer Lett.* 2004, 209, 171-176.

(60) Kim, J. H.; Lee, T. R. *Langmuir* 2007, 23, 6504-6509.

(61) Kim, J. H.; Bryan, W. W.; Lee, T. R. *Langmuir* 2008, 24, 11147-11152.

(62) Wiley, B.; Sun, Y.; Xia, Y. *Acc. Chem. Res*. 2007, 40, 1067-1076.

(63) Noguez, C. *J. Phys. Chem. C* 2007, 111, 3806-3819.

(64) Hu, M.; Chen, J.; Li, Z. Y.; Au, L.; Hartland, G. V.; Li, X.; Marquez, M.; Xia, Y. *Chem. Soc. Rev.* 2006, 35, 1084-1094.

(65) El-Sayed, M. A. *Acc. Chem. Res.* 2001, 34, 257-264.

(66) Graf, C.; Van Blaaderen, A. *Langmuir* 2002, 18, 524-534.

(67) Oldenburg, S. J.; Averitt, R. D.; Westcott, S. L.; Halas, N. J. Chem. Phys. Lett. 1998, 288, 243-247.

(68) Gorelikov, I.; Field, L. M.; Kumacheva, E. J. *Am. Chem. Soc.* 2004, 126,15938-15939.

(69) Klar, T.; Perner, M.; Grosse, S.; von Plessen, G.; Spirkl, W.; Feldman, J. *Phys. Rev. Lett.* 1998, *80*, 4249-4252.

(70) Sonnichsen, C.; Franzl, T.; Wilk, T.; von Plessen, G.; Feldman, J.; Wilson,O.; Mulvaney, P. *Phys. Rev.* 2002, *88*, 077402/1-077402/4.

(71) N'Gom, M.; Ringnalda, J.; Mansfield, J. F.; Agarwal, A.; Kotov, N.; Zaluzec,N. J.; Norris, T. B. *Nano Lett.* 2008, *8*, 3200-3204.

(72) Muskens, O. L.; Bachelier, G.; Fatti, N. D.; Vallee, F.; Brioude, A.; Jiang, X.; Pileni, M. P. *J. Phys. Chem. C* 2008, *112*, 8917-8921.

(73) Tran, C. D.; Cui, Y.; Smirnov, S. *Anal. Chem.* 1998, *70*, 4701-4708.

(74) Tran, C. D. *J. Near-Infrared Spectrosc.* 2000, *8*, 87-99.

(75) Khait, O.; Smirnov, S.; Tran, C. D. *Anal. Chem.* 2001, *73*, 732-739.

(76) Tran, C. D. *Appl. Spectrosc. Rev.* 2003, *38*, 133-153.

(77) Tran, C. D. *Anal. Lett.* 2005, *38*, 735-752.

(78) Morris, M. D. *Microscopic and Spectroscopic Imaging of the Chemical State*; Marcel Dekker: New York, 1993.

(79) Tran, C. D. *Anal. Chem.* 1992, *64*, 971A-981A.

(80) Tran, C. D. *Talanta* 1997, *45*, 237-248.

(81) Kihm, K. D.; Banerjee, A.; Choi, C. K.; Takagi, T. *Exp. Fluids* 2004, 37, 811-814.

(82) Tuteja, A.; Mackay, M. E.; Narayanan, S.; Asokan, S.; Wong, M. S. *Nano Lett.* 2007, 7, 1276-1281.

(83) Ertas, G.; Suzer, S. J. *Nanosci. Nanotechnol.* 2007, 7, 4333-4338.

(84) Sanghamitra, N. J. M.; Mazumdar, S. *Langmuir* 2008, 24, 3439-3445.

(85) Ghosh, S. K.; Nath, S.; Kundu, S.; Esumi, K.; Pal, T. *J. Phys. Chem. B* 2004, 108, 13963-13971.

(86) Mie, G. *Ann. Phys*. 1908, *25*, 377-445.

(87) Aden, A. L.; Kerker, M. *J. Appl. Phys.* 1951, *22*, 1242-1246.

(88) Mulvaney, P. *Langmuir* 1996, *12*, 788-800.

(89) Miller, M. M.; Lazarides, A. A. Abstract of Papers, 231st ACS National Meeting, Atlanta, GA, 2006.

(90) Miller, M. M.; Lazarides, A. A. *J. Phys. Chem. B* 2005, *109*, 21556-21565.

(91) Thomas, K. G.; Zajicek, J. ; Kamat, P. V. *Langmuir* 2002, 18, 3722-3727.

(92) Ghosh, S. K.; Nath, S.; Kundu, S.; Esumi, K.; Pal, T. *Appl. Spectrosc.* 2005, 59, 844-847.

(93) Kim, J. H.; Lee, T. R. *Chem. Mater.* 2004, 16, 3647-3651.

(94) Liu, S.; Liu, X.; Li, F.; Fang, Y.; Wang, Y.; Yu, J. *J. Appl. Polym. Sci.* 2008, 109, 4036-4042.

(95) Sun, B.; Lin, Y.; Wu, P.; Siesler, H. W. *Macromolecules* 2008, 41, 1512-1520.

(96) Kawasaki, H.; Sasaki, S.; Maeda, H. *Langmuir* 1998, 14, 773-776.

(97) Suzuki, M. *Nature* 1990, 344, 562-565.

(98) Pelton, R. *Adv. Colloid Interface Sci.* 2000, 85, 1-33.

(99) Jeong, B.; Bae, Y. H.; Lee, D. S.; Kim, S. W. *Nature* 1997, 388, 860-862.

(100) Bergbreiter, D. E.; Case, B. L.; Liu, Y. S.; Caraway, J. W. *Macromolecules* 1998, 31, 6053-6062.

(101) Zhou, J.; Cai, T.; Tang, S.; Marquez, M.; Hu, Z. *Langmuir* 2006, 22, 863-866.

(102) Inoue, T.; Chen, G.; Nakamae, K.; Hoffman, A. S. *J. Controlled Release* 1997, 49, 167-176.

(103) Winnik, F. M. *Polymer* 1990, 31, 2125-2134.

(104) Pelton, R. H.; Pelton, H. M.; Morphesis, A.; Rowell, R. L. *Langmuir* 1989, 5, 816-818.

(105) De Groot, C. J.; Van Luyn, M. J. A.; Van Dijk-Wolthuis, W. N. E.; Cadee, J. A.; Plantinga, J. A.; Otter, W. D.; Hennink, W. E. *Biomaterials* 2001, 22, 1197-1203.

(106) Shibayama, M.; Mizutani, S.; Nomura, S. *Macromolecules* 1996, *29*, 2019-2024.

(107) Zhou, S.; Chu, B. *J. Phys. Chem. B* 1998, *102*, 1364-1371.

(108) Snowden, M. J.; Chowdhry, B. Z.; Vincent, B.; Morris, G. E. *J. Chem. Soc. Faraday Trans.* 1996, *92*, 5013-5016.

(109) Lamanna, R.; Sobolev, A. P.; Masci, G.; Bontempo, D.; Crescenzi, V.; Serge, A. L. *Polymer Preprints* 2003, *44*, 406-407.

(110) Datta, A.; Das, S.; Mandal, D.; Pal, S.; Bhattacharyya, K. *Langmuir* 1997, *13*, 6922-6926.

(111) Iwai, K.; Hanasaki, K.; Yamamoto, M. *J. Luminescence* 2000, *87-89*, 1289-1291.

(112) Masci, G.; Cametti, C. *J. Phys. Chem. B* 2009, *113*, 11421-11428.

(113) Fisher, M.; Tran, C. D. *Anal. Chem.* 1999, *71*, 953-959.

(114) Fisher, M.; Tran, C. D. *Anal. Chem.* 1999, *71*, 2255-2261.

(115) Tran, C. D.; Grishko, V. I.; Challa, S. *J. Phys. Chem. B* 2008, *112*, 14548-14559.

(116) Mejac, I.; Bryan, W. W.; Lee, T. R.; Tran, C. D. *Anal. Chem.* 2009, *81*, 6687-6694.

(117) Schmidt, P.; Dybal, J.; Trchova, M. *Vib. Spectrosc.* 2006, *42*, 278-283.

(118) Czarmecki, M. A.; Haufa, K. Z. *J. Phys. Chem. A* 2005, *109*, 1015-1021.

(119) Langford, V. S.; McKinley, A. J.; Quckenden, T. I. *J. Phys. Chem. A* 2001, *105*, 8916-8921.

(120) Waggener, W. C. *Anal. Chem.* 1956, *30*, 1569-1570.

(121) Harvey, D. K.; Feierabend, K. J.; Black, J. C.; Vaida, V. *J. Mol. Spectrosc.* 2005, *229*, 151-157.

(122) Geuken, B.; Meersman, F.; Nies, E. *J. Phys. Chem. B* 2008, *112*, 4474-4477.

(123) Peppas, N. A.; Huang, Y.; Torres-Lugo, M.; Ward, J. H.; Zhang, J. *Annu. Rev. Biomed. Eng.* 2000, *2*, 9-29.

(124) Hirotsu, S.; Hirokawa, Y.; Tanaka, T. *J. Chem. Phys.* 1987, *87*, 1392-1395.

(125) Hirokawa, Y.; Tanaka, T. *J. Chem. Phys.* 1984, *81*, 6379-6380.

(126) Li, Y.; Tanaka, T. *Annu. Rev. Mater. Sci.* 1992, *22*, 243-277.

(127) Jones, C. D.; Lyon, L. A. *J. Am. Chem. Soc.* 2003, 125, 460-465.

(128) Jones, C. D.; Lyon, L. A. *Macromolecules* 2003, 36, 1988-1993.

(129) Kreibig, U.; Vollmer, M. *Optical Properties of Metal Clusters*, Springer, Berlin, Germany, 1995.

(130) Skrabalak, S. E.; Chen, J.; Au, L.; Lu, X.; Li, X.; Xia, Y. *Adv. Mater.* 2007, 19, 3177-3184.

(131) Elghanian, R.; Storhoff, J. J.; Mucic, R. C.; Letsinger, R. L.; Mirkin, C. A. *Science* 1997, 277, 1078-1081.

(132) Skrabalak, S. E.; Au, L.; Lu, X.; Li, X.; Xia, Y. *Nanomedicine* 2007, 2, 657-668.

(133) Jones, C. D.; Lyon, L. A. *Macromolecules* 2000, 33, 8301-8306.

(134) Skrabalak, S. E.; Au, L.; Li, X.; Xia, Y. *Nature Protoc.* 2007, 2, 2182-2190.

(135) Lapotko, D. *Fut. Med.* 2009, 4, 813-845.

(136) Lyon, L. A.; Debord, J. D.; Debord, S. B.; Jones, C. D.; McGrath, J. G.; Serpe, M. J. *J. Phys. Chem. B* 2004, 108, 19099-19108.

(137) Mejac, I.; Park, H. H.; Bryan, W. W.; Lee, T. R.; Tran, C. D. *Anal. Chem.* 2010, 81, 6687-6694.

(138) *American Cancer Society: Cancer Facts and Figures* - 2010, Atlanta, GA, American Cancer Society, 2010.

(139) Ratner, D.; Peacocke, M.; Zhang, H.; Ping, X. L.; Tsou, H. C. *J. Am. Acad. Dermatol*. 2001, 44, 293-297.

(140) Marghoob, A.; Kopf, A. W.; Bart, R. S.; Sanfilippo, L.; Silverman, M. K.; Lee, P.; Levy, E.; Vossaert, K. A.; Yadav, S.; Abadir, M. *J. Am. Acad. Dermatol.* 993, 28, 22-28.

(141) Gallagher, R. P.; Hill, G. B.; Bajdik, C. D.; Fincham, S.; Coldman, A. J.; McLean, D. I.; Threlfall, W. J. *Arch. Dermatol*. 1995, 131, 157-163.

(142) Abeloff, M. D.; Armitage, J. O.; Niederhuber, J. E.; Kastan, M. B.; McKenna, W. G.; *Abelloff's Clinical Oncology*, Churchill Livingstone, 2008.

(143) Habif, T. P.; *Clinical Dermatology*, Mosby, 2009.

(144) Neville, J. A.; Welch, E.; Leffell, D.*J. Nat. Clin. Pract. Oncol*. 2007, 4, 462-469.

(145) Ridky, T. W. *J. Am. Acad. Dermatol.* 2007, 57,484-501.

(146) Gallagher, R. P.; Ma, B.; McLean, D. I.; Yang, C. P.; Ho, V.; Carruthers, J. A.; Warshawski, L. M. *J. Am. Acad. Dermatol.* 1990, 23, 413-421.

(147) Gniadecka, M.; Wulf, H. C.; Nielsen, O. F.; Christensen, D. H.; Hercogova, J. *Photochem. Photobiol.* 1997, 66, 418-423.

(148) Lauridsen, R. K.; Everland, H.; Nielsen, L. F.; Engelson, S. B.; Norgaard, L. *Skin Res. Technol.* 2003, 9, 137-146.

(149) Sahlin, K. *Int. J. Sports Med.* 1992, 13, S157-S160.

(150) Mancini, D. M.; Bolinger, L.; Li, H.; Kendrick, K.; Chance, B.; Wilson, J. R. *J. Appl. Physiol.* 1994, 77, 2740-2747.

(151) Dreassi, E.; Ceramelli, G.; Fabbri, L.; Vocioni, F.; Bartalini, P.; Corti, P. *Analyst* 1997, 122, 767-770.

(152) Berman, E. S. F.; Wu, L.; Fortson, S. L.; Kulp, K. S.; Nelson, D. O.; Wu, K. J. *Surf. Interface Anal.* 2009, 41, 97-104.

(153) Klecka, W. R.; Discriminant Analysis, Sage Publications, 1980.

(154) Huang, Z.; Lui, H.; McLean, D. I.; Korbelik, M.; Zeng, H. *Photochem. Photobiol.* 2005, 81, 1219-1226.

(155) Skrobot, V. L.; Castro, E. V. R.; Pereira, R. C. C.; Pasa, V. M. D.; Fortes, I. C. P. *Energy Fuels* 2007, 21, 3394-3400.

(156) Sorich, M. J.; Miners, J. O.; McKinnon, R. A.; Winkler, D. A.; Burden, F. R., Smith, P. A.; *J. Chem. Inf. Comput. Sci.* 2003, 43, 2019-2024.

(157) Zhao, J.; Huang, Z.; Zeng, H.; McLean, D.; Lui, H. *Proc. SPIE* 2008, 6842, 684209/1-648209/7.

(158) Ye, J.; Janardan, R.; Li, Q. *Adv. Neural Inf. Process. Syst.* 2004, 17, 1569-1576.

(159) Barker, M.; Rayens, W. *J. Chemometr.* 2003, 17, 166-173.

(160) Westerhuis, J. A.; Hoefsloot, H. C. J,; Smit, S.; Vis, D. J.; Smilde, A. K.; van Velzen, E. J. J.; van Duijnhoven, J. P. M.; van Dorsten, F. A. *Metabolomics* 2008, 4, 81-89.